Structural health monitoring of adhesive bonded single-lap joints in composite materials by fiber-optic distributed sensing system

（分布型光ファイバセンサを用いた複合材料シングルラップ接着継手の構造ヘルスモニタリング）

Submitted to the Graduate School of Engineering,
The University of Tokyo for the Degree of Doctor of Engineering,

Department of Systems Innovation
The University of Tokyo

寧　霄光

Ning Xiaoguang

December 2013

Contents

Chapter 1

Introduction

1.1. Background

The use of adhesive-bonded joints especially in composite structures has been increasing in recent year for decent properties such like light in weight, less source of stress concentration and better fatigue properties. However concerns in the practical application, such as joint quality variety depending on manufacturing, and joint condition sensitive to environmental degradation, affect reliability and applicability of adhesive-bonded joints.

The common defects in adhesive-bonded joints, which can cause joint failure, such as cracks often occur in adhesive layer or at adhesive/adherend interface. The complex structure and poor disassembly of joint make the inspection and maintenance difficult, thus effort has been put on the development of non-destructive inspection (NDI) techniques for adhesive-bonded joints.

However, although the performances of NDI techniques on detecting defects in bonding area are well demonstrated, they have several disadvantages. The major one is that, the NDI system is usually complex and huge, which consists of many devices and sensors. The complex device installation and wiring works make the NDI usually used for on-ground inspection, which induces two problems, the first is high inspection cost especially for aging structures needing intensively inspection, the second is the faint effect on preventing catastrophic failure of the structure during service, which is relatively often for adhesive-bonded joints in aggressive environment or with bad initial joint quality.

In order to solve these problems, an inspection/maintenance method is high desired, which provides real-time monitoring of the joint conditions since manufactured to detect defects to aid in the further inspection, strength assessment, and life prediction. Considering the desires, the modern maintenance strategies suggesting real-time on-board monitoring and automatic structural condition assessment such as structural health monitoring (SHM) are expected to give a better solution for adhesive-bonded joints.

Among the sensing techniques for SHM, optical fiber sensor (OFS) is promising for SHM of joint for two unique features: the small sensor size, which makes it easy to be embedded into bonding area for measurement, and the ability of distributed sensing, which enables high precision of structural/mechanical condition monitoring and damage detection.

Among OFSs, the long length fiber Bragg grating (FBG) sensor associated with distributed sensing technique based on optical frequency domain reflectometry (OFDR) is considered to be an ideal technique for adhesive-bonded joints for three reasons. First, it can provide strain distribution

measurement along FBG with spatial resolution of less than 1 mm, which is very high even among the OFSs. Second, the system is relatively simple comparing with other high-spatial-resolution OFS techniques, which means it is easier to be installed on structure for on-board monitoring for structures with limited space such as airplanes. Third, it can record all the information in each measurement, which means not only strain but also other information such as FBG spectra can be obtained during monitoring, thus more information of structure can be estimated.

However, the SHM method for adhesive-bonded joints using OFS hasn't been given enough attention. The dynamic continuous measurement for joint condition monitoring and the damage detection based on the measurement using OFS, which are the important steps of SHM, haven't been demonstrated.

Therefore, this study was carried out, and the ultimate objective is to develop an SHM method for adhesive-bonded joints using OFS sensing techniques.

1.2. Objectives of this study

The ultimate objective of this study is to develop an SHM method for adhesive-bonded joints using OFS sensing techniques.
The SHM method development consists of several steps including operational evaluation of structure, sensing technique development, data acquisition, data analysis and diagnostics, structural condition assessment, damage detection and report, etc. This is a huge work, and it is difficult to achieve all the steps. Thus in this study, I only focused on the fundamental but important steps.

The specific goals/objectives are shown as following:

(1). Study objects analysis and OFS technique development
There are many forms of adhesive-bonded joints specialized in different load bearing, instead of discussing all the forms this study will only focus on a specific joint form. The joint form and target damage of it should be representative, so the developed method may be applied to other joint forms. In order to determine that, background information of adhesive-bonded joints need to be studied.
There are many kinds of OFS associated with different interrogation methods, it is important to decide which one to use. Background study is necessary to determine the OFS technique that most suit purposes of this study. After that, the OFS sensing system for this study should be developed considering the acquirements of this study based on the chosen technique.

(2). Dynamic strain distribution measurement in adhesive-bonded joint
To achieve real-time monitoring, the dynamic measurement of damage indicator, the strain distribution, in adhesive-bonded joints using developed OFS sensing system should be carried out. Before the measurement, the preparation works including specimen manufacturing, OFS embedment and test design need to be done carefully. After the measurement, besides the result discussion, the measured data should be used to evaluate the measurement and sensing system in aspects such as accuracy and stability.

(3). Damage detection and further applications
The detection method of target damage based on analysis of damage indicator should be developed. And the measurements in tests should be used to estimate the damage occurred in tests to confirm the detection method. After that, based on the measurements analysis, more damage detection methods may be proposed. And besides target damage detection, more subjects which the OFS sensing technique may achieve should be considered.

1.3. Construction of this thesis

The construction of this thesis is shown in Fig. 2-1.

In chapter 1, the background and objectives of this study are briefly introduced.

In chapter 2, the background information of adhesive-bonded joint and SHM are studied. Based on discussion, the joint form and target damage considered in this study are specified, the specific objectives for this study are defined.

In chapter 3, the background information of OFS is introduced. The principle of OFS sensing technique involved in this study is introduced in detail. The development process of the OFS sensing system for this study is introduced in aspects of system specification, development and evaluation.

In chapter 4, the OFS embedment procedure for adhesive-bonded joint is developed and introduced. The joint specimen with embedded FBG in interface between adhesive and adherend according to the procedure is made. And based on the embed position control, the three-dimensional finite element model of joint including embedded OFS is built to aid measurement analysis. The specimen is subjected to static and cyclic load, during tests the developed sensing system is employed for dynamic strain distribution measurement. The measurement accuracy and sampling rate are evaluated.

In chapter 5, a damage detection method based on strain distribution variation is proposed, and the cracks occurred in cyclic load test are estimated by it using embedded FBG measurement results. The irregular FBG spectra around crack front and overlap end during tests are investigated, another crack detection method based on examining FBG spectra is proposed. Three future subjects to improve applicability of OFS sensing technique developed in this study in SHM for adhesive-boned joints are proposed.

In chapter 6, the final conclusions of this study are made.

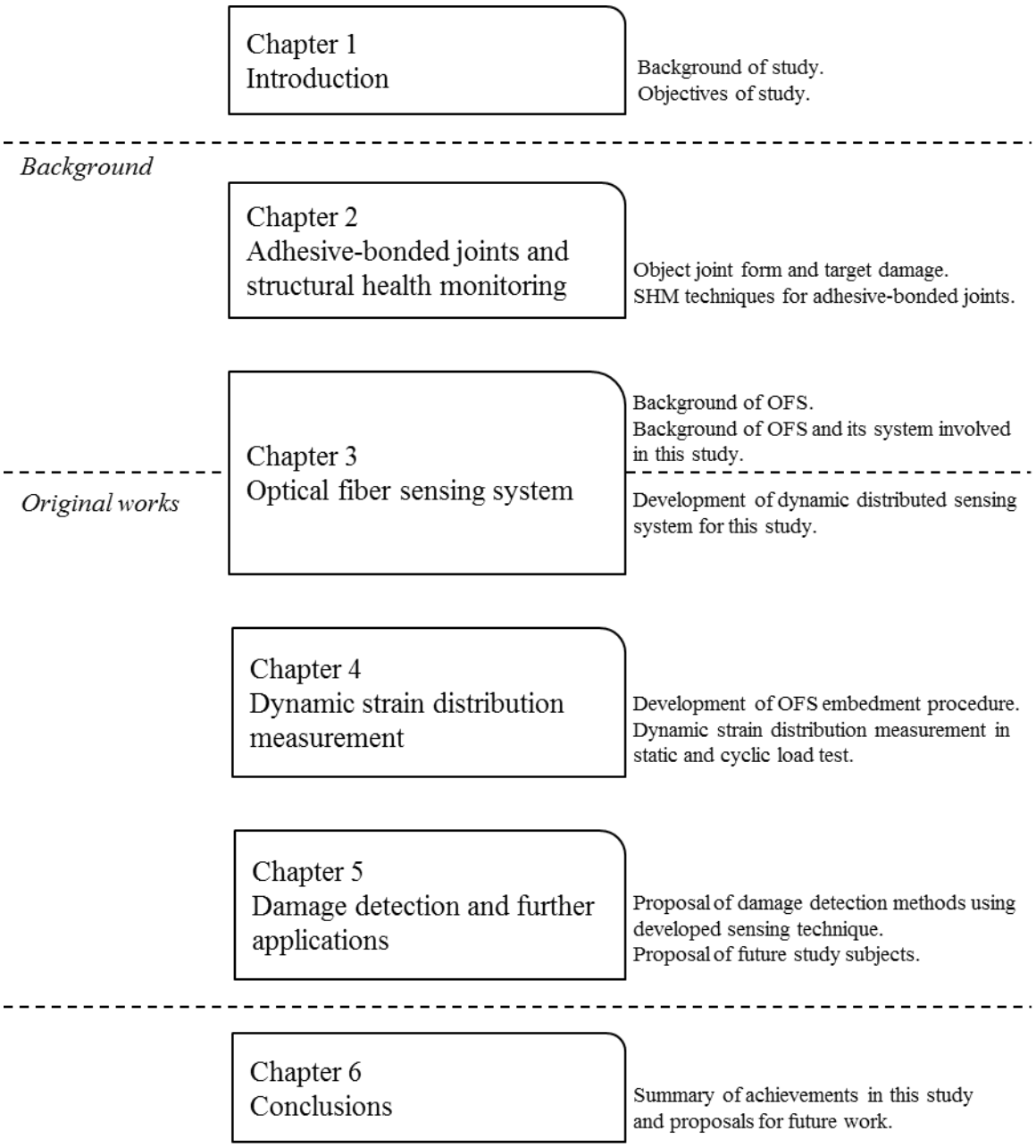

Fig. 2-1. Construction of this thesis

Chapter 2

Adhesive-bonded joints and structural health monitoring

2.1. Adhesive-bonded joints

The adhesive-bonded joint is an important joint form with many advantages such as light weight, less stress concentration sources, smooth adherend surface and so on. The use of adhesive-bonded joints has been increasing in recent years for structure weight reduction and energy conservation, especially associated with composite materials which has light weight, high strength, and attracts engineers' attention in many industrial fields.

However in practical applications, the applicability of adhesive-bonded joints is affected by concerns such as the initial joint strength which highly depends on manufacturing and long-term joint integrity which is sensitive to service environment. The inspection/maintenance methods are highly desired to improve the applicability of adhesive-bonded joints

In this chapter, the basic information of adhesive-bonded joints is introduced in aspects of adhesion principles, joint geometric configurations, joint strength, defect types and failure modes, theoretical and numerical analysis methods and non-destructive inspection techniques. The study object and target damage are defined in summary of the first section. The specific objectives are defined in summary of the second section

2.1.1. Joining methods and Joints

The most structures consist of a number of individual components which must be connected to form an integral load transmission path. These connections are often referred to as joints[1]. According to the design of structure, the joints can be achieved in many methods, mechanical fastening such as bolting and riveting, welding or brazing for connecting metallic components, and the adhesive-bonded joints. Each joint form can be the weakest member and need careful design, manufacture and maintenance to keep the structure from catastrophic failure.

Mechanical fastening

The mechanical fastening employs a variety of fasteners such as nuts and bolts, screws and rivets to assemble the individual components and transmit load. It can be applied in various structures and materials, and particularly suitable for thin sheet sections. The manufacture of mechanical fastening can be simple and controllable, and the disassembly for inspection after manufacture is possible. However, a hole or space in other shapes on the substrates is needed for fastener, for which the strength of the structure can be influenced. During service, the stress concentration occurs on substrates and the fatigue durability is relatively low[2].

In mechanical fastening, the load is transmitted at the contact surface between the hole on substrate and fastener, so the joint strength usually depends on the strength of contact surface of substrate and shear strength of fastener. The failure mode of mechanical fastening depends on parameters such as the load form and direction, joint geometric configuration and environmental conditions. Some typical failure modes are shown in Fig. 2-1.

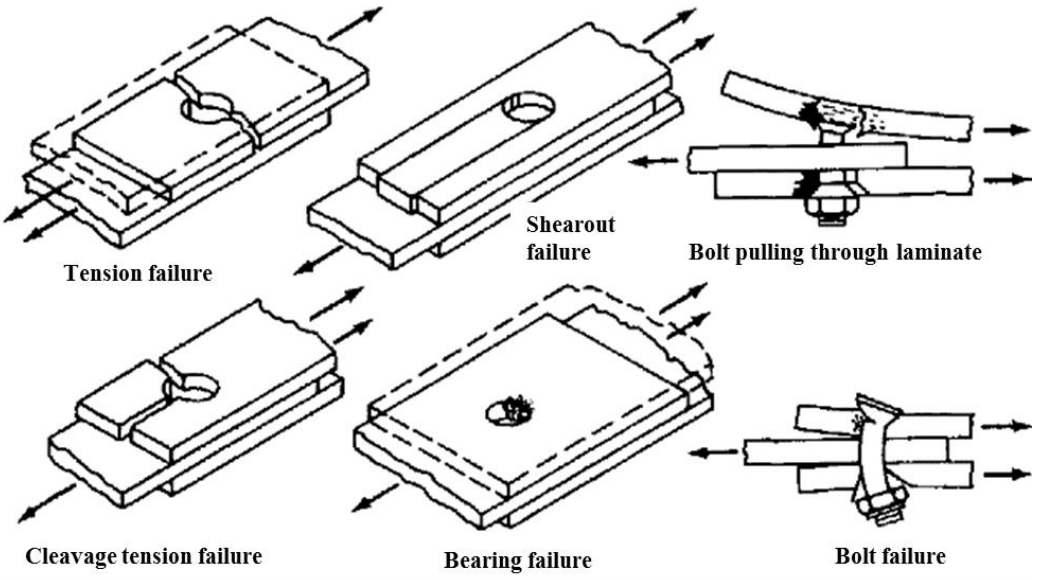

Fig. 2-1. Typical failure modes of mechanical fastening joints[2]

Welding

Welding is a process which joins materials, usually metals, by melting the work pieces and adding a filler material to form a pool of molten material that becomes a joint after cooling. The process is usually accompanied by appreciable interatomic penetration takes place at the original boundary surfaces of materials. After welding, the boundaries more or less disappear, and integrating crystals develop across them. The strength of welding joint is generally higher than mechanical fastening joint, and the air tightness and water tightness are better. On the other hand, problems such as the residual

stress generates in welding region due to thermal expansion of substrate during welding process and joint quality depending on manufacture skill can affect the joint reliability.

The welding joint can be achieved in various geometric configurations, for examples, several types of arc welding joint are shown in Fig. 2-2. There are many types of welding such as metal arc, atomic hydrogen, submerged arc, resistance butt, flash, spot, stitch, stud and projection. The arc welding and spot welding are two common types widely used in many industrial fields.

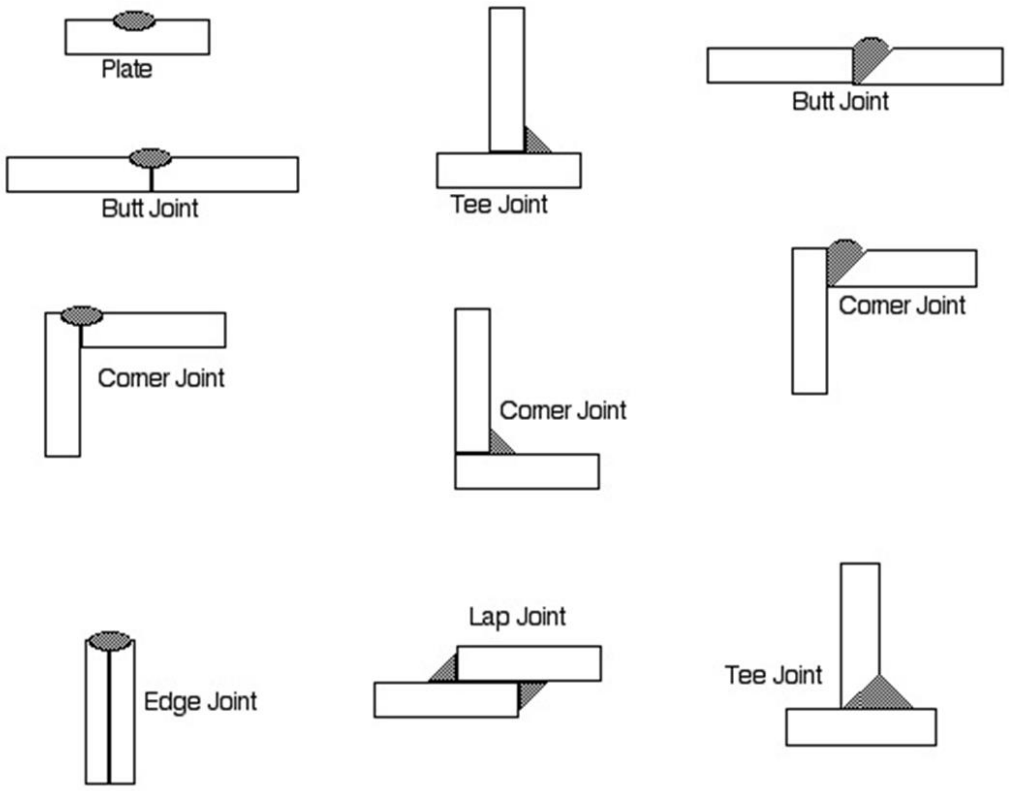

Fig. 2-2. Typical welding joint forms[2]

Adhesive bonding

Adhesive bonding employs adhesive between two or more adherends to join them by adhesive force after adhesive curing. Comparing with mechanical fastening using rivets or screws which provides point joining at contact surface between fastener and substrates, the adhesive bonding provides area joining at bonding area by which stress concentration can be reduced. Comparing with welding which is usually applied to metal materials, the adhesive bonding has much wider application range and can bond dissimilar materials. In many industrial fields, adhesive bonding enables development of innovative design concepts, structural configurations and new material exploitation for its unique features shown in

Table 2-1. The limitations which need to be considered when design and apply structure involving

adhesive bonding are also shown.

In recent years, for the increasing concern about environment and energy, adhesive bonding is considered as a promising joining method for structures especially the transportation means to reduce the structure weight and energy cost. The weight of adhesive is lighter than fastener and adding material in welding, and adhesive bonding can be applied to join the high-strength light-weight advanced materials such as honeycomb structures and fiber reinforced plastic (FRP) composite materials[3].

On the other hand, the quality of adhesive bonding can be various depending on manufacturing. During manufacturing, for adhesive, the adhesive quality, curing conditions, cooling conditions, filet control and adhesive layer thickness can affect the joint quality. And for adherends, the adherend material and surface treatment can cause large influence. Thus the quality evaluation after manufacturing is important for each adhesive-bonded joint in order to manage the strength and capacity of the whole structure. However, the disassembly of adhesive-boned components can be difficult, for which inspection techniques such as non-destructive inspection (NDI) techniques are highly desired. During service, the strength and service life of adhesive-bonded joint are sensitive to environmental degradation and the mechanical condition monitoring techniques are considered to be important to avoid catastrophic failure[45].

Table 2-1. Advantages and limitations of adhesive-bonded joints

Advantages	Limitations
Ability to form light weight, strong and stiff structures	Cannot be disassembled
Ability to join dissimilar materials	Residual stresses due to manufacturing
Improved stress distribution, no stress concentration in adherends	Limits to thickness joined with simple configurations
Enhanced fatigue properties due to improved stress distribution	Sensitive to peel or through thickness stress
Improved corrosion resistance	Poor resistance to elevated temperature and fire
Smooth surface finishes	Prone to environmental degradation
Bonding process can be automated, cost-effective joining	Inspection can be difficult

2.1.2. Adhesive-bonded joint

Adhesive and adhesion

An adhesive may be defined as the material which can be applied to surfaces of materials in order to join them together and resist separation. Adhesive is the general term including cement, glue, paste, etc. and they are used interchangeably. The term adhesion often refers to the attraction between the substances, it is the interatomic and intermolecular interaction at the interface of two surfaces[6]. Adhesion is a multi-disciplinary topic including surface chemistry, polymer chemistry, physics, rheology and other subjects. It is difficult to explain the adhesion phenomena in a single mechanism, the investigation and debate on it have lasted for decades. There are mainly six mechanisms or theories that could provide explanation for the adhesion process, and each of them seems to be promising in explaining particular phenomena associated with adhesive bonding.

a) Mechanical interlocking model
b) Electronic theory or electrostatic theory
c) Weak boundary layer theory
d) Adsorption theory
e) Diffusion or interdiffusion theory
f) Chemical bonding theory

These models are helpful not only for the understanding of adhesion phenomena but also for optimal bonding procedure design.

Joint configuration and stress distribution

The materials being bonded are usually referred to as the substrates or adherends. The latter term is commonly used when the materials are considered as a part of the joint. Adhesive-bonded joints are typically achieved by bonding thin substrates together in a lap or strap-joint geometry when the substrates are in the same plane. Some common joint forms, lap strap, step and scarf, are shown in Fig. 2-3.

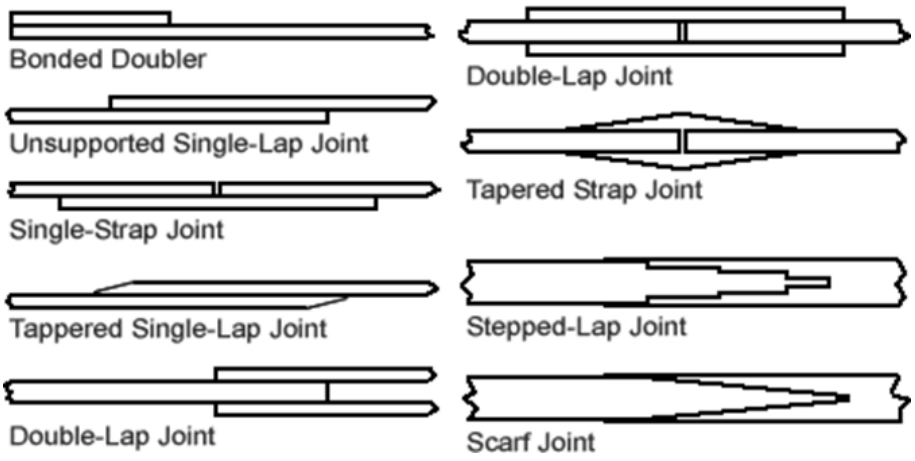

Fig. 2-3. Typical adhesive-boned joint forms[7]

Usually the strength of the polymeric adhesive is relatively low compared with the bonded substrates, and the geometry of the adhesive-bonded joint is designed based on the strength of both. The strength of structural adhesives rarely exceeds 100 MPa, which is typically substantially less than the strength of the substrates. Therefore the bonding area needs to be substantially larger than the load carrying cross-sectional area of the substrates to prevent premature failure in the adhesive bond[7].

For the adhesive-bonded lap and strap joint the stress/strain distribution in overlap bonding area is highly non-uniform and concentrates at the overlap ends. The main reasons for this can be considered as the dramatic geometry change at the end of the overlap and axial deformation of the adherends.

For example, the shear stress and peel stress (through-thickness stress) distribution in adhesive layer, which can be calculated by theoretical or numerical method, of a lap joint loaded in tension is shown in Fig. 2-4. The force applied on the joint is not co-linear, which induces the bending moment on overlap ends and finally causes the joint deformation. If the adherends are rigid and don't deform axially, the shear stress distribution should be uniform in overlap area. In reality, however, the adherends deform under the bending moment and the shear stress distribution is not uniform and concentrates at the overlap ends as shown in figure. 4. Thus since the area under the shear stress distribution must be equal to the load applied to the adherend per unit width, a joint with deforming adherends will always have a higher shear stress at the ends of the overlap than a joint with rigid adherends. Although the lap joint is loaded in shear, the peel stress will be induced in the adhesive layer for the joint deformation. The peel stress distribution is similar with shear stress distribution, it is not uniform throughout the overlap and reaches maximum at the overlap ends. The peel stress is often tensile and it can negatively influence the strength of adhesive layer and even cause delamination in fiber reinforced adherends with low transverse strength[7]. Many efforts have been made to improve the joint geometric design, such as by tapering the substrates towards the overlap end, to reduce the unfavorable stress concentration at overlap ends.

For most structures, the strength of structure is determined by the strength of their joints. When using adhesive-bonded joints, the joint strength can usually be achieved stronger than the surrounding

structure by using tapering techniques. The bond strength with respect to the joint type and tapering is shown in Fig. 2-5. The adhesive-bonded joints should always be designed to be stronger than the surrounding structure to ensure tolerance to initial flaws or other unpredictable defects during manufacturing and service.

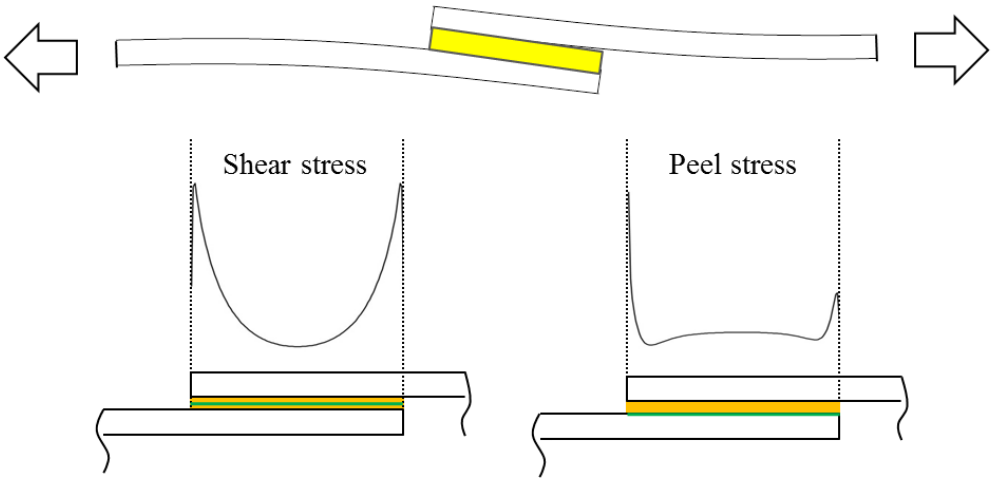

Fig. 2-4. Deformation of adhesive-bonded single-lap joint and stress distribution in bonding area

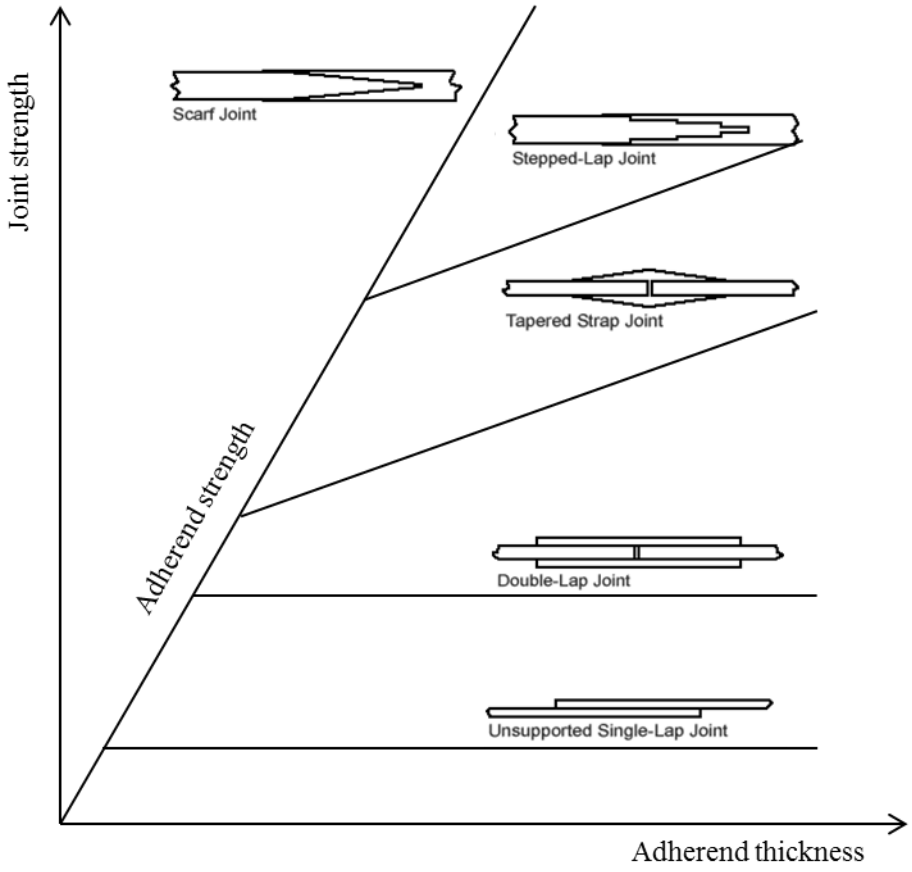

Fig. 2-5. Strength of adhesive-bonded joints in different joint forms

Typical defects and failure modes in adhesive-bonded joints

In review of defect types for adhesive-bonded joints by R. D. Adams[8], the two prime areas of defects in adhesive-bonded joints are the adhesive layer and the adhesive/adherend interface zone considering both the initial defects and in-service defects.

The common defects found in adhesive layer were introduced as shown in Fig. 2-6. Porosity is caused by volatiles and entrained gases in the adhesive layer. Voids are sometimes formed by the coalescence of markedly porous areas, but are more often caused by air entrapment during laying of the adhesive by volatiles and other gases given off, or by insufficient adhesive being applied. The phenomenon of gas voids in adhesive layer has been observed during joint manufacturing in this study, which will be discussed in chapter 4.

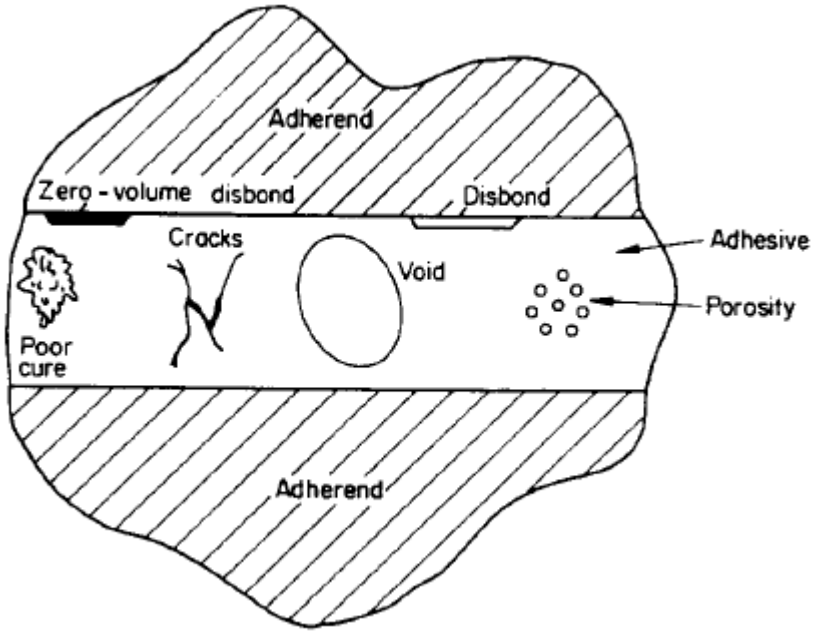

Fig. 2-6. Common defects in adhesive layer[8]

For the defects at adhesive/adherend interface, if the adherend surface is contaminated by oil deposits or loose oxide layers before bonding, or if the adhesive is left too long after mixing and forms a ‘skin’, the interface bond may be weak. A complete lack of bond is, effectively, a zero-volume void at the interface and this can be very difficult to detect. For these reasons, great care has to be taken when preparing adherend surfaces.

During service, damages tend to occur in the weak area in adhesive layer and at adhesive/adherend interface as described above. And in addition to various stresses which can lead to crack formation and general deterioration, adhesive-bonded joints are particularly susceptible to aggressive chemicals and moisture. The adhesive may be degraded so that its strength and stiffness are lower, although its ductility may be improved.

The failure of adhesive-bonded joints can happen at different location and in a variety of failure modes. It can initiate in the adhesive or in the adherend, depending on the geometrical configuration, the adhesive and adherend material manufacturing procedure and so forth. When a lap or strap-joint bonded by the tough adhesive is loaded to failure, the failure sequence in adhesive layer is usually: yielding, damage initiation and growth and final fracture. These events usually start at the overlap end and propagate towards the overlap center.

It is difficult to describe and define all the possible failure modes, especially for adhesive-bonded composite joints. And the failure modes are classified into four general groups taking composite joints into account as well as shown in Fig. 2-7:

a) Adherend failure due to bending, tension or compression etc.
b) Adherend-adhesive interfacial failure
c) Cohesive failure
d) Out-of-plane adherend failure due to delamination in composite adherend

Fig. 2-8 depicts some possible cohesive and adhesive failure modes in an adhesive-bonded single-lap joint with and without adhesive spew filet. Figure (a) and (b) indicates the possible damage initiation locations and the possible damage growth directions[1]. Figure (c) to (e) depicts the possible damage propagation path in the overlap length direction, the first one is in adhesive layer between the two adhesive/adherend interfaces, the second is at the adhesive/adherend interface and the third is a wavy path.

Usually it is difficult to predict precisely the failure mode of an adhesive-bonded joint. But by improvement of manufacture procedure to control the geometric configuration and the choice on adhesive and adherend material, the range can be narrow down to mentioned four groups.

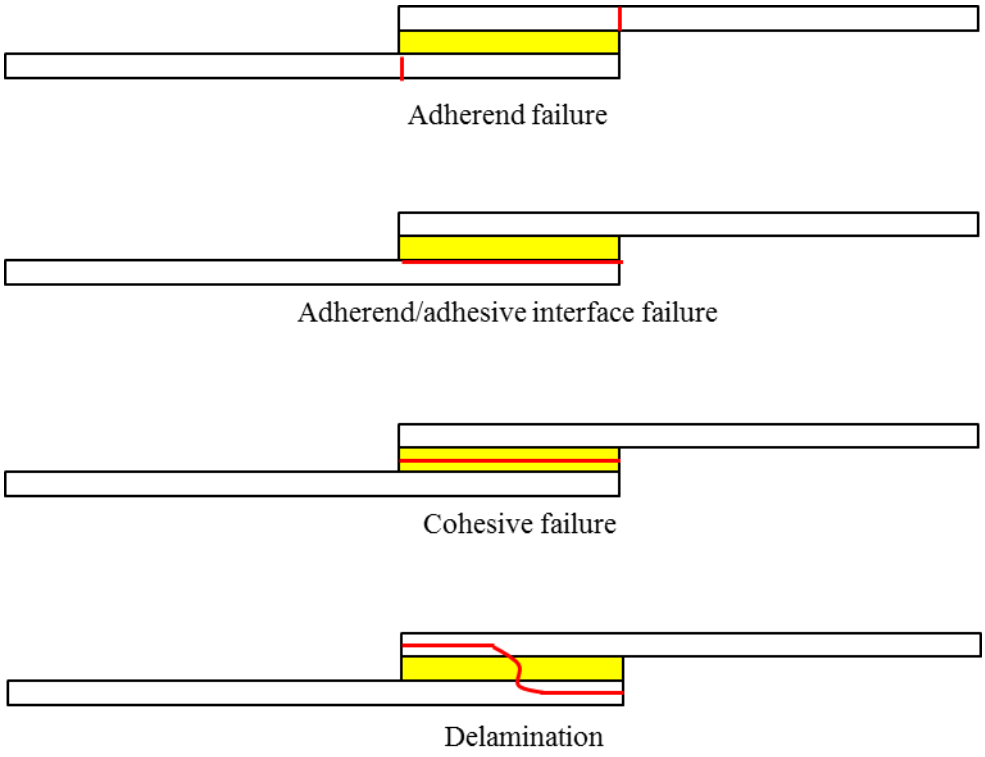

Fig. 2-7. Typical failure modes of adhesive-bonded joints

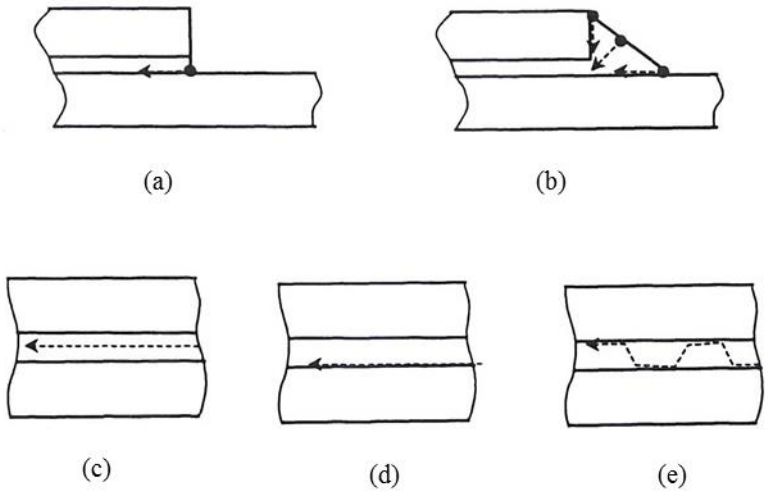

Fig. 2-8. Cohesive and adhesive failure modes of joint with and without adhesive spew filet[1]

Stress analysis techniques for adhesive-bonded joints

The stress analysis in adhesive-bonded joints is very important for the joint strength evaluation, fracture condition assessment and service life prediction.

However, due to differential straining in adherends, adhesive-bonded joints inevitably experience stress elevations, especially near the ends of overlap where load transfer takes place. Since a bonded joint represents a multi-layer structure involving two adherends and an adhesive layer, the stress states

that exist at various levels in a bonded joint are very complex. Many efforts have been made to develop and improve the stress analysis methods for adhesive-bonded joints in past decades, and the theoretical and numerical methods are two main approaches among them.

The simple model for a single-lap joint considers the both adherends as rigid bodies and thus the adhesive is subjected to pure shear. Volkersen abandoned the rigid adherend assumption and allowed the adherends deformation when loaded in tension[9]. As the result, it was shown that the non-uniform shear stress distribution in the overlap and the shear stress at the overlap end is much higher than that in the middle.

To make a more detailed discussion on his theory, the single-lap joint is shown in Fig. 2-9, and the effects of loading the joint in tension with both inextensible and elastic substrates are shown respectively. In both cases the substrates bears the full load F, just before the joint overlap and transmits it gradually to the other substrate through the adhesive. Thus the stress in substrate 1 will be highest at A and gradually diminish towards B where it will be zero and the converse will hold for substrate 2. In the case of loaded joint with inextensible substrates, the non-deformable substrates will move as solid blocks and the adhesive layer will possess a uniform distribution of longitudinal shear strain/stress. Therefore the stress field variation in substrates is not important if the substrates are inextensible. However, in practice, the substrates behave at least as elastic materials. For elastic substrates the tensile strain in substrate 1 at A is larger than at B, with the converse for substrate 2. This strain must progressively reduce over the bonded overlap length. Therefore, the deformation will be as shown in figure (c), and the shear stress distribution will be as shown schematically in figure (d), with the largest shear strains and stresses, in the adhesive occurring at the very ends of the overlap, at points C and D. Note, that assuming continuity of the adhesive/substrate interface, the uniformly sheared parallelogram in figure (b) becomes distorted to the shape illustrated in figure (c), and this is known as differential shear.

In Volkersen's study, the stresses in the adhesive arising from the differential shear strains were first analyzed. The maximum shear stress, τ_{12max}, in the adhesive is related to the applied shear stress, τ_0, by:

$$\eta_{cmax} = \frac{\tau_{12max}}{\tau_0} \qquad \text{Eq. 2-1}$$

where η_c is the stress concentration and the value of τ_0 is given by:

$$\tau_0 = \frac{F}{(bonded\ area)} = \frac{F}{bl_a} \qquad \text{Eq. 2-2}$$

where F is the applied tensile load and b is the width of the joint.

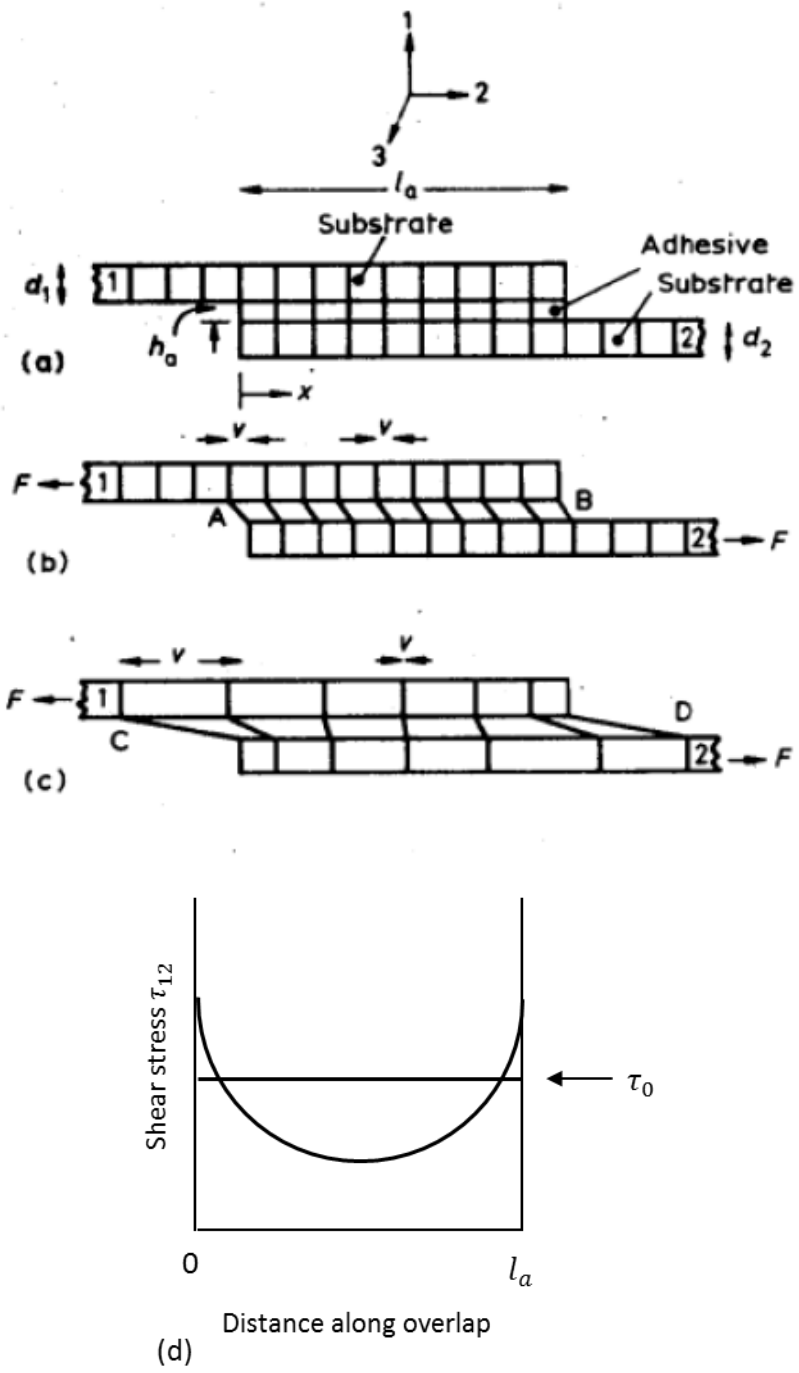

Fig. 2-9. Schematic representation of single-lap joint and distribution of elastic shear stress in the adhesive layer[6]

The situation considered by Volkersen, whilst it indicates the importance of various parameters on the potential strength of single-lap joint, is incomplete in that it takes no account of the tensile stresses generated in the adhesive as a result of the eccentricity of the loading of the joint.

Golands and Reissner[10] recognized from laboratory experiments with lap joints that the bending of the substrates outside the joint region had a pronounced effect upon the stress distribution in the joint itself. They assumed that the adhesive and substrates behaved as linear elastic and expressed the effect of the

bending of the substrates in their bending moment factor κ, and associated rotation factor κ^*. The two parameters are not independent but κ is usually the dominant term, which is dimensionless and is the ratio of the existing bending moment just before the bonded overlap to the value of this moment for inflexible substrates:

$$\frac{1}{\kappa} = 1 + 2(2)^{1/2} tanh\left\{\left(\frac{3}{2}(1-\upsilon_s^2)\right)^{1/2} \frac{l_a}{2d}\left(\frac{F}{E_s bd}\right)^{1/2}\right\} \qquad \text{Eq. 2-3}$$

where υ_s is the Poisson's ratio of the substrate and d is the thickness of the substrate. The resulting response of peel stresses which vary dramatically over the overlap length were also identified and discussed.

Based on works of Volkersen, Golands and Reissner, development in stress analysis theory and method was made by many researchers in past decades. Only brief introductions are made here. In Golands and Reissner's theory, the bondline thickness of the joint was assumed to have negelectable effect on determination of the edge bending moment. Hart-Smith et al.[11] improved the theory by considering the individual deformations of the upper and lower adherends. A further development was conducted by Oplinger[12] who took into account the large deflection effect in the joint overlap and presented a more detailed analysis. The finite element analysis (FEA) enables more accurate analysis on the joints and has been under intensive study. Wooley et al.[13] carried out a geometrically linear analysis on single-lap joint and performed parametric studies. Crocombe A.D. et al.[14] performed a two-dimensional linear analysis to study the influence of spew fillet on the stress distribution of the single-lap joint. Tsai et al.[15] performed a two-dimensional geometrically nonlinear analysis to compare with the theoretical analysis. Chan and Vedhagiri[16] performed an analysis using three-dimensional FE model to investigate the stress distributions in laminated composite joints with multiple pin loads. Richardson et al.[17] presented a comparison between the two- and three-dimensional FEA of adhesive bonded joints, their results showed that 2-D FE solution is adequate for a number of bonded joints.

Non-destructive inspection (NDI) techniques

The use of adhesive-bonded joints has been increasing for their advantages in areas that have been dominated by mechanical fastening and welding joints. Although the modern adhesives have been improved in strength, modulus and toughness, there still exist some typical concerns including joint strength evaluation and long-term durability. Bond deterioration in aging structures and original bond strength after manufacturing are now critical issues[18].

The current NDI techniques have been playing an important role in damage measurement and characterization in offline inspection using portable sensors, and aid in the mechanical condition assessment associated with post-inspection failure test for adhesive-boned joints.

Although the NDI may not be considered as effective and economical especially for long-term monitoring, it may be employed by advanced maintenance concept such as structural health monitoring (SHM). The brief information of some typical NDI techniques[19] for defect and damage detection in adhesive-bonded joints is introduced in this section.

a) Visual techniques

As one of the most basic inspection methods, visual inspection can identify obvious defects and reasonably small defects associated with simple magnification. Dye penetrant method can be applied for improvement of visualization of defects at surface and free edges of joints. The basic visual inspection method usually requires low skill levels, however, it is expensive and not effective. The assessment is made mainly by human based on experience.

b) Ultrasonic methods

Ultrasonic inspection is the most widely used inspection technique for the NDI of adhesive-bonded joints. The inspection usually employs either with a single transducer in pulse-echo mode or with two transducers in through-transmission mode. Using either of them, the transducer needs to be coupled to the structure through a liquid or solid medium because the impedance doesn't match between air and solid materials. Several measurement types can be achieved when using basic ultrasonic inspection equipment with water or gel coupling for transducer, and many methods of displaying the test results are also available. The most common methods should be the A, B and C scans[20].

The A scan usually gives time history of the echo signals received by the receiving transducer. This technique can be used to quantify bond strength, Fig. 2-10 shows a series of signals detected in joints with decreasing bond strength. The results show that the signal amplitude is affected by the physics of the changing bond.

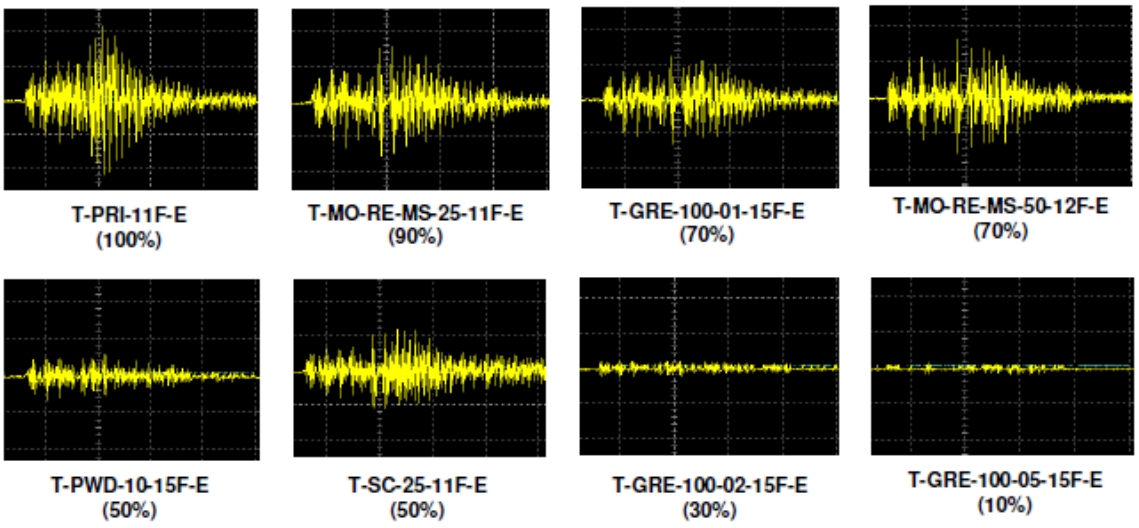

Fig. 2-10. Inspection results of ultrasonic A scan (bond strength is indicated by percentage numbers below each graphs)[20]

For the B scan result, the vertical axis is the time axis in A scan result, and the horizontal axis gives information of position. Thus the cross-section image of the component can be built. A B scan inspection result of joints in good bond and porous bond is shown in Fig. 2-11.

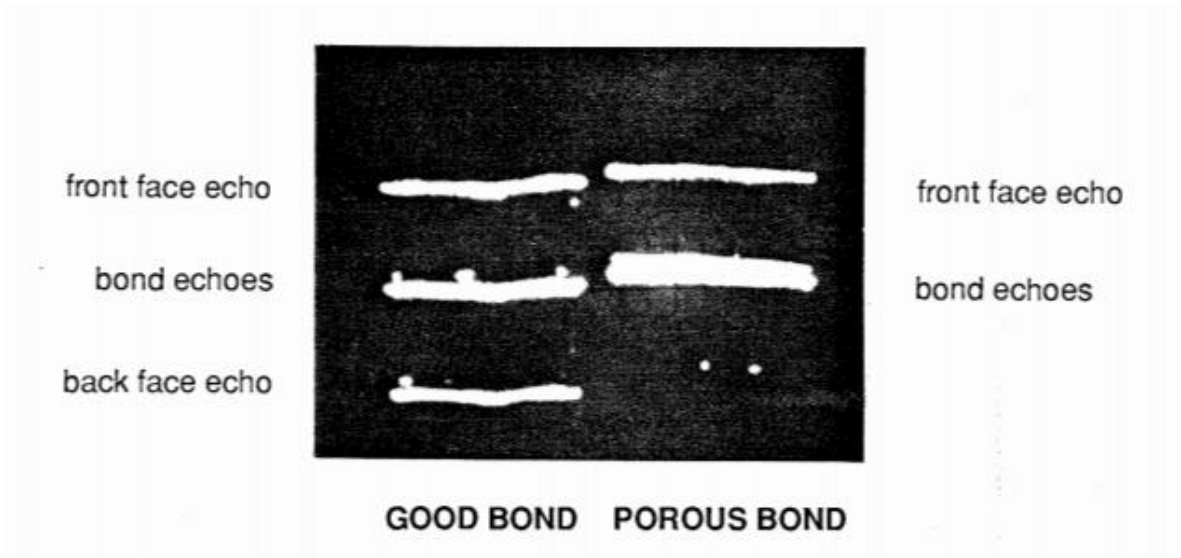

Fig. 2-11. B Scan in a carbon fiber composite lap joint (joint thickness of 3.7 mm)[20]

Based on B scan, if the amplitude of a particular echo is monitored at each point on the surface of work, a C scan can be produced. As shown in Fig. 2-12, in C scan inspection results, the color brightness becomes darker as the bond becomes weaker, which is caused by the decreasing of signal amplitude.

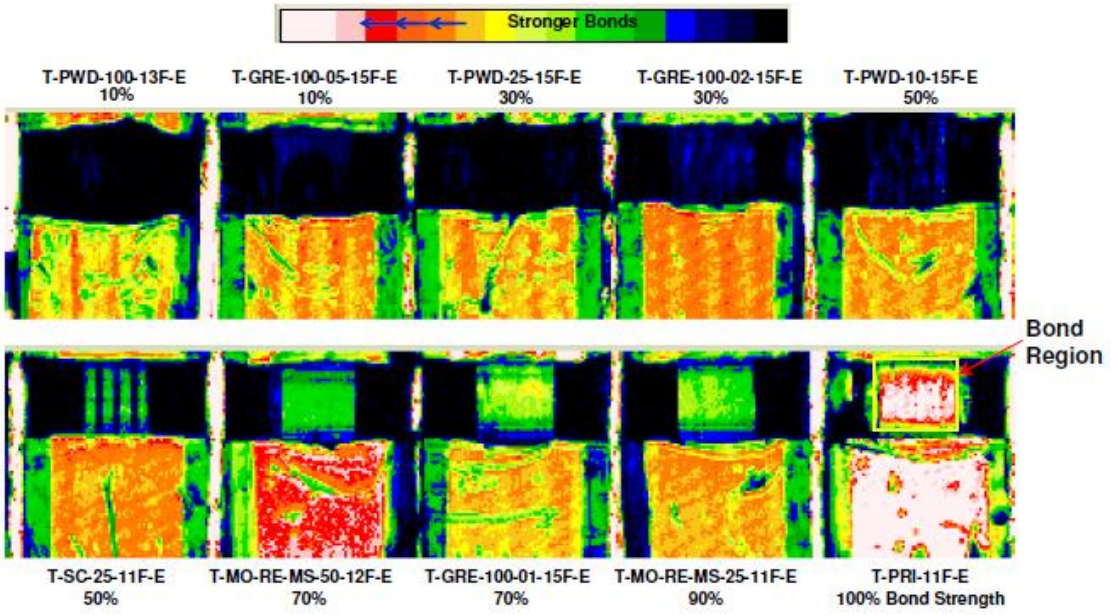

Fig. 2-12. C scan inspection results of decreasing bond strength[20]

In many adhesive-boned joints, the thickness and modulus of the adherends may be assumed to be reliably constant, hence, any change in the frequency or amplitude of the resonance wave may relate not only to the presence of voids but also to the modulus and thickness of a non-voided adhesive layer and to the strength of the joint. One such instrument widely used in industry is the Fokker Bond Tester[21] which works between 30 kHz and 1 MHz and measures difference in resonance frequency and the amplitude of the standing waves.

Usually a series of joints differing in strength, typically achieved by varying the adhesive layer thickness, is prepared and examined with the Fokker Bond Tester. The non-destructive tests are correlated with subsequent destructive tests and a calibration curve obtained. A typical relationship is shown in Fig. 2-13, the 'Right Shift' is a decrease in frequency and a 'Left Shift' is an increase in frequency. Once the required strength of the joint is known these calibration curves can be used to establish acceptance limits based upon reading of the instrument, which may now be used for quality control.

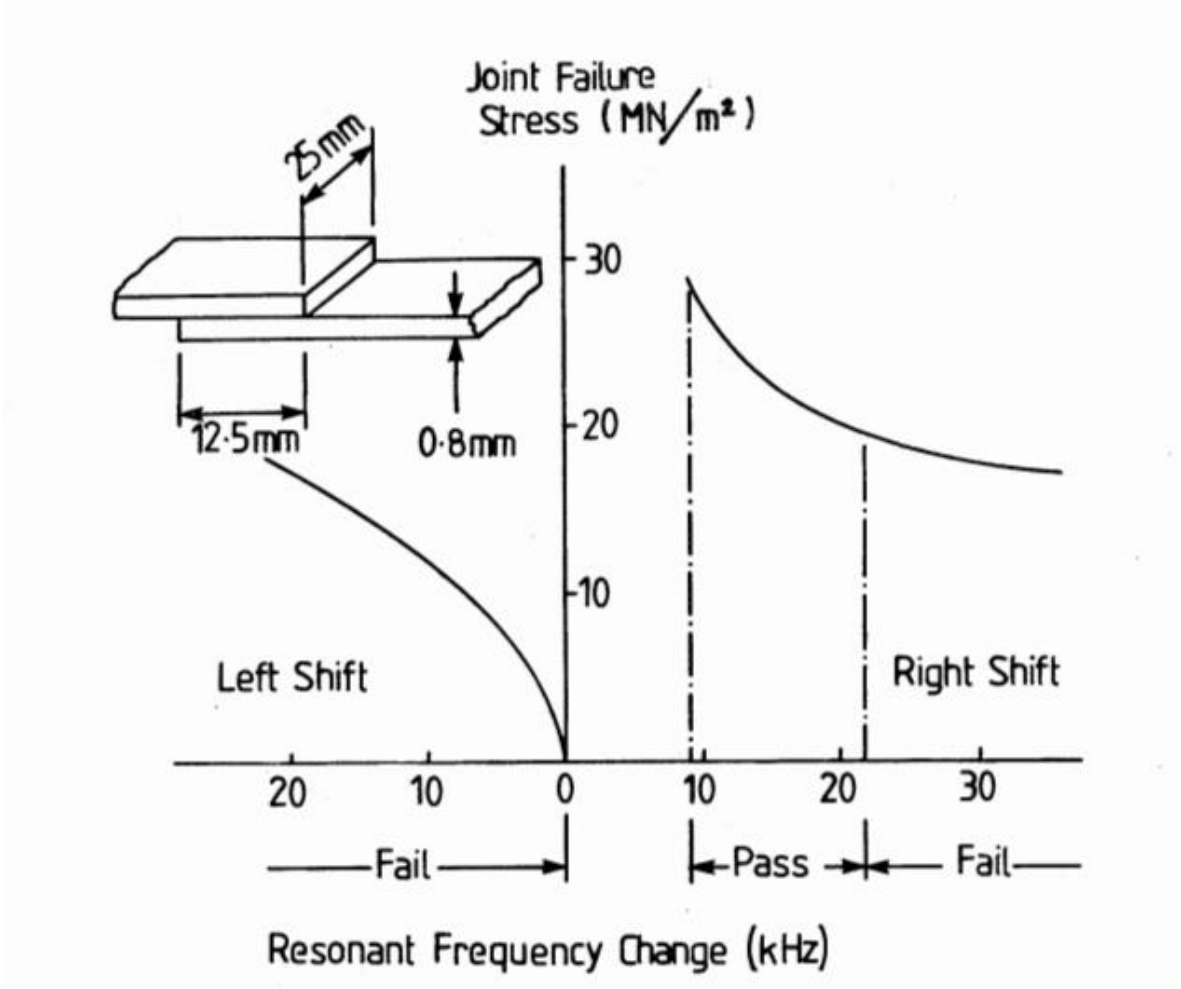

Fig. 2-13. Correlation curve between resonant frequency changes and failure stress for a Fokker Bond Tester MK II

c) Acoustic emission

Acoustic emission can be used to detect adhesion failure induced by fracture, but the joint needs to be loaded at about 50% of its failure load[22]. During inspection, the sensitive narrowband piezoelectric transducers are positioned on the surface of the structure, and by which the stress waves emitted by crack propagation and micro cracking can be received. The time of the first signal arrival enables the locating of the defect. The amplitude of the signals is used as indicator of the future life of the joint.

d) Radiography

The conventional X-ray techniques are seldom used on metal-metal adhesive-bonded joints because the polymeric adhesive is much less dense than the adherends. Metallic fillers[23] can be used to enhance the contrast and tapering or voids in bonding area can be shown. For joints in composite materials, the density of fiber reinforced plastics adherends has a similar order to that of the adhesive, thus X-rays can be used by choosing a proper energy and flux.

During specimen manufacturing in this study, the X-ray inspection has been employed to detect the voids in adhesive layer after joint bonding, the more introduction will be shown in chapter 4.

e) Thermal methods

By heating one surface of an adhesive-bonded structure and observing the temperature rise of the opposite face, the disbond area, which resists the heat transfer, can be observed as cool areas in the result[24]. Alternatively, if the heated face is scanned, disbonds will show as hot areas. Temperature sensing is normally done with a scanned infrared camera. Heat pulses or moving heat sources have been in conjunction with video recording of the transient thermal response[25].

f) Microwave

Microwave assisted NDI techniques can be used mainly on non-metallic materials to determine the moisture content degree by measuring the microwave absorption. Its application in adhesive-bonded joints has had very limited success.

And there are other techniques such as acoustic transmission[26], impedance methods and leaky lamb wave[27]. The NDI techniques have shown good performance in both laboratory tests and industry use in defects detection in adhesive-bonded joints and assessment of joint strength.

The basic aim of NDI techniques should be the direct correlation of some parameter measureable with the failure property to be measured or predicted, without impairing the effectiveness of the bonded part for its intended application. However, it appears that few of the NDI techniques employ directly correlate with any critical failure property. Most techniques such as ultrasonic methods and radiography attempts to find defects in the joint, based on inspection most decisions need to be done by human based on experience. And from the view of practical application, most NDI systems consists of a variety of devices and the following complex installation and wiring work, which means the

inspection needs to be carried out in a particular place, or at least the structure should be off-line for inspection. The direct consequences will be the high cost of inspection and the shortened service life of structure. The on-ground inspection can also lead to another disadvantage, the faint effect on preventing catastrophic failure of the structure during inspection interval, which is relatively often occurs on adhesive-bonded joint in aggressive environment or attacked by impact load. The modern maintenance strategies suggesting real-time on-board monitoring and automatic structural condition assessment such as structural health monitoring are expected to give a better solution for adhesive-bonded joint, the further discussion will be shown later in this chapter.

2.1.3. Summary

There are various advantages in using adhesive-boned joints over mechanical fastening and welding joints including light weight, less stress concentration, better fatigue properties, smooth substrate surface and so forth. However, they haven't been fully accepted and applied by engineers for some concerns, such as the initial joint strength which highly depends on manufacturing and long-term joint integrity which is sensitive to service environment. The complex geometric configuration and poor disassembly of adhesive-bonded joints makes it a big challenge for joint inspection and evaluation. Although the analytical methods have been developed for decades and can provide detailed stress/strain information based on knowledge of joint geometry, material properties and applied load, the strict joint manufacture according to specification is difficult and incongruity in geometry such as adhesive layer thickness or spew filet can largely affect the analysis accuracy. The NDI techniques are good at detecting and characterizing detects and damages both for joint quality evaluation and scheduled inspection. However they are expensive especially for aging structures which need intensive inspection, and can hardly provide real-time monitoring which can help to avoid catastrophic failure due to unexpected load or environment.

A maintenance or health manage method is highly desired for adhesive-boned joints, it should provide real-time monitoring of the structural and mechanical conditions since manufacture, and detect and report the defects to aid in the further inspection and joint strength assessment. In this way, the inspection cost can be reduced, and safety and structure service life can be improved. The SHM is considered as a promising concept, and it will be introduced in next section.

The ultimate objective of this study is to develop the SHM methods for adhesive-bonded joints.

The adhesive-bonded single-lap joint is used as study object because it is the basic form of lap joints which has been widely used in modern structures such as wind turbine blade, and it is geometrically simple for specimen manufacturing, and it is a representative joint form which has been studied in numerous reports, the reference is easy to find. There are various types of adhesive-bonded joint, discussion on each is difficult, so the use of SHM methods for single-lap joints are supposed to be extended to other joint forms.

The target damage is the crack occurred in adhesive layer or at adhesive/adherend interface, because it is the common reason for joint failure, and it can be produced easily in laboratory.

2.2. Structural health monitoring

The modern society relies heavily on the structural and mechanical systems such as buildings, bridges, aircrafts, power generation systems, rotating machinery and so on. Many of these structures are near their original design life, and the replacement cannot be easily achieved. Damage detection techniques are being developed and implemented so that they can be safely used even if their operation is beyond the designed service life. Also, for the newly designed and manufactured structures, the novel materials whose long-term behaviors are not well understood may be used. And in order for more cost-effective designs, the new structures may be built with lower safety margins. These circumstances require that the onset of damage in new structures can be detected at the possible early period in order to prevent structure failure that may cause loss of lives and economic consequences.

Usually six disciplines are involved when carry out the damage detection in structure. Structural health monitoring (SHM), condition monitoring (CM), non-destructive evaluation (NDE) also referred as non-destructive testing (NDT), health and usage monitoring system (HUMS), statistical process control (SPC) and damage prognosis (DP).

The SHM usually refers to the process of implementing a damage detection strategy including the observation of structure over time using periodically dynamic measurement, the extraction of damage-indicating features and the structure health assessment based on the analysis of these features. For long-term SHM, the output of this process is the periodically updated information regarding the ability of the structure to perform its function under the ageing and degradation due to the operational environments. For the extreme events, such as earthquake or unexpected loading, the SHM could be used to provide real-time information about the structure performance and aid in the assessment of structure integrity.

The SHM has the potential in cost control for structure maintenance especially for ageing structures which demand more intensive maintenance. Compared with the conventional time-based maintenance based on the designed schedule, the SHM can provide the damage detection and report, by which the condition-based maintenance can be achieved and the over inspection and maintenance can be avoided.

In this section, the SHM will be briefly introduced in aspects of SHM process and axioms, SHM development and application, SHM for adhesive-bonded joints.

2.2.1. SHM process

The SHM is a complex and case-based process, and generally it can be broken down into four steps[28]

described below.

a) Operational evaluation

The different structure has different function, performance, loading condition, service environment and specific requirements. For each particular structure, the goal of operational evaluation is to determine the SHM requirements including the damage types, operation and environmental conditions, and limitations on data acquisition such as cost, installation procedure, environmental concerns, etc.

b) Data acquisition

All aspects of the measurement is determined in detail in this process, such as the sensing technique, sensor location, measurement range and accuracy, sampling rate, normalizing and cleansing data, etc. The sensing technique and data acquisition hardware to be used are usually decided based on consideration of cost as a major role. If failure mode caused by fatigue crack growth is taken into consideration, the quasi-continuous data at short time intervals should be collected once the critical crack initiated.

c) Feature selection

The goal of feature selection process is to determine what characteristics of the data can be used for damage determination. For this process, the common method is through robust testing of a structure with incremental damage states and finding the changes in corresponding data. The feature that indicates a damage state but does not respond to the environmental or operational variations is considered as ideal.

d) Feature discrimination

The feature discrimination process determines the measured values which can be used as indicators of damage. Usually the measurement provided by SHM sensing system during monitoring does not indicate the damage directly and statistical model needs to be developed that specifies the feature of indicator. Three methods are commonly used for statistical model development: supervised learning, unsupervised learning and outlier detection.

2.2.2. Development of SHM

To SHM, the accident of Aloha Airlines Flight 243 in 1988 is considered as a special event which leads to the beginning of the intensive study on the structural condition and integrity monitoring as complement of conventional structure maintenance and damage detection strategy. A part of the fuselage was tore off due to a hole opened up in the fuselage during the flight, and the Aloha flight 243 with the missing section is shown in Fig. 2-14. The hole initiated at the mechanical fastening lap joint in fuselage, although the poor maintenance and harsh service environment (frequent and short distance flight, corrosive environment) contributed to the accident, it was caused by the phenomena termed “multisite damage” or “wide spread fatigue damage” which was failed to be predicted and inspected.

For this accident, the engineers realized that the conventional maintenance method designed based on the knowledge of materials, loading conditions and damage behaviors cannot guarantee the structural integrity in circumstance such as the insufficient knowledge, unexpected loading and environmental conditions, or operational false. In the past thirty years the increase in the number of studies regarding SHM and damage detection techniques has been significant, and the transition of SHM as a research topic to practical application has been carried out in various structural systems.

Fig. 2-14. Aloha Airlines Flight 243[28]

In this section, the developments in SHM technology are summarized in three distinct application areas. More detailed information can be found in references.

a) Rotating machinery applications

The application in rotating machinery is considered one of the most successful applications for SHM. The periodically dynamic measurement of acceleration and displacement is carried out to monitor the structural and mechanical condition and aid in the assessment of the structure performance. The commercialization of SHM process from data measurement to data analysis has been successful, and the reasons can be considered as the relatively simple and stable service conditions including the loading and environmental conditions, the well-understand damage behavior and the efficient and cost effective sensing techniques.

b) Offshore oil platforms

During the 1970s and 1980s the considerable efforts were made by oil industry to develop vibration-based damage detection methods for offshore platforms. This damage detection problem is very different from the rotating machinery because the damage location is unknown and the most areas of the structure are not readily accessible for measurement. For the SHM application, many practical problems were encountered such as measurement difficulties caused by platform machine noise, instrumentation difficulties in hostile environments, changing mass caused by marine growth and varying fluid storage levels.

c) Aerospace structures

The aerospace community paid attention on the damage detection technology during the late 1970s and early 1980s for a variety of civilian and defense applications. One of the most notable SHM systems that have made the transition from research to practice is the space shuttle modal inspection system (SMIS) program. It has been successfully used to locate the damaged components covered by the thermal protection system and all orbiter vehicles have been periodically subjected to SMIS testing since 1987[29]. Since the mid-1990s, studies of damage detection for composite materials have been increasing for the development of a composite fuel tank for a reusable launch vehicle as well as the increasing use of composite materials in all types of commercial and military aircraft[30].

2.2.3. SHM techniques for adhesive-bonded joints

The SHM seems very promising in solving the two typical concerns of adhesive-boned joints application, the initial joint strength and long-term joint integrity. The long-term monitoring since the manufacturing offered by SHM can improve the joint safety and reduce the high maintenance cost induced by over inspection. However, the complete SHM strategy for adhesive-bonded joints hasn't been reported.

As mentioned, the NDI techniques have been well developed for damage detection of adhesive-bonded joints. They usually employ portable sensors in offline inspection and are good at damage measurement and characterization. However, the NDI techniques can hardly be used directly for SHM for the requirements such as the sensor should be permanently installed on the joint, the dynamic measurement of the damage indicator should be carried out and the damage detection and report based on the automatic data analysis should be achieved. In this section, some particular studies on SHM techniques for adhesive-bonded joints were introduced, and the specific goals and objectives of this study are presented.

Backface strain (BFS) method using strain gauges

In Shenoy's study[31], two strain gauges were bonded on surface of adhesive-bonded single-lap joint for dynamic measurement during the fatigue load test. In the test, the crack initiated and propagated in adhesive layer and finally caused the failure of joint. The sensor arrangement is shown in Fig. 2-15. The relation between the strain variation and the crack growth was built based on the measurement. Thus by this relation, the crack can be evaluated through strain measurement.

This study introduced the BFS as the indicator of crack in bonding area, however, the sensor location is far from the adhesive layer where the crack occurs and the crack-strain relation can be sensitive to the joint geometry and environment. The strain inside the adhesive layer is considered to have more significant response to the crack growth, but the strain gauge can hardly be embedded into the joint for

measurement.

More information about BFS method can be found in reference[323334].

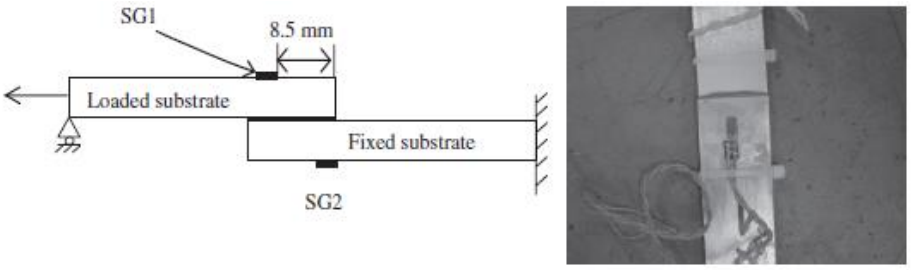

Fig. 2-15. Sensor arrangement in Shenoy's study.

Optical fiber sensor (OFS)

The OFS is a very promising sensing technique for SHM. It can be used to measure various parameters especially strain and temperature, and it possesses many unique features such as small size and flexibility, distributed measurement, EMI immunity and so on. More information about OFS will be introduced in Chapter 3. Many reports have demonstrated the embedment of OFS into composite materials, adhesive-boned joints and repairs for measurement[353637]. The embedded measurement of OFS has been provided feasible. Some studies on the adhesive-bonded joints are discussed here.

In J. Palaniappan et al.'s study[38], chirped FBG (CFBG) sensors were embedded into composite adherends of adhesive-bonded single-lap joints located 0.5 mm from the adhesive bondline as shown in Fig. 2-16. During fatigue load tests, the CFBG sensors were used to detect the disbond at adhesive/adherend interface. Considering difficulties of using the CFBG sensor for non-homogeneous strain distribution measurement, C. Schizas et al. employed the quasi-continuous FBG sensors in their study[39]. Five FBG sensors were embedded between second and third layer of a composite adherend of an adhesive-bonded single-lap joint with pre-crack as shown in Fig. 2-17. The strain variation on five FBG sensors was recorded throughout the quasi-static monotonic test to evaluate the crack propagation. Their study showed the strain distribution in joint overlap direction can be a better indicator for crack in bonding area than the strain at a particular location. However, the detection accuracy in their study was not enough to describe crack behavior in detail due to the low spatial resolution of the sensing technique.

H. Igawa and H. Murayama et al. have demonstrated a sensing system using the long length FBG sensor based on optical frequency domain reflectometry (OFDR) which can provide strain distribution measurement with high spatial resolution[40]. Later, H. Murayama et al. embedded a 100 mm-length FBG into the bonding area of an adhesive-bonded single-lap joint (Fig. 2-18) and measured longitudinal strain distribution in the whole overlap area with spatial resolution less than 1 mm in static load test[41]. The measurement was confirmed by finite element analysis (FEA), and the agreement was good as shown in Fig. 2-19. Although the damage detection was not included in their

study, this distributed sensing system is considered ideal for high accuracy crack detection and monitoring.

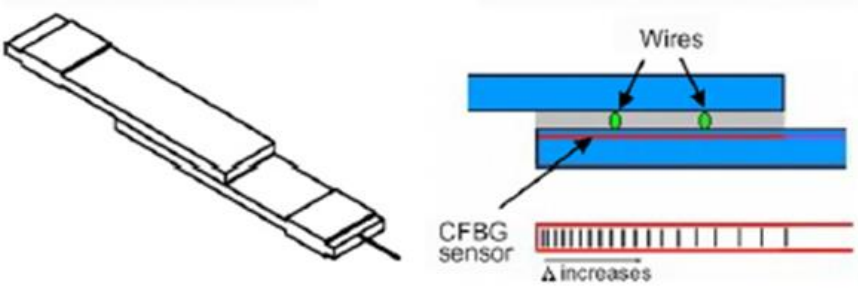

Fig. 2-16. Sensor embedment in J. Palaniappan et al.'s study.

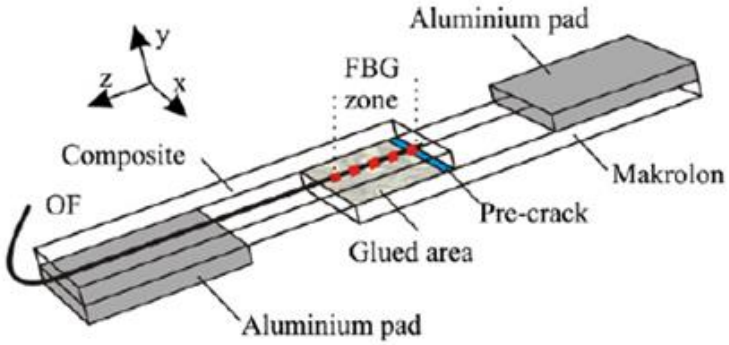

Fig. 2-17. Sensor embedment in C. Schizas et al.'s study.

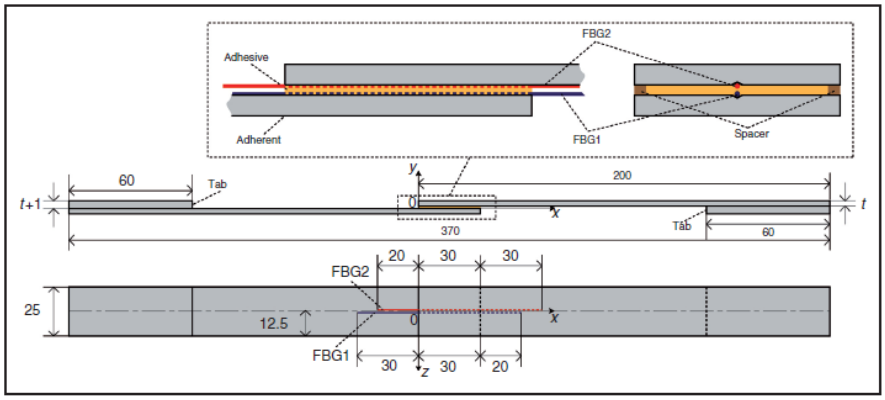

Fig. 2-18. Sensor embedment in H. Murayama et al.'s study.

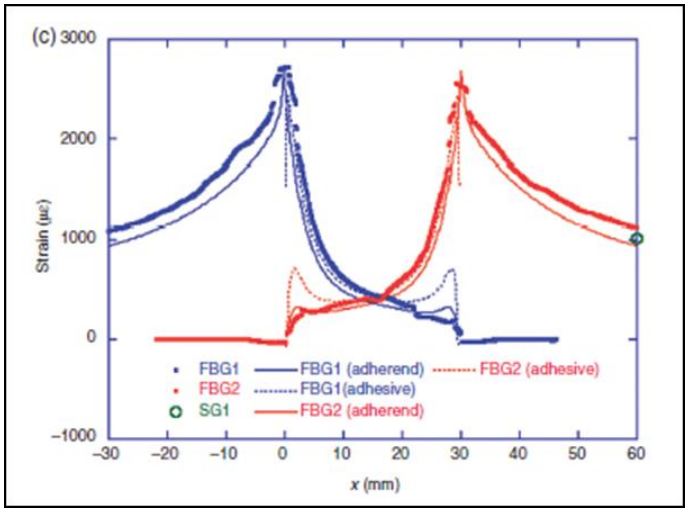

Fig. 2-19. Comparison of strain distribution obtained by measurement with FEA

2.2.4. Summary

The SHM techniques have been developed for decades, the solution has been brought by modern sensing techniques such as OFS for the inspection/sensing tasks which can hard be completed by conventional techniques.

About the SHM techniques for adhesive-bonded joints, the strain distribution in adhesive layer along overlap length direction can be a good indicator for the crack initiates in bonding area and propagates along the overlap length direction of adhesive-bonded joint. In order to measure this parameter, two requirements should be met: the sensor should be embedded into adhesive layer or adhesive/adherend interface for measurement, the sensing system should be capable of dynamic measurement of strain distribution. The distributed sensing system based on OFDR using long length FBG is considered qualified for this task, it can provide distributed strain measurement with high spatial resolution and the FBG sensor can be embedded into adhesive layer for measurement. However, the system used in reference 36 was designed for static measurement, the development should be made to enable the dynamic measurement. The embedment method of FBG for SHM should also be considered. The new system needs to be test in both static and dynamic loading and crack detection method based on the measurement should be developed.

The objectives of this study is to develop a dynamic distributed OFS sensing system, measure the longitudinal strain distribution by the embedded OFS and propose the target damage detection method based on measurement.

Reference

[1] L. Y. Tong and G. P. Steven, Analysis and design of structural bonded joints, Kluwer academic publishers, 1999
[2] J. A. Speck, Mechanical Fastening, Joining, and Assembly, Taylor & Francis, 1997
[3] M. D. Banea and L. F. M. da Silva, Adhesively bonded joints in composite materials: An overview, Proceedings of the Institution of Mechanical Engineers, Part L: Journal of Materials: Design and Applications, vol.223, pp.1-18, 2009
[4] W. R. Broughton and R. D. Mera, Environmental Degradation of Adhesive Joints Accelerated Testing, NPL Report CMMT(A) 197, 1999
[5] A. D. Crocombe, Durability modelling concepts and tools for the cohesive environmental degradation of bonded structures, International Journal of Adhesion and Adhesives, vol.17, pp.229-238, 1997
[6] A. J. Kinloch, Adhesion and adhesives, Springer, 1987
[7] L. Y. Tong and C. Soutis, Recent advances in structural joints and repairs for composite materials, Kluwer academic publishers, 2003
[8] R. D. Adams and P. Cawley, A review of defect types and nondestructive testing techniques for composites and bonded joints, NDT International, vol.21, pp.208-222, 1988
[9] O. Volkersen, Die Nietkraftverteilung in zugbeanspruchten Nietverbindungen mit konstanten Laschenquershnitten, Luftfahrforschung, vol.15, pp.41-47, 1938
[10] M. Goland and E. Reissner, The stresses in cemented joints, J Appl Mech, vol.11, pp.A17-A21, 1944
[11] L. J. Hart-Smith, Adhesive bonded single-lap joints – technical report, NASA-CR-112236, 1973
[12] D. W. Oplinger, A layered beam theory for single lap joints. Army Materials Tech Lab Report MTL, 1991
[13] G. R. Wooley and D. R. Carver, Stress concentration factors for bonded lap joint, J Aircraft, vol.8, pp.817–820, 1971
[14] A. D. Crocombe and R. D. Adams, Influence of the spew fillet and other parameters on the stress distribution in the single-lap joint, J Adhesion, vol.13, pp.141-155, 1981
[15] M. Y. Tsai and J. Morton, An evaluation of analytical and numerical solutions to the single-lap joint, Int J Solids Struct, vol.31, pp.2537–2563, 1994
[16] W. S. Chan and S. Vedhagiri, Analysis of composite bonded/bolted joints used in repairing, J Composite Materials, vol.35, pp.1045-1061, 2001
[17] G. Richardson, et al., A comparison of two- and three-dimensional finite element analysis of adhesive joints, Int J Adhesion and Adhesives, vol.13, pp.193-200, 1993
[18] D. Roach, K. Rackow, R. Duvall, Innovative Use of Adhesive Interface Characteristics to Nondestructively Quantify the Strength of Bonded Joints, 10th European Conference on Non-Destructive Testing, 2010
[19] N. Cheraghi, M.J. Riley, and F. Taheri, A novel approach for detection of damage in adhesively bonded joints in plastic pipes based on vibration method using piezoelectric sensors, Systems, Man and Cybernetics, 2005 IEEE International Conference, vol.4, pp.3472-3478, 2005
[20] C. C. H. Guyott, P. Cawley and R. D. Adamas, The non-destructive testing of adhesively bonded structure: a review, J Adhesion, vol.20, pp.129-159, 1986
[21] C. C. H. Guyott, P. Cawley and R. D. Adamas, Use of the Fokker Bond Tester on Joints with Varying Adhesive Thickness, Proceedings of the Institution of Mechanical Engineers, Part B: Journal of Engineering Manufacture, vol.201, pp.41-49
[22] G. J. Curtis, Nondestructive testing of adhesively-bonded structures with acoustic methods, Ultrasonic Testing – Non-conventional Testing Techniques, Wiley, Chichester, 1982
[23] E. Segal and S. Kenig, Acceptance criteria for NDE of adhesively bonded structures, Material Evaluation, vol.47, pp.921-927, 1989
[24] C. E. Bakis and K. L. Reifsnider, Adiabatic thermoelastic measurements. Edited by: Pendleton and Tuttle. Manual on experimental methods for mechanical testing of composites, Amsterdam: Elsevier Applied Science, 1989
[25] W. N. Reynolds, Inspection of laminates and adhesive bonds by pulse-video thermography, NDT

International, vol.21, pp.229-232, 1988
[26] R. F. Wegman and T. R. Tullos, Nondestructive inspection, Noyes Publ., Park Ridge, NJ, 1992
[27] Y. Bar-Cohen and A. K. Mal, Nondestructive inspection and quality control end-product, Nondestructive Evaluation of Adhesive-bonded Composite Joints, Engineered Materials Handbook, Cleveland, OH: ASM Int., 1990: 777-84
[28] C. R. Farrar and K. Worden, Structural Health Monitoring: A Machine Learning Perspective, John Wiley & Sons, 2013
[29] D. L. Hunt, S. P. Weiss, et al., Development and implementation of a shuttle modal inspection system, Sound and Vibration, vol.24, pp.34-42, 1990
[30] C. Boller and M. Buderath, Fatigue in aerostructures – where structural health monitoring can contribute to a complex subject, Phil. Trans. R. Soc. A, vol.365, pp.561-587, 2006
[31] V. Shenoy, I. A. Ashcroft, G.W. Critchlowb, A. D. Crocombe, M. M. AbdelWahab, An investigation into the crack initiation and propagation behavior of bonded single-lap joints using backface strain, International Journal of Adhesion & Adhesives, vol.29, pp.361-371, 2009
[32] W. J. D. Shaw and W. Zhao, Back face strain calibration for crack length measurements, ASTM J Test Eval, vol.22, pp.512–516, 1994
[33] C. J. Gilbert, J. M. McNaney, R. H. Dauskardt, and R. O. Ritchie, Back-Face Strain Compliance and Electrical-Potential Crack Length Calibrations for the Disk-Shaped Compact-Tension DC(T) Specimen, ASTM J Test Eval, vol.22, pp.117-120, 1994
[34] A. D. Crocombe, C. Y. Ong, C. M. Chan, M. A. Wahab, I. A. Ashcroft, Investigating fatigue damage evolution in adhesively bonded structures using backface strain measurement, J Adhesion, vol.78, pp.745-776, 2002
[35] S. Takeda, Y. Okabe, N. Takeda, Delamination detection in CFRP laminates with embedded small-diameter fiber Bragg grating sensors, Composites: Part A, vol.33, pp.971-980, 2002
[36] Y. Okabe, S. Yashiro, T. Kosaka and N. Takeda, Detection of transverse cracks in CFRP composites using embedded fiber Bragg grating sensors, Smart material structure, vol.9, pp.832-838, 2000
[37] I. McKenzie, R. Jones, I. H. Marshall, S. Galea, Optical fibre sensors for health monitoring of bonded repair systems, Coposite Structures, vol.50, pp.405-416, 2000
[38] J. Palaniappan, S. L. Ogin, A. M. Thorne, G. T. Reed, A. D. Crocombe, T. F. Capell, S. C. Tjin and L. Mohanty, Disbond growth detection in composite–composite single-lap joints using chirped FBG sensors, Composites Science and Technology vol.68, pp.2410-2417, 2008
[39] C. Schizas, et al., Monitoring of non-homogeneous strains in composites with embedded wavelength multiplexed fiber Bragg gratings: A methodological study, Composite Structures, vol.94, pp.987-994, 2012
[40] H. Igawa, H. Murayama, T. Kasai, I. Yamaguchi, K. Kageyama and K. Ohta, Measurements of strain distributions with a long gauge FBG sensor using optical frequency domain reflectometry, Proc. of SPIE, vol.5855, pp.547-550, 2005
[41] H. Murayama, K. Kageyama, K. Uzawa, K. Ohara and H. Igawa, Strain monitoring of a single-lap joint with embedded fiber-optic distributed sensors, Structural Health Monitoring, vol.11, pp.325-344, 2011

Chapter 3

Optical fiber sensing system

An optical fiber sensor (OFS) is a sensor that uses optical fiber either as the sensing element or as the signal transmission device in a sensing system. The OFS can be generally grouped into two basic classes referred to as extrinsic, or hybrid, sensors and intrinsic, or all-fiber, sensor[1]. In the case of extrinsic OFS, an optical fiber leads up to a "black box" that impresses information onto the light beam in response to an environmental effect. The information could be impressed in terms of intensity, phase, frequency, polarization, spectral content, or other methods. An optical fiber then carries the light with the environmentally impressed information back to an optical and/or electronic processor. In some cases the input optical fiber also acts as the output fiber.

In the case of intrinsic OFS, an optical fiber is used to carry the light beam, and the environmental effect impresses information onto the light beam while it is in the fiber. Each of these classes of fibers in turn has many subclasses with, in some cases, sub-subclasses that consist of large numbers of fiber sensors. Comparing with the conventional sensors based on mechanical or electrical transducers, the OFS possesses many unique advantages and is promising for SHM system.

In this chapter, the optical fiber sensor and sensing system will be introduced in aspects of basic principle, advantages and measurands, distributed sensing technique. The OFS sensing technique involved in this study will be introduced in aspects of sensor type, sensing system principle and development process of dynamic distribution sensing system.

3.1. Optical fiber sensor

3.1.1. Optical fiber

An optical fiber is a flexible fiber that can function as a waveguide or "light pipe" to transmit light between the two ends of the fiber. It is usually made of silica glass and slightly thicker than a human hair. As shown in Fig. 3-1, a typical optical fiber consists of a silica glass core with higher refractive index, a cladding with lower refractive index and a coating layer.

When the light is injected into the optical fiber core at the incident angle within the acceptance angle range, the light will propagate in the core by total refraction between core and cladding as shown in Fig. 3-2. This can be described by Snell's law[2] of reflection as shown below.

$$n_1 sin\phi_1 = n_2 sin\phi_2 \qquad \text{Eq. 3-1}$$

Where n_1 and n_2 are the refractive indices of medium 1 and 2, ϕ_1 and ϕ_2 are the angles of incident and refracted rays respectively. The total refraction can be described as below.

$$\sin\phi_1 > sin\phi_c = \frac{n_2}{n_1} \qquad \text{Eq. 3-2}$$

where ϕ_c is the critical angle.

In the fiber core, the light propagates as an electromagnetic wave along the fiber. The two components, the electric field and the magnetic field form patterns across the fiber. These patterns are called modes of transmission. Modes means methods - hence methods of transmission[3]. An optic fiber that carries more than one mode is called a multimode fiber. In a given piece of fiber, there are only a set number of possible modes. This is because each mode is a pattern of electric and magnetic fields having a physical size. The dimensions of the core determine how many modes or patterns can exist in the core - the larger the core, the more modes.

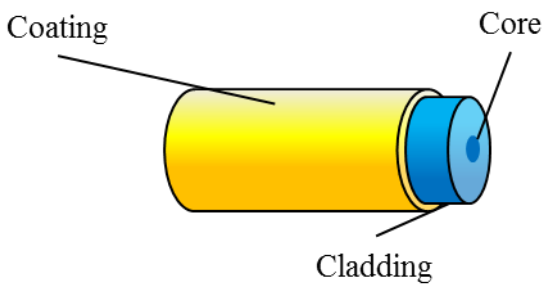

Fig. 3-1. Configuration of optical fiber

Three basic optical fibers are shown in Fig. 3-3: (a) single-mode step-index fiber, (b) multimode step-index fiber and (c) multimode graded-index fiber. The single-mode fibers propagate only one light mode at one time while the multimode fiber can propagate hundreds of light modes. The refractive index in the core of the graded-index fiber varies depending on the distance from the fiber axis, while the core in step-index fiber possesses the same refractive index throughout the fiber. The optical fiber used as OFS is mainly the single-mode.

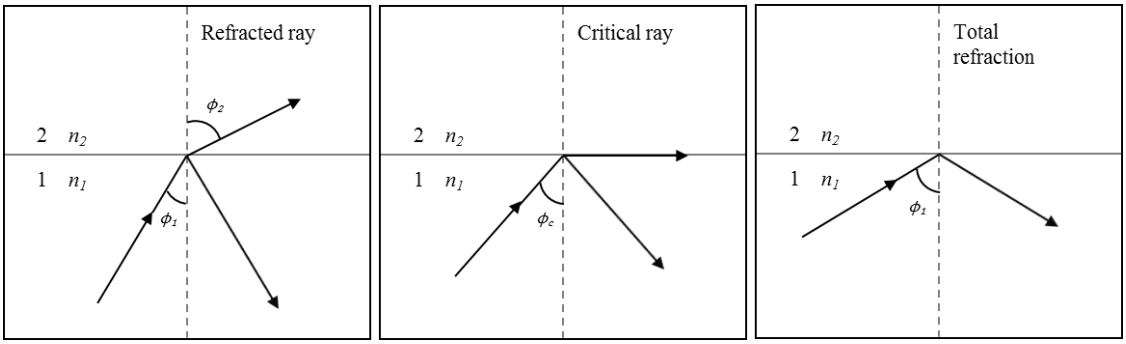

Fig. 3-2. Reflection and refraction of light

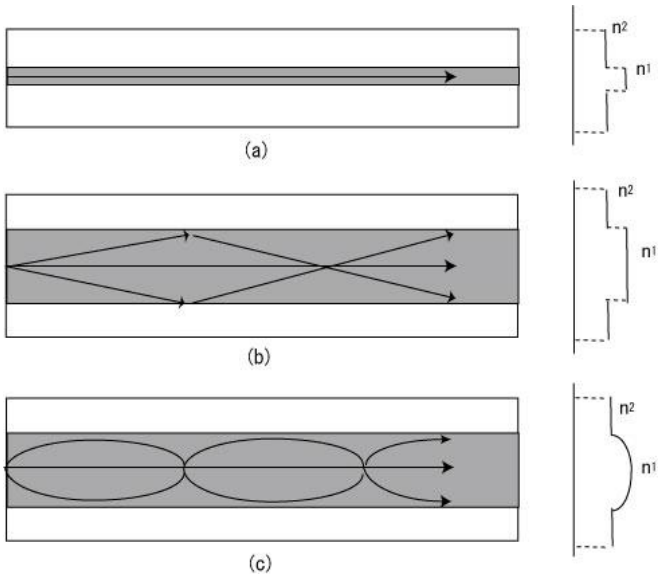

Fig. 3-3. Light transmission modes in optical fiber[1]

3.1.2. Advantages and measrands of OFS

Comparing with the conventional mechanic-electric sensor, the OFSs have various advantages, and the typical ones are shown below.

a) Light weight and thin diameter
b) Flexibility

c) Immunity to electromagnetic interference
d) High sensitivity
e) Anti-explosion
f) High strength, durability and anti-corrosion
g) Multiplexing capabilities

These features are useful in practical applications. The smaller and lighter sensor induces lower influence on the mechanical condition of the object structure. The OFSs can be used in the corrosive, explosive or electromagnetic environment. And for the multiplexing capabilities, the quasi-distributed or distributed measurement can be achieved by using one OFS instead of a number of point sensors and the complex wiring work[4]. Thus the OFS is considered as the more efficient and effective sensing technique, and has been used to measure various parameters[5] including: strain, temperature, pressure/acoustic, current/voltage, chemical/gas, rotation, vibration/acceleration, bending/torsion, displacement, and etc. Fig. 3-4 shows the distribution of papers presented at the 15th Optical Fiber Sensors Conference according to measurands of interest. The most intensively investigated measurands are the strain and temperature. Fig. 3-5 shows the OFS techniques discussed in papers presented at OFS-15. The fiber grating sensors are absolutely the most widely studied topic.

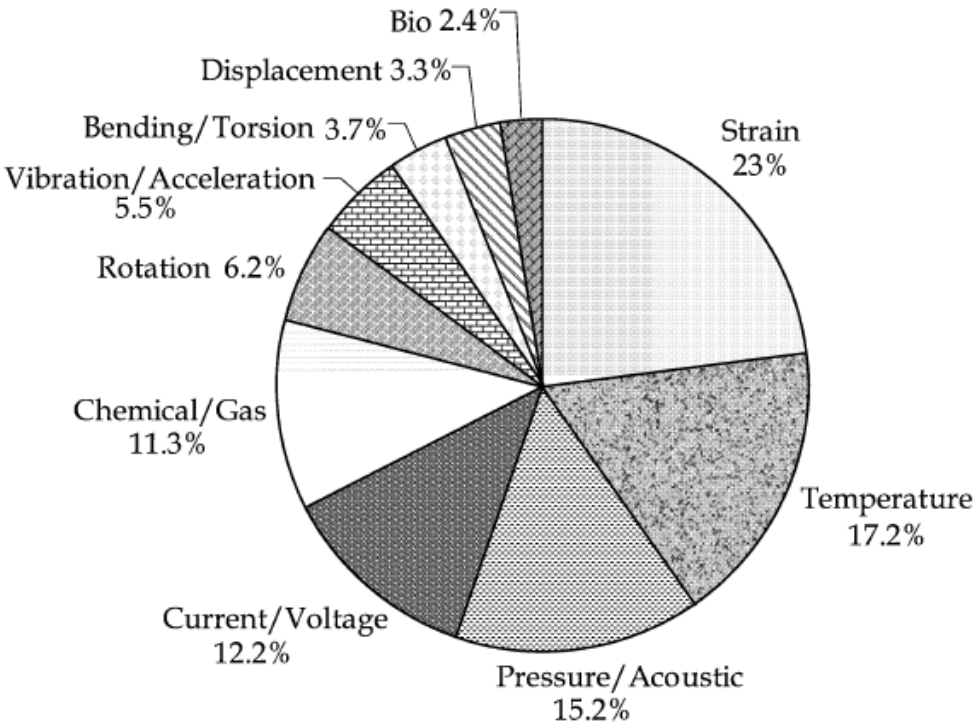

Fig. 3-4. Distribution of papers according to measurands

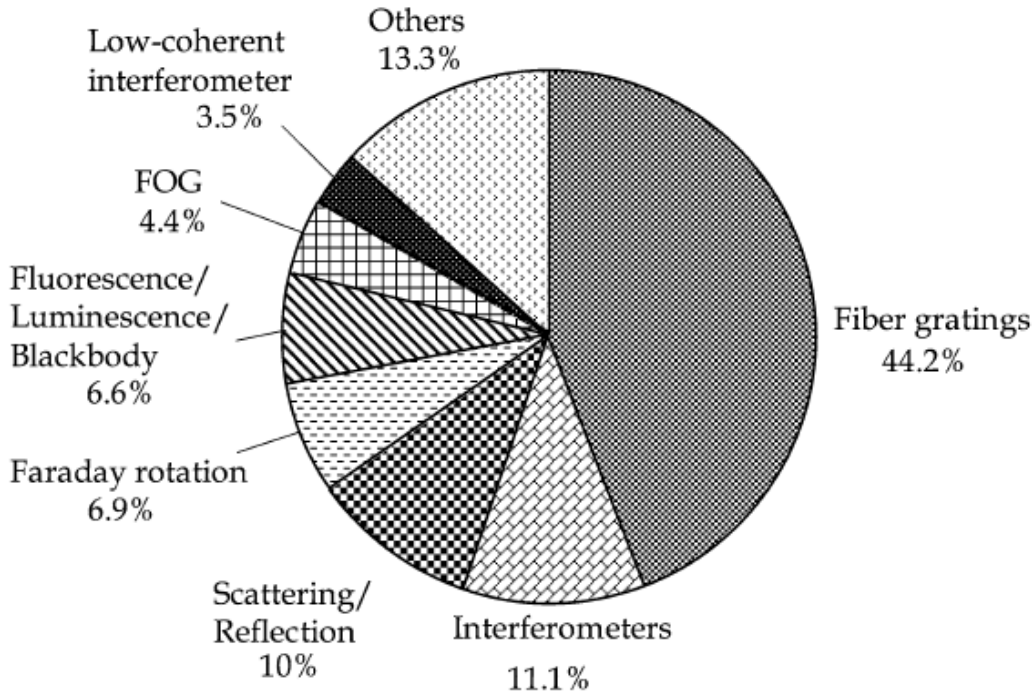

Fig. 3-5. Distribution of papers according to techniques

3.1.3. Distributed measurement using OFS

For the excellent transmission capabilities of the optical fiber, the distance between the sensing system and the measuring point can be of many kilometers. And because of the multiplexing capabilities, a number of measuring points can be multiplexed along a single optical fiber, and full distributed measurements with high spatial resolution can be achieved.

According to the spatial distribution of the measurand, the OFS sensing techniques can be classified as (Fig. 3-6)[6],

a) Point sensing, the measurement is carried out at discrete points accessed by different channels. It means that each sensor provides measurement at one point.
b) Integrated sensing, the measurement of an area along a portion of optical fiber, and the result is the integrated value, which is usually the average value.
c) Quasi-distributed sensing, measurement of the object variable at discrete points of space situated in an area along a portion of an optical fiber.
d) Distributed sensing, the measurement that allows the determination of the value of the object variable in a continuous way at each point of space with a given spatial resolution in an area along

a portion of an optical fiber.

For SHM on a large-scale structure, the capability of distributed sensing of OFS is of great importance when the damage location is difficult to predict and a large area needs to be monitored. The number of sensor and the installation and wiring work of the whole system can be reduced and simplified. For a relatively small-scale structure with complex variable such as a joint, the OFS can provide the measurement of variable profile with high spatial resolution. In decades, the OFS sensing technique has been developed continuously for the higher spatial resolution, some representative examples are given in[789].

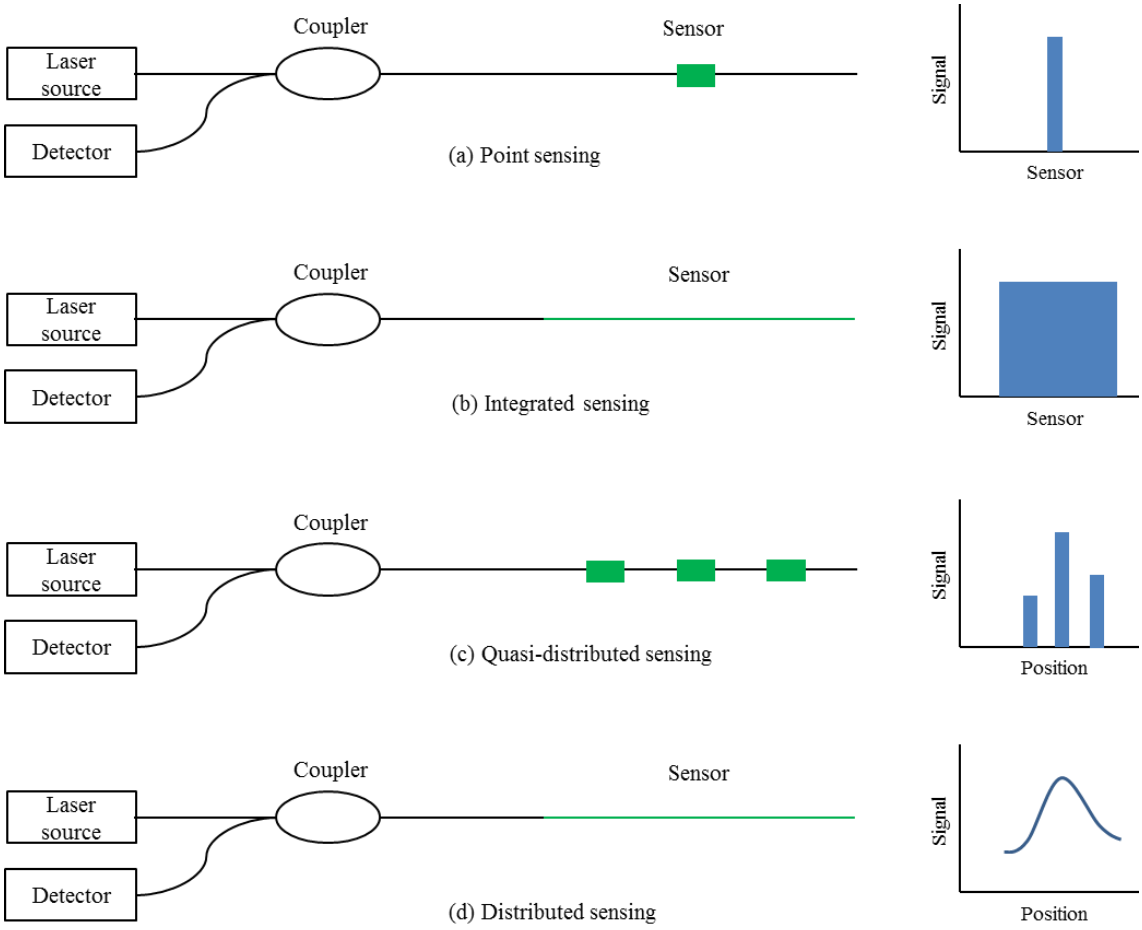

Fig. 3-6. Classification of OFS sensing technique

3.1.4. Distributed OFS sensing techniques

In order to determine the proper OFS technique for this study, the OFS techniques have been studied. Since there are already many good reviews about this topic, in this section, some advanced OFS techniques which can provide distributed strain measurement with high spatial resolution are

introduced.

Brillouin optical time domain reflectometry (BOTDR)

Stimulated Brillouin scattering has been regarded as a useful sensing mechanism for distributed temperature or strain measurement in civil structures and materials, since the Brillouin frequency shift has a linear dependence on both strain and temperature. As one of the recent developments, a prototype double-pulse BOTDR (DP-BOTDR) has been developed by Y. Sakairi, et al.[10] The system was confirmed to be capable of measuring distributed Brillouin frequency shift, i.e., the strain and temperature distribution with spatial resolution of 20 cm and accuracy of ±1 MHz, i.e. ±20 micro strain. The schematic diagram and photo of DP-BOTDR system are shown in Fig. 3-7. It consists of pulse signal generator, high-speed sampling A/D converter and other electric components are embedded in the PXI platform, which manages synchronous control and operation. Optical signals are processed in an optical unit.

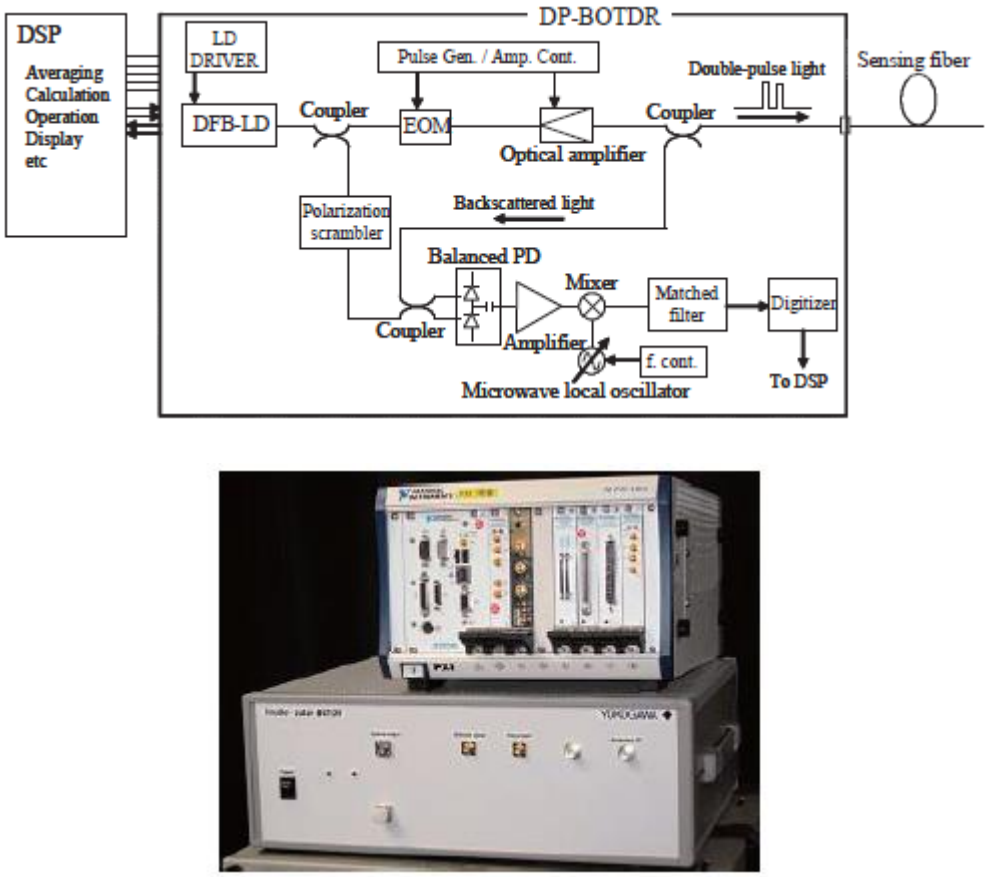

Fig. 3-7. The schematic diagram and photo of DP-BOTDR system

Brillouin optical correlation domain analysis (BOCDA)

Among sensing techniques using Brillouin scattering, a correlation-based Brillouin sensing system, called Brillouin optical correlation domain analysis (BOCDA), has been proposed and developed for the past few years[111213]. The system is based on the interaction of frequency-modulated continuous waves for both probe and pump waves. The BOCDA shows unique features of random accessibility of measurement position, high spatial resolution (1 cm), and high speed (~57 Hz). Fig. 3-8 (a) shows a schematic of the BOCDA system.

In 2006, a BOCDA system with spatial resolution of less than 1.6 mm was used to demonstrate distributed strain measurements by K. Y. Song, et al.[14] In the report, as shown in Fig. 3-8 (b), they simplified the system by introducing a novel beat lock-in detection where choppers are applied two times to both pump and probe waves at different frequencies, and only one lock-in amplifier is used at the beat frequency of them.

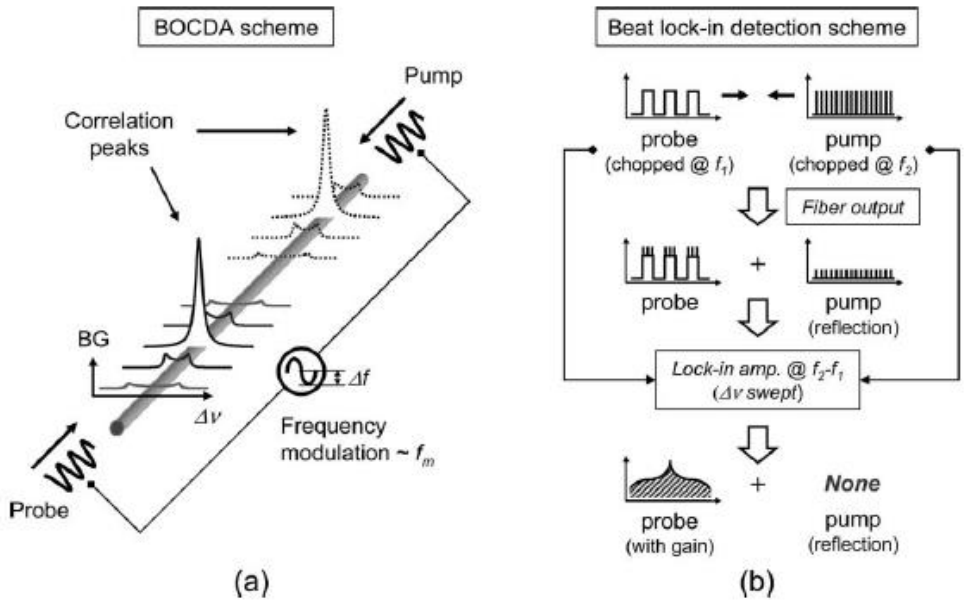

Fig. 3-8. (a) Operation scheme of the BOCDA system, (b) Schematic of beat lock-in detection

Rayleigh scatter based sensing techniques

In 1998, M. Froggatt and J. Moore introduced a method that uses a tunable external cavity diode laser to measure the reflected intensity of a reflector–fiber system as a function of wavelength[15]. The cross correlation of the Rayleigh scatter spectra from a selected section of fiber in the strained and unstrained states was used to determine the spectral shift resulting from the applied strain for strain calculation. Using this method, they demonstrated the measurement for strains of less than 60 micro strain in laboratory environment, and measurement accuracy of 5 micro strain over 30 cm was

achieved.

In 2006, the sensing technique using Rayleigh was improved by S. T. Kreger, et al.[16] They used swept wavelength interferometry (SWI) to measure the Rayleigh backscatter as a function of length in standard telecom-grade single mode and gradient index multimode fibers. By their method, the spatial resolution of strain measurement was improved to millimeter range over tens of meters of fiber, and accuracy was improved to better than 1 micro strain.

Optical frequency domain reflectometry (OFDR)

OFDR is a tunable laser-based frequency domain technique that has several distinct advantages over time domain and low coherence techniques[1718]. Specifically, OFDR has advantages in that it is capable of sub-millimeter resolution measurements over multiple tens of meters of optical length with high sensitivity and dynamic range. The technique has been employed in sensing systems using FBG sensor and Rayleigh-scatter based sensor[19] to achieve high measurement spatial resolution. As the sensing technique used in this study, the OFDR will be introduced in detail later.

Discussion

There are many OFSs associated with many sensing systems capable for distributed strain measurement with spatial resolution of millimeter range, they all have advantages and limitations, it is difficult to say which one is the best. But the proper technique for this study can be determined, which is long length FBG associated with sensing system based on OFDR. Comparing with the scatter based OFS, the FBG can provide strong and stable signal, which litter affected by perturbation of system especially the laser source, this is important for long-period measurement. OFDR method enables the FBG for strain measurement with high spatial resolution. The whole system will be introduced in detail in next section.

3.2. OFS sensing technique used in this study

The distributed sensing system based on OFDR using FBG sensor was employed in this study. However, the SHM of adhesive-bonded joints requires dynamic measurement and the sensing system used in previous studies was designed for static measurement. Thus a new sensing system based on OFDR which is capable of dynamic measurement was designed and developed. The principle of the two systems are the same, the improvements were made mainly on the critical devices. In this section, firstly, the basic principle of FBG was introduced, then the principle of sensing system based on OFDR was explained using the previous system as example, and finally the new system was introduced.

3.2.1. Fiber Bragg grating

Fiber Bragg grating (FBG) is an intrinsic device with periodic perturbation of refractive index in the core of an optical fiber. In recent years, several fabrication methods of FBG have been developed. In 1978, in Hill et al.'s study[20], the formation method of reflective-index gratings in an optical fiber by launching intense Argon-ion laser radiation into a germanosilicate fiber was reported. In 1989, the gratings in an optical fiber were fabricated by Meltz et al.[21] using the transverse holographic method. When the spectrally broadband light is injected into the FBG, the narrowband component will be reflected by the gratings as shown in Fig. 3-9. The wavelength of the component, which is called Bragg wavelength, is given by

$$\lambda_B = 2n_{eff}\Lambda \qquad \text{Eq. 3-3}$$

where Λ is the grating period, and n_{eff} is the effective refractive index of fiber core. The FBG is usually used as a filter device in fiber-optic communication system.

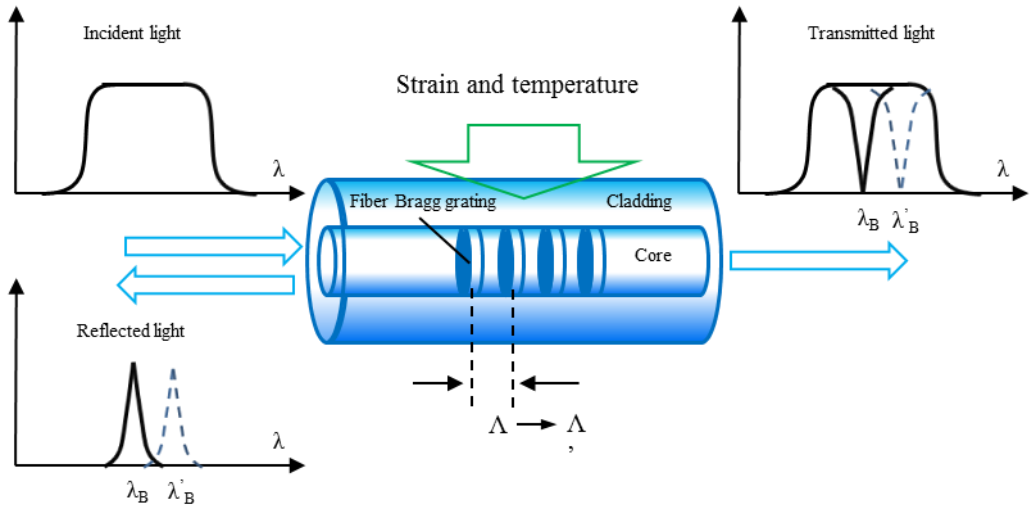

Fig. 3-9. Configuration and principle of FBG

When the external perturbation such as strain or temperature was applied on FBG, the shift of Bragg wavelength can be observed in reflected spectrum. And by analyzing the wavelength shift, the strain or temperature variation can be evaluated. Thus the FBG can be used as a strain and temperature sensor. The Bragg wavelength shift $\Delta\lambda_B$ caused by strain and temperature change can be expressed by[22],

$$\Delta\lambda_B = 2n\Lambda\left(\left\{1-\frac{n^2}{2}\left[P_{12}-\nu\left(P_{11}+P_{12}\right)\right]\right\}\Delta\varepsilon+\left[\alpha+\frac{\left(\frac{dn}{dT}\right)}{n}\right]\Delta T\right) \quad \text{Eq. 3-4}$$

where $\Delta\varepsilon$ and ΔT are the strain and temperature change, P_{ij} are the Pockel's (piezo) coefficients of the stress-optic tensor, ν is the Poisson's ratio, and α is the coefficient of thermal expansion (CTE) of the fiber material. The factor $\{\left(\frac{n^2}{2}\right)[P_{12}-\nu(P_{11}+P_{12})]\}$ has a numerical value of 0.22 approximately. Thus when the temperature is constant, the measured strain response can be expressed by

$$\frac{1}{\lambda_B}\frac{\delta\lambda_B}{\delta\varepsilon} = 0.78\times10^{-6}\ \ \mu\varepsilon^{-1} \quad \text{Eq. 3-5}$$

This responsivity gives a "rule-of-thumb" measure of the grating shift with strain of 1 nm per 1000 μm at 1.3 m. For silica fibers, the thermal response is dominated by the dn/dT effect, which contributes about 95% to the observed shift. The normalized thermal responsivity at constant strain is given by

.

$$\frac{1}{\lambda_B}\frac{\delta\lambda_B}{\delta T} = 6.67\times10^{-6}\ \ {}^{o}C^{-1} \quad \text{Eq. 3-6}$$

Because both strain and temperature change contribute to the wavelength shift and it is difficult to distinguish the response component in reflected spectrum, another FBG is usually employed as reference in practical measurement.

The FBG sensor has been intensively studied and applied widely for SHM. One of the reasons is that, the FBG sensor with multiple gratings in a single optical fiber is suitable for quasi-distributed and distributed measurement. Wavelength division multiplexing (WDM) and time division multiplexing (TDM) are two sensing techniques widely used for achieving quasi-distributed measurement using FBG. Generally the multiplexed sensor number is around 20 by WDM technique, and the number can reach about 100 by TDM technique.

As mentioned in Chapter 2, recently, the distributed sensing technique based on optical frequency domain reflectometry (OFDR) using long length FBG sensor was developed. The distributed strain measurement with spatial resolution less than 1 mm has been successfully demonstrated by this system. The distributed sensing system based on OFDR using 100 mm FBG sensor was employed in this study for the high spatial resolution and reliable measurement.

3.2.2. Principle of distributed sensing system based on OFDR

The arrangement of previous sensing system based on OFDR using long length FBG sensor is shown in Fig. 3-10. The layout of this system is similar to the one reported by B. A. Childers et al[23]. It consists of a wavelength tunable laser source (TLS), a computer, an A/D convertor and an interferometer including three broadband reflectors (R1, R2, R3), two photodiode detectors (D1, D2) and three 3 dB couplers (C1, C2, C3).

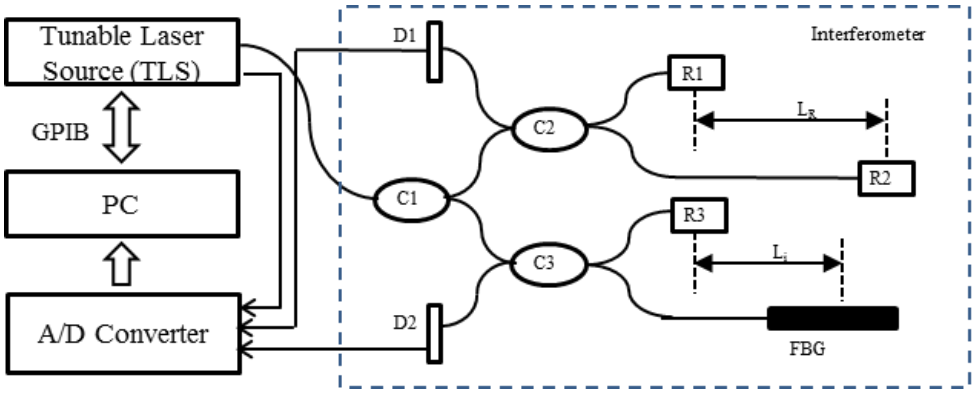

Fig. 3-10. Arrangement of sensing system based on OFDR (for static measurement)

During the measurement, the TLS sweeps the wavelength λ of the incident light, which is then diverged by C1 and proceeds into C2 and C3. The interference signal of reflected light from R3 and from each grating on FBG is observed by D2. The interference signal D_2 can be expressed by

$$D_2 = \sum_i R_i(k)\cos(2n_{eff}L_i k) \qquad \text{Eq. 3-7}$$

where k is the wavenumber of the incident light which is defined by $k = 2\pi/\lambda$, $R_i(k)$ is the reflected spectrum from i-th grating on FBG, L_i is the distance between R3 and the i-th grating.

The information of grating location on FBG is included in the frequency component of signal D_2. Thus, by applying digital signal analysis techniques, such as fast Fourier transform (FFT), the reflected spectrum from each grating in the FBG can be separated. In order for this, an external interferometer is needed because signal D_2 should be acquired at the constant wavenumber interval.

In this system, the interferometer consists of D1, C2, R1 and R2 is used as the external interferometer. In the similar manner, the interference signal D_1 observed by D1 is given by

$$D_1 = cos(2n_{eff}L_R k) \qquad \text{Eq. 3-8}$$

where L_R is the distance between the reflectors R1 and R2. Fig. 3-11 shows an example of signal D_1 when the TLS tunes from 1550 nm. From the figure, it can be seen that as the TLS tunes, the signal

D_1 varies in a cycle depending on the wavenumber interval Δk, which can be expressed by

$$\Delta_k = \frac{\pi}{n_{eff} L_R} \quad \text{Eq. 3-9}$$

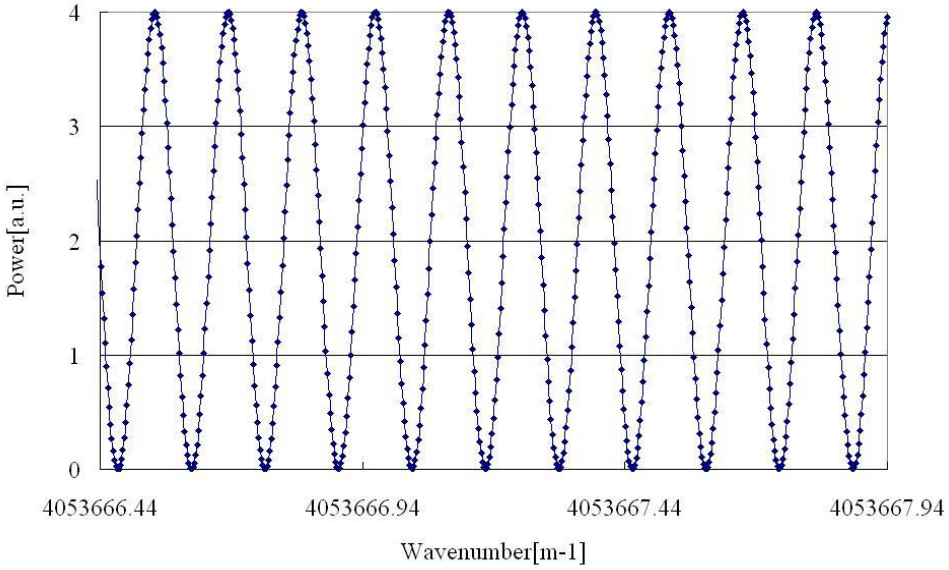

Fig. 3-11. Signal D_1 when the TLS tunes from 1550 nm

3.2.3. Signal processing

After acquisition, the signal D_2 is transmitted to computer for recording and signal processing based on short-time Fourier transform (STFT). In signal processing, a sliding window function is used to extract a portion of the D_2 signal (Fig. 3-12) in a wavenumber range for applying fast Fourier transform (FFT) to calculate the amplitude distribution along the frequency (position) direction. Then the window slides with prescribed distance for the same process until the whole wavenumber range is covered. In this way, the reflected spectrum at an arbitrary position on FBG can be obtained and a spectrogram contains the reflected spectrum at each position on FBG can be drawn. An example of the spectrogram is shown in Fig. 3-13, the horizontal and vertical axis indicates the wavelength and position on FBG, respectively, and the color indicates the amplitude.

For this signal processing method, the readout resolution of wavelength $\Delta\lambda$ and position Δd can be expressed by equations

$$\Delta\lambda = (N_w - N_0)\frac{\lambda_2 - \lambda_1}{2\pi\left(\frac{1}{\lambda_1} - \frac{1}{\lambda_2}\right)}\Delta k \qquad \text{Eq. 3-10}$$

$$\Delta d = \frac{\pi}{N_{FTT} n_{eff} \Delta k} \qquad \text{Eq. 3-11}$$

where N_w is the window length, N_o is the overlap number, N_{FFT} is the length of FFT, λ_1 and λ_2 are the start and end wavelength of the wavelength swept by TLS during measurement, respectively.

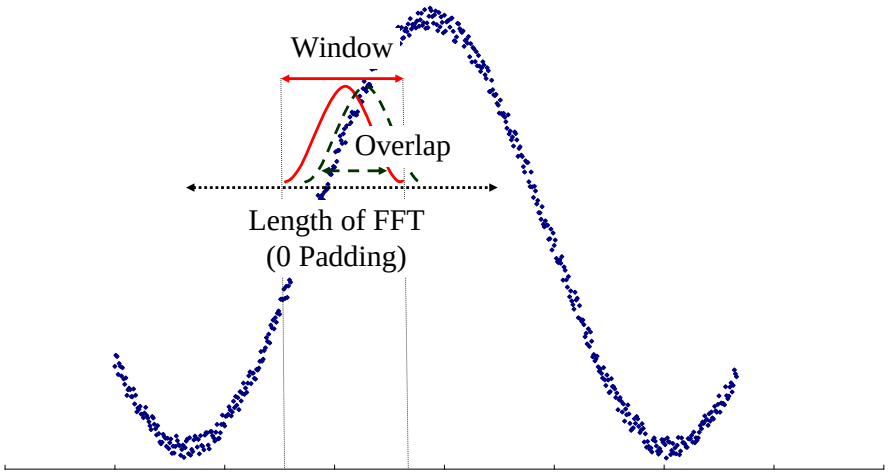

Fig. 3-12. Method of applying FFT to the signal

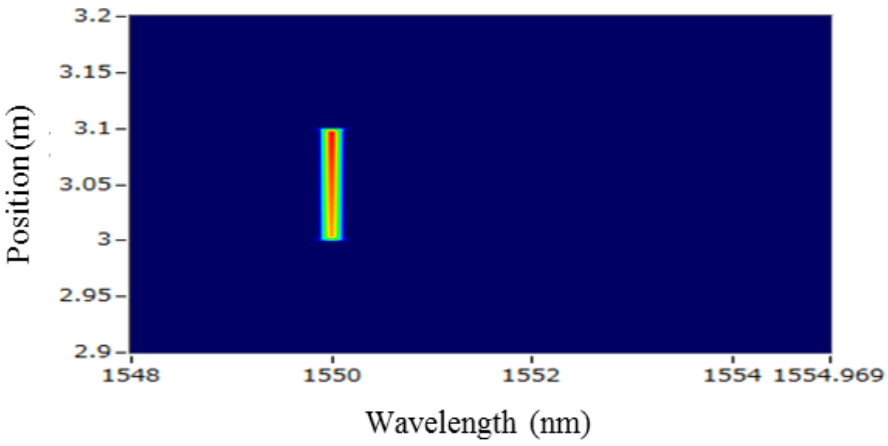

Fig. 3-13. Spectrogram obtained by Fourier transform analysis

3.2.4. Bragg wavelength determination methods and spatial resolution

By using the distributed sensing system based on OFDR, the reflected spectrum from each position on FBG can be obtained. The next step is to determine the Bragg wavelength (center wavelength) of the spectra and compare it with the initial Bragg wavelength so that the wavelength shift can be measured. Several determination methods have been developed[24], and the full width at half maximum (FWHM) method and the centroid method are employed in this study.

The FWHM method is explained in Fig. 3-14. The center wavelength is defined as the wavelength coordinate of the center of the full width in spectrum at half maximum.

The centroid method is shown in Fig. 3-15. The center wavelength is defined as the wavelength coordinate of the centroid of the spectrum area. If the x axis indicates the wavelength and y axis indicates the power, the center wavelength obtained by centroid method can be expressed by

$$x = \frac{\int_A ydA}{\int_A dA} \qquad \text{Eq. 3-12}$$

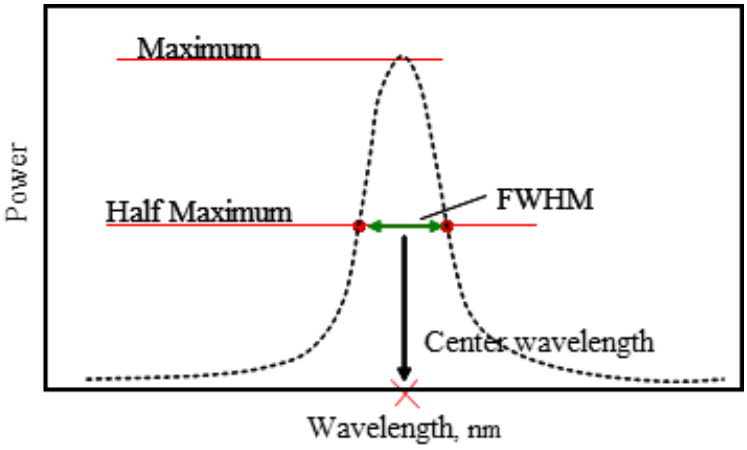

Fig. 3-14. FWHM method

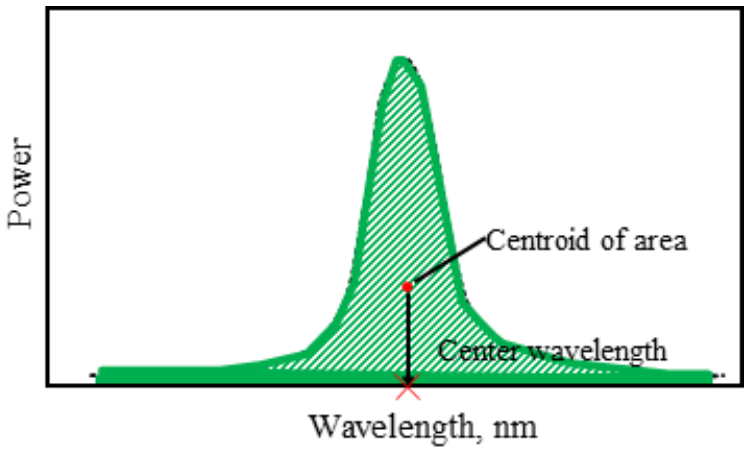

Fig. 3-15. Centroid method

When the spectrum is regular with a single peak, there is no much difference between the center wavelengths obtained by two methods. However, in the case when the spectrum is not regular and with multiple peaks, which is very common due to the lateral load or sharply varying strain on FBG in practical measurement, the two methods give different result as shown in Fig. 3-16.

In this study, the spatial resolution of the sensing system is defined as the response distance to the step strain. The response distance is explained in Fig. 3-17, it is defined as the distance between the position where the measured strain reaches 10% and 90% of applied strain. For the sensing system based on OFDR, the spatial resolution depends on the window length. The better spatial resolution can be achieved by the longer window length[25]. The center wavelength determination method can also affect the spatial resolution. In this study, the FWHM method was proved to has better spatial resolution than centroid method by simulation, this will be dicussed in detail in Section 3.3.3.

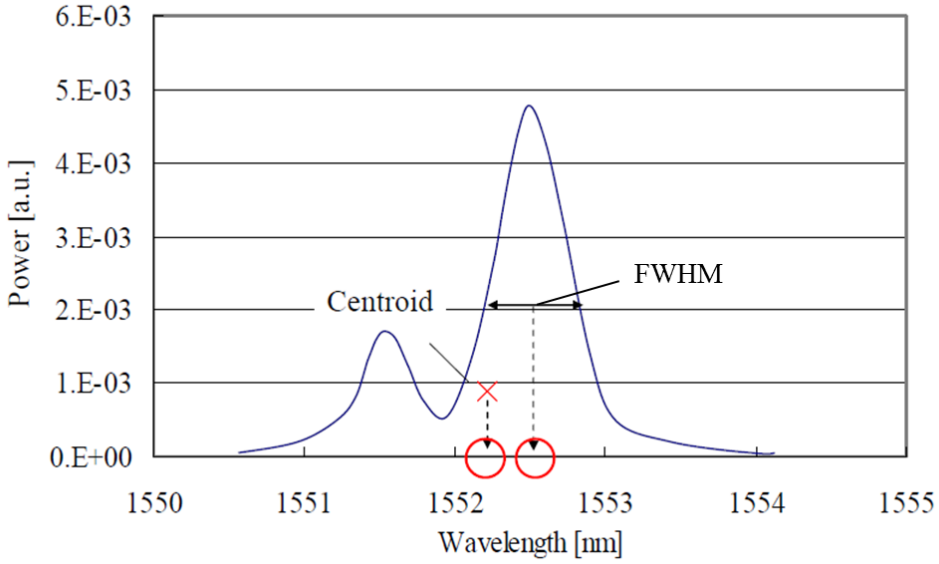

Fig. 3-16. Center wavelength obtained by two methods in an irregular spectrum

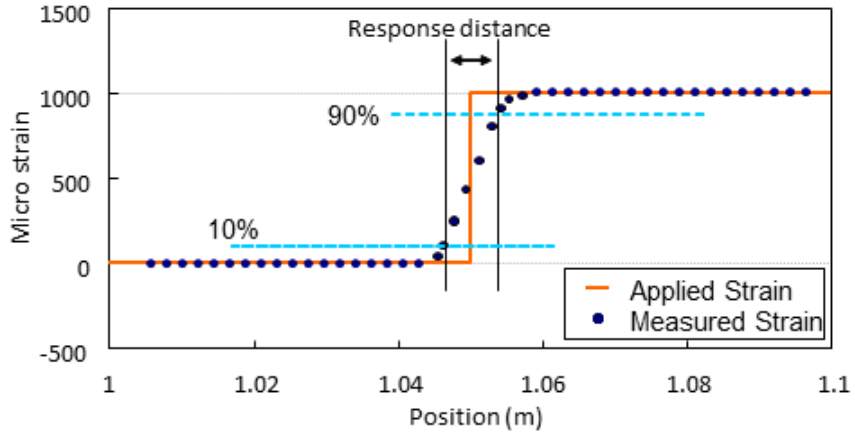

Fig. 3-17. Definition of response distance

The conditions and requirements of the meausrement should be considered when choosing the center wavelength determination method in practical measurement. The FWHM is more sensitive and can provide measurement with better spatial resolution, but it is also sensitive to the environmental disturbance such as variation of TLS power and false measurement may be obtained. The centroid method is believed to be more stable, it can provide smooth measurement to the sharply varying strain and has better resistence against environmental disturbance, which is considered important for long-term dynamic measurement. Thus in this study, because the strain distribution in adhesive layer is not uniform and concentrates at overlap ends, the centroid method was employed in dynamic measurement for its stability, and the FWHM method was employed for evaluating the accuracy of measurement for its high accuracy.

3.3. Distributed sensing system based on OFDR for dynamic measurement

There are two basic requiements for sensing system in this study, distributed sensing and dynamic sensing capacity. Since the previous system was not designed for dynamic measurement and a complete measurement will take 2 to 3 seconds, it cannot be used directly for the measurement with stable and relatively high frequency. Therefore, a new sensing system is needed, which should be also based on OFDR to achieve the distributed measurement with high spatial resolution and should be capbale of dynamic measurement. This can be ahieved through the improvement on critical devices and employing the similar arrangement as the previous system.

In this section, the distributed sensing system based on OFDR for dynamic measurement developed and employed in this study is introduced in three aspects, system specification, development and evaluation.

3.3.1. Specifications of dynamic distributed sensing system

The specifications of a sensing system should be made based on the consideration of measurement conditions and requirements such as the object measurands, measurement frequency (sampling rate) and measurement accuracy. In this study, the specifications were made based on consideration of the requirements of the dynamic measurement in dynamic load test on three parameters: sampling rate, measurement range and spatial resolution. Usually, the specification should be determined in detail considering the load conditions. In our case, the load conditions of dynamic load test were not determined in advance, and some conditions needed to be determined according to the sensing system capacities, thus the sensing system specifications and load conditions were determined at the same time. Although the detailed load conditions were not determined, some basic concepts were decided:

a) The specimen for test is an adhesive-boned joint of composite adherends.
b) The load should be cyclic sinusoidal load in tensile with the load ratio of 0.1.
c) The test should last until the specimen failure.
d) The test duration should be appropriate considering the data storage.
e) The crack should be controlled to initiate and propagate in bonding area in adhesive layer or at adhesive/adherend interface at the appropriate propagation speed.
f) A microscope will be used to take photograph of crack to monitor the crack growth.

Pilot tests were also carried out to aid in the determination of system specifications and load conditions.

1. Sampling rate

The process of determining the sampling rate is shown in Fig. 3-18. Because the FBG is sensitive to temperature change, the relatively low load frequency was considered in order to avoid the heat generated from the composite in test. In the pilot test, the load frequency of 0.5 Hz was found to be convenient for microscope observation. Thus the load frequency for cyclic load test was determined as 0.5 Hz.

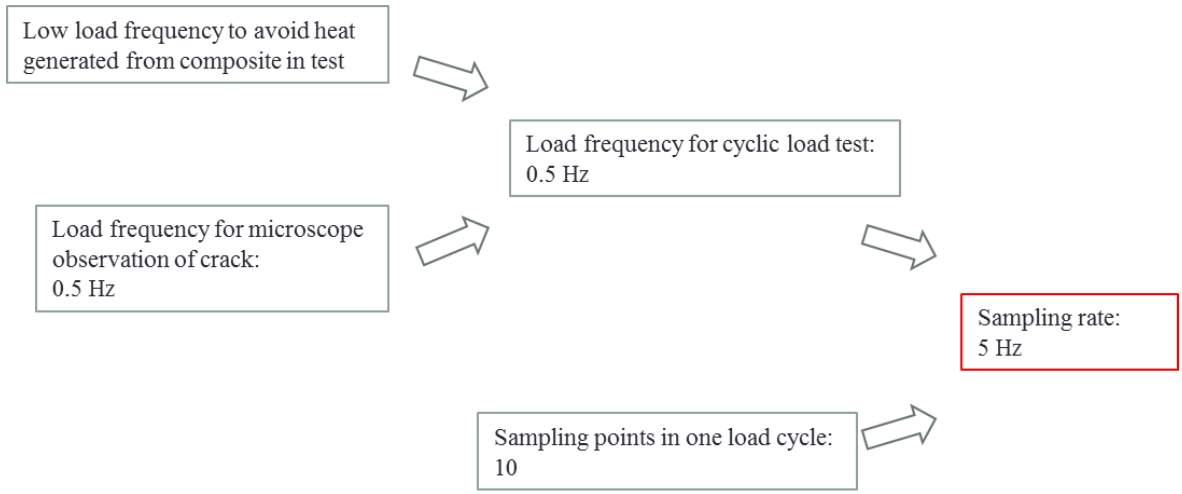

Fig. 3-18. Determination of specification on sampling rate

In each load cycle, the measurements at the maximum load and minimum load were considered important for the joint condition monitoring. However, in real measurement, it is difficult to obtain measurement at maximum/minimum load in each cycle because the sensing system does not synchronize with the test machine completely. Although this problem can be solved by increasing the sampling points in each cycle, this number is limited by sensing system capacity. Thus the appropriate number of sampling points in one cycle should be determined. In this study, the number of sampling

points in one load cycle was determined as 10. The largest possible difference between the real measurement and measurement at maximum/minimum load is 5% of the measurement at maximum/minimum load which was considered to be acceptable.
Thus, the sampling rate of dynamic sensing system was determined as 5 Hz.

2. Measurement range

The process of determining the measurement range is shown in Fig. 3-19. In the case of previous sensing system, the recorded data file containing all information in one measurement is around 1 MB, the data file size of dynamic sensing system was assumed to be the same because the same system principle. The dynamic measurement will produce large number of data file, and the data storage and analysis will be difficult if the data is too large. The total data file size of 500 GB was considered appropriate, and considering the sampling points in one load cycle, the total number of load cycle was determined as 50000. In order to achieve this, and considering the load frequency and load ratio, the maximum load of cyclic load was determined to be in the range of 250 kgf to 400 kgf through pilot tests. The crack length with respect to load cycle at different maximum load in pilot tests was shown in Fig. 3-20. The maximum crack length was found to be 10 mm. Considering the maximum load and maximum crack length, the FE analysis was carried out and the maximum longitudinal strain in bonding area was found to be 2650 με. Thus the measurement range was determined to be 0 to 3000 με, and considering the Eq. 3-5, the wavelength sweep range of TLS in dynamic sensing system should be wider than 10 nm.

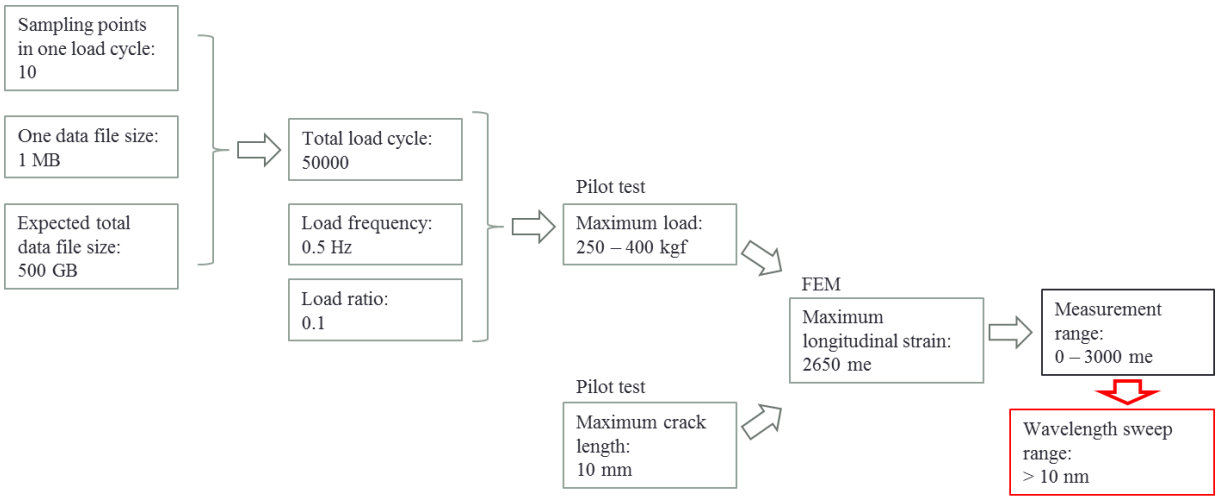

Fig. 3-19. Determination of specification on measurement range

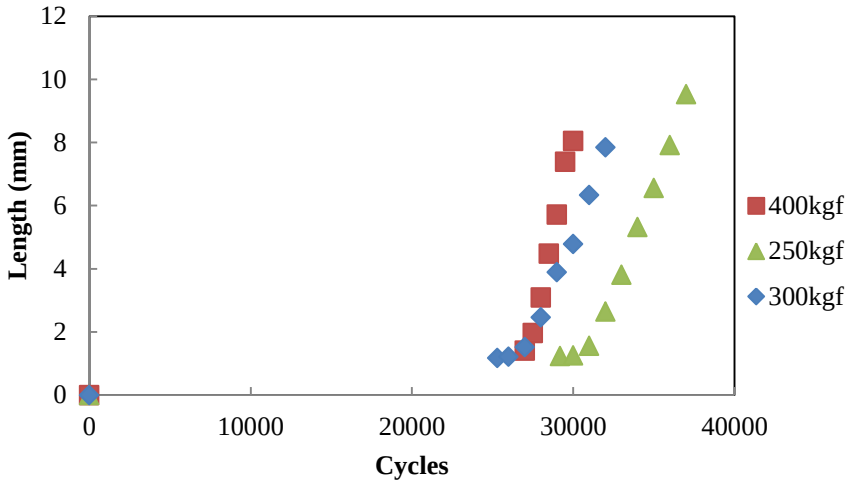

Fig. 3-20. Crack length in pilot tests with different maximum load

3. Spatial resolution

The process of determining the spatial resolution is shown in Fig. 3-21. For the distributed measurement in adhesive-bonded joint, the higher spatial resolution means the better description of the non-uniform strain distribution which is important for condition assessment of the join. Considering the maximum load, the FE analyses were carried out using the model meshed with various element sizes along overlap length direction. The element size which can describe the strain distribution was found to be 1 mm, thus the spatial resolution of dynamic distributed sensing system was determined as 1 mm. Because the spatial resolution of sensing system depends on the window length and by using the previous system the measurement with spatial resolution of less than 1 mm had been achieved when the window length was 400 pm, the window length of dynamic distributed sensing system was determined as 400 pm or higher.

The dynamic distributed sensing system specifications and load conditions are summarized in Table 3-1.

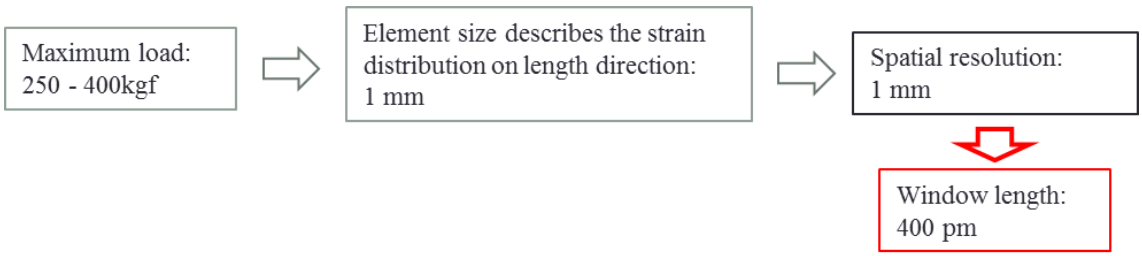

Fig. 3-21. Determination of specification on spatial resolution

Table 3-1. Dynamic distributed sensing system specifications and load conditions for cyclic load test

Cyclic load test conditions		Sensing system specifications	
Load frequency	0.5 Hz	Sampling rate	> 5 Hz
Wave form	sinusoidal	Wavelength sweep range	> 10 nm
Maximum load	250 – 400 kgf	Window length	400 pm
Load ratio	0.1		

3.3.2. Development of dynamic distributed sensing system

The dynamic distributed sensing system based on OFDR was manufactured by Lazoc Inc. according to the specifications (Fig. 3-22). The arrangement is shown in Fig. 3-23, improvements were made on devices in blue border. The TLS was customized based on TSL-510 (Santec Corporation) to improve the wavelength swept speed, the high speed A/D converter board (APX-500/ADM-414EX, Avaldata Corporation) and the high speed storage board (APX-880, Avaldata Corporation) were employed to increase the data transmission and record speed. The brief comparison of the devices with the previous system is shown in Table 3-2.

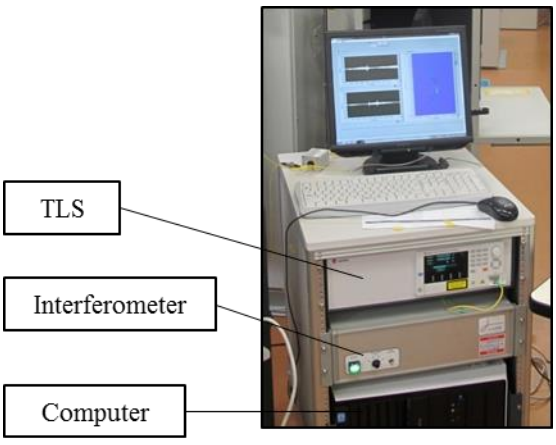

Fig. 3-22. Dynamic distributed sensing system

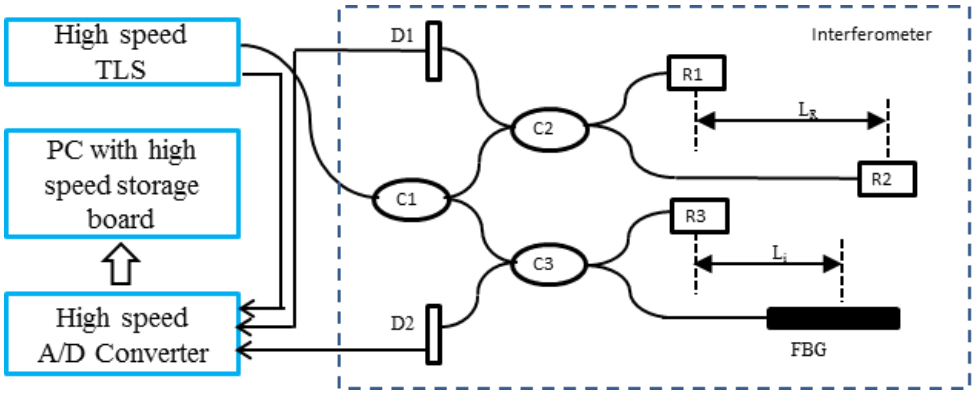

Fig. 3-23. Arrangement of sensing system based on OFDR (for dynamic measurement)

During the dynamic measurement, the TLS sweeps wavelength at the prescribed rate and range. In each wavelength sweeping cycle, the A/D convertor samples the signal D_2 in data acquisition wavelength range and transmit it to computer for real-time analysis and record. All the process is completed before the next measurement cycle. The measurement can be reproduced at any time by processing the recorded D_2 signal using the same method as the real-time signal processing. The results discussed in this thesis were based on the post-test data processing.

Table 3-2. Device comparison between two systems

Sensing system based on OFDR	For static measurement	For dynamic measurement
TLS	AQ4321A (Ando Electric Co., Ltd)	TSL-510 (Santec corporation)
Wavelength sweep speed (max)	100 nm/s	> 1000 nm/s
A/D converter	PCI-6115 (National Instruments corporation)	APX-500 /ADM-414EX (Avaldata corporation)
Sampling rate	10 MHz	400 MHz
Storage board on PC		APX-880 (Avaldata corporation)
Storage speed		17000 MB/s

3.3.3. Evaluation of dynamic distributed sensing system

Evaluation was carried out on two important parameters of developed sensing system, sampling rate and spatial resolution. The sampling rate of system was evaluated by cyclic load test which will be introduced in chapter 4 in detail. The spatial resolution evaluation is carried out by system simulation and introduced in this section.

According to the difination, the step strain load should be applied to FBG to check the spatial

resolution of the sensing system. But in real condition, the step strain is very difficult to achieve, thus the simulation of the system was carried out for the evaluation of the spatial resolution. The detailed information of simulation method can be found in[26].

In simulation, the 100 mm long FBG with Bragg wavelength of 1550 nm is at position of 5.000 m to 5.100 m. 1000 micro strain was applied on FBG at position of 5.000 m to 5.051 m. Other parameters used in simulation are shown in Table 3-3, where L_{R3} is the distance between D2 and R3, and L_G is the distance between the beginning of FBG and R3. The simulated spectrograms are shown in Fig. 3-24. Then the simulated D_2 data was analyzed by FWHM and centroid method to calculate the center wavelength distribution. The window length of 400 pm and 800 pm were used for calculation and other settings are shown in
Table 3-4.

Table 3-3. Simulation parameters

Parameter	Value
L_R (m)	20
n	1.46
L_{R3} (m)	1
L_G (m)	5
TLS sweep range (nm)	1546 - 1554

Table 3-4. Center wavelength distribution calculation settings

Setting	Value
Wavelength resolution (pm)	20
Readout position resolution (mm)	0.15
Window length (pm)	400/800
Window type	Hanning

As the result, the center wavelength distribution results are shown in Fig. 3-25 and Fig. 3-26. The spatial resolutions calculated by two methods at two window lengths are summarized in Table 3-5. From the result, the centroid method showed worse spatial resolution comparing with the FWHM method in both window lengths of 400 and 800 pm. And when using the same center wavelength determination method, spatial resolution can be improved by increasing window length. The best spatial resolution showed in evaluation was 0.61 mm achieved by using FWHM method and 800 pm window length.

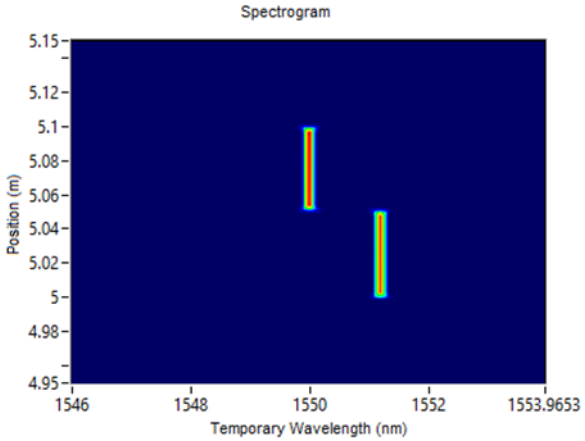

(a) Window length 400 pm

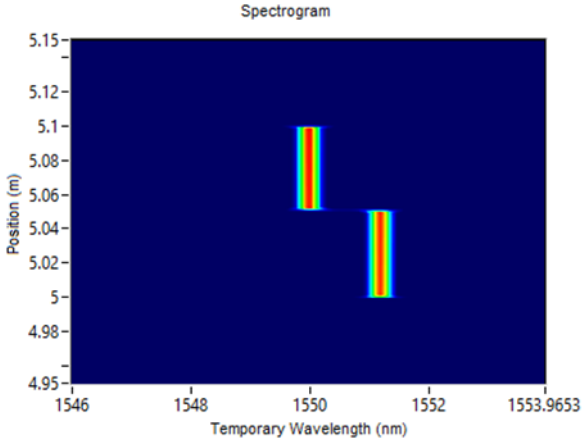

(b) Window length: 800 pm

Fig. 3-24. Simulated spectrograms using window length of 400 pm and 800 pm

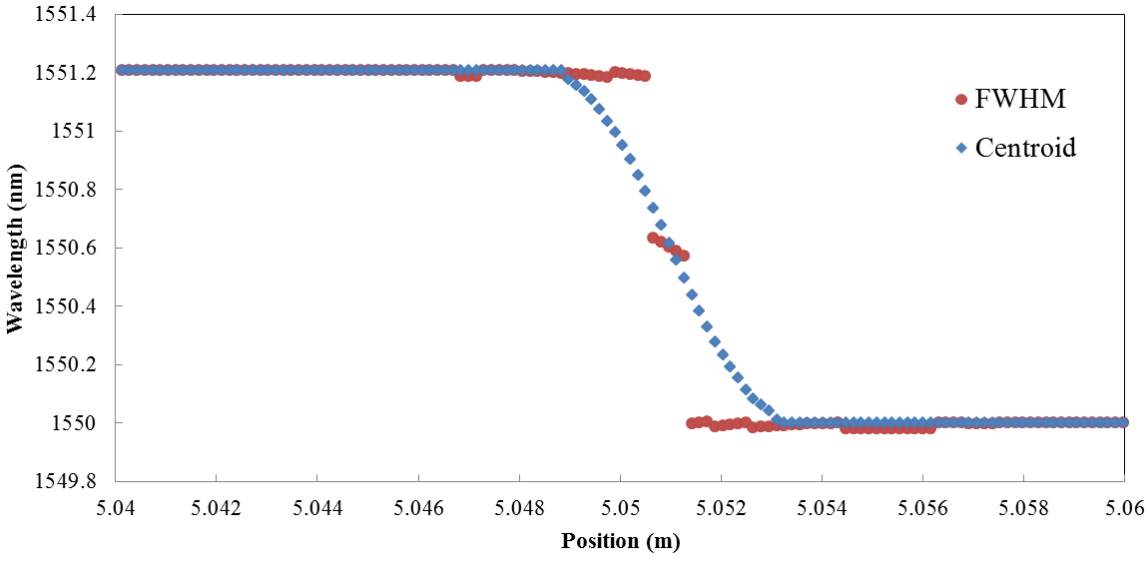

Fig. 3-25. Response center wavelength distribution to step load using window length of 400 pm

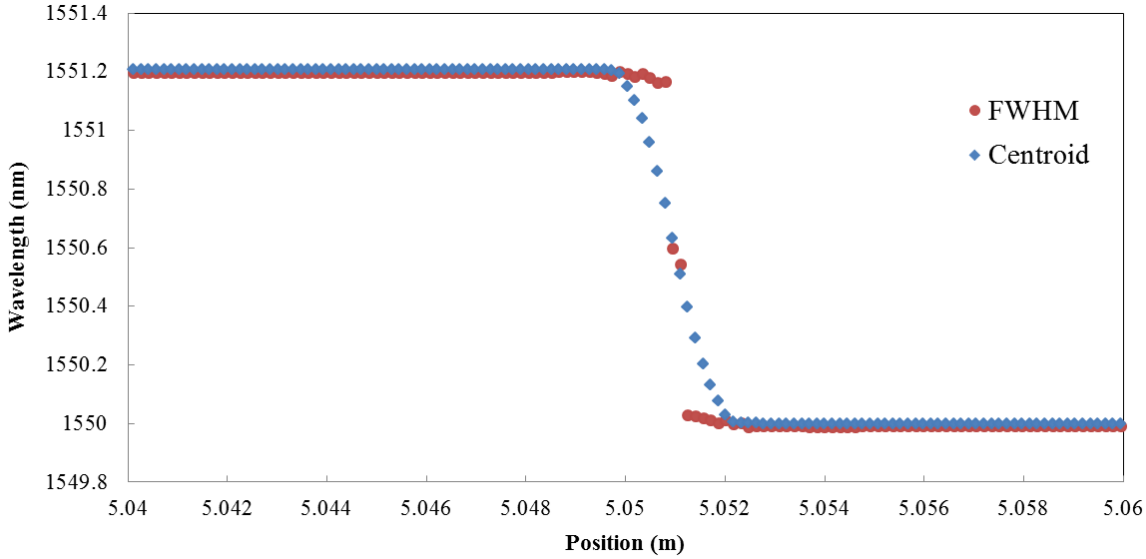

Fig. 3-26. Response center wavelength distribution to step load using window length of 800 pm

Table 3-5. Spatial resolution of two methods using different window length

Window length (pm)	Centroid	FWHM
400	2.90	0.92
800	1.53	0.61

3.4. Summary

The long length FBG associated with distributed sensing system based on OFDR can achieve measurement with high spatial resolution of less than 1 mm, which is suitable for high precision strain measurement and damage detection in adhesive-bonded joint when joint overlap length is relatively short. Thus this sensing technique was employed in this study. In order to carry out dynamic measurement to achieve real-time strain measurement and damage detection of joint in service, the dynamic distributed sensing system was designed and developed based on the cyclic test conditions. The spatial resolution of developed system was proved to be less than 1 mm as the specification.

Reference

[1] S. Z. Yin, P. B. Ruffin, F. T. S. Yu, Fiber optic sensors, Taylor & Francis Group, 2008
[2] H. Golnabi, Design of an optical fiber sensor for linear thermal expansion measurement, Optics & Laser Technology, vol. 34, pp.389-394, 2002
[3] J. Crisp, Introduction to fiber optics, Billdes Ltd, 1996
[4] A. D. Kersey, A Review of Recent Developments in Fiber Optic Sensor Technology, Optical fiber technology, vol.2, pp.291-317, 1996
[5] B. Lee, Review of the present status of optical fiber sensors, Optical fiber technology, vol.9, pp.57-79, 2003
[6] J. M. Lopez-Higuera, L. R. Cobo, A. Q. Incera and A. Cobo, Fiber Optic Sensors in Structural Health Monitoring, Journal of lightwave technology, vol.29, pp.587-608
[7] T. Kurashima, T. Horiguchi and M. Tateda, Distributed-temperature sensing using stimulated Brillouin scattering in optical silica fibers, Opt. Lett., vol.15, pp.1038-1040, 1990
[8] X. Bao, J. Dhliwayo, N. Heron, D. J. Webb and D. A. Jackson, Experimental and theoretical studies on a distributed temperature sensor based on Brillouin scattering, Journal of Lightwave Technology, vol.13, pp.1340-1348, 1995
[9] H. Igawa, K. Ohta, T. Kasai, I. Yamaguchi, H. Murayama and K. Kageyama, Distributed measurements with a long gauge FBG sensor using optical frequency domain reflectometry (1st report, system investigation using optical simulation model), J. Solid Mech. Mater. Eng., vol.2 pp.1-11, 2008
[10] Y. Sakairi, S. Matsuura, S. Adachi and Y. Koyamada, Prototype double-pulse BOTDR for measuring distributed strain with 20-cm spatial resolution, SICE Annual Conference, pp.1106-1109, 2008
[11] K. Hotate and T. Hasegawa, Measurement of Brillouin gain spectrum distribution along an optical fiber with a high spatial resolution using a novel correlation-based technique—Demonstration of 45cm spatial resolution, Proc. Intern. Conf. on Optical Fiber Sensors (OFS-13), pp.337-340, 1999
[12] K. Hotate and T. Hasegawa, Measurement of Brillouin gain spectrum distribution along an optical fiber by direct frequency modulation of a laser diode, Proc. SPIE, vol.3860-44, pp.306-316, 1999
[13] K. Hotate and M. Tanaka, Distribution fiber Brillouin strain sensing with 1 cm spatial resolution by correlation-based continuous-wave technique, IEEE Photonic Technology Letters, vol.14, pp.179-181, 2002
[14] K. Y. Song, Z. He and K. Hotate, Distributed strain measurement with millimeter-order spatial resolution based on Brillouin optical correlation domain analysis, Optics Letters, vol.31, pp.2526-2528, 2006
[15] M. Froggatt and J. Moore, High-spatial-resolution distributed strain measurement in optical fiber with Rayleigh scatter, Applied Optics, vol.37, pp.1735-1740, 1998
[16] S. T. Kreger, D. K. Gifford, M. E. Froggatt, B. J. Soller and M. S. Wolfe, High resolution distributed strain or temperature measurements in single-and multi-mode fiber using swept-wavelength interferometry, Optical Fiber Sensors, 2006, Cancun, Mexico
[17] U. Glombitza and E. Brinkmeyer, Optical frequency domain reflectometry for characterization of single-mode integrated optical waveguides, J. Lightwave Tech, vol.11, pp.1377-1384, 1993
[18] J. P. von der Weid, R. Passy, G. Mussi, and N. Gisin, On the characterization of optical fiber network components with optical frequency domain reflectometry, J. Lightwave Tech, vol.15, pp.1131-1141, 1997
[19] B. J. Soller, M. Wolfe and M. E. Froggatt, Polarization resolved measurement of Rayleigh backscatter in fiber-optic components, OFC Technical Digest, Los Angeles, paper NWD3, 2005
[20] K. O. Hill, Y. Fujii, D. C. Johnson and B. S. Kawasaki, Photosensitivity in optical fiber waveguides: application to reflection filter fabrication, Applied Physics Letters, vol.32, no.10, pp.647-649, 1978
[21] G. Meltz, W. W. Morey and W. H. Glenn, Formation of Bragg gratings in optical fibers by a transverse holographic method, Optics Letters, vol.14, no.15, pp.823-825, 1989
[22] A. D. Kersey, M. A. Davis, J. Patrick, M. LeBlanc, K. P. Koo, C. G. Askins, M. A. Putnam and E. J. Friebele, Fiber Grating Sensors, Journal of Lightwave Technology, vol.15, pp.1442-1463, 1997
[23] B. A. Childers, M. E. Froggatt, S. G. Allison, et al., Use of 3000 Bragg grating strain sensors distributed on four eight-meter optical fibers during static load tests of a composite structure, Proc. of

SPIE, vol.4332, pp.133-142

[24] Y. Q. li, Y. Xie and G. Z. Yao, Comparison of peak searching algorithms for wavelength demodulation in fiber Bragg grating sensors, ICIECS 2nd International Conference, 2010

[25] G. Akiyama, graduation thesis, Department of Systems Innovation, School of Engineering, The University of Tokyo, 2006

[26] D. Wada, doctoral dissertation, School of Engineering, The University of Tokyo, 2012

Chapter 4

Dynamic strain distribution measurement

In this study, we focus on the crack occurs in adhesive-bonded joint in adhesive layer or at the adhesive/adherend interface. The stain distribution in overlap length direction is considered as the damage indicator, through the monitoring of which the crack should be evaluated. For this purpose, the measurement of the damage indicator is an important process, works including the sensing system development, sensor installation, data acquisition and data storage need to be considered to achieve the reliable measurement.

The development of sensing system used in this study has been introduced in the previous chapter. The FBG sensor employed by the system is specialized at measuring strain along its longitudinal strain. Considering the direction of damage indicator – strain distribution, the FBG should be aligned in the overlap length direction for measurement. From the analysis of previous studies on SHM techniques of adhesive-bonded joints, the strain distribution near the damage location is highly desired, which means the FBG needs to be embedded into the joint in adhesive layer or at the adhesive/adherend interface. Considering the features of OFS, the embedded measurement is feasible, but there was no good demonstration in previous studies.

In study field of composite material and structure, S. Takeda et al. embedded an FBG sensor into carbon fiber reinforced plastic laminates to detect delamination in CFRP cross-ply laminates[1]. The embedment was evaluated by microscope inspection, and the reflected spectra were confirmed by theoretical calculation. Other studies using the similar embedment method can be found[234]. It seems that composite material is an ideal host for OFS embedment, and considering the increasing application of adhesive-bonded in composite structures, the adhesive-bonded joint made of composite is used and the FBG is embedded into the composite component for measurement in this study. Besides the sensor embedment other issues need to be considered such as the temperature compensation, sensor protection, dynamic data acquisition and storage, management of huge data.

This chapter introduces the process of the damage indicator measurement in aspects of specimen manufacturing, FE model, static load test, cyclic load test, results and problems and future works.

4.1. Specimen manufacturing

4.1.1. Specimen design

As mentioned in chapter 2, there are various joint forms of adhesive-bonded joint, it is difficult to discuss all the joint forms. The single-lap joint is chosen as the study object for its simple geometry, and if the SHM method is successfully developed, it can also be used on other joint forms through proper modification.

The adhesive-bonded single-lap joint specimen was designed based on ISO 4587:1995. This standard is usually used for the determination of tensile lap-shear strength of bonded assemblies using an adhesive-bonded single-lap joint. In this study, only the configuration of the joint was referred. The specimen configuration is shown in Fig. 4-1. The two adherends made of unidirectional carbon fiber reinforced plastic (CFRP) were adhered by the film adhesives to form a single-lap joint. Each CFRP adherend is made of 10 pieces of prepregs, and the thickness is about 1.5 mm. The fiber direction of CFRP was aligned with the overlap length direction (*z*). The overlap length and thickness of the adhesive layer are 25.0 mm and 0.2 mm respectively. The adhesive film contains support structure of non-woven polyester mat.

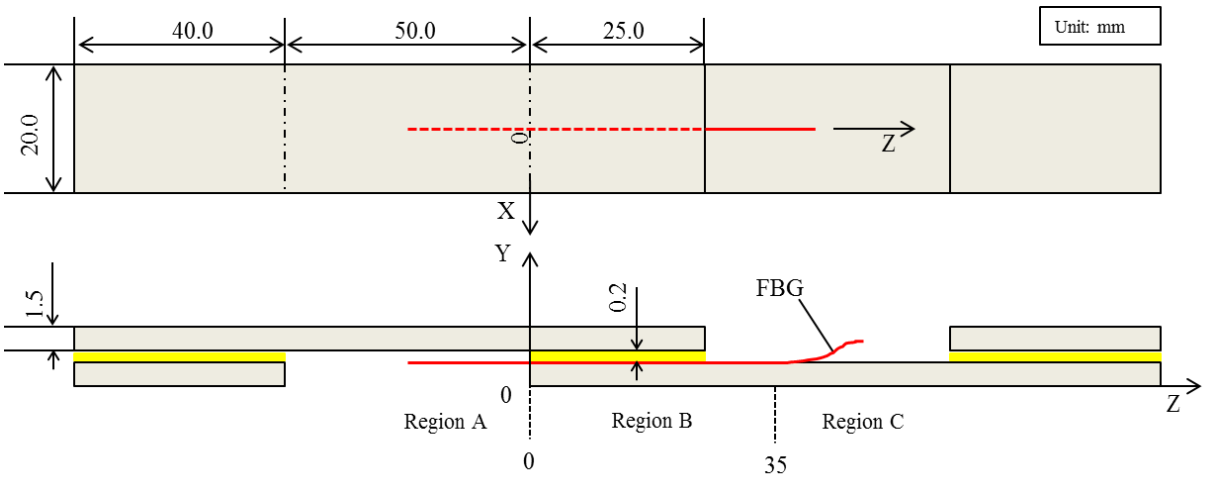

Fig. 4-1. Joint specimen configuration

The polyimide coated FBG sensor, whose length and diameter are about 95 mm and 150 μm, was designed to be embedded into the surface of one of the CFRP adherends in the center in width along the fiber direction. The portion of FBG in region B shown in the figure is completely embedded, while the portion in region A and C were free for temperature compensation in measurement. The product information of adherend, adhesive and FBG can be found in Table 4-1.

Table 4-1. Product information of specimen components

	Material	Product name	Manufacturer
Adherend	Carbon Fiber Reinforced Plastic (CFRP)	Q-A111E	Toho Tenax Co., Ltd
Adhesive	Film adhesive	Newport 102	Newport Adhesive and Composites, Inc
Sensor	FBG		Fujikura Ltd

4.1.2. Adherend curing and FBG embedment

The FBG sensor has been embedded into the adhesive-bonded joint for strain measurement in Schizas's study and Murayama's study. However, the embedment was not perfect. In Schizas's study, the FBG was embedded between the second and third layer in composite adherend, not the adhesive/adherend interface where the strain is considered to show better response to the crack. In Murayama's study, the FBG was embedded in the groove on surface of adherends, the position of FBG and the bonding quality between FBG and adherend were difficult to control.
In this study, we aim to improve the FBG embedment. There are basically four goals for the embedment.

a. The FBG should be embedded into the adhesive/adherend interface.
b. The embed position of FBG can be controlled.
c. The embedment should have no significant influence on strength of host structure or FBG function.
d. The host structure should provide protection for embedded FBG during measurement.

The FBG embedment procedure in this study consists of two steps as shown in Fig. 4-2. In order to embed the FBG into the adhesive/adherend interface, the FBG was designed to be embedded into the surface of CFRP adherend during the CFRP curing. Then the CFRP adherend with embedded FBG will be adhered to form a single-lap joint, and the FBG will be embedded into the interface consequently. The CFRP curing process and FBG embedment are introduced in this section.

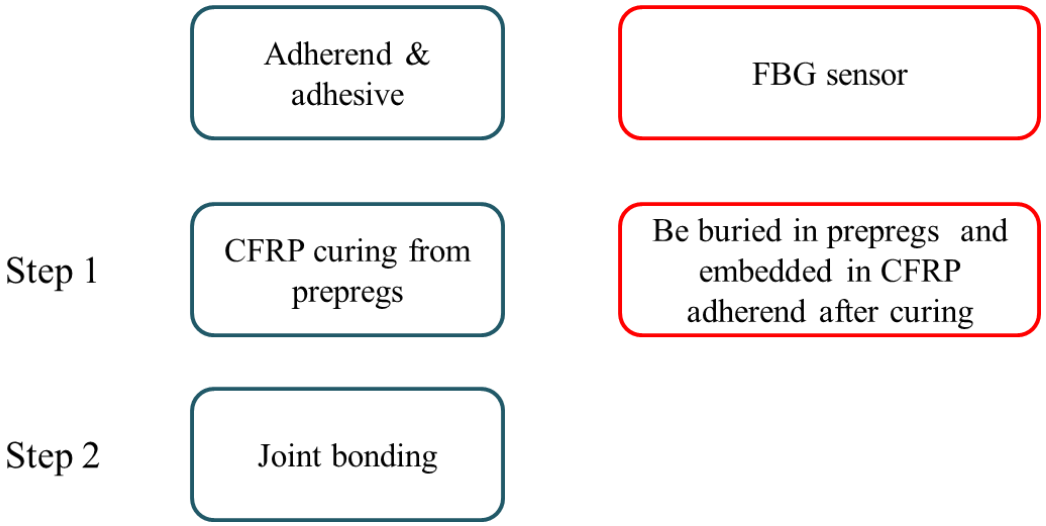

Fig. 4-2. FBG embedment steps

The CFRP curing setup is shown in Fig. 4-3. The dimensions of curing jig are shown in Fig.XX. The FBG fiber was slightly stretched and adhered to the center at bottom of curing jig by adhesive tapes (Fig. 4-5), the portion with gratings was aligned at the designed position. Ten pieces of CFRP prepregs were stacked as $[0_{10}]$ and put upon the FBG (Fig. 4-6). The white cubes at two ends of prepregs were made of silicon rubber, which were used to stop the leaked epoxy resin from prepregs during curing. In region C, the release film (PTFE) were inserted between the FBG and prepregs to prevent this portion from being embeded, consequently the embed length was controlled.

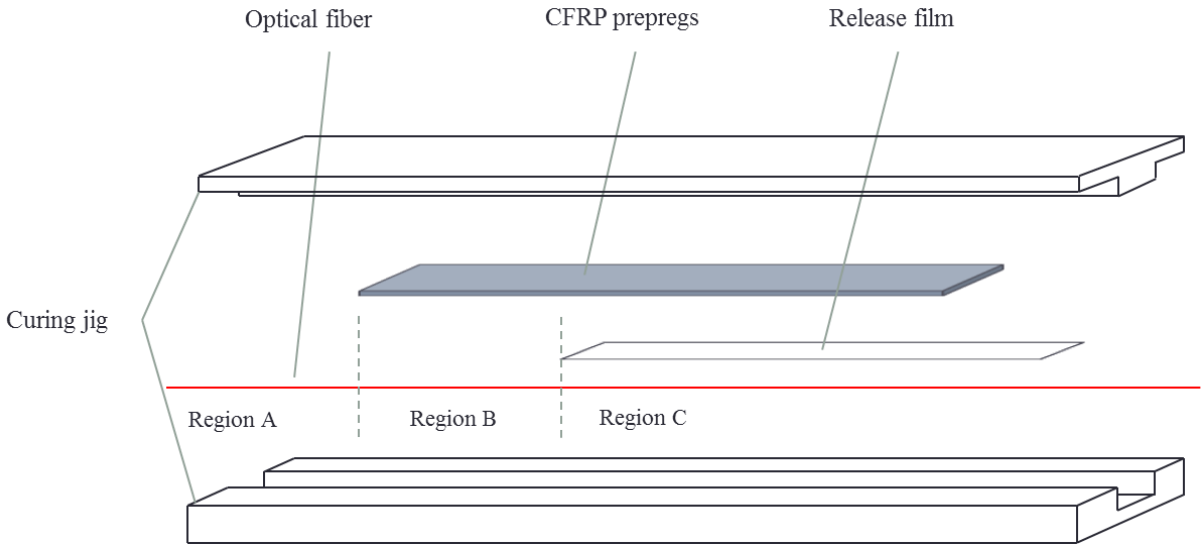

Fig. 4-3. CFRP curing setup

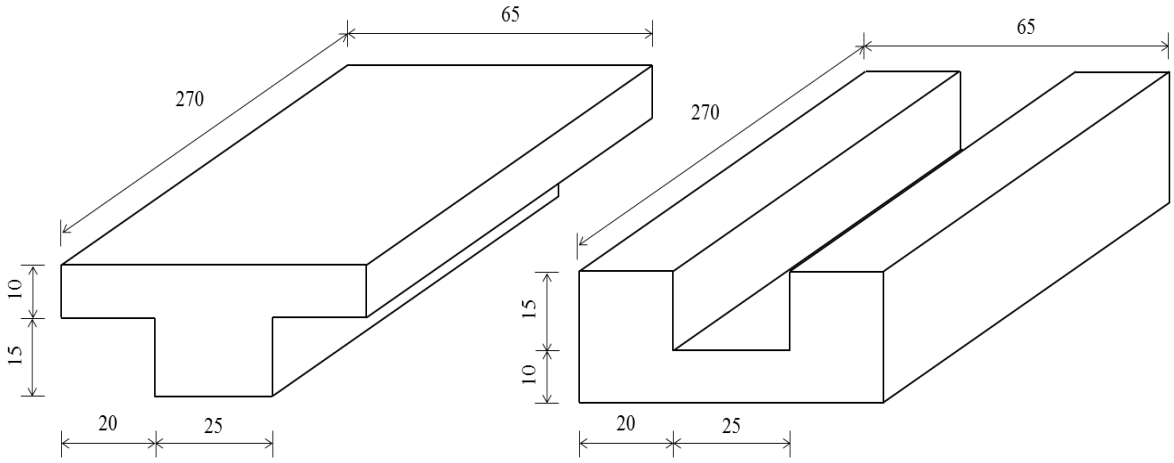

Fig. 4-4. Dimensions of curing jig (unit: mm)

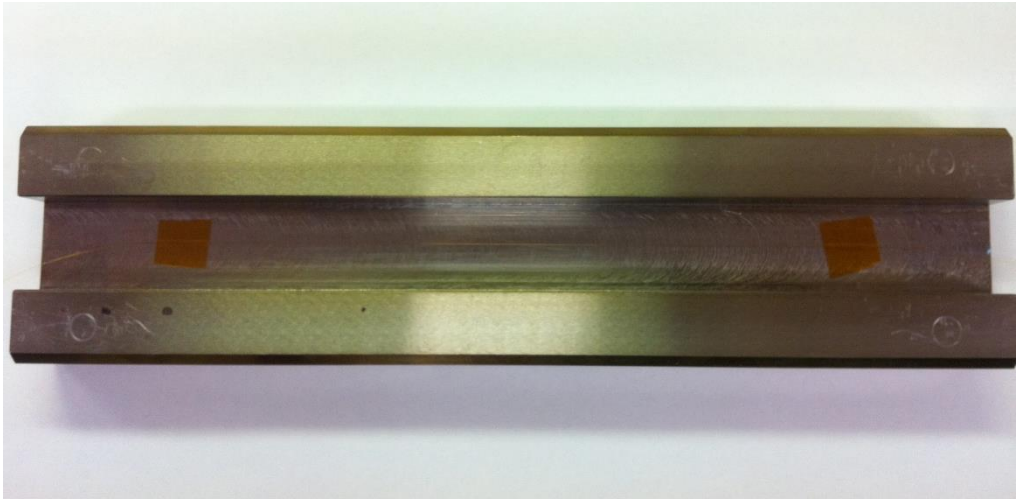

Fig. 4-5. The FBG fixed in the bottom curing jig

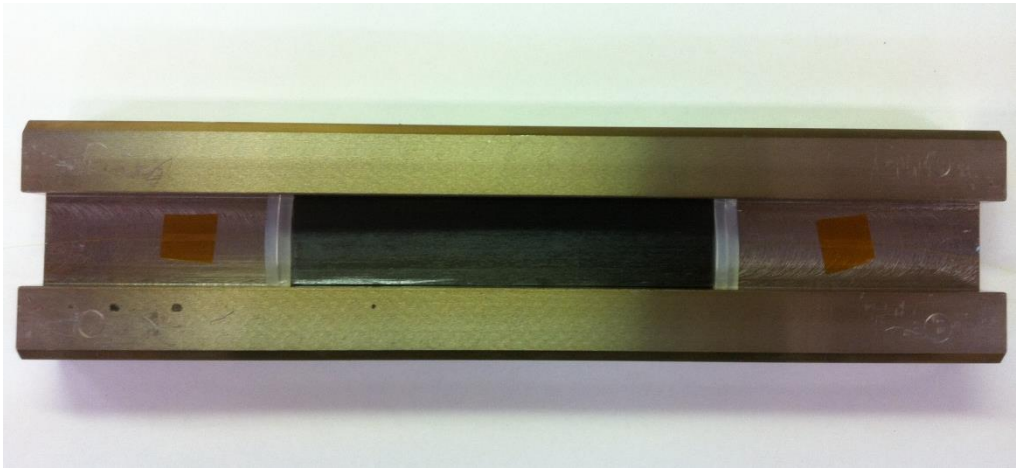

Fig. 4-6. The stacked CFRP prepregs upon the FBG in curing jig

The properties of CFRP prepregs are shown in Table 4-2. The CFRP curing conditions are shown in Fig. 4-7. The curing was carried out on mini test press machine (Toyoseiki seisaku-sho, Ltd.) (Fig. 4-8).
In order to test the embedment procedure, an optical fiber was embedded as dummy sensor. The CFRP adherend with embedded optical fiber after curing was shown in Fig. 4-9. The optical fiber was firmly embedded into CFRP plate in region B, and was embed free in region A and C. As shown in Fig. 4-10, the cross-section photograph of CFRP in region B was taken by microscope to confirm the embedment. The layer structure in dark gray is the cured CFRP plate, in which the 125 μm diameter circle indicating the cladding of optical fiber can be observed. It showed that the optical fiber was successfully embedded into the surface of the CFRP and its shape was maintained well during the process. An optical meter (AQ2150A, Ando Electric Co., Ltd.) was used to monitor the light transmission in optical fiber during the whole curing process (Fig. 4-11), and no significant power loss was found.

Table 4-2. The properties of CFRP prepregs

Tenax-J prepreg	
Carbon fiber	150 g/m^2
Resin content	33%
Prepreg sheet weight	222.9 g/m^2
Gel time	12 min

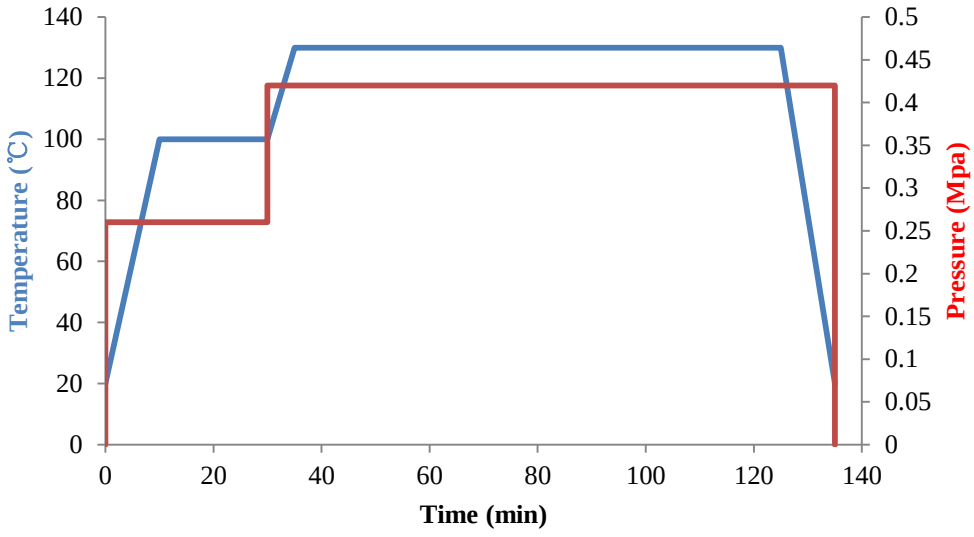

Fig. 4-7. CFRP curing conditions

Fig. 4-8. Mini test press machine for CFRP curing

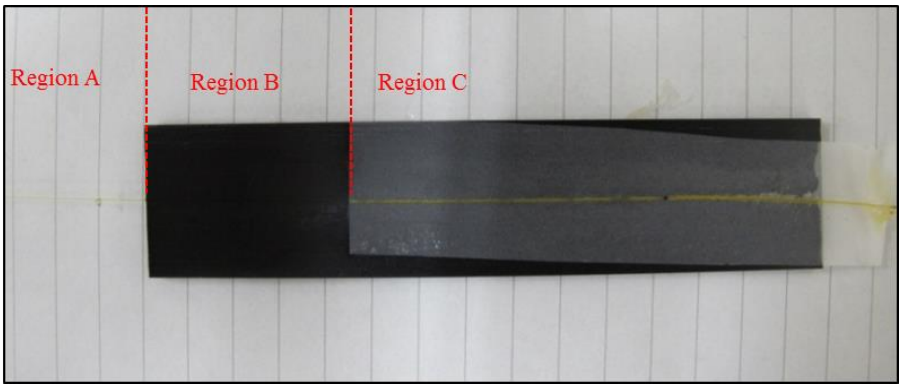

Fig. 4-9. The CFRP adherend with embedded optical fiber after curing

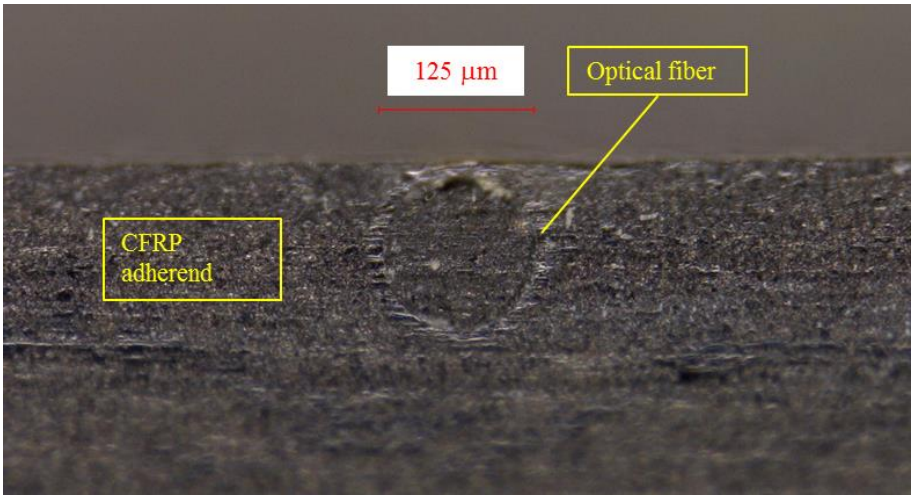

Fig. 4-10. Cross-section photograph of CFRP with embedded optical fiber

Fig. 4-11. An optical meter used to monitor the curing process

4.1.3. Joint bonding

The CFRP adherend with embedded optical fiber was adhered with another CFRP adherend to form a single-lap joint. The properties of the adhesive film are shown in Table 4-3. The recommended curing conditions on product manual are: 170 kPa, 1.7 ℃/min ramp to 130 ℃, hold for 45 minutes, cool to less than 60 ℃. In this study, in order to reduce the voids in adhesive layer, the adhesive curing conditions were modified to: hold for 10 min at 60 ℃, hold for 20 min at 80 ℃, hold for 10 min at 100 ℃, hold for 45 min at 130 ℃. The x-ray photos of adhesive layer cured by manual and modified conditions are shown in Fig. 4-12, it can be observed that the void area was reduced, the bonding quality has been improved.

Table 4-3. The properties of the adhesive film

Thickness	0.2 mm
Weight	0.06 psf
Curing temperature	121 ℃
Gel time (135 ℃)	4-7 min
Specific gravity	1.2
Support	Non-woven polyester mat (HC)

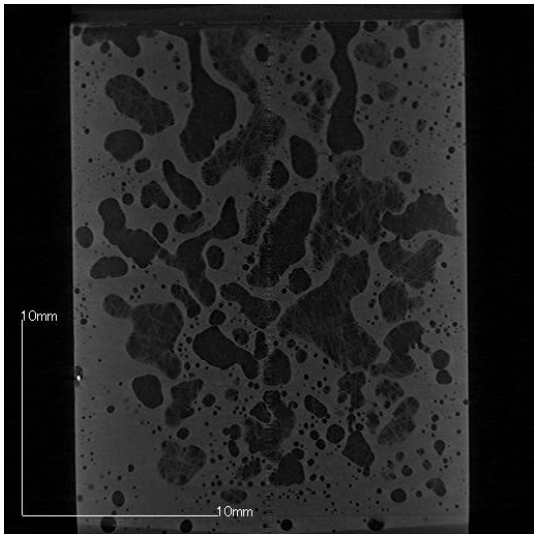

(a)

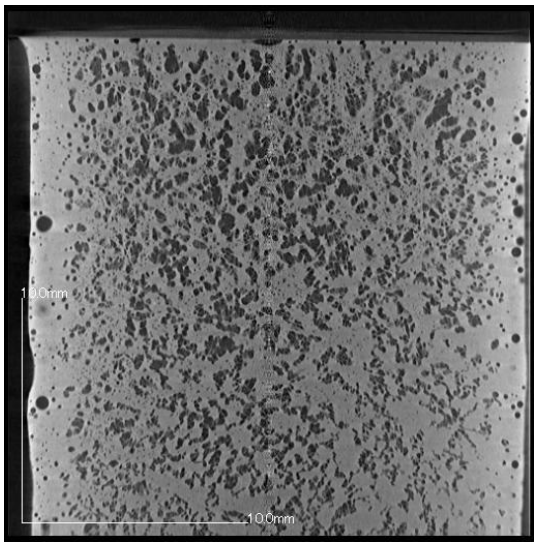

(b)

Fig. 4-12. The x-ray photos of adhesive layer cured by (a) manual and (b) modified conditions

The adhesive curing was carried out in a bonding jig (Fig. 4-13), the jig design is shown in Fig. 4-14 and Fig. 4-15. The heat and pressure were applied by test press (YSR-10 H/C, Shinto Metal Industries Corporation) (Fig. 4-16). The optical meter was employed in this process, and no significant power loss was found.

The bonded single-lap joint is shown in Fig. 4-17. In this way, the optical fiber was embedded into the adhesive/adherend interface. However, as shown in Fig. 4-18, the spew filet at overlap end between region A and B could not be removed due to the existence of optical fiber, this end is called filet end and the other is called square end in this study.

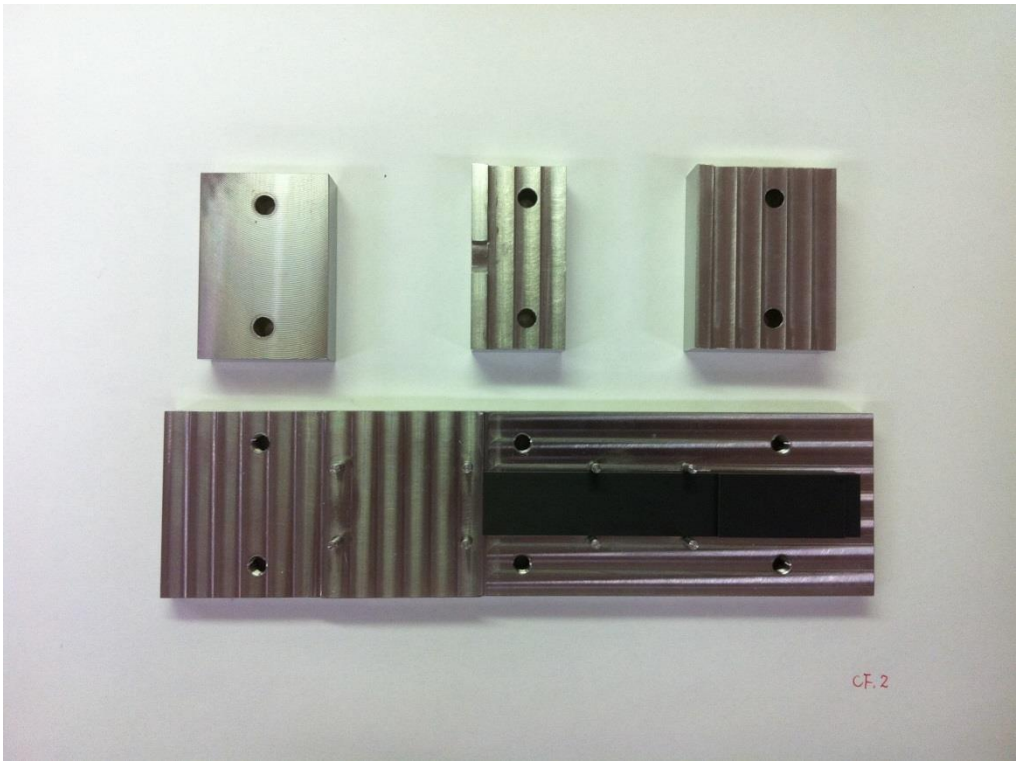

Fig. 4-13. Bonding jig

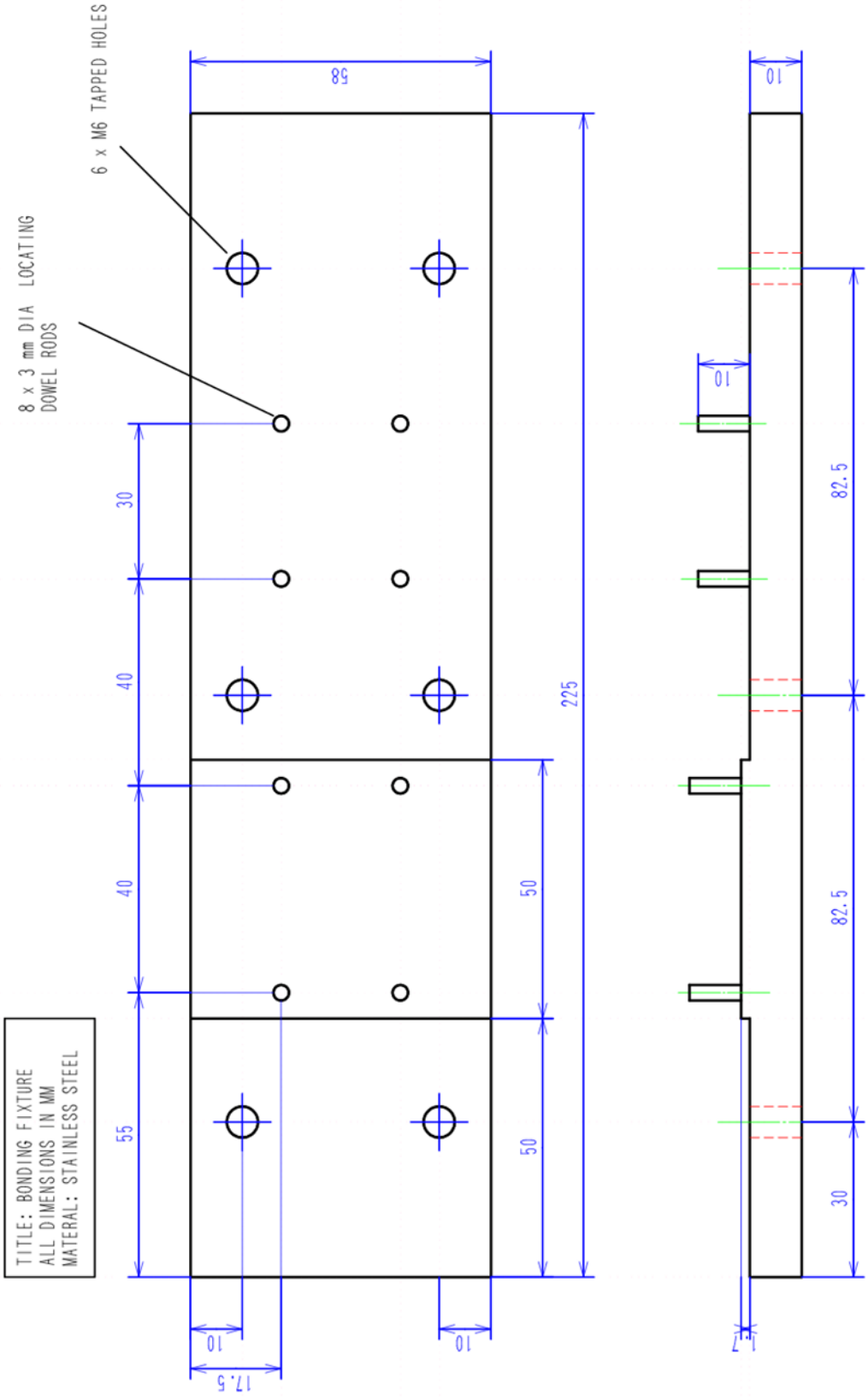

Fig. 4-14. Bonding jig design (base)

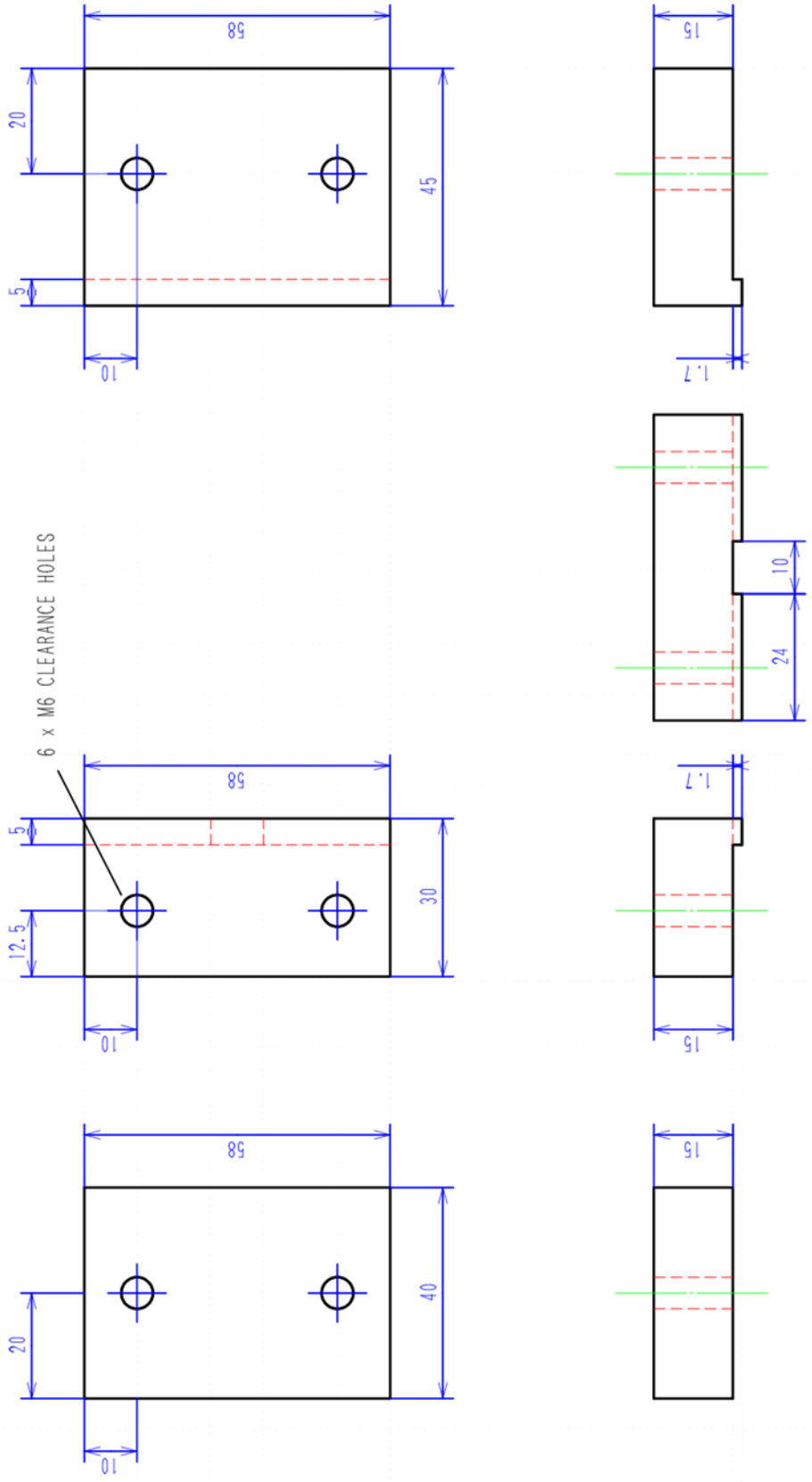

Fig. 4-15. Bonding jig design (clamps)

Fig. 4-16. Test press for joint bonding

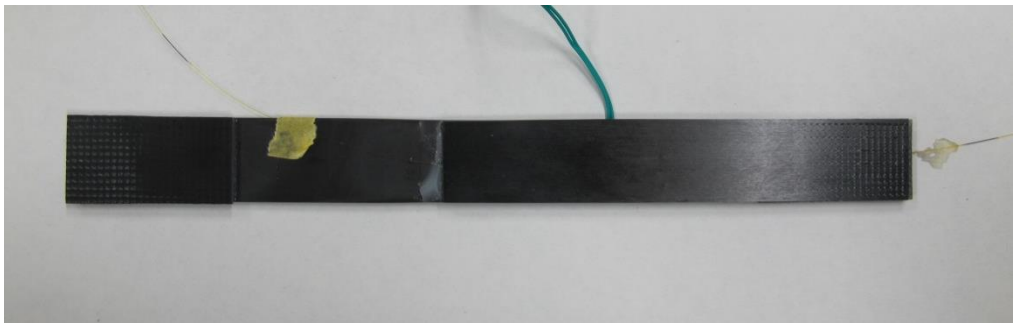

Fig. 4-17. The adhesive-bonded single-lap joint with embedded optical fiber

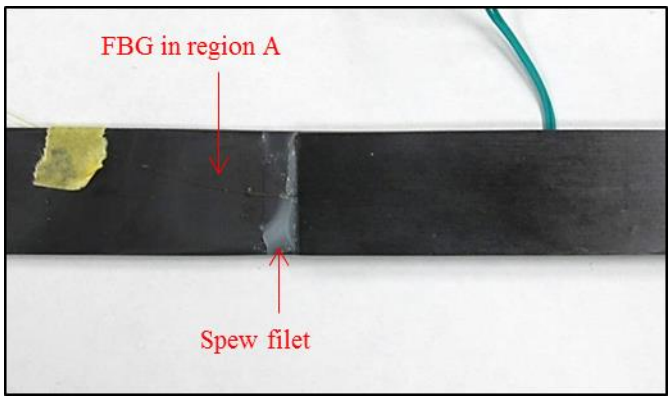

Fig. 4-18. The filet end of joint

In order to evaluate influence of the optical fiber embedment on joint tensile strength, tests were carried out on the specimens with and without the embedded optical fiber. The results of tensile strength are shown in Fig. 4-19, the blue bars indicate the joint specimen without embedded optical fiber, while red bar indicate the specimen with embedded optical fiber. In the result, no significant tensile strength loss can be observed when the joint is embedded with the optical fiber using the procedure of this study.

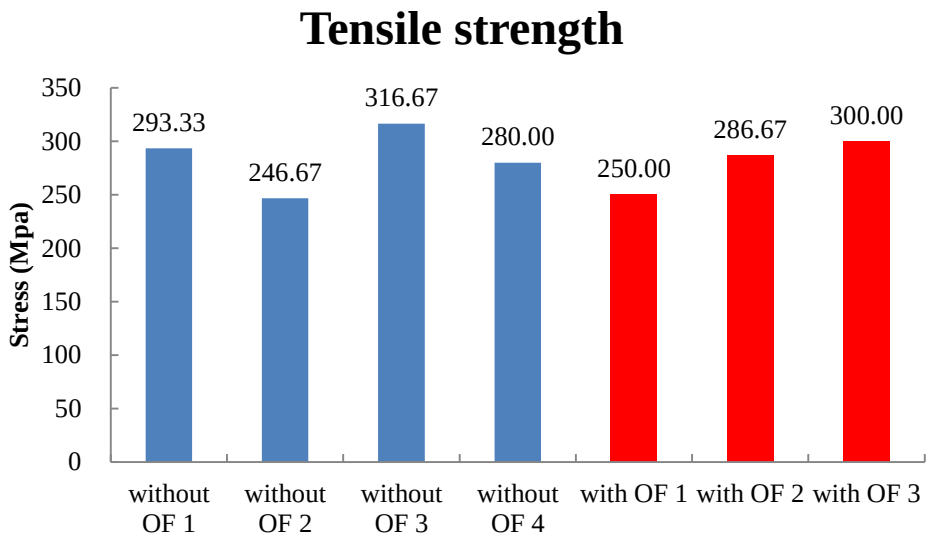

Fig. 4-19. Tensile strength of joint with and without embedded optical fiber

4.2. FE model

4.2.1. Modeling of joint specimen

In joint studies, the theoretical and numerical analysis method are usually used as reference for the measurement. In this study, the FE analysis has been employed for providing reference for the strain distribution measurement, because the joint with complex geometry (embedded OFS, spew filet) can be modeled and analyzed conveniently by it.

The FE analysis has been employed in many studies as an effective method to provide reference for OFS measurement. However, in the case of embedded measurement, the embedded OFS was not included in FE model in any report. The analysis result such as stress and strain field at the OFS embed location on the host model were employed as the equivalent result to fiber core of OFS. Considering the analysis result in fiber core of embedded FBG is not always equal to the host structure at embed location and the reflected spectra from FBG can be affected by the strain and stress field, we built a detailed joint specimen FE model including embedded FBG to improve the evaluation of FBG measurement in this study.

In order to reduce the calculation time, a three-dimensional symmetric FE model of the joint specimen with embedded FBG was built according to the practical specimen and FBG geometry and location of

FBG. The joint is modeled from x=-50 to x=50, the tabs are not included.

About the modeling process, the CFRP adherends and adhesive layer were modeled separately. A circular slot of 0.1500 mm diameter was cut on a CFRP adherend at the FBG embedding location, a solid ring with thickness of 0.0125 mm was extruded in the slot to build the coating of FBG fiber, and a 0.1250 mm diameter solid cylinder was extruded inside the solid ring to build the cladding and core. The internal boundaries of components were kept during extrusions. After building embedded FBG, the adherends and adhesive layer were bonded to build the single-lap joint. The debonding boundary condition can be inserted at the adhesive/adherend interface to build the crack when necessary.

The FE model is shown in Fig. 4-20, the symmetric plane is parallel to plane zy and intersects x axis at x=0.0, the dark green area indicates CFRP adherends, the gray area indicates the adhesive layer. The mesh was refined at overlap ends, adhesive layer, FBG model and a portion of adherend which contains the FBG model. Hexahedral and pentahedral element, which are capable of geometrically nonlinear analysis, were used to mesh the model. The fine mesh around the embedded FBG is shown in Fig. 4-21. The FBG model includes two components, the light blue area indicates cladding and core and the orange area indicates the coating. The material properties are shown in Table 4-4, the CFRP is defined as orthotropic and the adhesive and fiber are isotropic. The material properties of CFRP and adhesive are obtained by tests, while the properties of optical fiber are common information.

In order to simulate the load tests, the joint model is constrained at one end, and loads are applied on the other end. All the boundary conditions are shown in Fig. 4-22, U means displacement constraint, UR means rotation constraint.

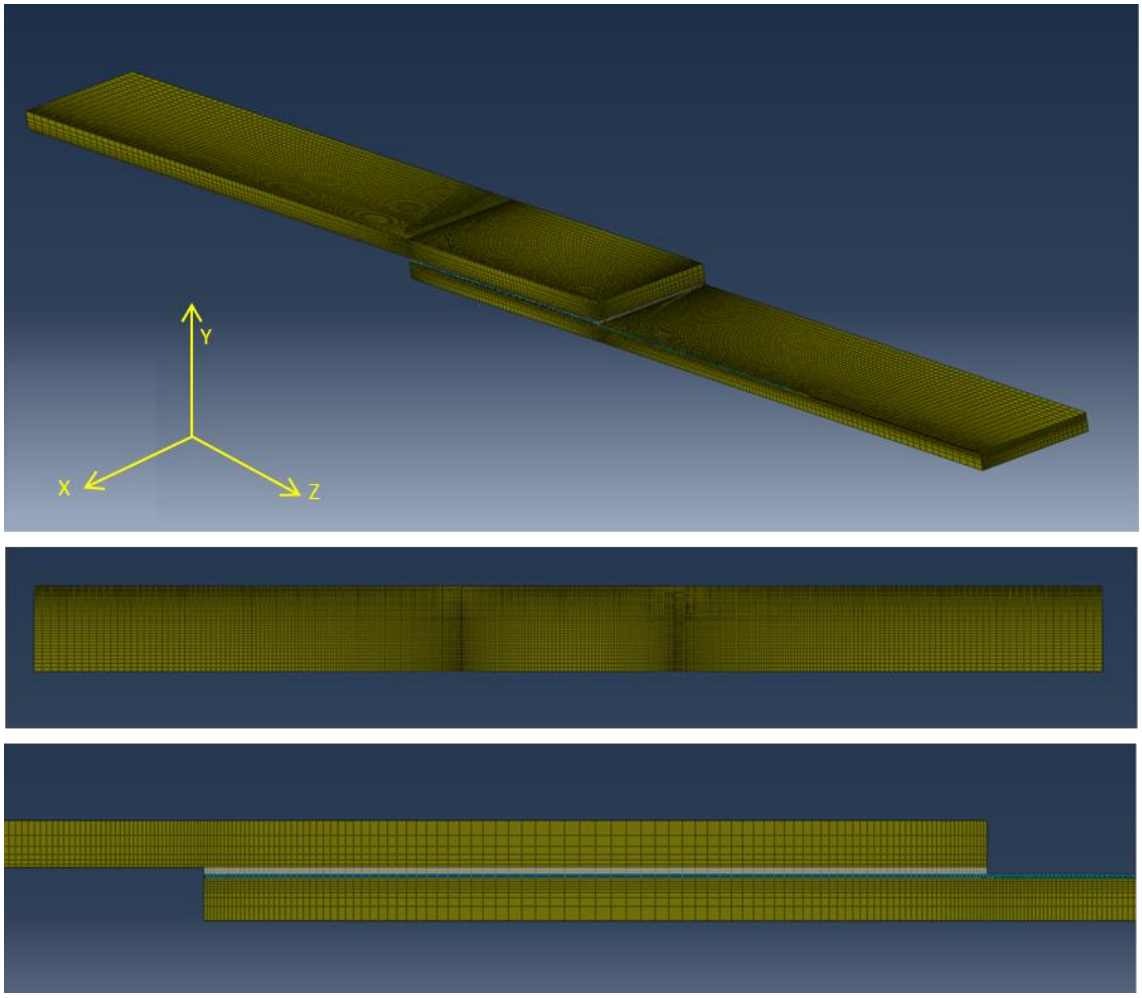

Fig. 4-20. FE model of joint with embedded OFS

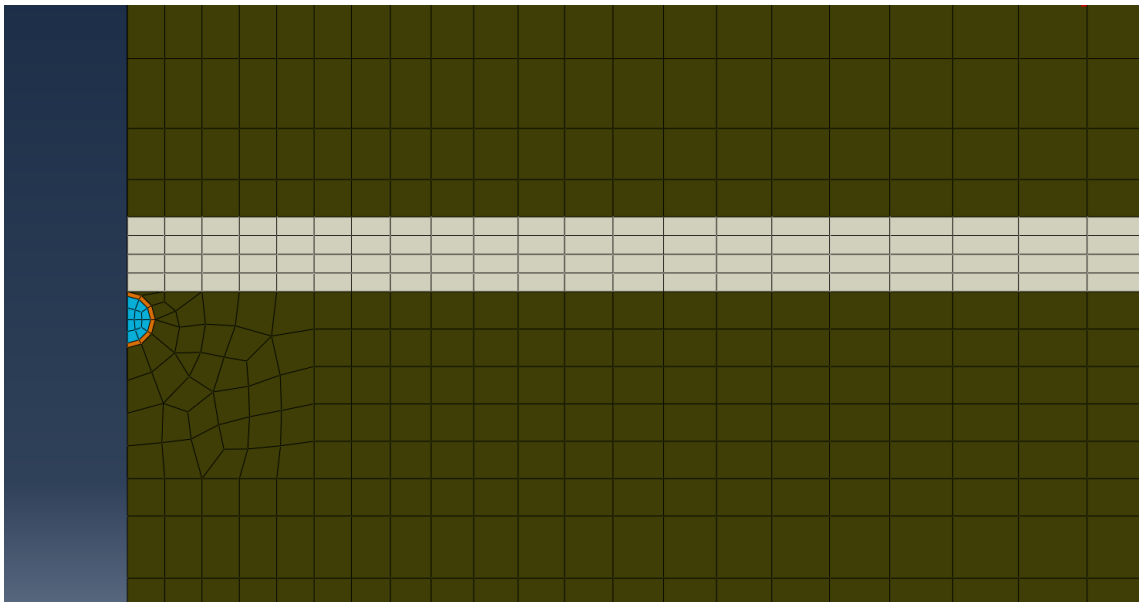

Fig. 4-21. The fine mesh around the embedded FBG

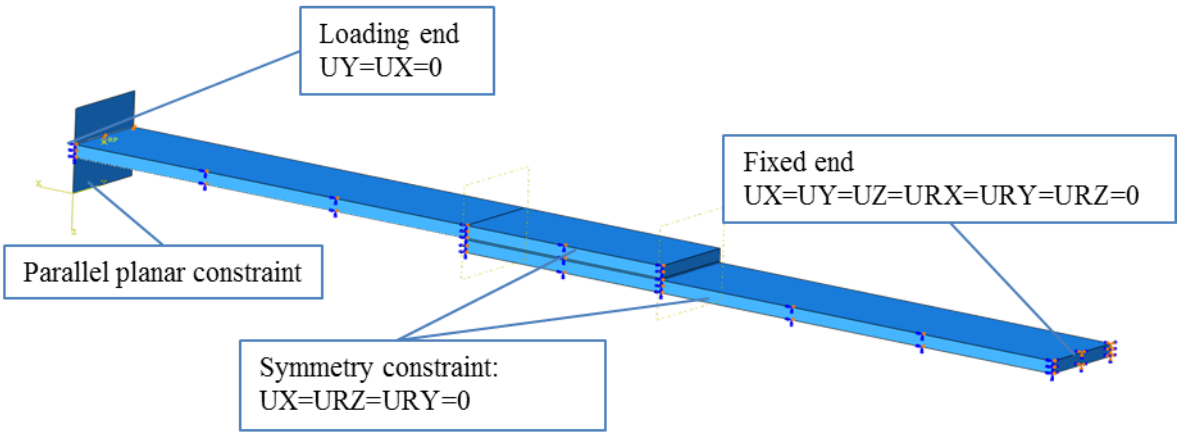

Fig. 4-22. Boundary conditions

Table 4-4. Material properties in FE model (unit of Young's modulus (E) and shear modulus (G): GPa)

	CFRP	Adhesive	Fiber core and cladding	Fiber coating
E_z (E)	154.6	3.3	73.1	3.0
E_y	9.8			
E_x	9.8			
ν_{zy} (ν)	0.35	0.39	0.16	0.30
ν_{yx}	0.45			
ν_{zx}	0.35			
G_{zy}	5.3			
G_{yx}	2.5			
G_{zx}	5.3			

4.2.2. FE analysis and discussion

In order to evaluate the FE model with embedded FBG, the calculation of stress and strain field on embedded FBG when joint specimen is subjected to static load was carried out using both the detailed model with FBG and a model without FBG. The load was tensile 200 kgf, the stress and strain field results on embedded FBG in *x*, *y* and *z* directions of two models were compared and shown in Fig. 4-23 and Fig. 4-24. The horizontal axis in figures indicates the position on FBG. For the model with FBG, the result in FBG fiber core was used for comparison, it is shown in red curve. And for the model without FBG, result on adherend at the embed location was used, it is shown in blue curve.

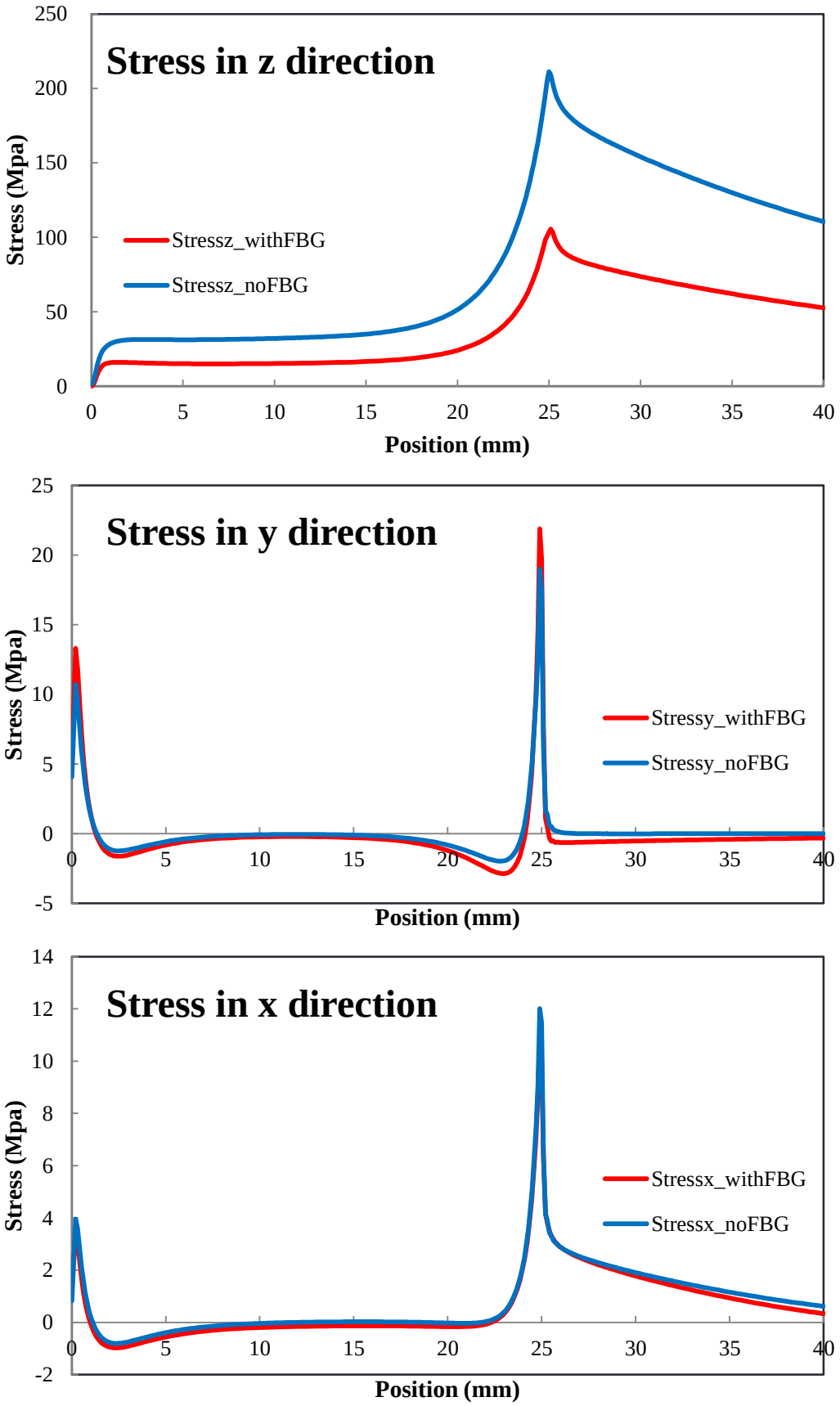

Fig. 4-23. The stress field simulated by FEA using model with and without embedded OFS

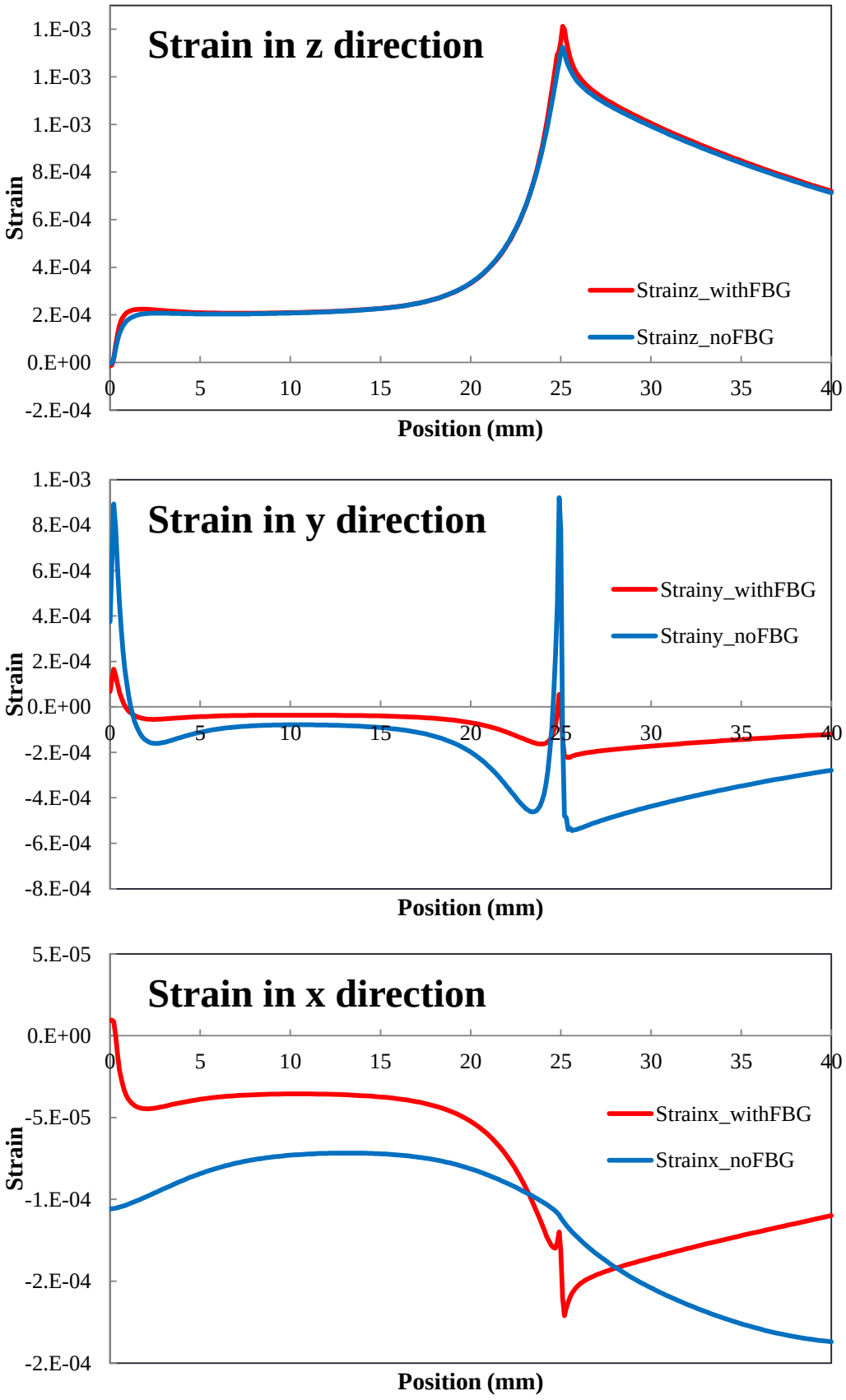

Fig. 4-24. The strain field simulated by FEA using model with and without embedded OFS

Significant difference can be observed in stress component in z direction at the both overlap ends and strain component in y direction around square end. The stress/strain in longitudinal direction can affect the measurement directly, and the stress/strain in transverse direction may affect the measurement by disturbing the FBG spectrum through birefringence effect. This means the inaccurate stress/strain analysis of embedded FBG will lead to the wrong evaluation or misunderstanding of the measurement result. Thus in this study, the FE model of joint specimen with embedded was employed for analysis, and the analysis result in fiber core was used for measurement evaluation and discussion.

4.3. Static load test

Although the main purpose of the measurement in this study is to measure the strain distribution dynamically under dynamic loading, which is the common working condition for the most of the structures, the measurement under static loading is considered as a special and simple case, for which even the sensing system designed for dynamic measurement should be able to provide a good solution. Thus the adhesive-bonded single-lap joint specimen with embedded FBG was prepared using procedure introduced in this chapter, the specimen was subjected to static loads and the dynamic distributed sensing system based on OFDR introduced in chapter 3 was employed for measurement at each load case, the measurement was carried out for two purposes: evaluation of the sensing system in practical measurement and investigation on the strain distribution in adhesive-bonded joint.
The test also employed strain gauge as reference for FE analysis and measurement, the test machine controller as recorder of test conditions and FE analysis as reference for strain distribution. The static test will be introduced in three aspects, test setup, loading and measurement conditions, results and discussions.

4.3.1. Test setup

The static load test was carried out on test machine, whose controller was employed to define the load conditions and record the load and displacement information during the test. A strain gauge was adhesively bonded to the surface of CFRP adherend in region C aside the embedded FBG, the gauge direction is along the overlap length direction, and the signal of strain gauge was recorded by an independent system throughout the test. The schematic diagram of test setup is shown in Fig. 4-25. After installing the specimen onto the test machine, the end of FBG near region A was connected to the dynamic distributed sensing system. The specimen installation is shown in Fig. 4-26. The specimen was hold by the clamps at its tabs, the load was applied directly by the clamps. The product information of devices used in the static load test can be found in Table 4-5.

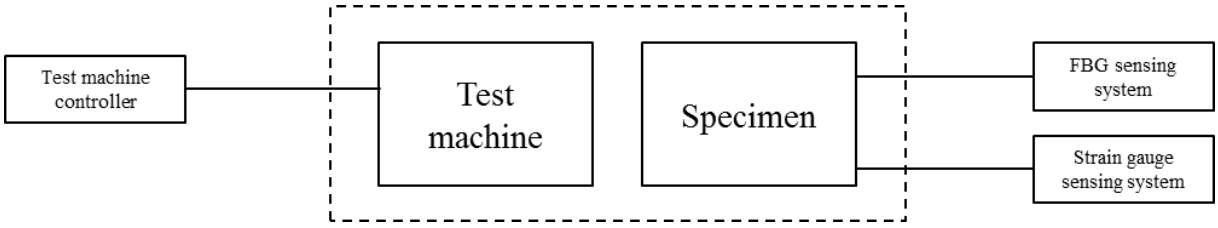

Fig. 4-25. Static load test setup

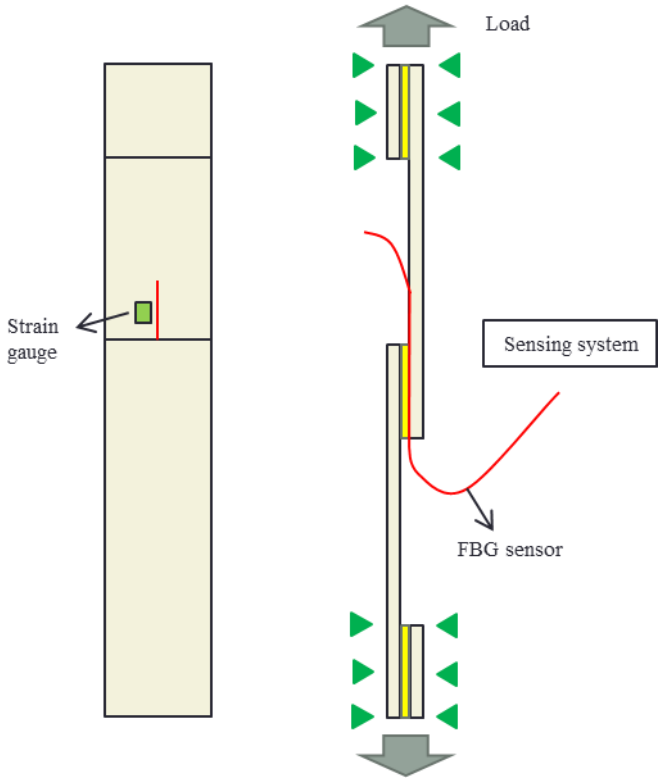

Fig. 4-26. Specimen installation

Table 4-5. Information of test devices

Devices	Product name	Manufacturer	Features
Test machine	SERVOPULSER EHF-UB5-20L	Shimazu Corporation	Maximum load: 5 ton
Strain gauge	FLA-1-11-1 LDA	Tokyo Sokki Kenkyujo Co., Ltd.	Length: 1 mm

4.3.2. Loading and measurement conditions

The loading condition for the static load test is shown in Table 4-6. Tensile load was applied to the specimen from 0 to 250 kgf with 50 kgf interval controlled by test machine controller using load control. The loading was stopped and held at each load case for about 5 minutes for FBG measurement, and the FBG sensing system carried out measurement for 5 seconds at each load case. The settings of FBG sensing system for measurement are shown in
Table 4-7, the wavelength sweep rate of TLS, which indicates the sampling rate of the system, was 5 Hz.

Table 4-6. The loading condition for the static load test

Load form	tensile, static
Load value (kgf)	0, 50, 100, 150, 200, 250
Load control method	Load control

Table 4-7. The setting of FBG sensing system for measurement

Wavelength sweep range (nm)	1546 ~ 1555
Wavelength acquisition range (nm)	1547 ~ 1554
Wavelength sweep rate (Hz)	5
Measurement timing	5 seconds at each load

4.3.3. Results and discussions

The parameters of FBG sensing system for wavelength/strain distribution calculation are shown in Table 4-8, the position resolution indicates the readout resolution of position in the results, the centroid method was used to calculate center wavelength in FBG spectrum for the stable measurement.

Table 4-8. The parameters of FBG sensing system for calculation

Position resolution (mm)	0.6
Wavelength resolution (pm)	20
Window length (pm)	400
Center wavelength determination method	Centroid

The measured spectrograms at each load case are shown in
Fig. 4-27, the vertical axis indicates the real position on FBG, its relation with the normalized position is shown in Fig. 4-28. From the spectrograms it can be seen that, the signal in embedded area varies

when the load increases, and the signal in free portion doesn't change with the load. And the signal is observed to be discontinuous at three positions: overlap beginning (filet end), overlap end (square end) and embedment end, the strain field varies significantly at these positions and the measurement may be disturbed.

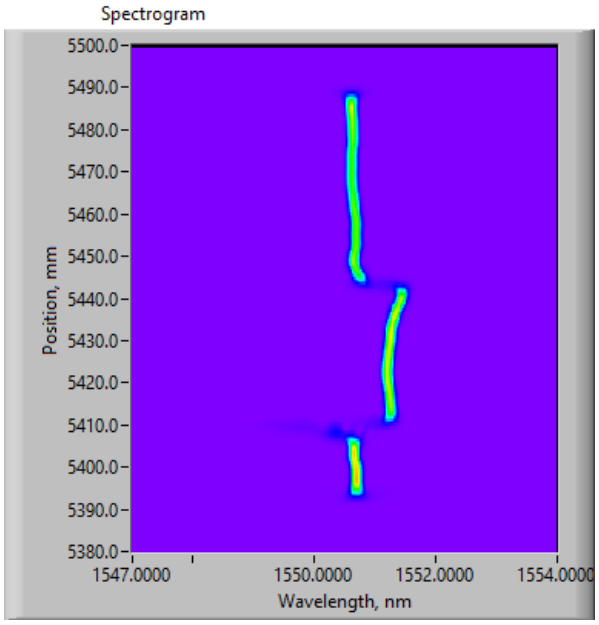

(a)

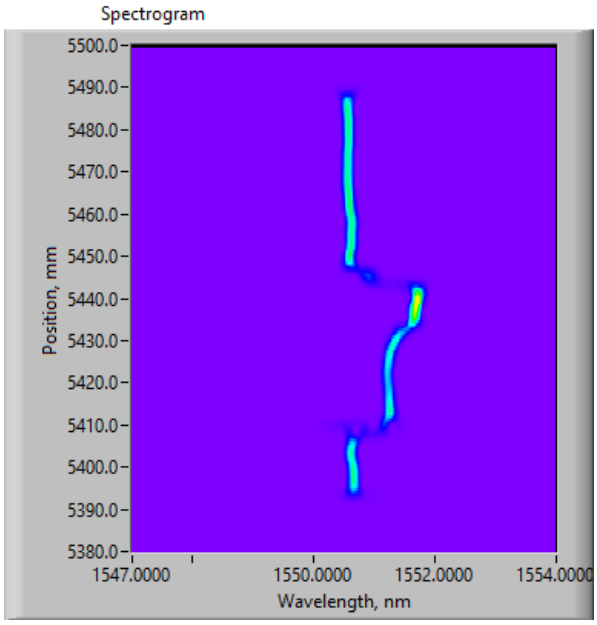

(b)

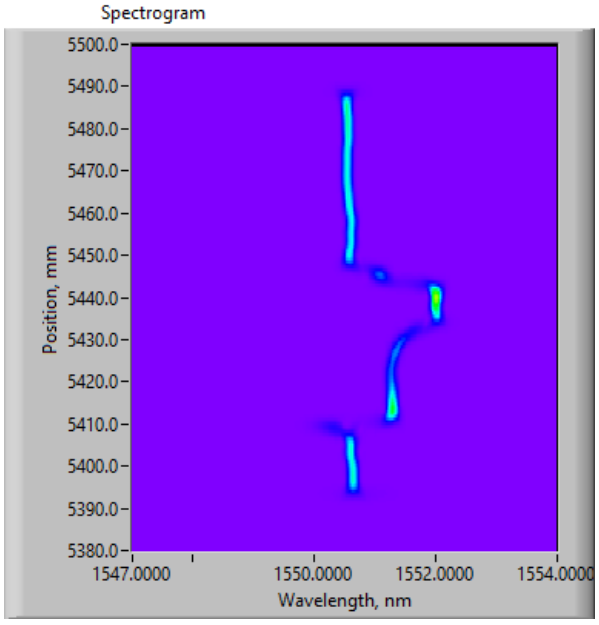

(c)

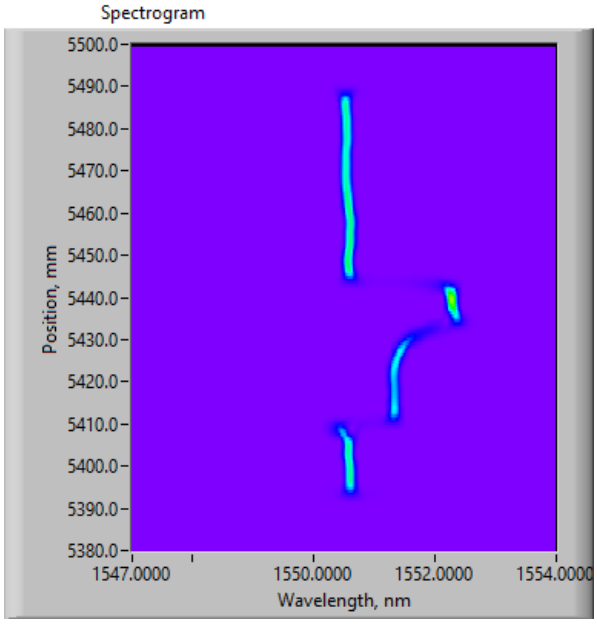

(d)

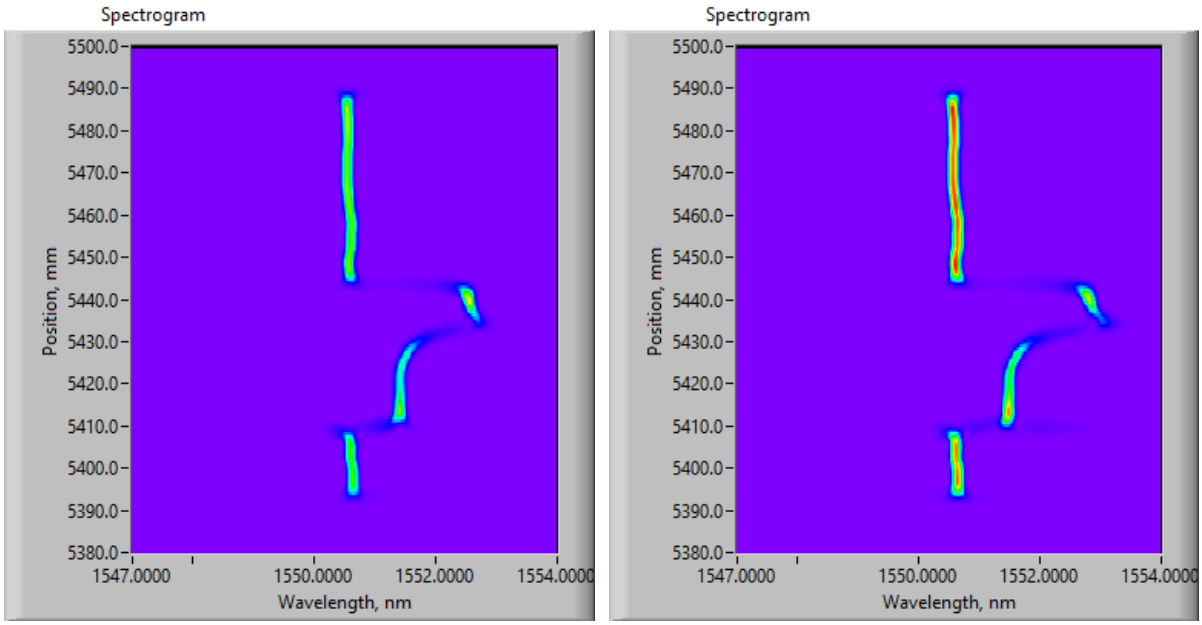

(e) (f)

Fig. 4-27. The measured spectrograms at load cases of (a) 0 kgf, (b) 50 kgf, (c) 100 kgf, (d) 150 kgf, (e) 200 kgf, (f) 250 kgf

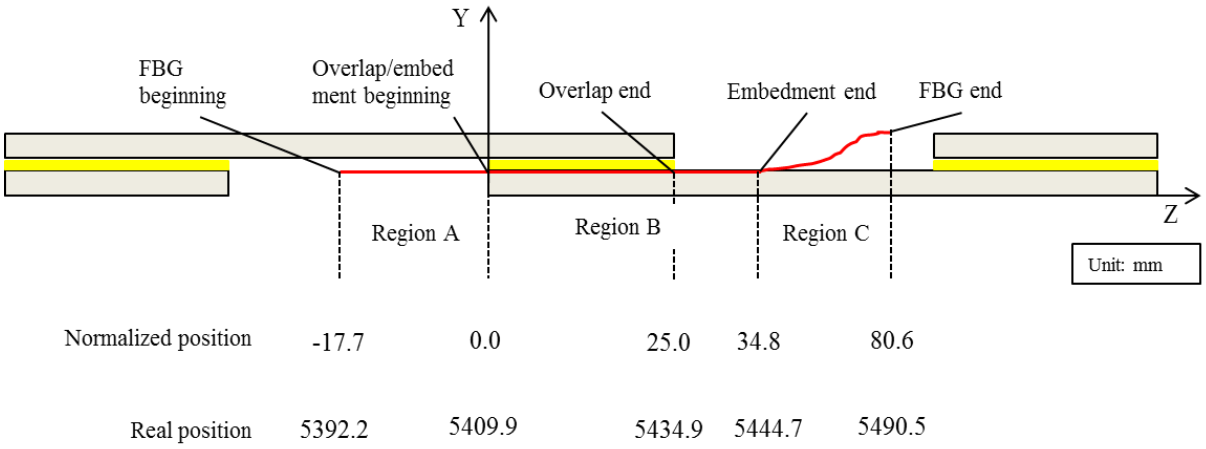

Fig. 4-28. The real position and normalized position on embedded FBG for static load test

The wavelength distributions at each load case are shown in Fig. 4-29, the horizontal axis in each figure indicates the normalized position on FBG, each figure contains ten measurements. From the figures it can be seen that, the measurements at each load case are smooth and stable, no disturbance or variation was found in signals. The comparison of the measurements at each load case is shown in Fig. 4-30, the average of measurements at each load case is used.

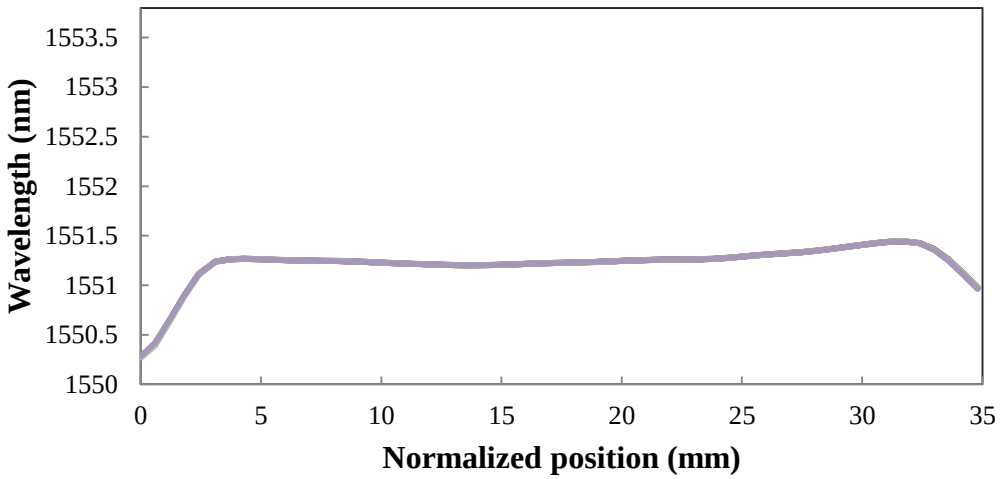

(a) Load case: 0 kgf

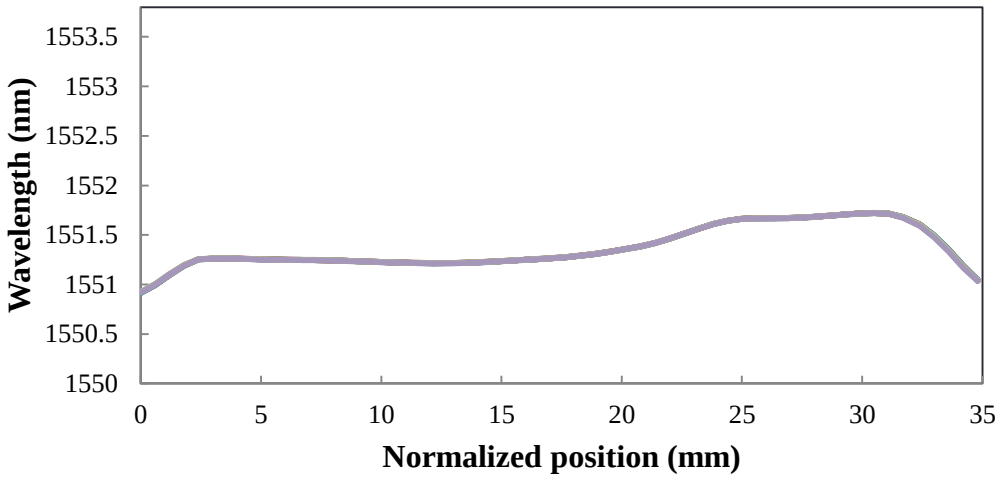

(b) Load case: 50 kgf

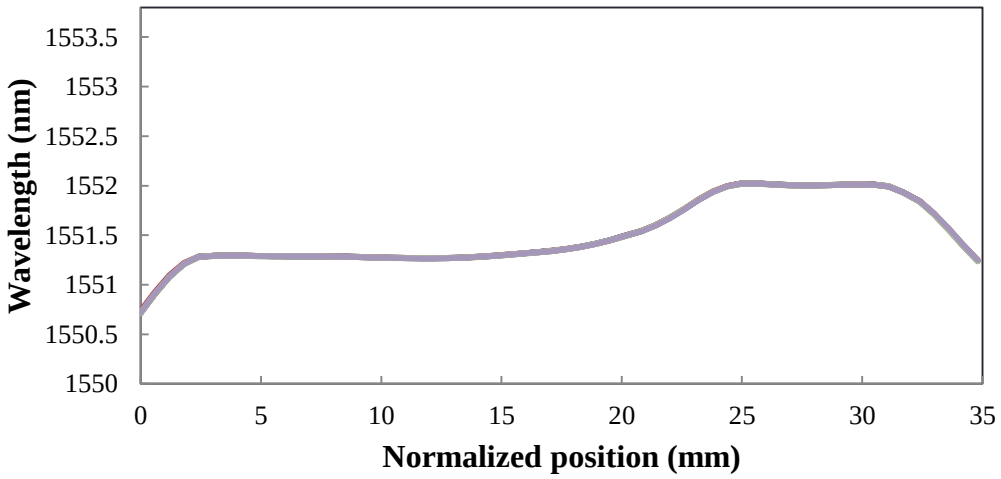

(c) Load case: 100 kgf

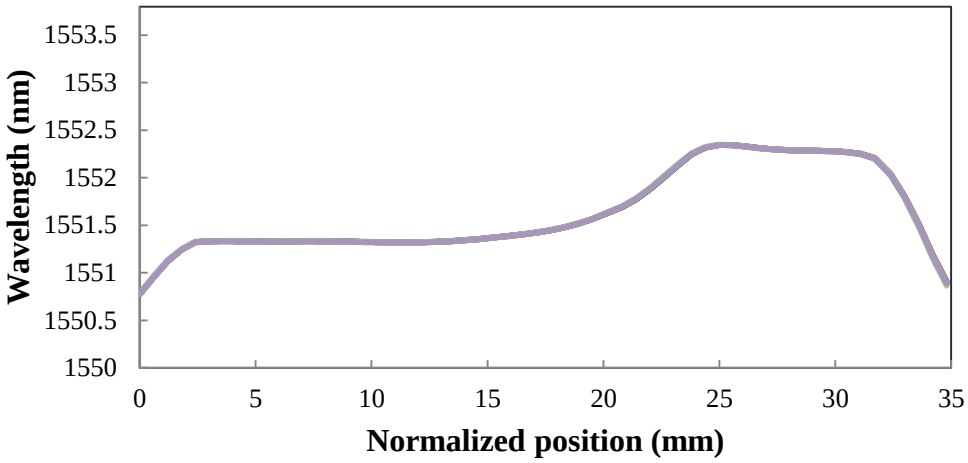

(d) Load case: 150 kgf

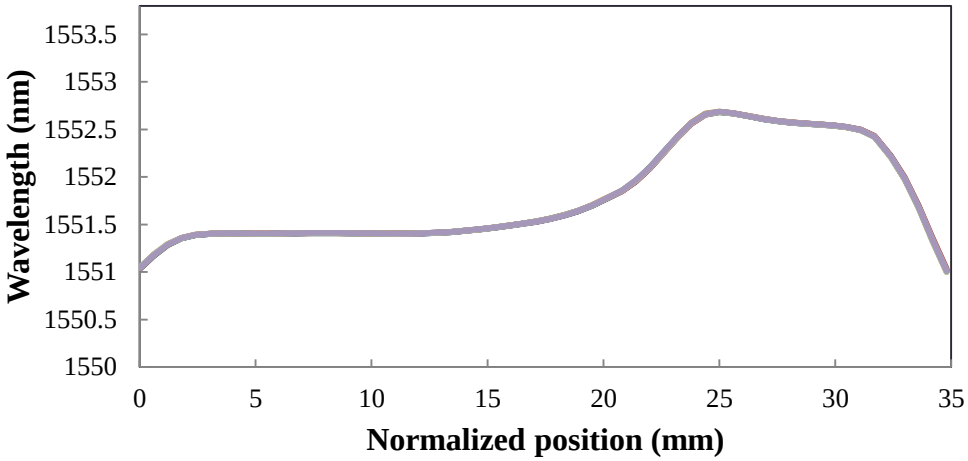

(e) Load case: 200 kgf

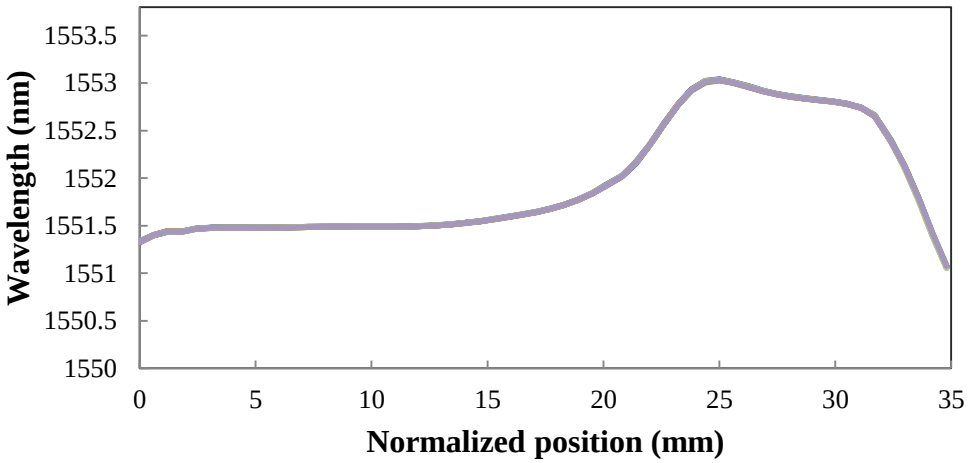

(f) Load case: 250 kgf

Fig. 4-29 The wavelength distributions at each load case

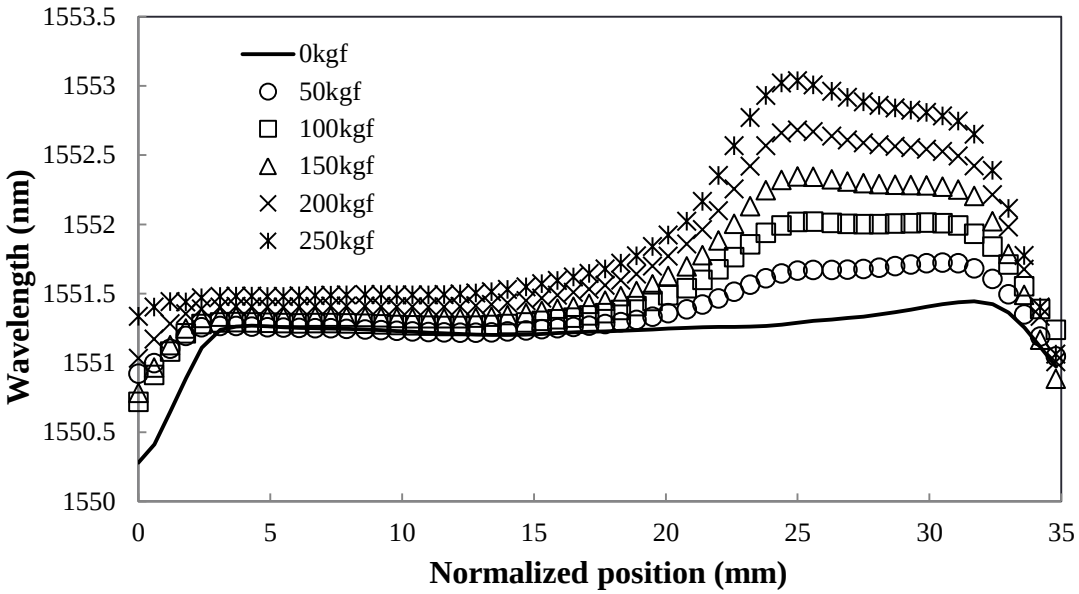

Fig. 4-30. The comparison of the measurements at each load case

The strain distributions at each load case were calculated based on the wavelength distributions. The measurement at 0 kgf was used as initial condition for the strain calculation, and the free portion of FBG near region C was used as temperature reference. In order to evaluate the accuracy of the measurement, the FE analysis was carried out using the FE model introduced previously considering the same loading conditions as the test. The strain measured by strain gauge, was used to confirm the FE analysis before comparing the FE analysis result and FBG measurement. The comparison of the strain measured by strain gauge and simulated by FE analysis at the same position at each load case is shown in Fig. 4-31. The agreement between the strain gauge measurement and FE analysis is found to be good at each load case, and this means the FE analysis results are reliable.

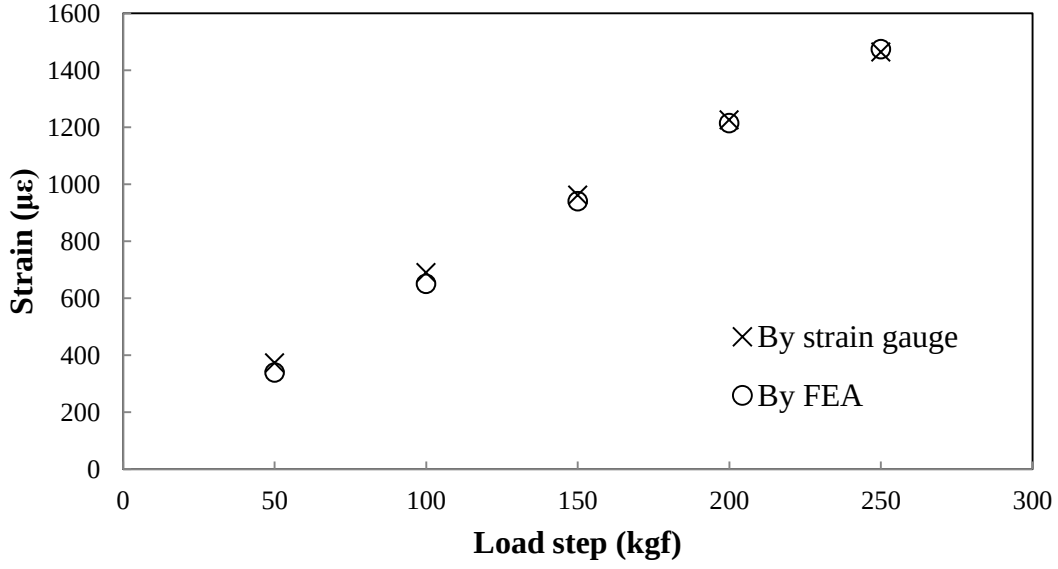

Fig. 4-31. FEA results were confirmed by strain gauge

Instead of discussing all the load cases, the strain distribution at 200 kgf load measured by FBG sensing system is used for result discussion. The comparison of strain distribution measured by FBG sensing system and simulated by FE analysis at load of 200 kgf is shown in Fig. 4-32.

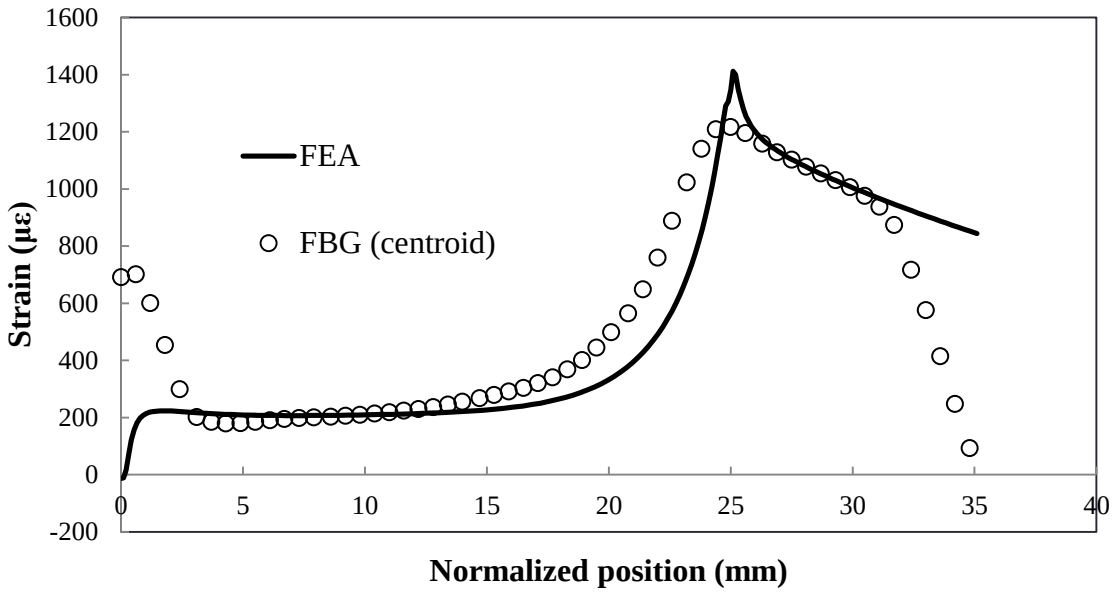

Fig. 4-32. The comparison of strain distribution obtained by FBG measurement and FEA

The horizontal axis indicates normalized position on FBG and vertical axis indicates strain along overlap length direction. From both the FBG and FEA results, the strain reaches a small peak around z=1.0. Then it increases gradually in area of (z=3.0 to 20.0) before entering the rapidly increase area (z=20.0 to 25.0). After reaching the peak at z=25.0 at the overlap end, it decreases gradually in FBG embedded area outside the overlap (z=25.0 to 35.0). The agreements between FBG measurements and FEA results are found to be good in strain gradually varying area in overlap and FBG embed area.

Bad agreements are found in three areas: overlap beginning (filet end), overlap end (square end) and embedment end, where the strain field varies significantly as mentioned. Thus the bad agreements are assumed to be caused by the insufficient spatial resolution of the strain calculation by centroid method. In order to confirm the assumption, the strain distribution was calculated again by the FWHM method, which was considered to have higher spatial resolution than centroid method, and compared with centroid and FEA result. The comparison is shown in Fig. 4-33.

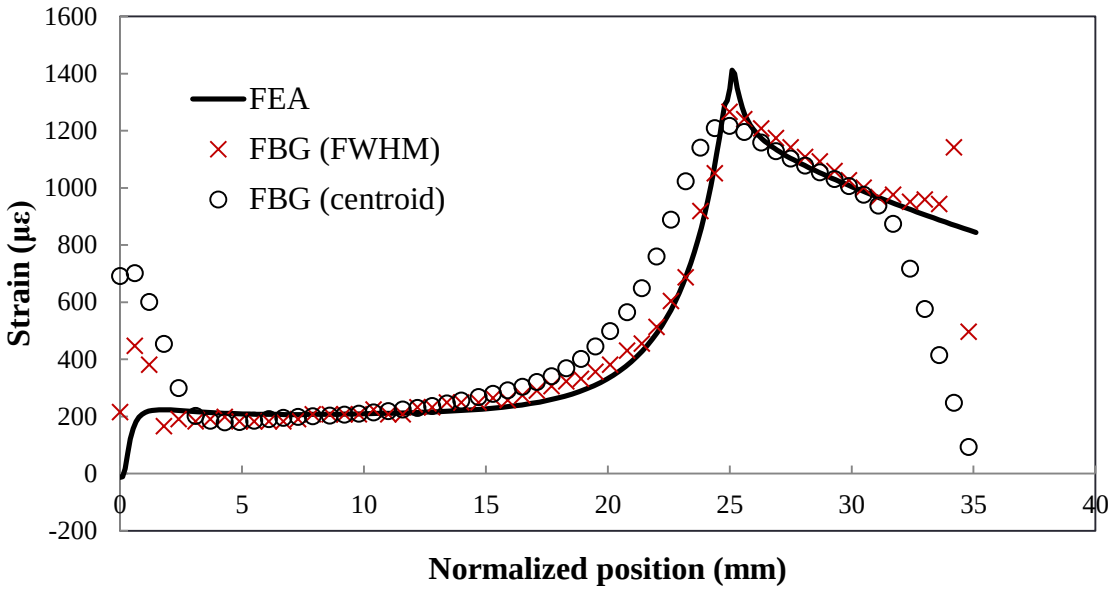

Fig. 4-33. The comparison of strain distribution obtained by FEA and FBG measurement calculated using two methods

The agreements between FWHM and FEA result are found to be good in areas of square end and FBG embedment end, indicating that the FWHM result described the strain variation in the two areas more precisely. However, difference still exists in filet end area, it was considered that, because the FBG in region A near the filet end was bonded into the spew filet, when specimen deformed due to the applied load large tensile force was applied onto the FBG portion in the filet.

The further investigation on the reason of difference between centroid and FEA result was carried out by simulating the measurement results. In the simulation, the strain distribution at 200 kgf obtained by FEA was applied on the FBG, and the simulated spectrogram is shown in Fig. 4-34. The simulation parameters are shown in Table 4-9, the simulated FBG range is from 5.0 m to 5.1 m.

Then both FWHM and centroid method were used to calculate strain distribution, the simulated results are compared with the input strain distribution and the practical measurements in Fig. 4-35. The solid line indicates the input strain distribution calculated by FEA, the marks in red are the simulated results and the marks in blue are the practical measurements, the cross indicates the results calculated by FWHM method, and circle indicates results calculated by centroid method.

In the figure, the simulation didn't show disagreements at the filet end because the FE model didn't consider the filet. In the strain rapidly increase area near the square end, the simulated centroid result increases faster than the FWHM result at the same position, but the FWHM result describes the input strain distribution better for its high spatial resolution and this pattern can be found in the real measurement. In area of the end of FBG embedment, the simulated centroid result returns to 0 gradually while the simulated FWHM shows the sharper response, and this pattern can also be found in the real measurement.

Table 4-9. Simulation parameters

L_R (m)	20
n	1.46
L_{R3} (m)	1
L_G (m)	5
TLS sweep range (nm)	1546 - 1554

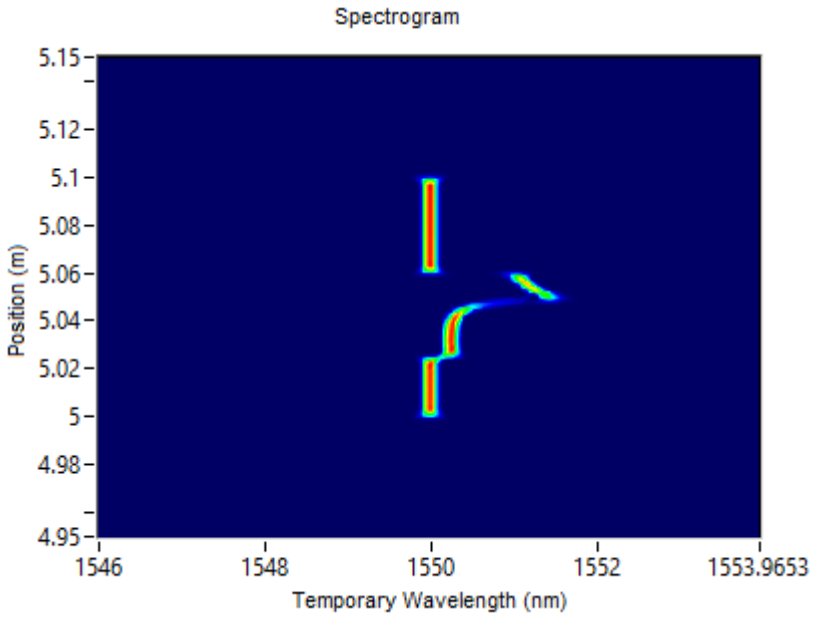

Fig. 4-34. Simulated spectrogram

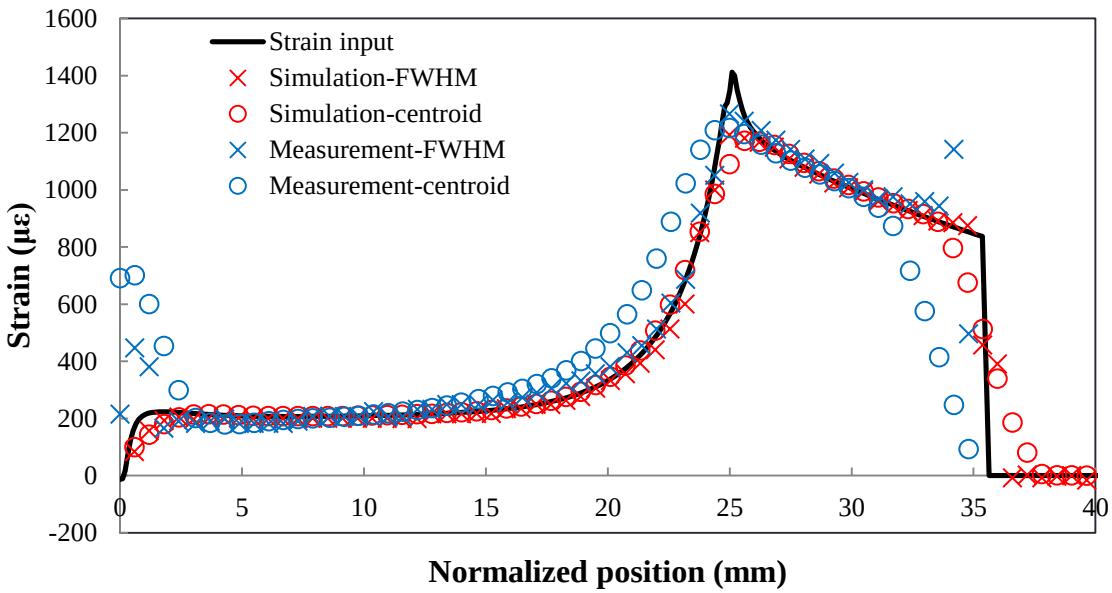

Fig. 4-35. Comparison of simulated measurement with input strain distribution and practical measurements

However, although the pattern is similar, between the simulated results and practical measurements, the difference in position in strain decreasing area in FBG embed end area is about 2 mm. About this discordance, we supposed it is because there exists a strain decreasing area around the FBG embed end (z=34.8), which was not included in input strain distribution, and the input just simply decrease strain to 0 at z=34.8. In order to confirm this assumption, at first we tried to find out the strain decrease area by checking the FBG spectra at the location near z=34.8. As shown in Fig. 4-36, the spectra in area from z=32.4 to z=34.8 are found to be irregular, which means the transverse stress/strain condition on FBG varied in this area, and this phenomenon may be caused by the ending of FBG embedment. Thus another strain distribution input was made considering the strain decreasing area, the strain returns to 0 at z=33.6 which is the middle of the area, and the simulation was carried out again. The simulated spectrogram is shown in Fig. 4-37. The simulated results are compared with the input strain distribution and the practical measurements in Fig. 4-38. This time the position difference reduces to about 0.5 mm, the assumption of strain decreasing area is considered to be meaningful.

As the conclusion, the bad agreements between measurement by centroid method and FEA simulation in strain sharply varied areas are caused by the insufficient spatial resolution of centroid method.

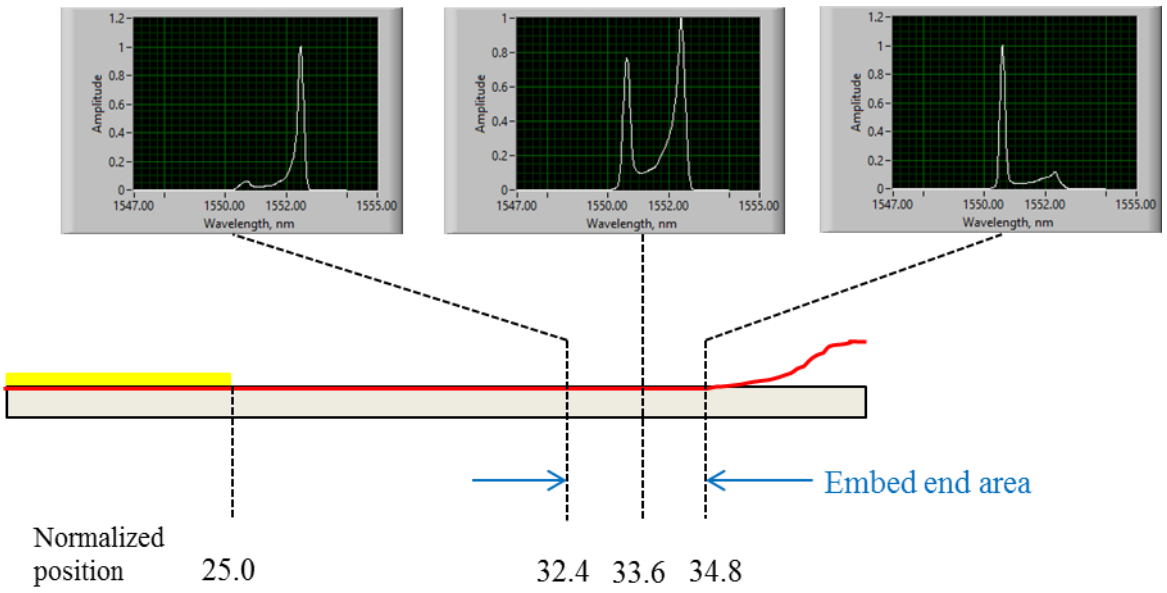

Fig. 4-36. FBG spectra around embed end

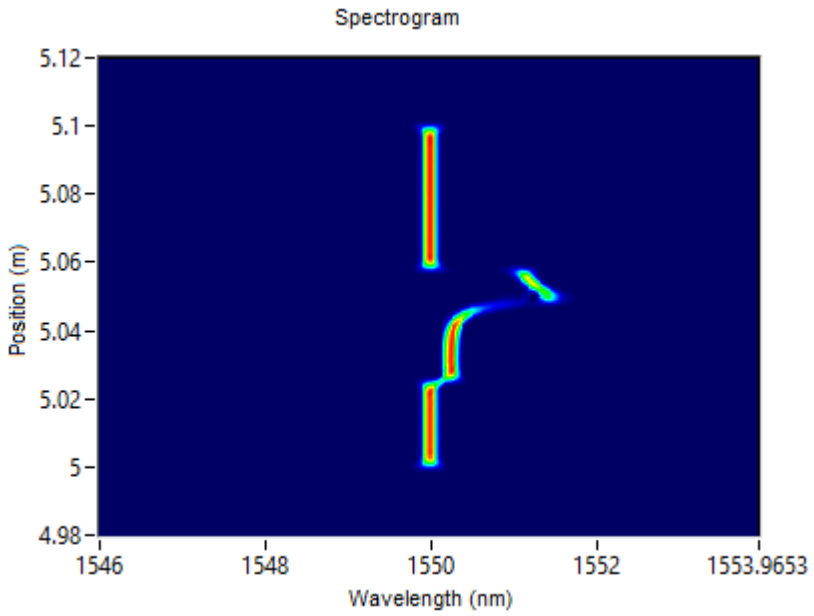

Fig. 4-37. Simulated spectrogram

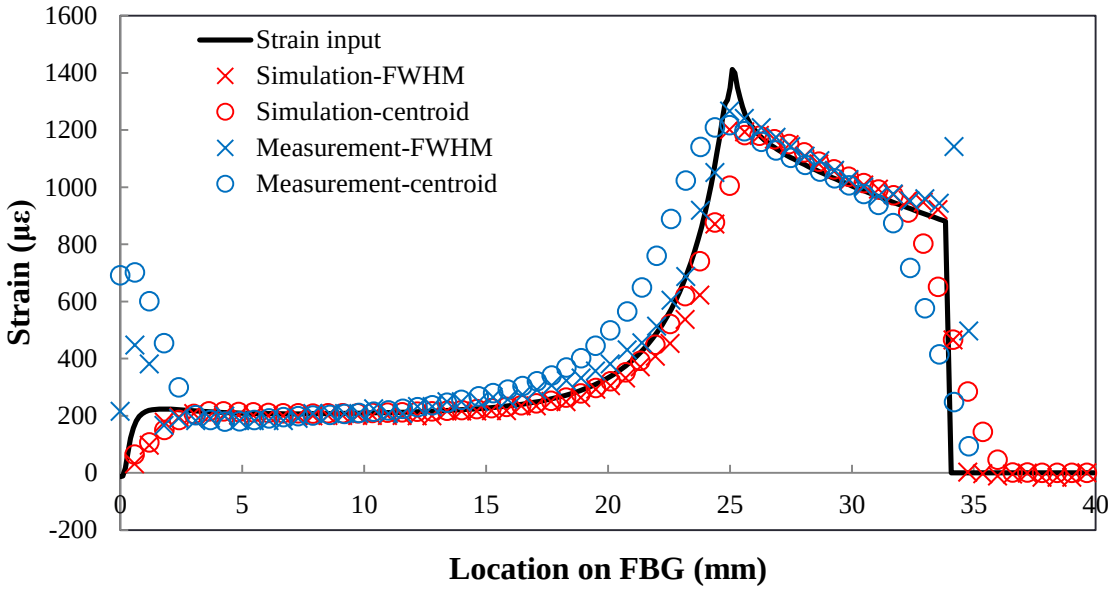

Fig. 4-38. Comparison of simulated measurement with input strain distribution and practical measurements

4.4. Cyclic load test

Before the dynamic load test, pilot tests were carried out to determine the load conditions for the dynamic load test, which was decided to be the cyclic load test, as mentioned in chapter 3. During the test, the crack was supposed to initiate in bonding area of the joint and propagate at appropriate speed until joint failure, and the duration of test should be appropriate. A new adhesive-bonded single-lap joint specimen with embedded FBG was made for cyclic test using the specimen manufacturing

procedure, and the dynamic distributed sensing system based on OFDR was employed. The purposes of the dynamic measurement in cyclic load test can be considered as: evaluation of the sensing system in long-period dynamic measurement, investigation on the strain distribution variation in adhesive-bonded joint during the crack propagation and prepare data of strain distribution for detection of crack.

The cyclic test employed strain gauge as reference for FE analysis and measurement, the test machine controller as recorder of test conditions, FE analysis as reference for strain distribution and microscope to measure the crack length. The cyclic test will be introduced in four aspects, pilot tests, test setup, loading and measurement conditions, results and discussions.

4.4.1. Pilot tests

Pilot tests using dummy joint specimen were carried out to determine load conditions for cyclic load test. As the result, the load frequency of 0.5 Hz was considered convenient for crack observation using microscope. The gradual crack propagation and appropriate test duration were achieved at maximum load between 250 kgf and 400 kgf with 0.1 load ratio. During tests, the crack initiated at filet end in the early period was observed, and it was not always the reason for joint failure. It was considered as an initial defect caused by the spew filet[5].

4.4.2. Test setup

The schematic diagram of test setup is shown in Fig. 4-39. The cyclic load test was carried out on test machine, whose controller was employed to define the load conditions and record the load and displacement information during the test. A strain gauge was adhesively bonded to the surface of adherend in region C at x=1.5, y=1.5, z=27.5, near the FBG embed location, the gauge direction is along the overlap length direction, and the signal of strain gauge was recorded by an independent system throughout the test. And as shown in Fig. 4-40, a microscope camera was set besides the test machine to take photos of joint specimen at x=10.0 both at maximum and minimum load to observe the cracks in bonding area during the test. The installation of specimen and strain gauge was the same with static test. The product information of devices used in the cyclic load test can be found in Table 4-10.

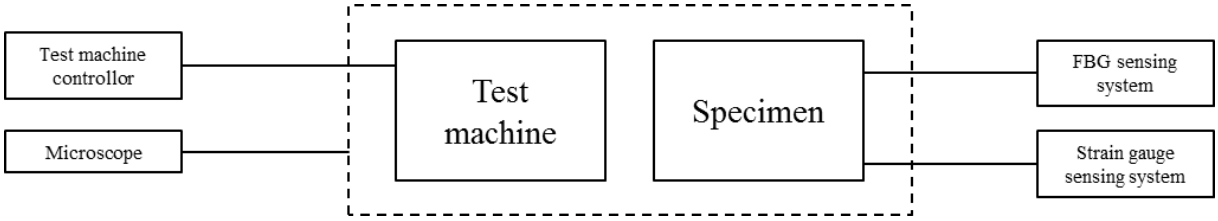

Fig. 4-39. Cyclic load test setup

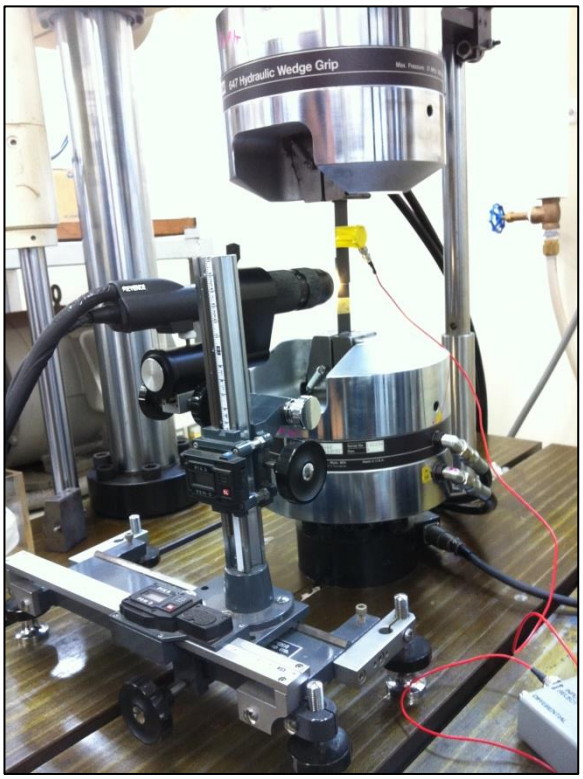

Fig. 4-40. Microscope camera employed in test

Table 4-10. Information of test devices in cyclic test

Devices	Product name	Manufacturer	Features
Test machine	SERVOPULSER EHF-UB5-20L	Shimazu Corporation	Maximum load: 5 ton
Strain gauge	FLA-1-11-1 LDA	Tokyo Sokki Kenkyujo Co., Ltd.	Length: 1 mm
Microscope controller	VHX-1000	Keyence Corporation	

4.4.3. Loading and measurement conditions

As shown in Table 4-11, load conditions for cyclic load test were determined as, 0.5 Hz load frequency, 0.1 load ratio, and sinusoidal wave. The test was divided into two steps according to the maximum load as shown in
Table 4-12. In step 1, in order to observe and measure the initial defect, the maximum load was 250 kgf and lasted for 28000 cycles since the beginning of test. After that, the load was gradually increased to 400 kgf in 1000 cycles without interrupting the loading to accelerate the test. The step 2 was from cycle 29000 to the specimen failure with maximum load of 400 kgf. During the period when the specimen was installed on the test machine and before the loading, the FBG and strain gauge sensing system were started at the same time to record the initial conditions for measurement.
Throughout the test, the FBG sensing system carried out measurement at sampling rate of 5 Hz, other settings can be found in
Table 4-13. The load and displacement in one load cycle were recorded by the test machine controller every 10 cycles with sampling rate of 50 Hz. The strain gauge sensing system acquired data at frequency of 10 Hz throughout the test. All the devices were set to the same system time.

Table 4-11. Load conditions for cyclic load test

Wave form	sinusoidal
Load frequency (Hz)	0.5
Maximum load (kgf)	250, 400
Load ratio	0.1

Table 4-12. Test steps

	Maximum load (kgf)	Load cycles
Step 1	250	0 ~ 28000
Step 2	400	29000 ~ test end

Table 4-13. Sensing system settings in cyclic load test

Wavelength sweep range (nm)	1545 ~ 1555
Wavelength acquisition range (nm)	1546 ~ 1554
Wavelength sweep rate (Hz)	5

4.4.4. Results and discussions

General results

The step 1 of cyclic load test lasted for 28000 cycles, then 1000 cycles were taken for load adjusting, the step 2 lasted for 13470 cycles, and the specimen ruptured in cycle of 42470. The test started at 11:52 on 27th and ended at 11:28 on 28th, the entire test lasted for about 23 hours and 36 minutes.

In the test, two cracks were observed in bonding area by the microscope. As shown in Fig. 4-41, crack 1 initiated at the filet end of overlap (z=0.0, y=1.5) in cycle 180, it propagated gradually along the interface between the adhesive layer and FBG embedding adherend and reached 1.7 mm in the end of test. It was considered as the initial defect due to spew filet. Crack 2 initiated at the square end of overlap (z=25.0, y=1.5) in cycle 31650, it propagated along the same interface and reached 11.3 mm in the test end. The crack length of two cracks measured by microscope with respect to the cycle number is shown in Fig. 4-42. The crack 2 was the reason for joint failure. The failure surface of the joint overlap was shown in Fig. 4-43. The non-uniform crack front of crack 2 was observed, the crack length at FBG embed location was 10.5 mm and crack length at microscope observation edge was 12.8 mm.

The FBG broke around the location of (z=0.0, y=1.5), where it had been bonded into the spew filet during the joint curing. However, in the embed area (region B), the FBG was found still firmly embedded in the CFRP adherend even after the specimen failure. It indicated that, by the embedment procedure developed in this study, the CFRP adherend can provide effective protection for embedded OFS during the measurement.

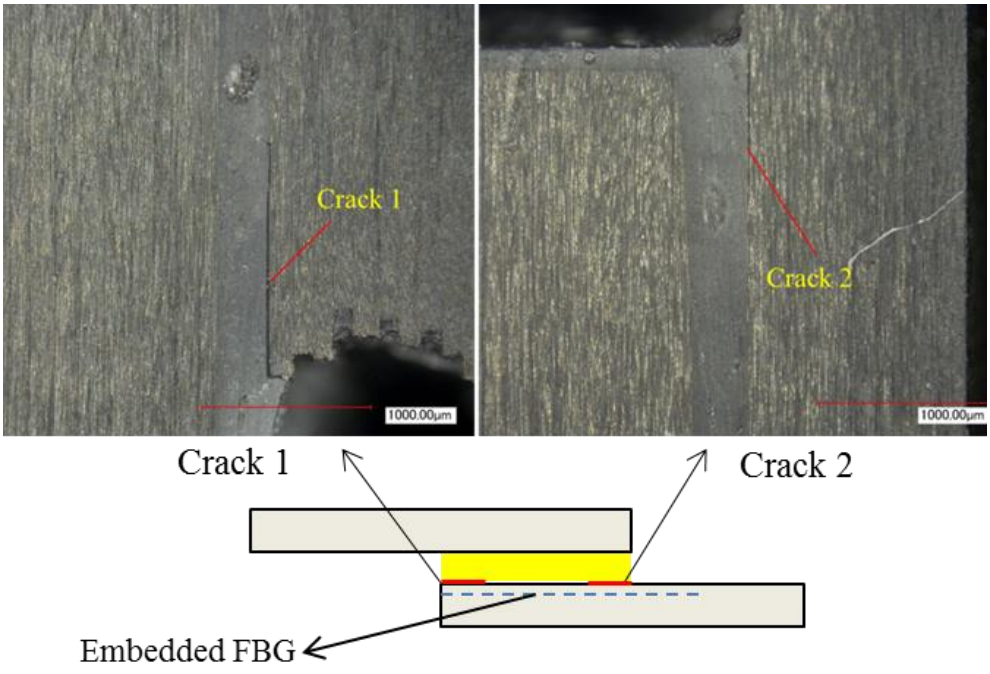

Fig. 4-41. Cracks occurred in joint in cyclic load test

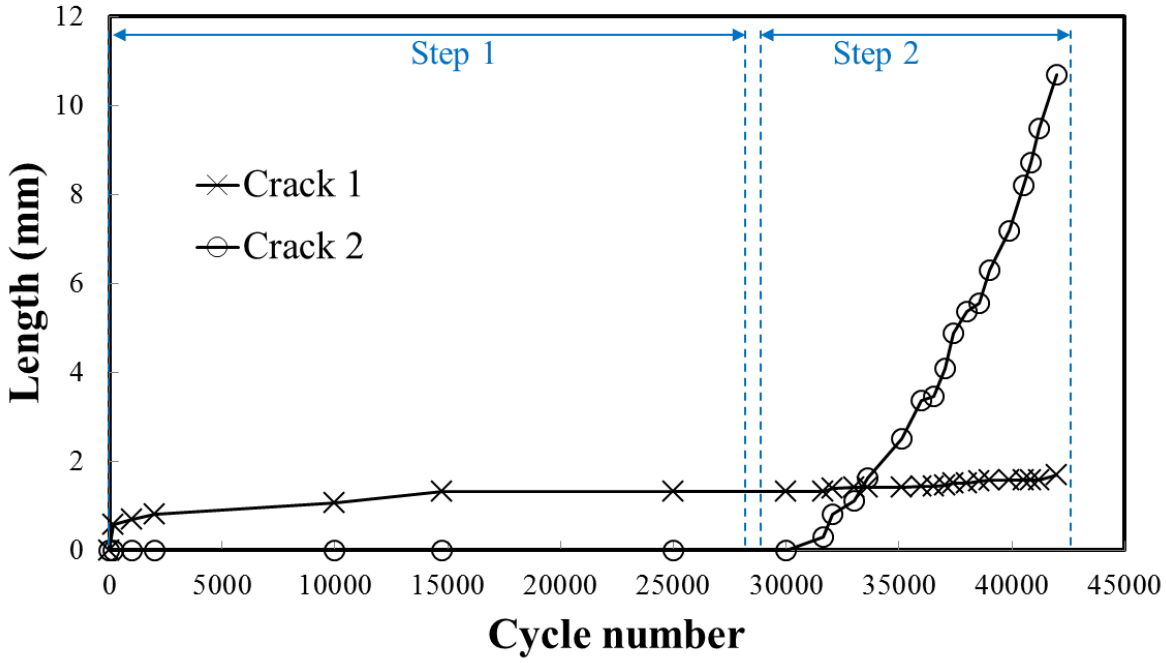

Fig. 4-42. Crack length measured by microscope in test

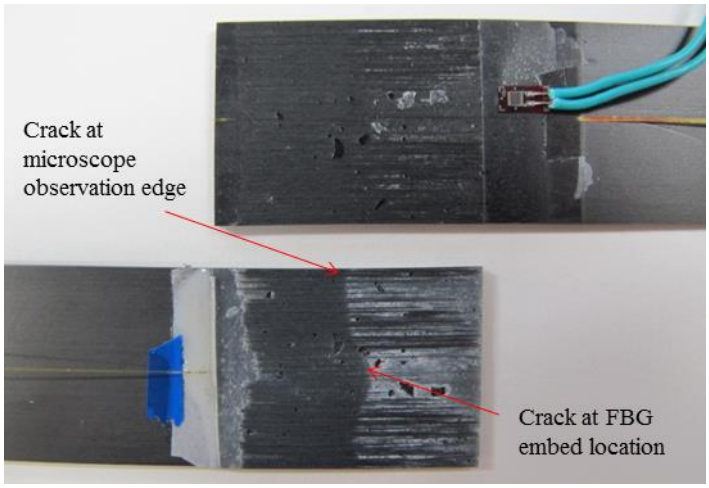

Fig. 4-43. The failure surface of the joint overlap

Longitudinal strain distribution measured by dynamic sensing system

The dynamic distributed sensing system based on OFDR recorded the D_2 signal throughout the cyclic load test. By analyzing the signal, the wavelength distribution at each moment can be reproduced and the FBG spectrum at an arbitrary position on FBG at each moment can be obtained. It is very difficult to show all the measurements, so the measurements of wavelength distribution in cycle 12857 are shown as an example in Fig. 4-44. Horizontal axis indicates position on FBG in region B with interval of 0.6 mm. The reflected FBG spectra at z=28.1 in cycle 12857 and 12858 were shown in Fig. 4-45, the Bragg wavelength shift with cyclic load can be clearly observed

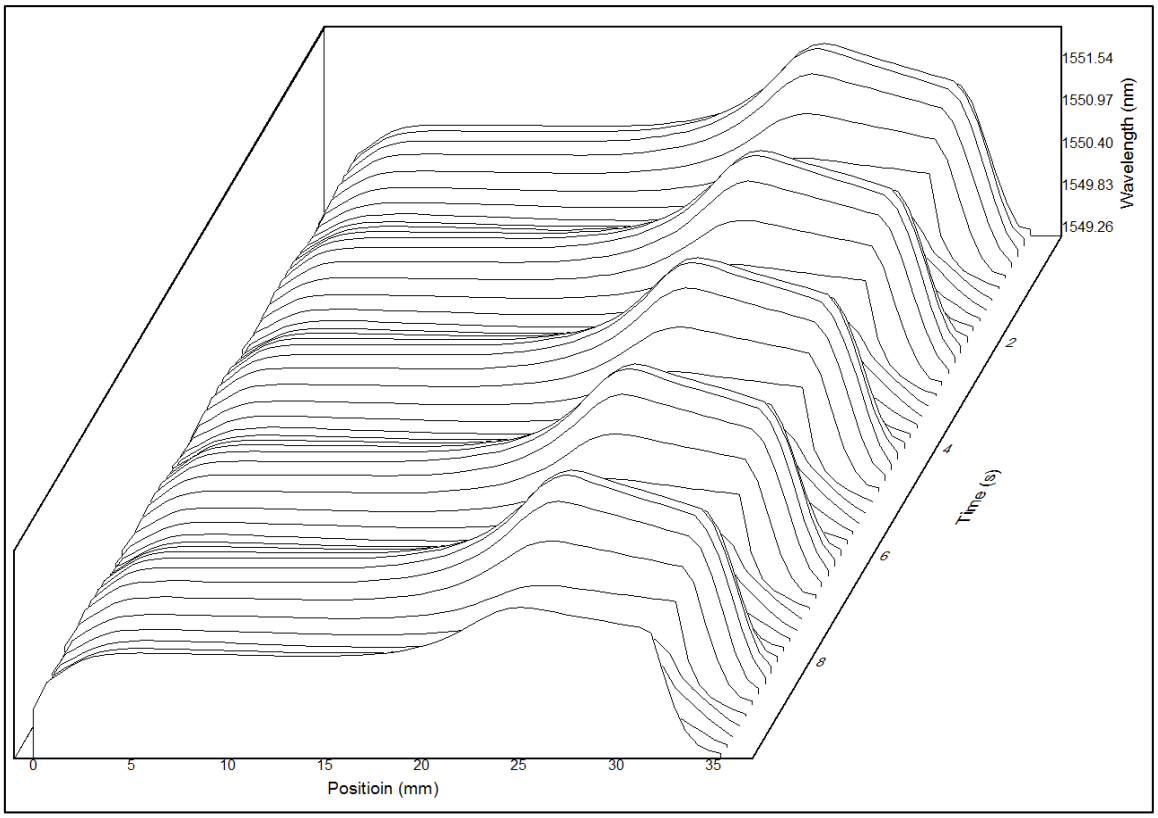

Fig. 4-44. Measured wavelength distribution in cycle 12857

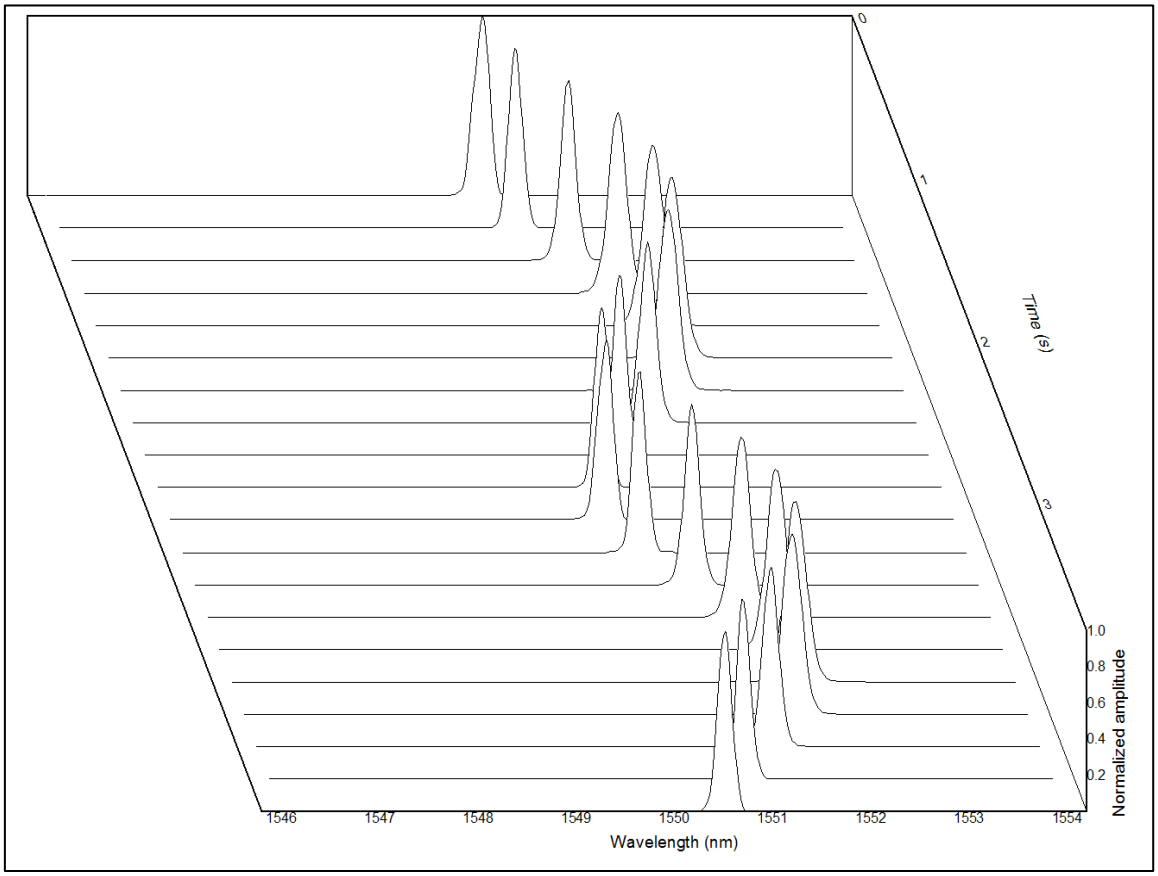

Fig. 4-45. The reflected FBG spectra at z=28.1 in cycle 12857 and 12858

The longitudinal strain distributions on FBG were calculated based on processing the recorded D_2 signal in cyclic load test. The measurement before loading was used as initial condition for calculation, measurement in region C was used as temperature reference, and centroid method was employed to determine the center wavelength in FBG spectra. For discussion, two load cycles were chosen each from step 1 and step 2, the longitudinal strain distribution measurement results at three particular loads in each cycle were calculated. The first is cycle 25000, the loads chosen in this cycle are 25 kgf, 172 kgf and 250 kgf. The second is 29000, the loads are 43 kgf, 242 kgf and 397 kgf. For both cases, crack 1 with length of 1.3 mm was observed.

The measured spectrograms at each load case of two cycles are shown in Fig. 4-46 and Fig. 4-47, the vertical axis indicates the real position on FBG, its relation with the normalized position is shown in Fig. 4-48. The parameters of FBG sensing system for wavelength/strain distribution calculation are shown in

Table 4-14.

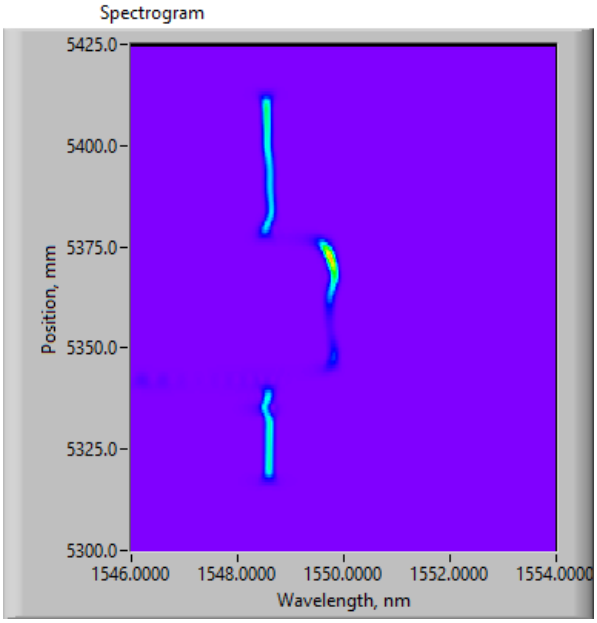

(a) cycle 25000, 25 kgf

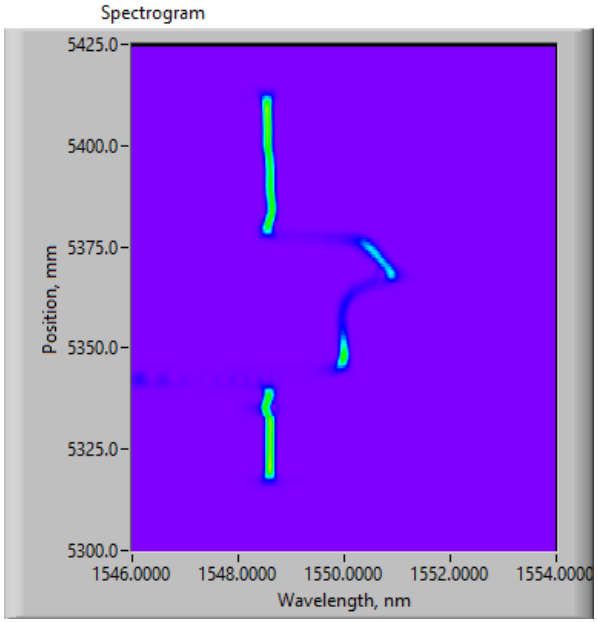

(b) cycle 25000, 172 kgf

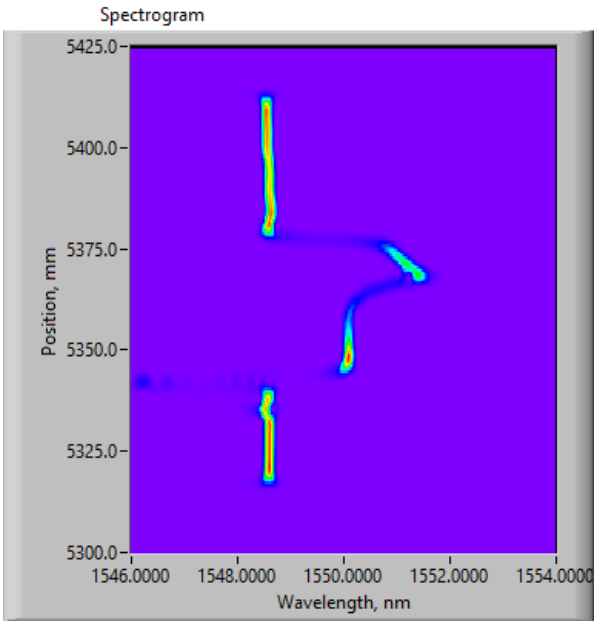

(c) cycle 25000, 250 kgf

Fig. 4-46. Measured spectrograms in cycle 25000

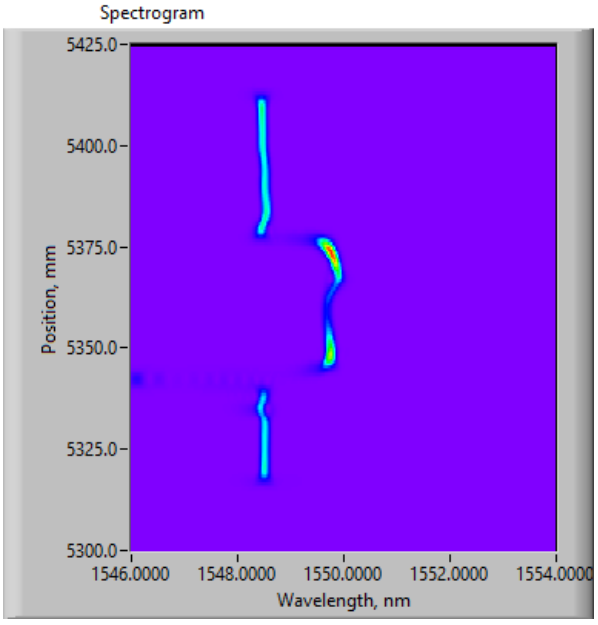

(a) cycle 29000, 43 kgf

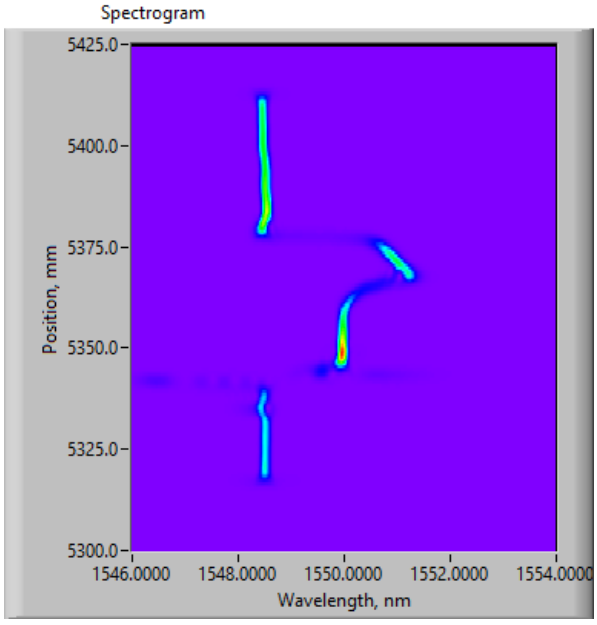

(b) cycle 29000, 242 kgf

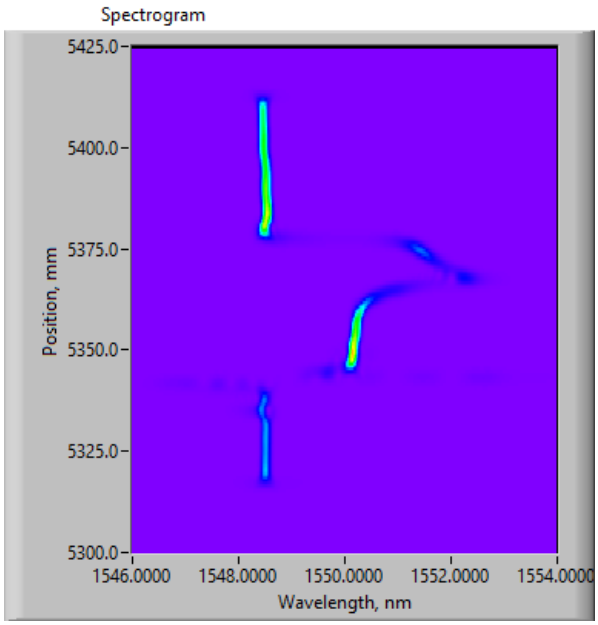

(f) cycle 29000, 397 kgf

Fig. 4-47. Measured spectrograms in cycle 29000

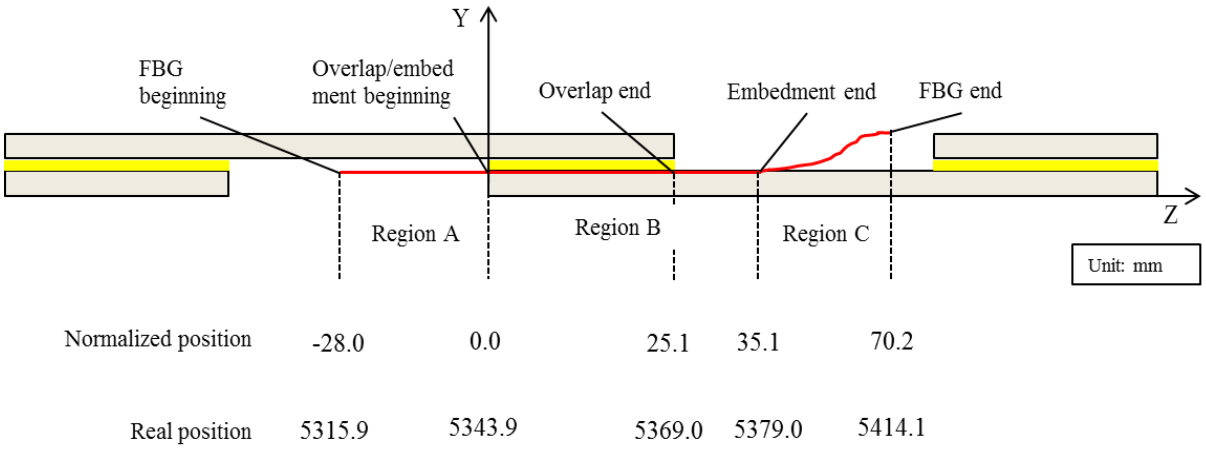

Fig. 4-48. The real position and normalized position on embedded FBG for cyclic load test

Table 4-14. The parameters of FBG sensing system for calculation

Position resolution (mm)	0.6
Wavelength resolution (pm)	20
Window length (pm)	400
Center wavelength determination method	Centroid

The crack in joint specimen was added to the FE model. FEA was performed to provide reference for strain distribution measurement, and before the comparison, as shown in Fig. 4-49, the strain measured by the strain gauge was used to confirm FEA results. In the figure, horizontal axis indicates the six

loads in two cycles, the circle indicates strain in overlap length direction measured by strain gauge and the cross indicates FEA result at the strain gauge location. The agreements were found to be good at all the six loads.

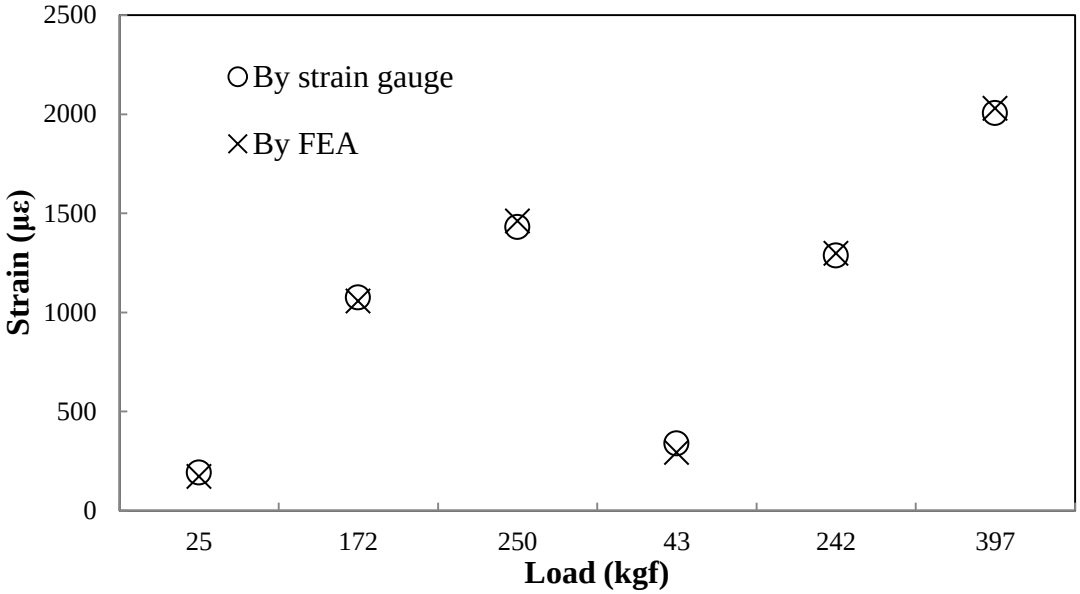

Fig. 4-49. FEA results were confirmed by strain gauge

The comparison of FBG measurement and FEA was shown in Fig. 4-50 and Fig. 4-51. The horizontal axis indicated normalized position on FBG and vertical axis indicated strain in overlap length direction. In a similar pattern with measurement in static test, from both the FBG and FEA results, the strain rose from 0 at the crack front location (z=1.3) and reached to a small peak around z=2.0. It increased gradually in area of (z=2.0 to 20.0) before entering the rapidly increase area (z=20.0 to 25.1). After reaching the peak at z=25.1 it decreased gradually in FBG embedded area outside the overlap (z=25.1 to 35.0). The agreements between FBG measurements and FEA results were found to be good in strain gradually increased area and FBG embed area. Bad agreements were found in three areas where the sharp strain variation existed: the crack front near filet end, the square end and FBG embed end.

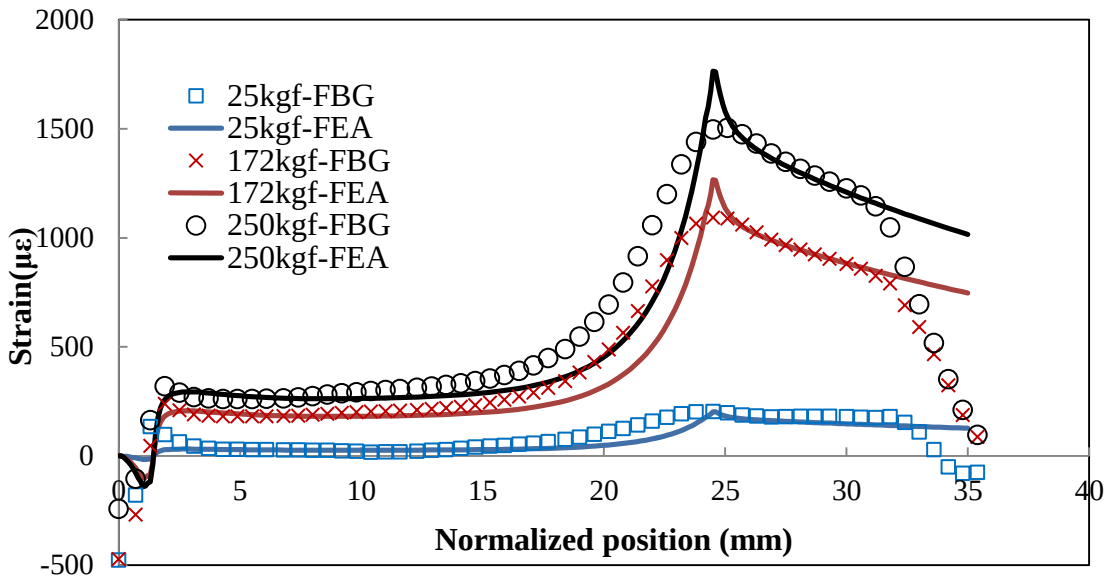

Fig. 4-50. The comparison of FBG measurement and FEA in cycle 25000

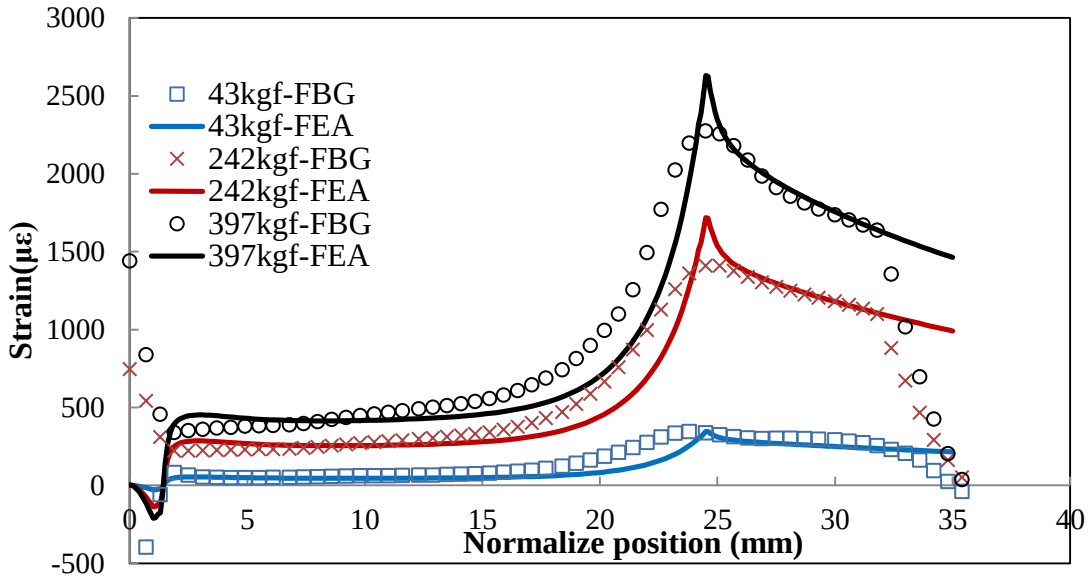

Fig. 4-51. The comparison of FBG measurement and FEA in cycle 29000

The bad agreements were assumed to be caused by the same reason as the measurement in static load test, which is the insufficient spatial resolution of the strain calculation by centroid method. Therefore, the strain distribution in overlap length direction was calculated by the full width half maximum (FWHM) method and compared with centroid and FEA result. For discussion, the comparison at 397 kgf in cycle 29000 is shown in Fig. 4-52. The solid line indicates FEA result, the circle and cross indicates centroid and FWHM result respectively. The agreements between FWHM and FEA result were found to be good in areas of square end and FBG embed end, indicating that the FWHM result described the strain variation in the two areas more precisely. However, big difference existed in filet end area, it was considered that, because the FBG in region A near the filet end was bonded into the

spew filet, when crack occurred and FBG embedding adherend was peeled from the filet, large tensile force would be applied to the FBG portion between the filet and adherend.

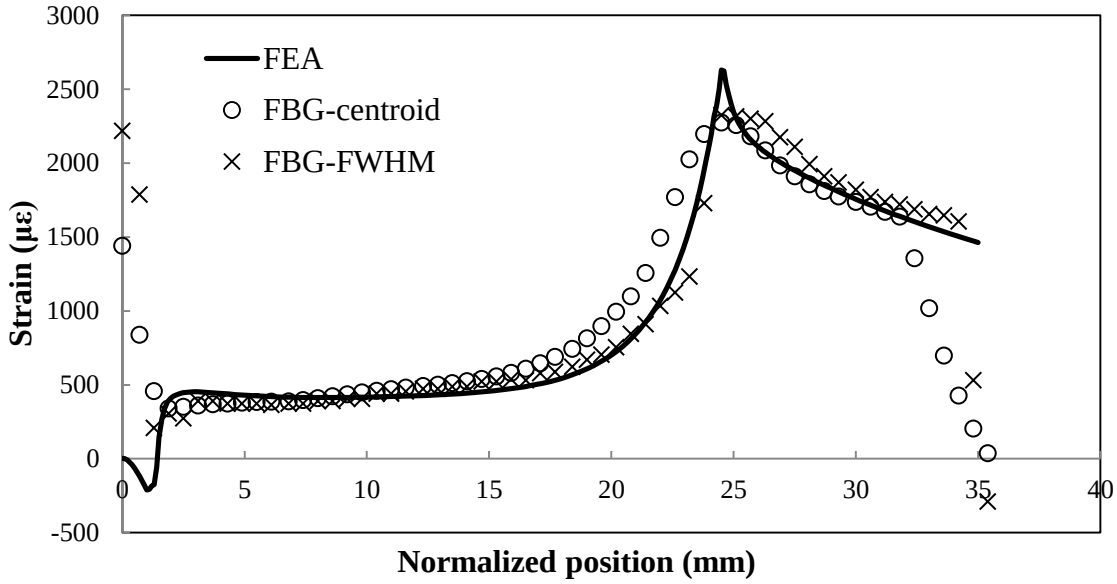

Fig. 4-52. The comparison of strain distribution obtained by FEA and FBG measurement calculated using two methods at 397 kgf in cycle 29000

Sensing system sampling rate

The cyclic load test shown in this section was the first time the dynamic distributed sensing system was used for continuously dynamic measurement during a relatively long period. The stability of sampling rate of the system, which was set to constant 5 Hz for the cyclic load test, was considered to be an important feature. Thus the measured data throughout cyclic test was used to evaluate the system sampling rate.

The main purpose of evaluation is to find out if the sampling rate of system was stable at 5 Hz throughout the cyclic load test. The evaluation method is to compare the strain measured by embedded FBG at the location near the adhered strain gauge in region C with the strain measured by strain gauge, the two measurements need to be extracted at the same time. The measurement time information of FBG sensing system was contained in measurement files, and the measurement time interval of strain gauge sensing system was counted and recorded in measurement files. Thus the measurement time recorded by FBG sensing system can be used as guide of sampling timing for analysis, and by calculating the interval of each timing for analysis, the measurement data of strain gauge can be extracted.

However, the FBG sensing system and strain gauge sensing system were controlled by two isolated computers, and even through the two systems were manually started simultaneously before loading, the first measurement of two systems may not occurred at the exact same time due to difference of

measurement principle and human factors. Therefore, in order to evaluate the sampling rate, at first the initial sampling timing of two systems were investigated. The method is to find out and match the time of measurement of the first load by the two systems. The measurements in period between system start and a short time after loading of FBG sensing system and strain gauge sensing system are shown in Fig. 4-53 and Fig. 4-54, respectively, the horizontal axis of both figure indicates the measurement number and vertical axis indicates measured wavelength and strain gauge signal respectively. The measurement time of first load in each graph, as indicated by red arrow, was defined as initial sampling timing for each system. The initial sampling timing of FBG sensing system is 11:52:14093 which was obtained from data file. The initial sampling timing of strain gauge is 97.9 second since the first measurement, the time interval was read from data file. In this way, we set the initial time for both systems, and now the measurement of two systems can be extracted at the same sampling timing during the test.

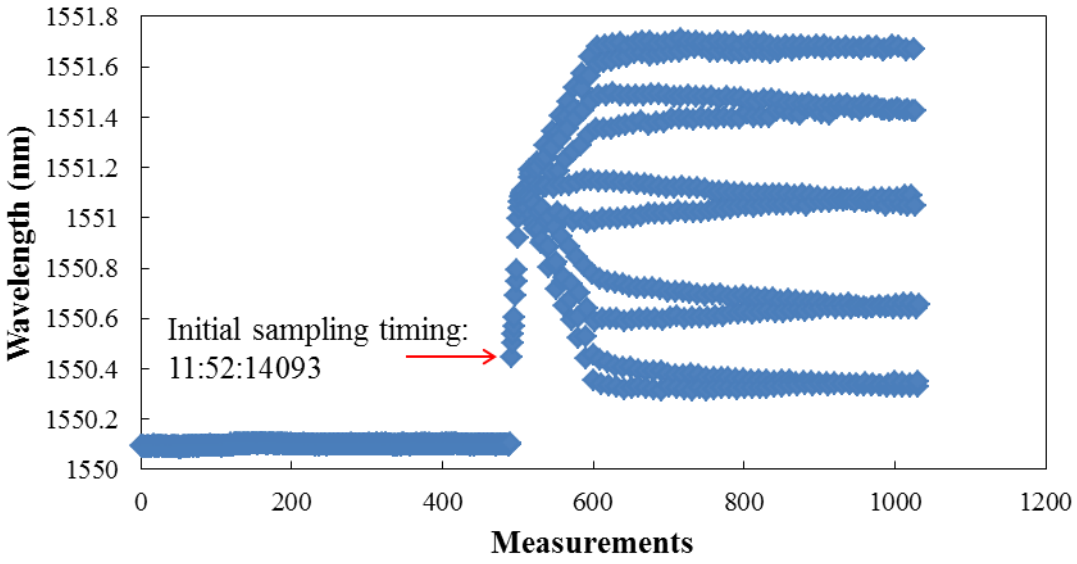

Fig. 4-53. Initial sampling timing of FBG sensing system

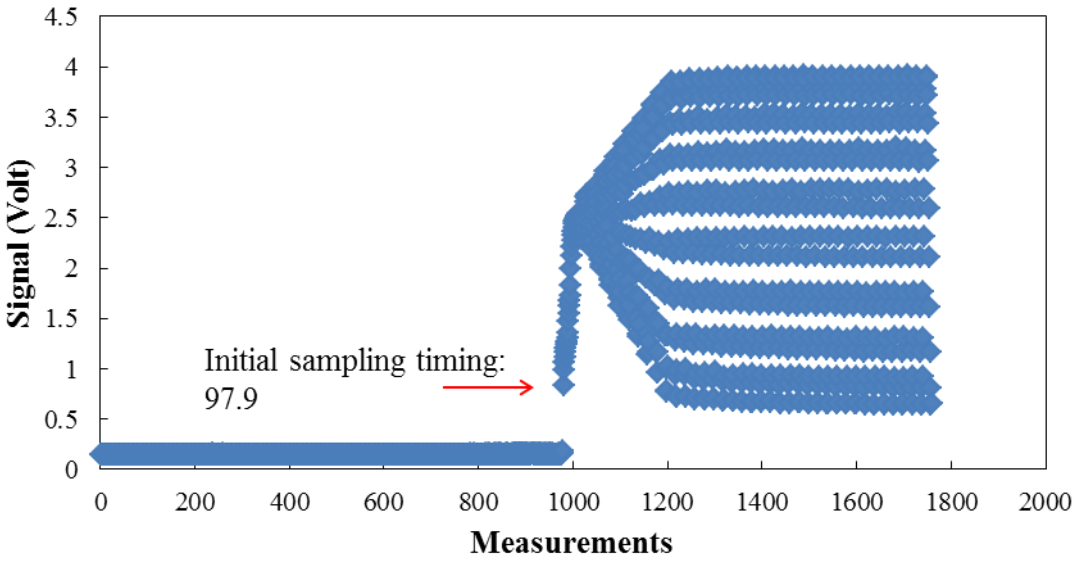

Fig. 4-54. Initial sampling timing of strain gauge sensing system

The sampling timings for analysis are shown in Table 4-15, eleven cases were defined and the time for each case was indicated by FBG system measurement file, the time interval between cases was 2 hours in test step 1 and step 2 and 3 hours in load adjust period. The FBG measurements (strain) in 5 seconds since the sampling time in each case were extracted and compared with the strain gauge measurements at each case. The comparisons are shown in Fig. 4-55, the horizontal axis indicates strain gauge measurement and vertical axis indicates FBG measurements. As the result, the elliptical curve can be observed in each graph, length of minor axis increased and length of major axis decreased with time elapse in cyclic load test.

Table 4-15. Sampling timings for analysis

	FBG	SG	Time interval (hour)
initial	115214093	97.9	
case 1	130006193	4170.0	
case 2	150146593	11470.4	2
case 3	165955093	18558.9	2
case 4	190135893	25859.7	2
case 5	210316893	33160.7	2
case 6	230125993	40249.8	2
case 7	10317193	47561.0	2
case 8	40231193	58315.0	3
case 9	60803893	65847.7	2
case 10	80624793	72948.6	2
case 11	100444093	80047.9	2

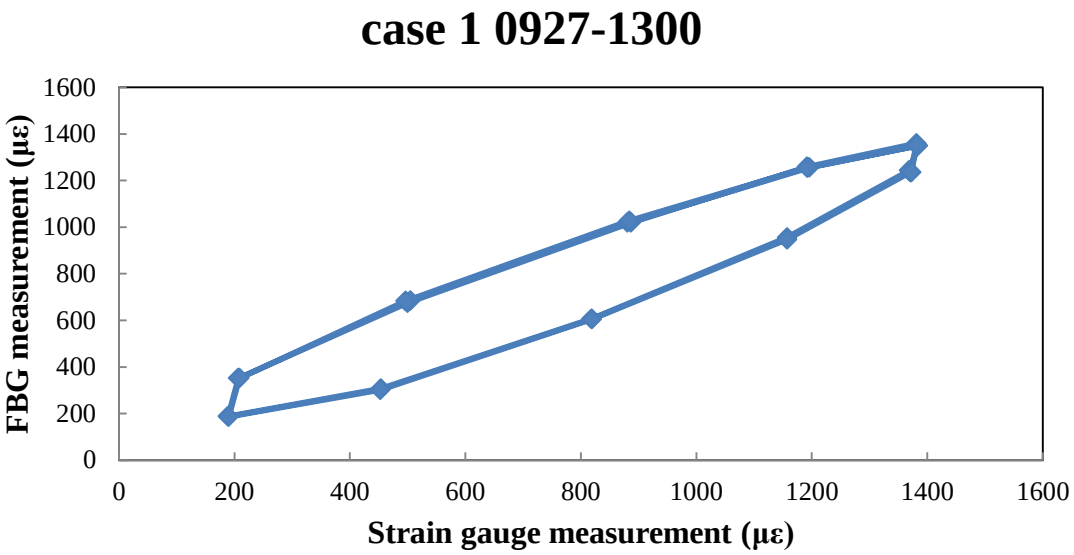
case 1 0927-1300
FBG measurement (με)
Strain gauge measurement (με)
0
200
400
600
800
1000
1200
1400
1600

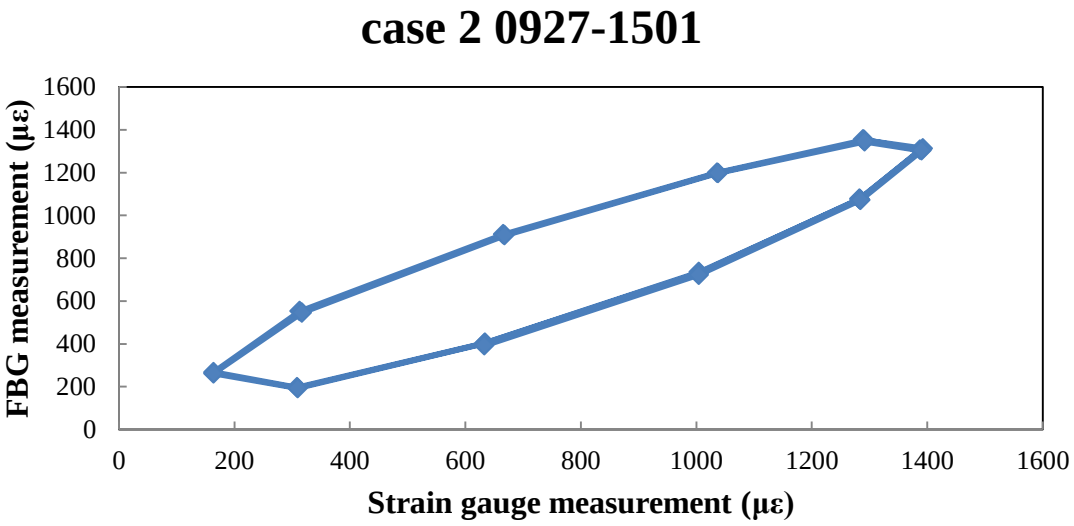
case 2 0927-1501
FBG measurement (με)
Strain gauge measurement (με)
0
200
400
600
800
1000
1200
1400
1600

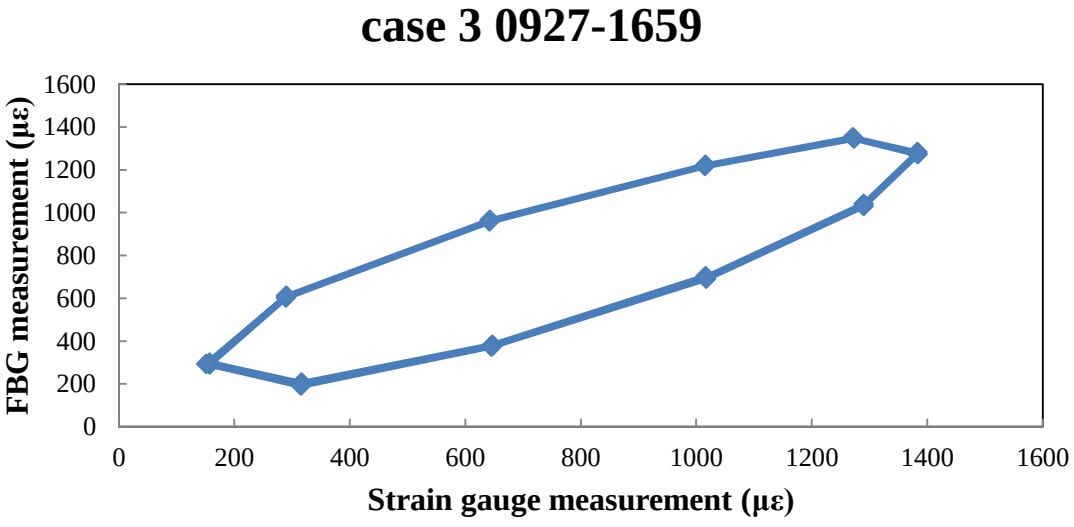
case 3 0927-1659
FBG measurement (με)
Strain gauge measurement (με)
0
200
400
600
800
1000
1200
1400
1600

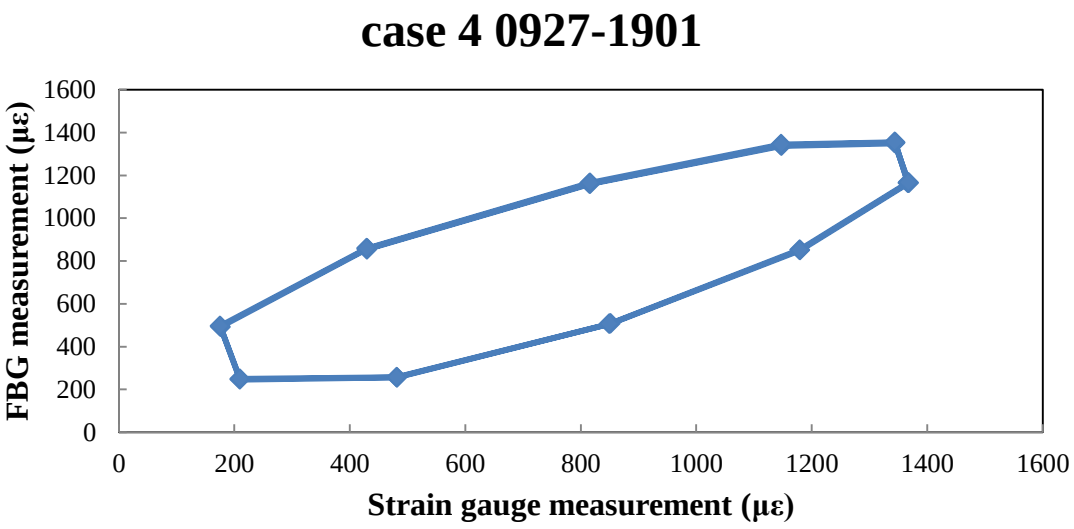
case 4 0927-1901
FBG measurement (με)
Strain gauge measurement (με)
0
200
400
600
800
1000
1200
1400
1600

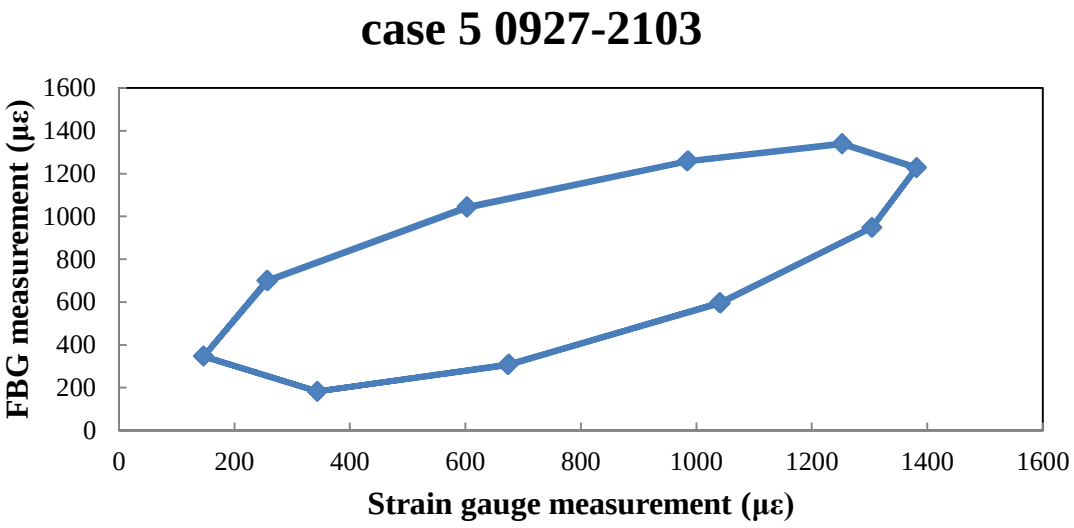
case 5 0927-2103
FBG measurement (με)
Strain gauge measurement (με)
0
200
400
600
800
1000
1200
1400
1600

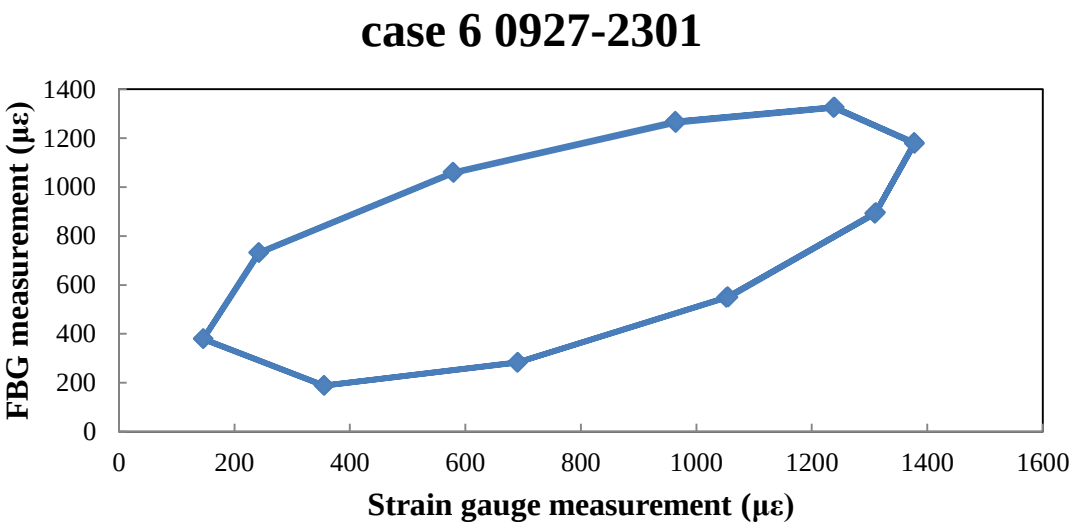
case 6 0927-2301
FBG measurement (με)
Strain gauge measurement (με)
0
200
400
600
800
1000
1200
1400
1600

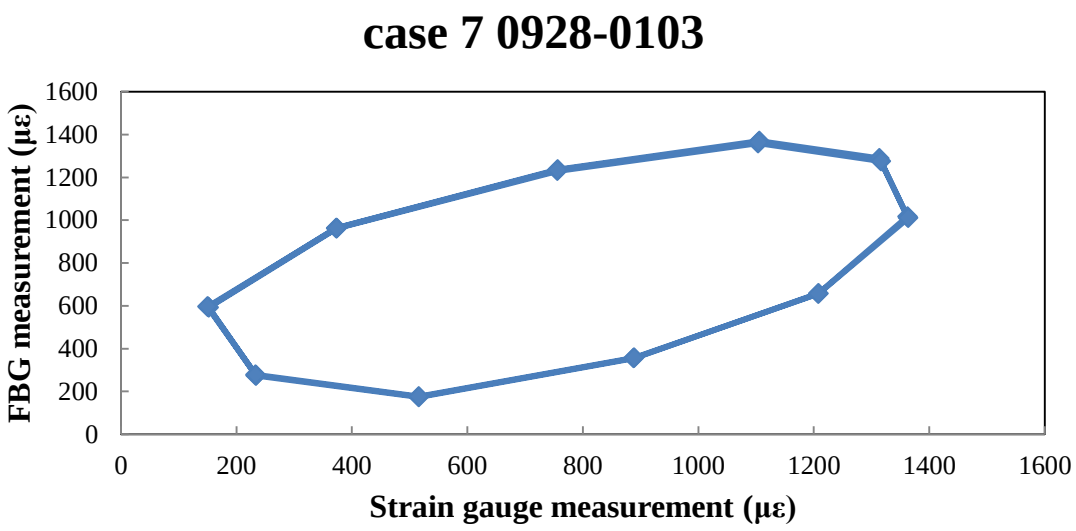
case 7 0928-0103
FBG measurement (με)
0
200
400
600
800
1000
1200
1400
1600
Strain gauge measurement (με)

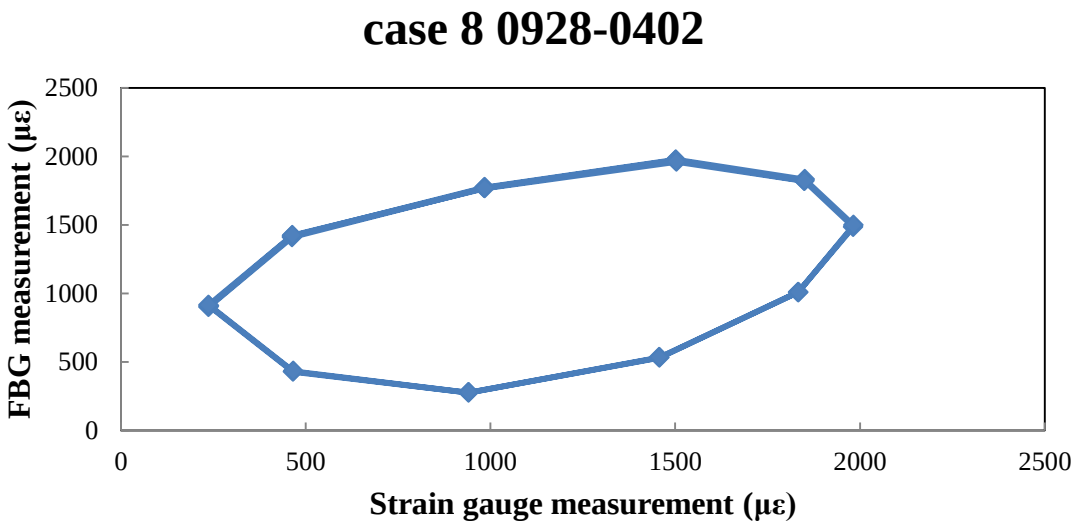
case 8 0928-0402
FBG measurement (με)
0
500
1000
1500
2000
2500
Strain gauge measurement (με)

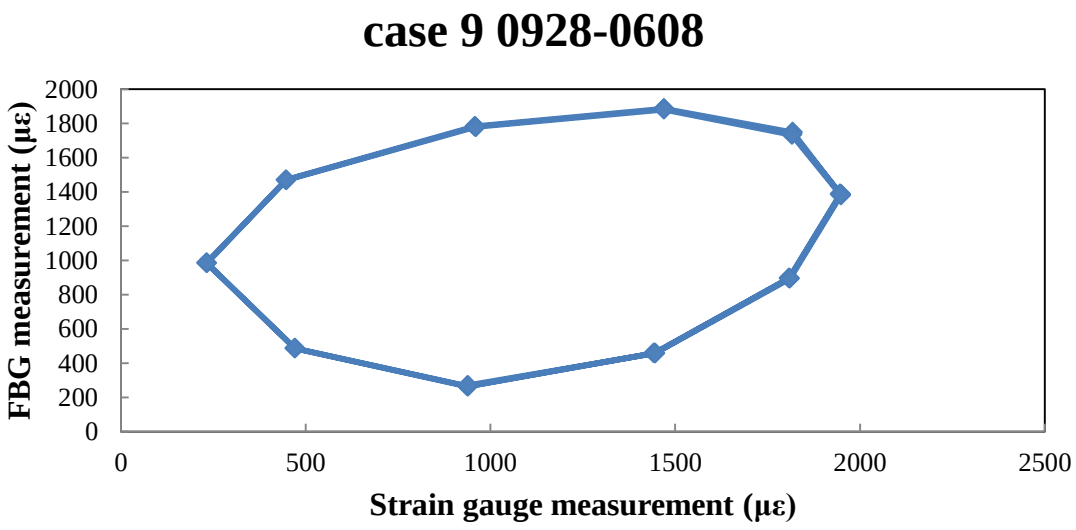
case 9 0928-0608
FBG measurement (με)
0
200
400
600
800
1000
1200
1400
1600
1800
2000
500
1000
1500
2000
2500
Strain gauge measurement (με)

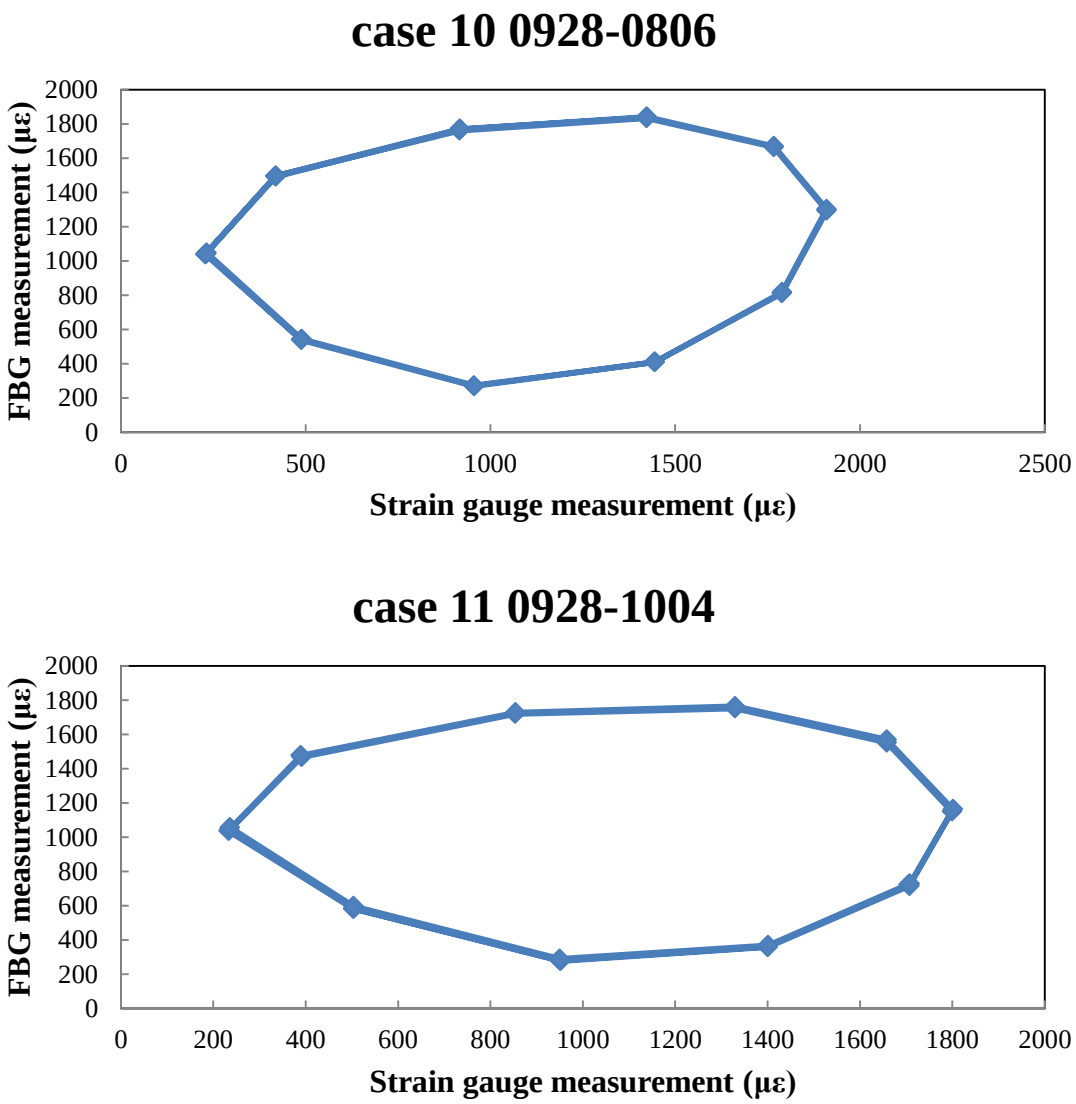

Fig. 4-55. Comparisons of strain measurement by FBG sensing system and strain gauge at 11analysis cases

We had assumed that there is difference between strain measurements by two systems, and in that case the comparison curve in each graph should be a straight line. The ellipse in graph indicated that, there is phase difference in measurement signals measured by two systems even at the same sampling timing, the real timings at when the two systems provide measurement at each case were not exactly the same, and of cause it was difficult to obtain the exact same timing because the two systems were controlled by two independent computer and program. And the shape variation of ellipse with time elapse indicated that, the phase difference in measurement signals of two systems varied during the test, which may be caused by difference in time interval determined by the two systems.

Further investigations were carried out on the phase difference of measurement signals by FBG sensing system and strain gauge sensing system. First, the phase difference at each analysis case was calculated, the method is to draw a fitting curve for measurements by two systems at each case and find out the time of first peak in the fitting curve, and the difference of peak time of measurements by

two systems were the phase difference. The fitting curve is shown in Fig. 4-56, it is drawn by Origin 9 using sinusoidal waveform, the first peak in fitting curve is indicated by red cross and the time at the peak can be read. The phase difference at each analysis case was shown in Table 4-16, the phase difference growth rate was also calculated using phase difference and time interval. The phase difference versus time using case 1 as 0 is shown in Fig. 4-57, horizontal axis indicates time increments at each analysis case, from the figure it can be observed that the phase difference is a straight line, which means the phase difference growth rate is constant, and this can also be confirmed by the calculated phase difference growth rate which is 0.0186 second per hour in average.

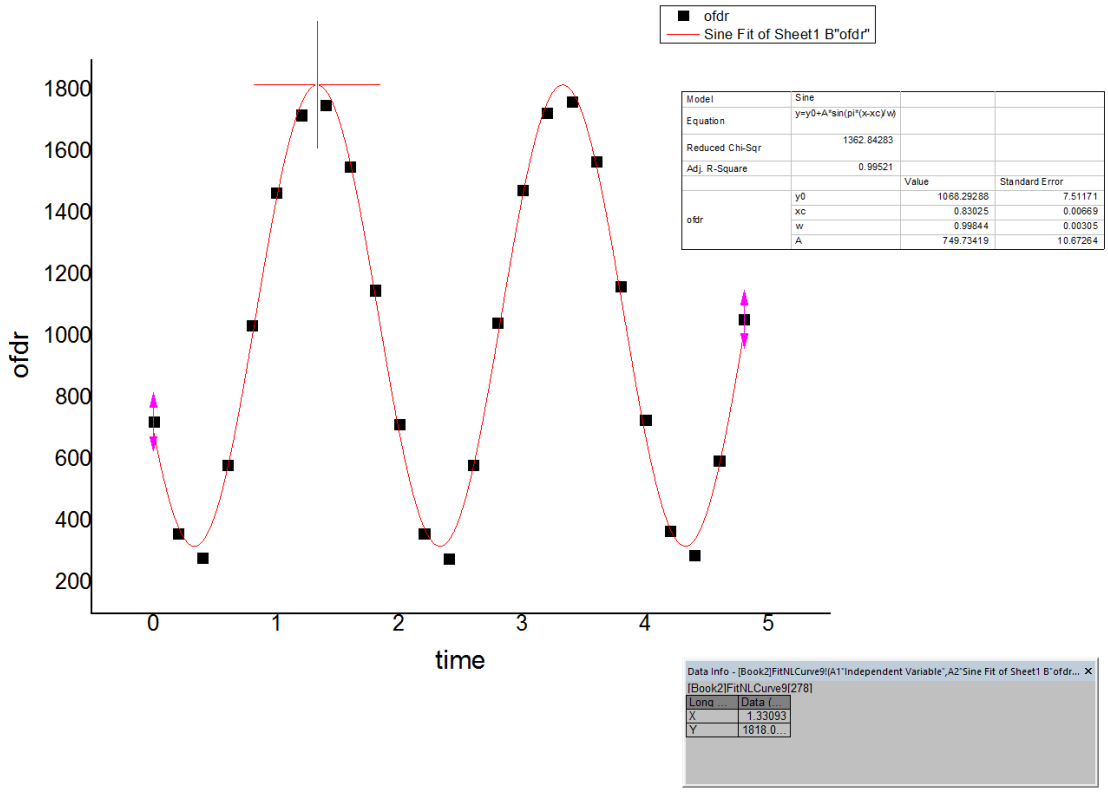

Fig. 4-56. Fitting curve and first peak in signal

Table 4-16. Phase difference between measurement by two systems

	OFDR	SG	Time interval (hour)	Phase difference (s)	Phase difference growth (s)	Phase difference growth rate (s/h)
initial	115214093	97.9				
case 1	130006193	4170.0		0.101		
case 2	150146593	11470.4	2	0.141	0.040	0.0200
case 3	165955093	18558.9	2	0.176	0.035	0.0175
case 4	190135893	25859.7	2	0.211	0.035	0.0175
case 5	210316893	33160.7	2	0.250	0.039	0.0195
case 6	230125993	40249.8	2	0.283	0.033	0.0165
case 7	10317193	47561.0	2	0.319	0.036	0.0180
case 8	40231193	58315.0	3	0.374	0.055	0.0183
case 9	60803893	65847.7	2	0.414	0.040	0.0200
case 10	80624793	72948.6	2	0.453	0.039	0.0195
case 11	100444093	80047.9	2	0.492	0.039	0.0195

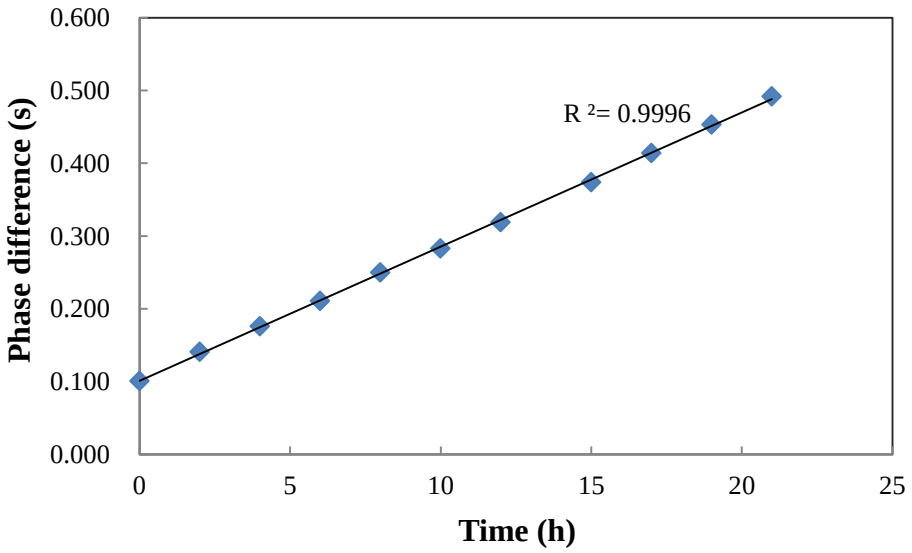

Fig. 4-57. Phase difference between measurement by two systems

Therefore, the constant phase difference growth rate of the phase of measurement signal by two systems indicated that, the sampling rate of dynamic distributed sensing system using embedded FBG was stable, at least as stable as the strain gauge sensing system. And considering that, the chance of phase difference variation between two systems beyond one period (2 seconds) is small and no such variation was observed during test and data analysis, the phase difference growth rate was about 0.0186 second per hour. The worst situation, if the strain gauge was stable at 10 Hz, and the data for discussion was 5 Hz, and all the phase difference was caused by inaccurate sampling rate of FBG

sensing system. The average phase difference in each sampling cycle will be about 1.03 micro second, and FBG sensing system is faster, which means the absolute sampling rate of FBG sensing is 5.0000258 Hz.

4.5. Summary

We developed an embedment procedure to embed the FBG into unidirectional CFRP, by which the FBG was embedded into the adhesive-bonded single-lap joint specimen at designed location. During the test, no strength loss of the joint or function loss of the sensor was found, and the embedment provided effective protection for FBG during measurement. Since the embedment location of FBG in CFRP adherend can be controlled and observed, the detailed FE model of joint specimen was built according to the real condition of embedded FBG. By using this model, the detailed information in fiber core of embedded FBG can be obtained. We believe that the detailed model with embedded FBG can evaluate the mechanical condition more accurately and help us to have the better understand on the FBG measurement. The adhesive-bonded single-lap joint specimen with embedded FBG made by using our procedure has been employed in static and cyclic load test. The dynamic distributed sensing system based on OFDR performs well in both tests. The measurements were examined by comparing with FEA results. The measurement described the strain distribution in joint well in strain gradually varied areas, bad agreements in strain sharply varied areas were found to be caused of the insufficient spatial resolution of centroid method. And the stability of sensing system was evaluated using the measurement data. The sampling rate was confirmed to be stable by comparison with the strain gauge measurement, and the phase difference growth rate between two systems was about 0.0186 second per hour.

4.6. Problems and future works

One of the important achievements of this study is the embedment method of OFS into adhesive-bonded joint. The embedment procedure has been proved to be feasible and effective, however, the joint made by using this procedure has a filet end which cannot be removed. The filet end has brought us many troubles and an improvement on the procedure is highly desired.

The dynamic distributed sensing system showed good performance in 23.5 hours cyclic load test, however, the real structure needs much longer period monitoring than this test. The sensing system should be tested in a long period test. There is a problem needs to be considered, the system based on OFDR generates large data file during measurement. In our

case, we got nearly 400 GB in the 23.5 hours test and it was not convenient to storage, transmit or analyze. However, this is the charming part of system based on OFDR, it can record all the information so the details of measurement such as spectrum at each position on FBG can be reproduced. So I think the measurement should be designed carefully according to the practical situation, in some occasions the sampling rate may be reduced or the information to be recorded may be simplified for long period monitoring.

The evaluation of sensing system sampling rate stability is considered important when using dynamic sensing system. And the evaluation test should be designed carefully whether with or without a reference system. In our case, we employed a reference system which was strain gauge sensing system, however, the data file of strain gauge sensing system didn't indicate the measurement time directly. And this brought a lot of trouble to us when doing the evaluation. Thus in the future, when there is a system needs to be evaluated, the reference system should record the real measurement time.

Reference

[1] S. Takeda, Y. Okabe and N. Takeda, Delamination detection in CFRP laminates with embedded small-diameter fiber Bragg grating sensors, Composites: Part A, vol.33, pp.971-980, 2002
[2] S. Takeda, T. Yamamoto, Y. Okabe and N. Takeda, Debonding monitoring of a composite repair patch using small-diameter FBG sensors, Proc. of SPIE, vol. 5390, pp. 495-504, 2004
[3] S. Takeda, Y. Okabe and N. Takeda, Monitoring of delamination growth in CFRP laminates using chirped FBG sensors, Journal of Intelligent Material Systems and Structures, vol. 19, pp. 437-444, 2008
[4] Y. Okabe, S. Yashiro, T. Kosaka and N. Takeda, Detection of transverse cracks in CFRP composites using embedded fiber Bragg grating sensors, Smart material structure, vol.9, pp.832-838, 2002
[5] M. Quaresimin and M. Ricotta, Fatigue behavior and damage evolution of single lap bonded joints in composite material, Composites Science and Technology, vol.66, pp.176-187

Chapter 5

Damage detection and further applications

In SHM, some of the data or information acquired by sensing techniques can be used directly for structural integrity assessment or damage detection, however, in the most occasions, the acquired data or information need to be analyzed by the particular method for assessment of the particular structural condition or detection of particular damage. Thus after acquiring the data, the next step of SHM is to find out how could we use the acquired data, which means application methods for acquired data need to be developed.

In our case, the data has been successfully acquired by the dynamic distributed sensing system in relatively long-period cyclic load test. Because of the unique feature of the system based on OFDR, the data includes the strain distribution and the FBG spectrum at each position on FBG, both of them are with high spatial resolution. The target damage of this study is the crack in bonding area, which had been controlled to occur and measured by microscope camera in cyclic test. An important goal of this chapter is to discuss the detection method of the crack by using acquired data.

In this chapter, at first the crack detection method based on strain distribution variation will be introduced and employed for detecting cracks occurred in cyclic load test. After that, the irregular FBG spectra around crack front location will be investigated, another crack detection method will be proposed based on examining the shape of spectra. Finally, proposals will be made on three future study subjects.

5.1. Crack detection of adhesive-bonded joint based on strain distribution

5.1.1. Crack detection method based on strain distribution

From the analysis of longitudinal strain distribution measured by embedded FBG, it has been observed that the strain distribution varied with crack propagation even under the constant load conditions. As mentioned if the strain distribution can be used as an indicator of crack conditions, and by building the relation between strain distribution variation and crack conditions, the crack may be evaluated at any time in test by analyzing the measured strain distribution.

In order to build the relation, at first we examined the measured strain distribution throughout cyclic load test. Since the sampling rate of sensing system was 5 Hz and load frequency was 0.5 Hz in cyclic load test, there are ten sets of data in a single load cycle, instead of examining all data in one cycle, the data at the maximum and minimum load were considered to be representative.

Thus strain distribution at the maximum and minimum load in one load cycle at the time when the crack length measured by microscope were examined and shown in Fig. 5-1 for discussion. The load cycle from which data was extracted is shown in each graph, red curve and blue curve indicated strain distribution at maximum and minimum load, respectively. The horizontal axis indicates position on FBG, and vertical axis indicates strain value.

The sampling time for discussion are summarized in

Table 5-1, only the time when crack propagated significantly is chosen. For the data analysis in this study, it is necessary to transform the number of load cycle into the real time, because the data files recorded by the sensing system were arranged in order of real time.

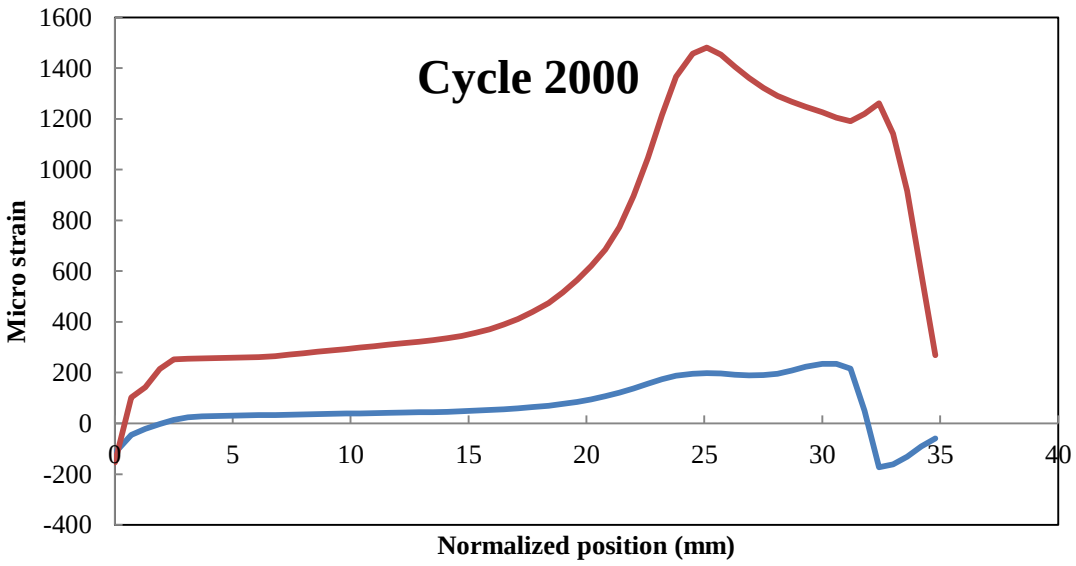

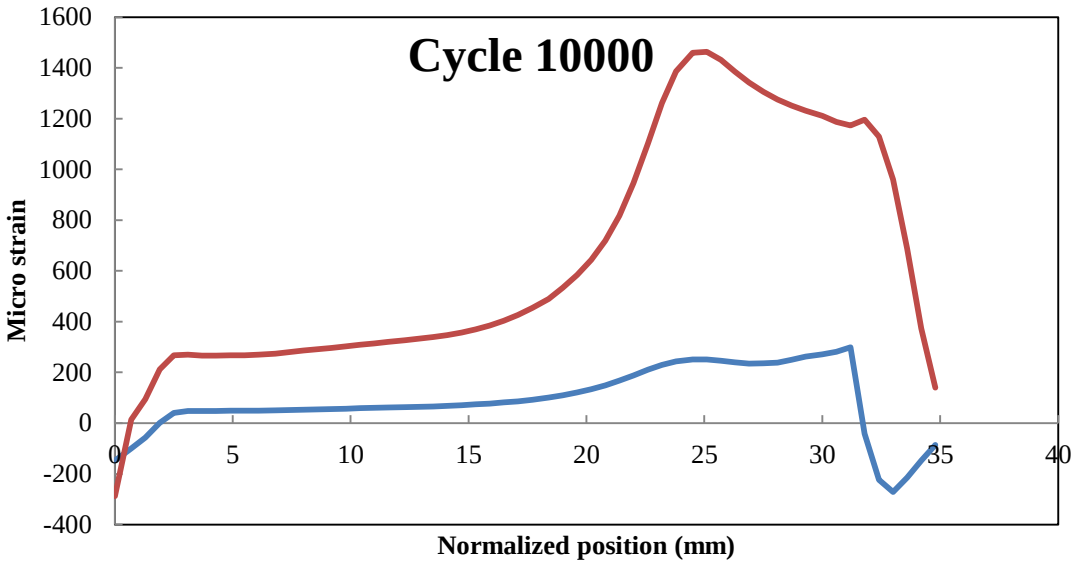
Cycle 10000
Micro strain
1600
1400
1200
1000
800
600
400
200
0
-200
-400
0
5
10
15
20
25
30
35
40
Normalized position (mm)

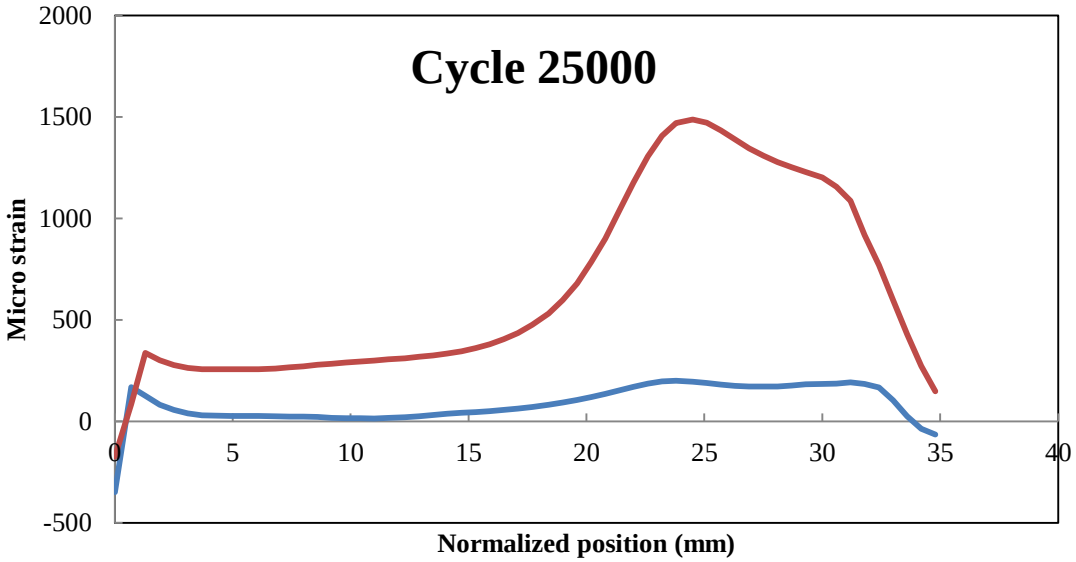
Cycle 25000
Micro strain
2000
1500
1000
500
0
-500
0
5
10
15
20
25
30
35
40
Normalized position (mm)

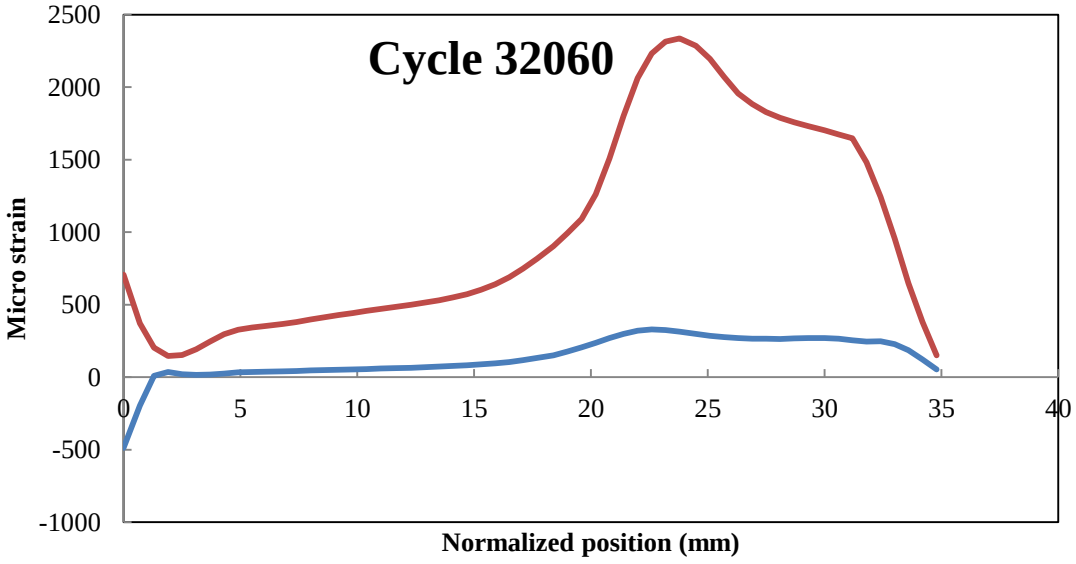
Cycle 32060
Micro strain
2500
2000
1500
1000
500
0
-500
-1000
0
5
10
15
20
25
30
35
40
Normalized position (mm)

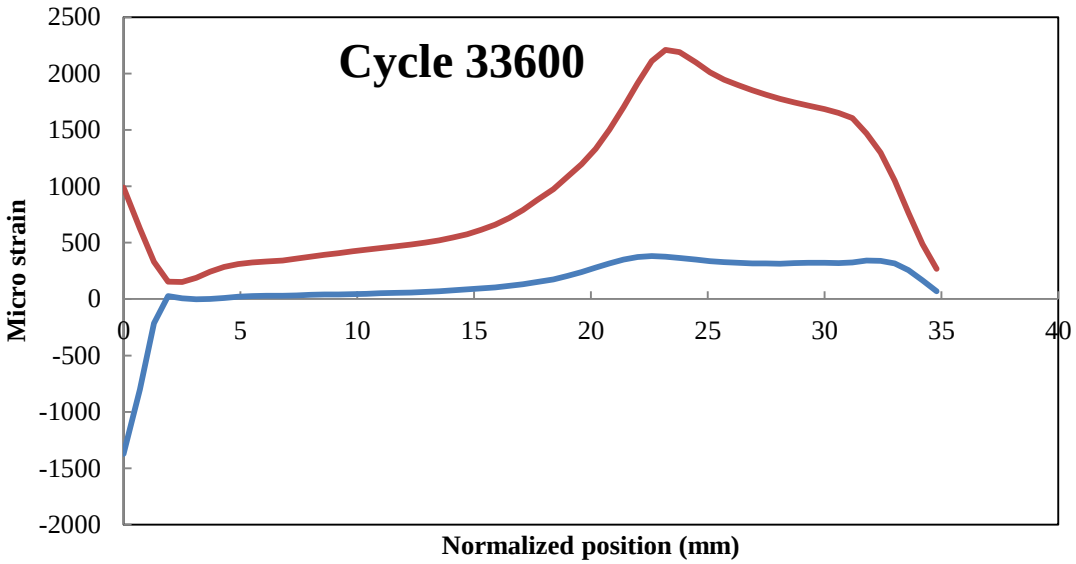
Cycle 33600
Micro strain
Normalized position (mm)
2500
2000
1500
1000
500
0
-500
-1000
-1500
-2000
0
5
10
15
20
25
30
35
40

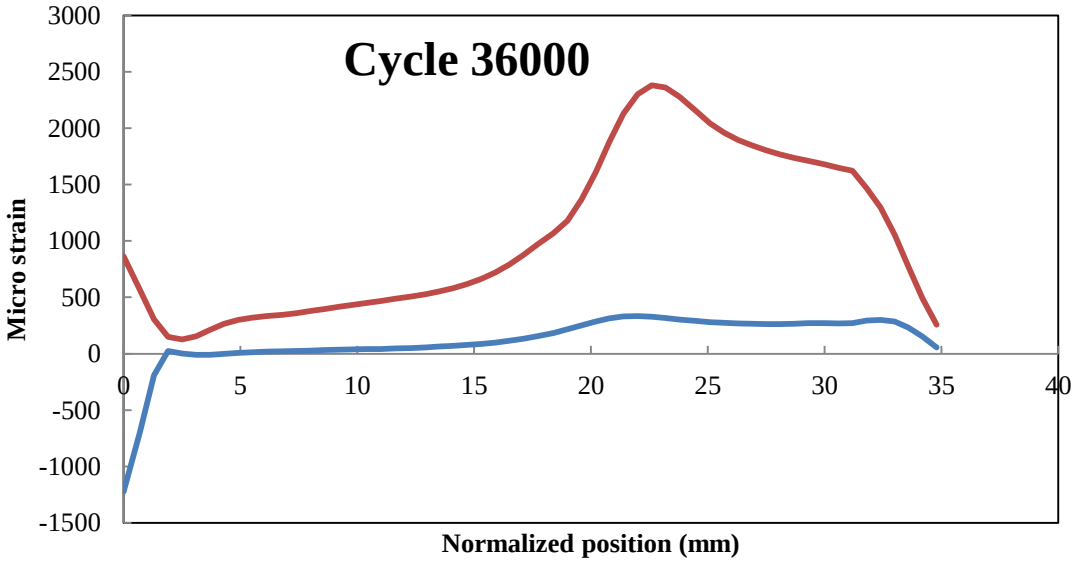
Cycle 36000
Micro strain
Normalized position (mm)
3000
2500
2000
1500
1000
500
0
-500
-1000
-1500
0
5
10
15
20
25
30
35
40

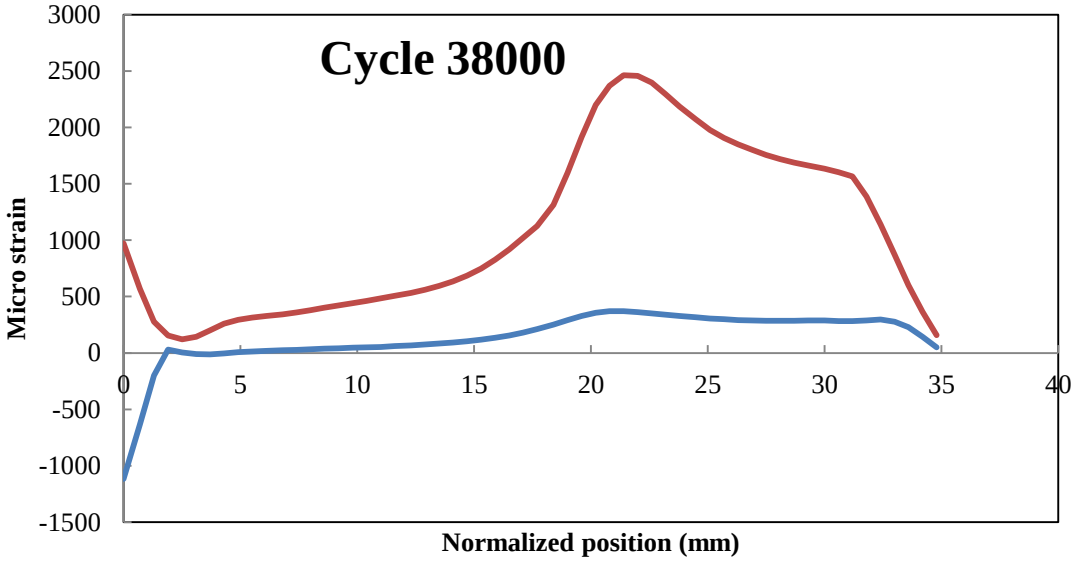
Cycle 38000
Micro strain
Normalized position (mm)
3000
2500
2000
1500
1000
500
0
-500
-1000
-1500
0
5
10
15
20
25
30
35
40

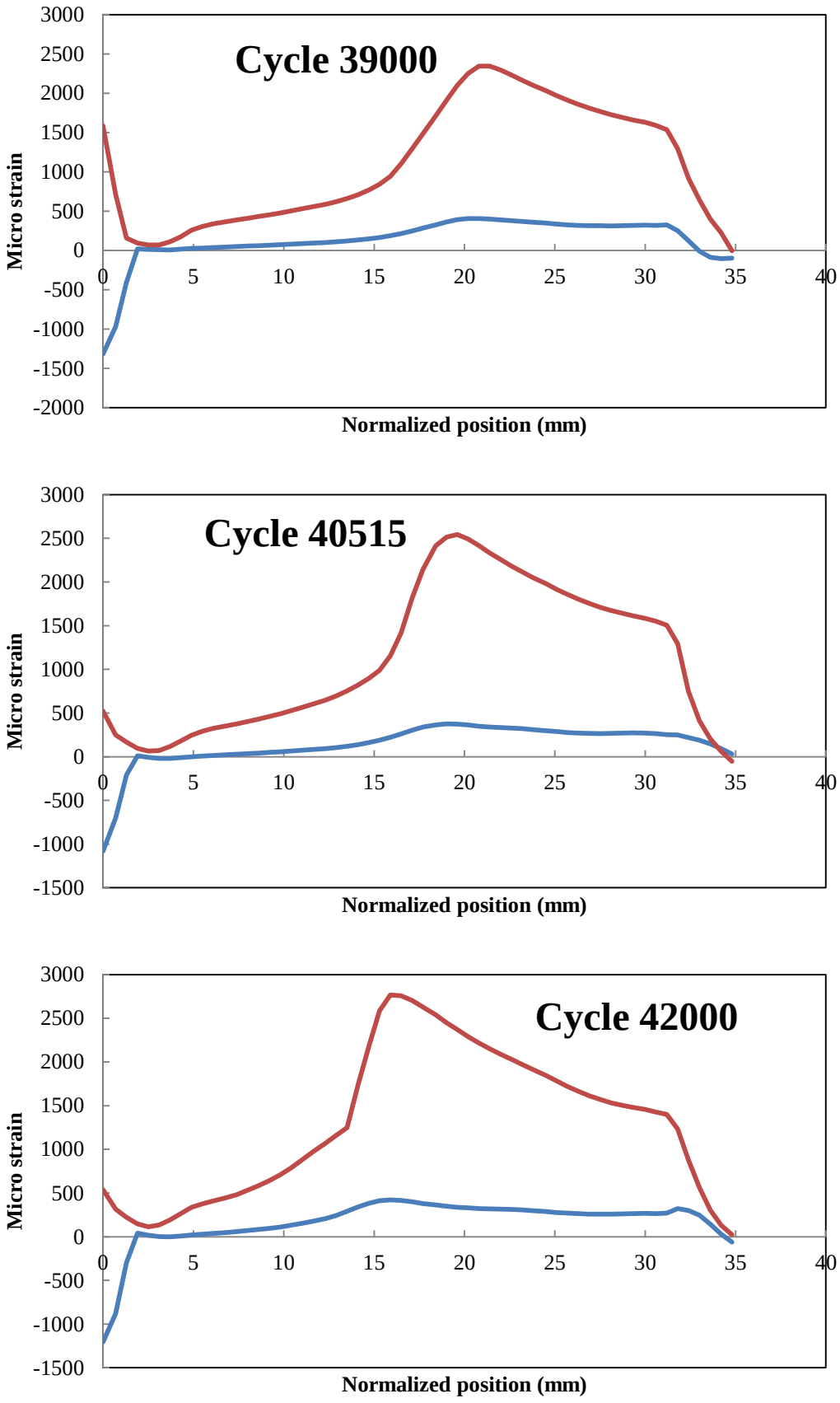

Fig. 5-1. Strain distributions in ten load cycles

Table 5-1. Summary of sampling time in ten cases

		crack length measured by microscope (mm)	
real time	cycle	crack 1	crack 2
12:58:40	2000	0.80	0.00
17:25:20	10000	1.06	0.00
01:45:20	25000	1.33	0.00
05:40:40	32060	1.40	0.80
06:32:00	33600	1.42	1.62
07:52:00	36000	1.43	3.37
08:58:40	38000	1.51	5.36
09:32:00	39000	1.58	6.31
10:22:30	40515	1.58	8.21
11:12:00	42000	1.70	10.70

From the figures, the strain distribution varied both in aspects of strain value and shape of distribution with the crack propagation. We noticed that, the positions of two peaks of strain at two overlap ends (z=0.0 and z=25.1) moved towards middle of overlap with crack propagation, which means the strain concentration position moved, and it may be caused by the shorten overlap length. If the relation of strain concentration position and crack length can be build, the crack length may be estimated based on analyzing the strain distribution.

And comparing with strain curve at minimum load, the positions of peak strain are easier to be identified in the curve shape at maximum load. Thus in this study, the strain distribution at maximum load in load cycle was investigated as the crack indicator.

FEA was carried out to investigate the strain distribution variation using the FE models with different crack length at the same load condition, in this way, the only factor, the crack length, can be analyzed. Although the cracks observed in cyclic load test initiated and propagated at interface between adhesive layer and adherend embedded with FBG, the FEA considered the more complex situations when the cracks from both overlap ends initiated and propagated at the both adhesive/adherend interfaces and in adhesive layer. The tensile load applied on models was 400 kgf. As shown in Fig. 5-2, four FE models were built, model 0 considers the joint with no crack and the FBG position is in lower adherend for all models, model 1 considers the two 2-mm-long cracks at interface between adhesive layer and lower aherend, model 2 considers the two 2-mm-long cracks at middle in thickness in adhesive layer, and model 3 considers two 2-mm-long cracks at interface between adhesive layer and upper aherend. The boundary conditions of FEA are the same with cyclic load test, the longitudinal strain distribution along the FBG position of each model was extracted for discussion. The strain distribution comparison is shown in Fig. 5-3.

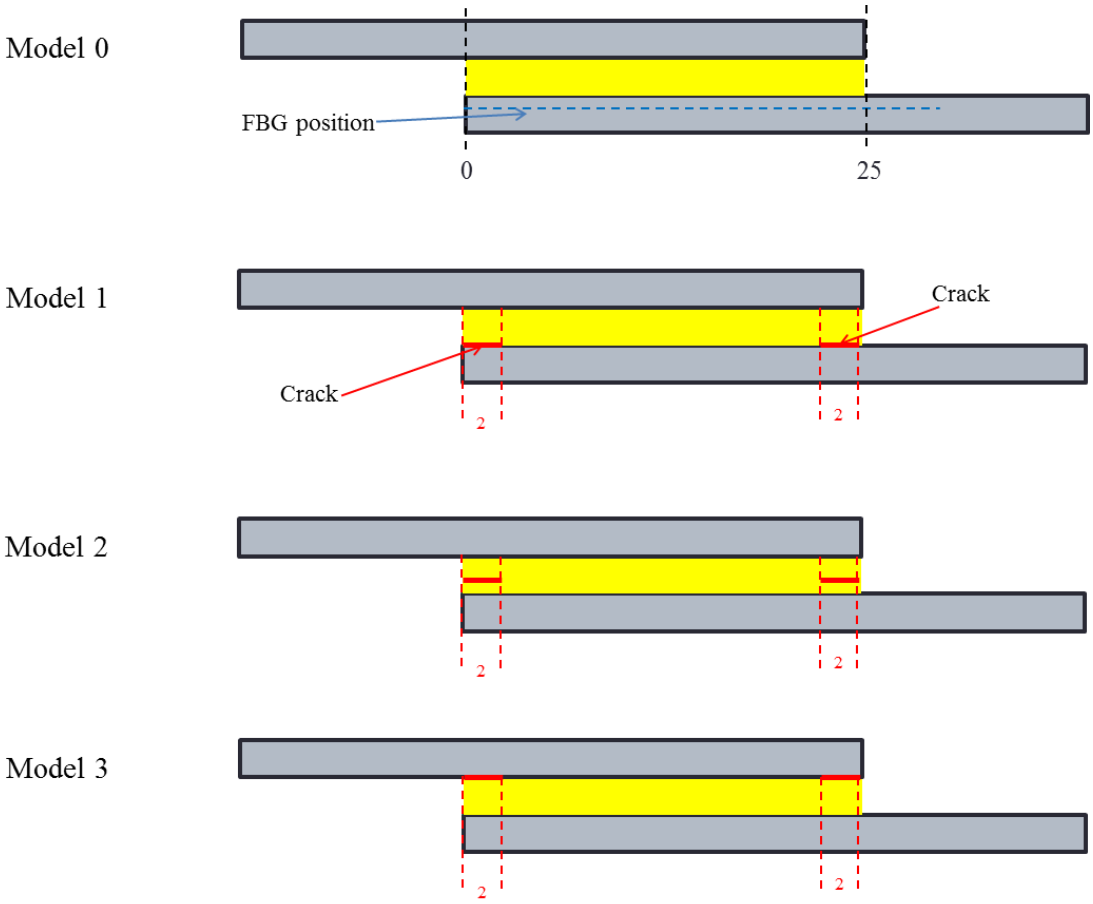

Fig. 5-2. Schematic diagram of FE models

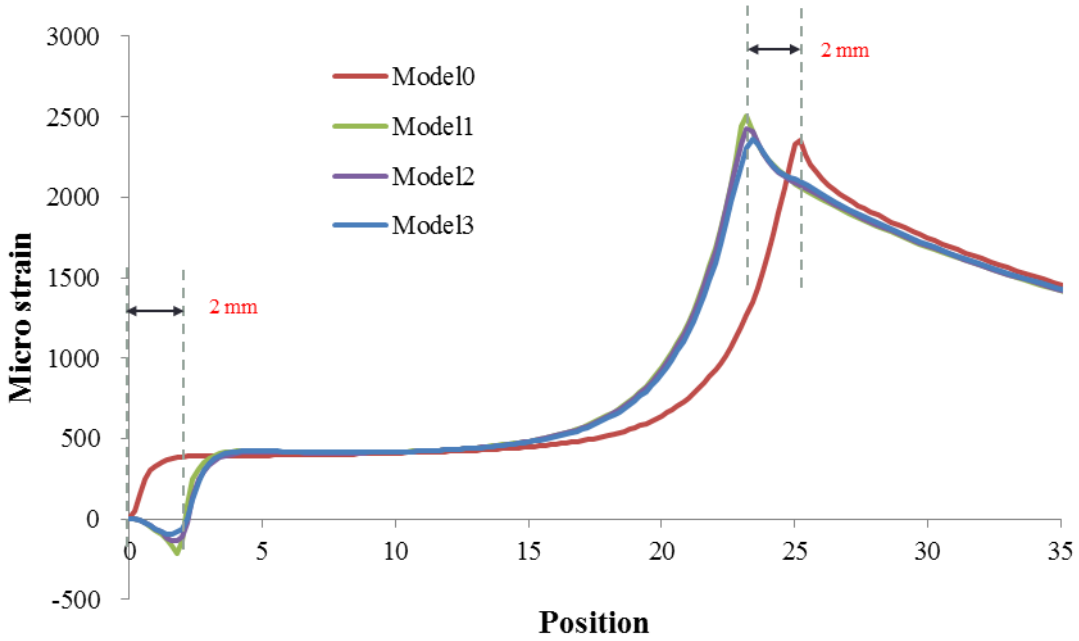

Fig. 5-3. Strain distribution results of FEA

From the analysis, in model 0 with no crack, the strain rose from 0 to a small peak at overlap beginning (z=0.0), and the maximum strain appeared at overlap end (z=25.0). In the models with cracks, a trough and the 0 strain appeared around the crack front location at z=2.0, and the maximum strain appeared at crack front location at z=23.0, this phenomena was considered to be caused of the shortened effective overlap length by cracks. Among the strain distributions of model 1, model 2 and model 3, similar pattern about crack front position was observed, and the only difference for the three cases is the strain value.

As an assumption, the positions of 0 strain and maximum strain in measured longitudinal strain distribution in overlap area may be used as indicators to estimate the crack front location and calculate crack length. And this method may be effective even the cracks occurred in adhesive layer or at the interface of adhesive and adherend without embedded FBG.

5.1.2. Detection of cracks occurred in cyclic load test

As mentioned, the strain distribution at maximum load in each load cycle was used to estimate the crack length, because the position of maximum strain is significant to be identified at maximum load. And because 0 strain could not be observed due to the filet, the trough of strain distribution at filet end was used as the equivalent indicator for crack 1.

By using the proposed method in last section, the cracks in cyclic test were estimated based on longitudinal strain distribution measured by embedded FBG. The crack length of crack 1 obtained by estimation and microscope measurement are compared in Fig. 5-4. The estimation showed good response to the crack propagation at the interval of 0.6 mm, which is the readout position resolution of sensing system, which indicated the accuracy of this method in this study.

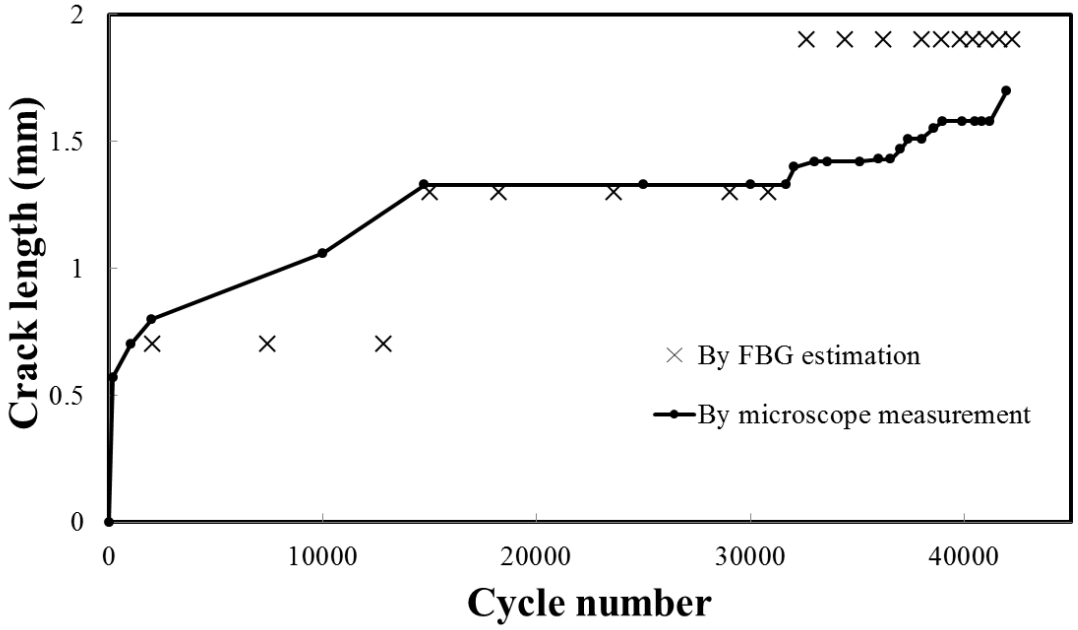

Fig. 5-4. Crack length measured by microscope and estimated based on strain distribution for crack 1

The comparison of crack 2 was shown in Fig. 5-5. The estimation suggested a 0.6 mm crack in cycles

of 18000 to 29000 which was failed to be captured by the microscope, the estimated crack length was longer than measurement at the beginning of step 2 and became shorter than measurement after cycle 32600 until test end.

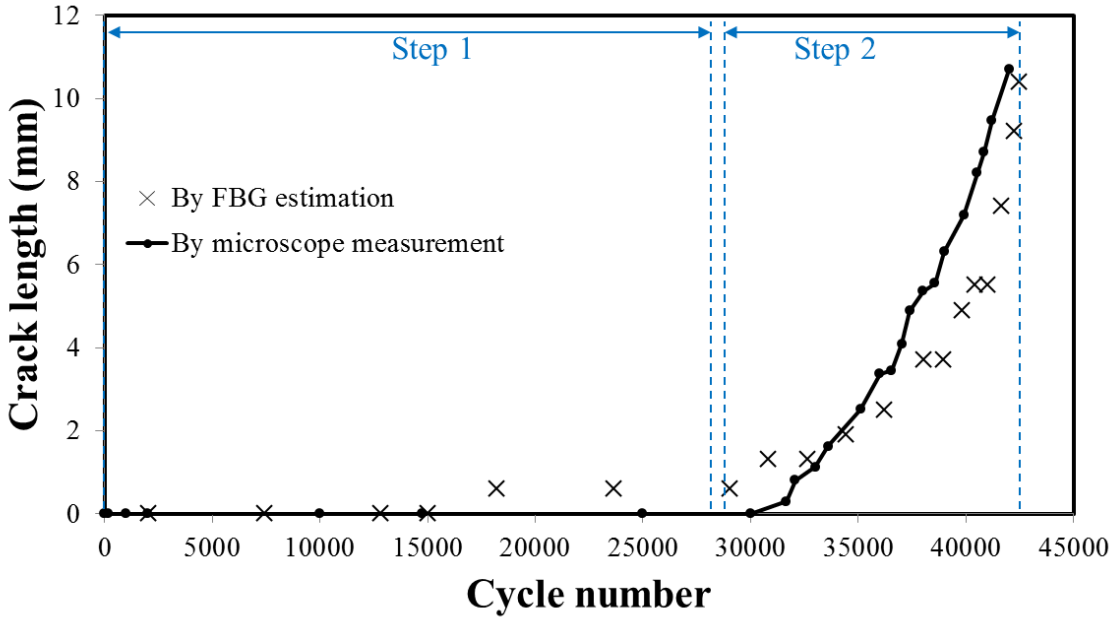

Fig. 5-5. Crack length measured by microscope and estimated based on strain distribution for crack 2

The reason for the difference was considered to be the non-uniform propagation speed of the crack front. At first, the crack initiated at the center in width direction (x) of overlap but did not propagate to the edges during cycle 18000 to 29000, then the center of crack front propagated faster than the edge at the beginning of step 2 and became slower from cycle 32600 until the test end. The maximum length of crack 2 by estimation was 10.4 mm, and it was confirmed by the observation of failure surface.

5.1.3. Discussions

The detection method of cracks occurred in adhesive layer or at adhesive/adherend interface of adhesive-bonded single-lap joint was developed based on analyzing longitudinal strain distribution. The method has been confirmed to be effective by estimations of cracks occurred in cyclic load test. By applying this method, the real-time crack detection may be achieved by dynamic distributed OFS sensing system introduced in this study with high accuracy.

5.2. Investigation on reflected FBG spectra around crack front location

In previous sections, the change of spectrogram and strain distribution measured by embedded FBG with crack propagation were examined and analyzed. By further investigation, we noticed that, the reflected FBG spectra at locations on crack propagation path also varied during crack propagation, and

the spectra at locations around different crack front were in some kind of pattern. If the pattern could be identified, the crack may be detected by observing the FBG spectrum. And this method will be more efficient because neither wavelength nor strain distribution needs to be calculated, so the error in calculation can be avoided.

For discussions in this section, at first the irregular FBG spectra at a typical sampling timing will be shown to address the problem. Then the attempt to find out the reason for irregular spectra by investigating birefringence effect induced by concentrated peel stress. Finally the strain growth rate around crack front was investigated and related to the width of irregular spectra, and the relationship was used to estimate the location of crack front.

5.2.1. Irregular spectra around crack front

As introduced in chapter 3, usually the reflected spectrum from grating on FBG detected by our sensing system should be regular with a single peak which indicates the Bragg wavelength. During data analysis, we notice that the FBG spectra become irregular around the crack front, which is estimated by using strain distribution method, which means it is the end of overlap and longitudinal and peel strain/stress concentrates at that location. Actually the same phenomena were also observed in static load test, in that case the irregular showed at overlap end.

Since the shape of spectra is difficult to describe, as an example, the spectra around crack front of crack 2 (z=23.8), at the maximum load in cycle of 30384 (04:45:00) in cyclic test are shown in Fig. 5-6, the figures are arranged by normalized position. The positions where the spectra are extracted for example are explained in Fig. 5-7. The spectra are taken from z=14.7 to z=25.1, the distance between spectra is the position resolution, 0.6 mm. The horizontal axis in each spectrum indicates wavelength and vertical axis indicates normalized amplitude using the maximum value as 1, because in this section we only investigate the shape of spectra. In this section the spectra are taken at maximum load for discussion.

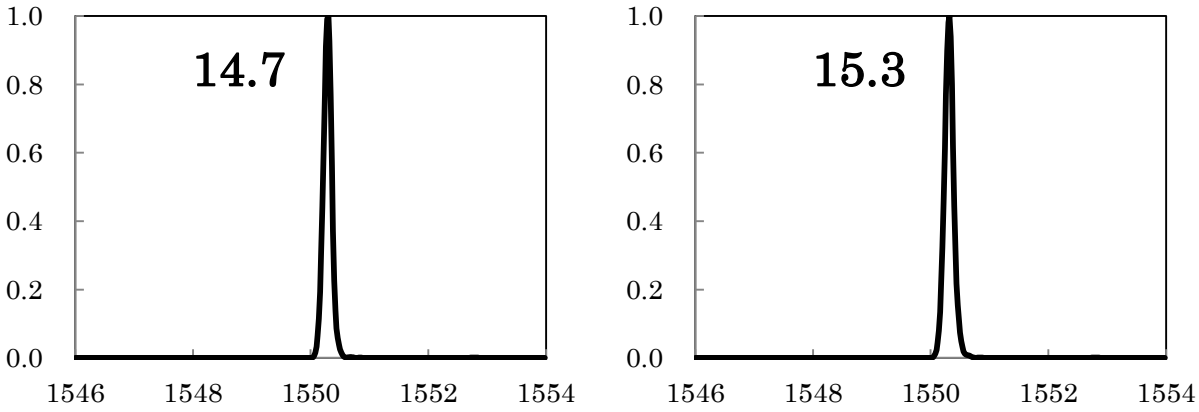

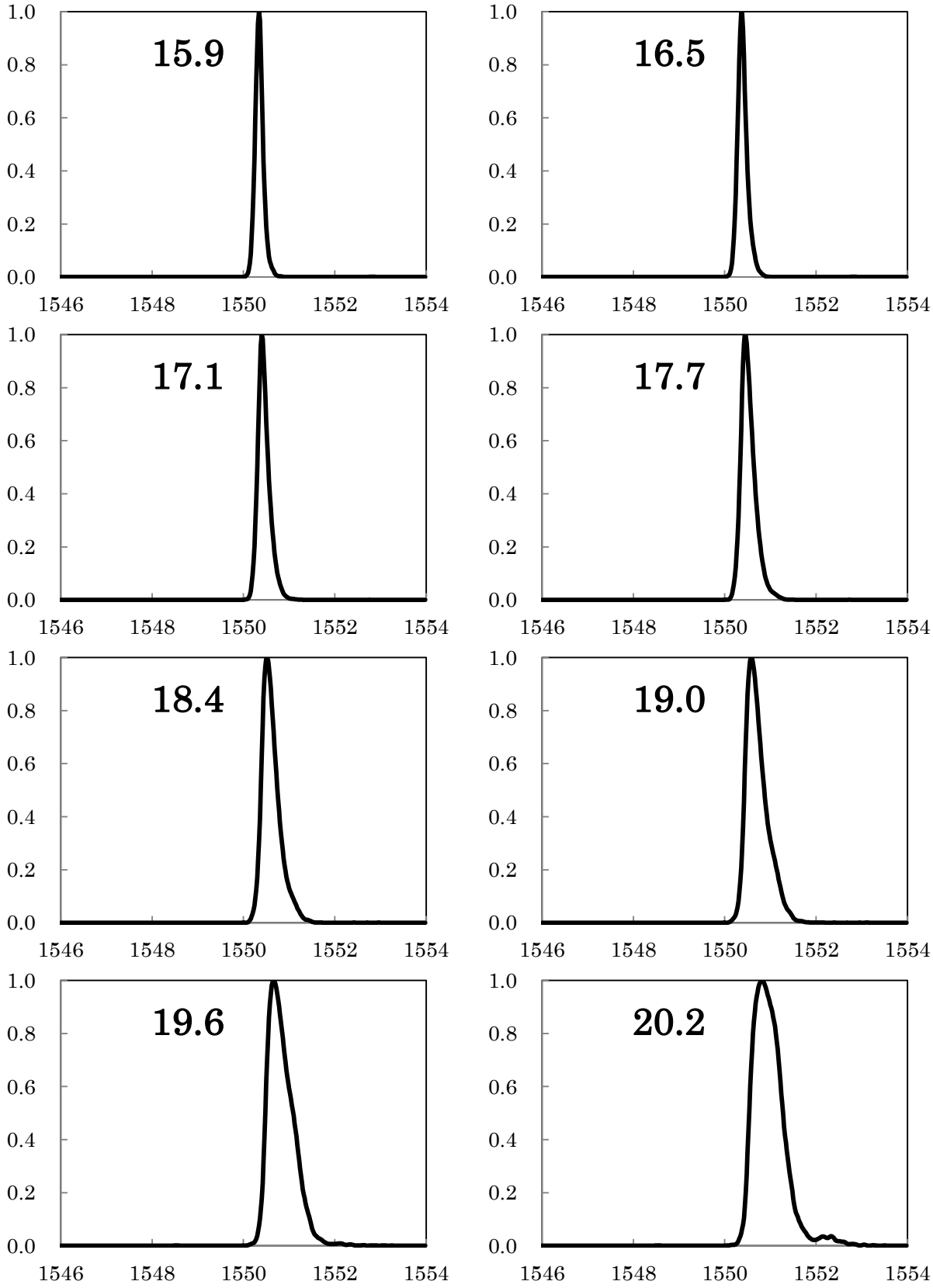
15.9
16.5
17.1
17.7
18.4
19.0
19.6
20.2
1.0
0.8
0.6
0.4
0.2
0.0
1546
1548
1550
1552
1554

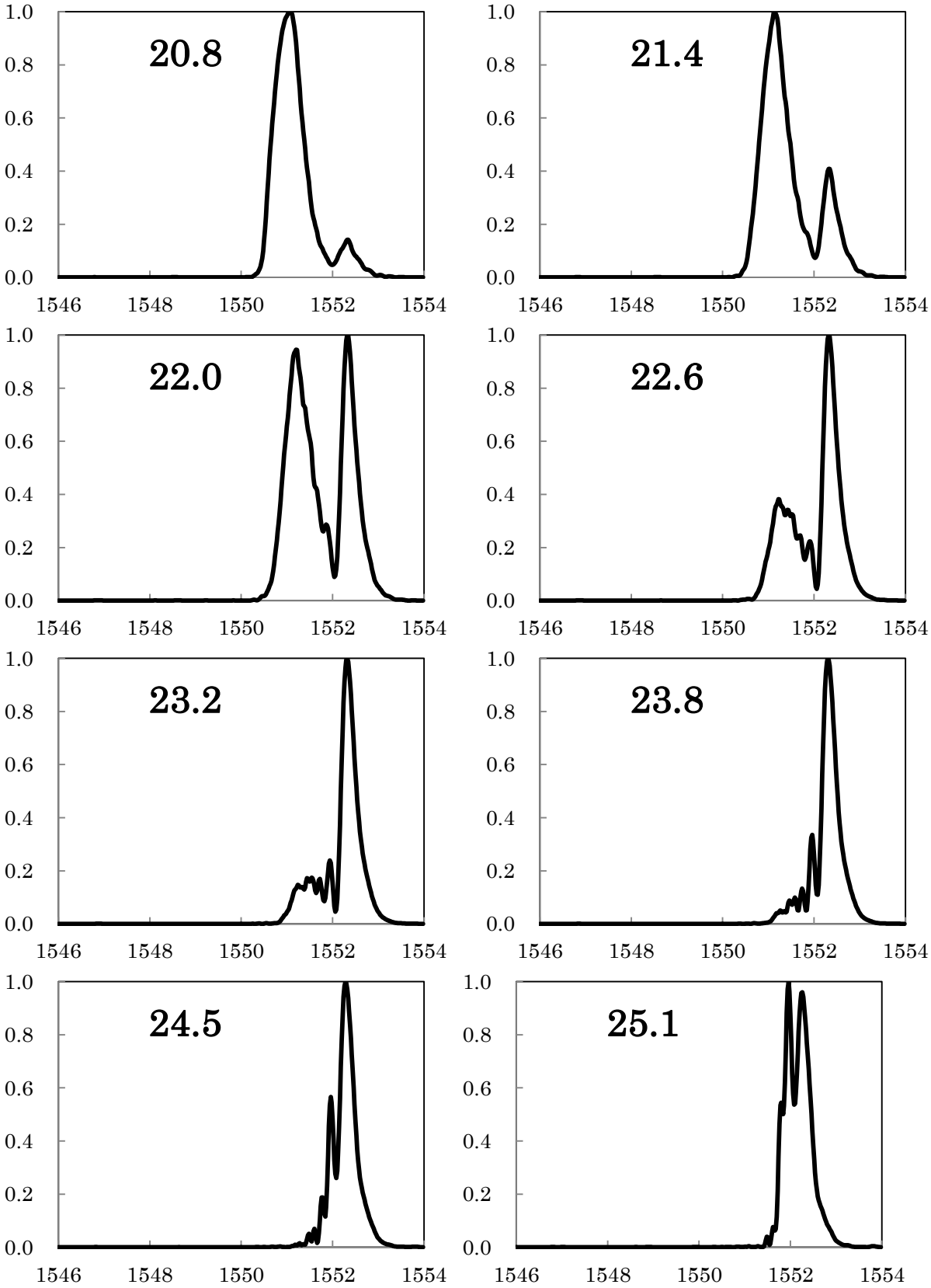

Fig. 5-6. FBG spectra around crack 2 (*z*=23.8) at maximum load in cycle of 30384

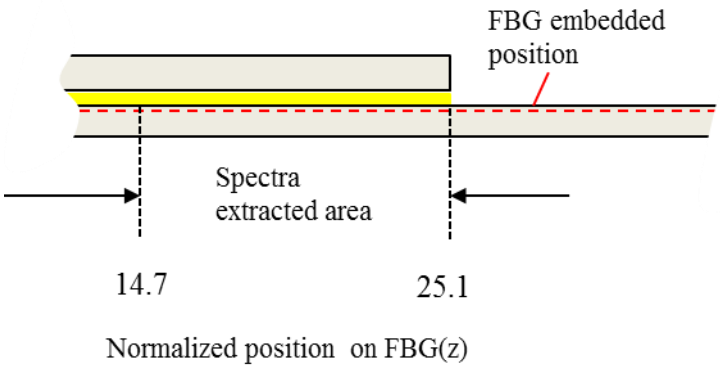

Fig. 5-7. Spectra extracted area

From the spectra figures, it can be observed that, from z=14.7 to z=19.6 the spectra are regular with a single peak, although the spectra at z=18.4, z=19 and z=19.6 became wider, the center wavelength can be obtained easily. From z=20.2 to z=25.1, the single peak spectrum split into two peaks or multiple peaks, the maximum width of spectrum showed at z=22 where spectrum split to two peaks with almost same amplitude.

5.2.2. Spectra split caused by birefringence effect

The reasons for spectra split around crack front are considered as in two aspects, the birefringence effect induced by peel stress concentration, and the sharply varied longitudinal strain field around crack front. In this section the spectra split caused by birefringence effect is investigated.

The birefringence effects on FBG have been analyzed by R. Gafsi and M. A. El-Sherif[1] when the grating zone is subjected to a static transverse load. The wavelength split in reflection spectrum is caused by the Bragg reflection wavelength variations for x-polarization and y-polarization due to the optical and mechanical property changes of FBG. As a result, the equations to calculate the reflection wavelength variation are given,

for x-polarization

$$(\Delta\lambda_B)_x = -\frac{(n_{eff})^3\Lambda_B}{E}\times\{(p_{11}-2\nu p_{12})\sigma_x+[(1-\nu)p_{12}-\nu p_{11}]\times(\sigma_y+\sigma_z)\} + 2\frac{n_{eff}\Lambda_B}{E}\times[\sigma_z-\nu(\sigma_x+\sigma_y)] \quad \text{Eq. 5-1}$$

and for y-polarization

$$(\Delta\lambda_B)_y = -\frac{(n_{eff})^3\Lambda_B}{E}\times\{(p_{11}-2\nu p_{12})\sigma_y+[(1-\nu)p_{12}-\nu p_{11}]\times(\sigma_x+\sigma_z)\} + 2\frac{n_{eff}\Lambda_B}{E}\times[\sigma_z-\nu(\sigma_x+\sigma_y)] \quad \text{Eq. 5-2}$$

where n_{eff}, Λ_B, p_{11} and p_{12} are effective refractive index of the core, periodicity of the grating, photoelastic coefficients of the FBG respectively, E and υ are Young's modulus and Poisson's ratio of fiber core respectively, σ_x, σ_y and σ_z are stress components on FBG in three principal directions.

In our case, in order to calculate the wavelength difference between two peaks in FBG reflection spectrum induced by concentrated peel stress around crack front, FEA was carried out to calculate stress field along the embedded FBG considering the joint geometry (crack at z=23.8) and loading (400 kgf) in cycle of 30384.

The stress field result in fiber core is shown in Fig. 5-8, it is clear that the stress on three directions concentrated around the crack front of crack 2. The stress field at z=23.8 was used for calculation and the result was compared with wavelength difference between two peaks measured in spectrum. The parameters for calculation are shown in

Table 5-2, the comparison is shown in

Table 5-3.

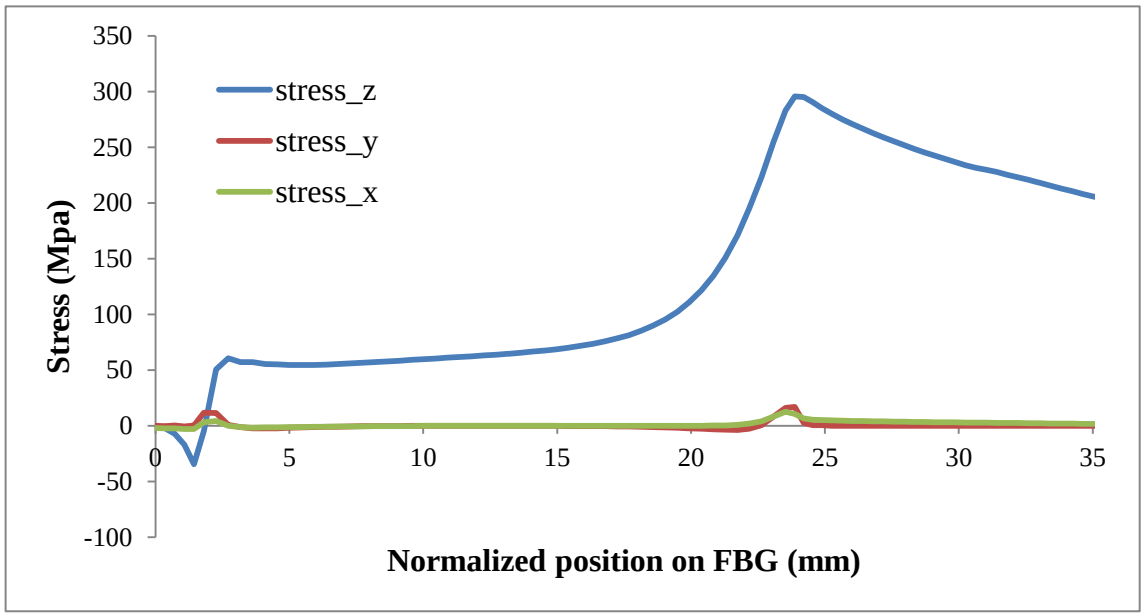

Fig. 5-8. Stress field on embedded FBG in cycle of 30384

Table 5-2. Parameters for birefringence effect calculation

	E	ν	Λ_B	n_{eff}	p_{11}	p_{12}	σ_x	σ_y	σ_z
z=23.8	7.31E+04	0.16	5.31E-04	1.46	0.113	0.252	10.6951	17.0166	295.4580

Table 5-3. Wavelength difference between two peaks measured in spectrum and calculated considering birefringence effect

	Wavelength difference (nm)	
	By measurement	By calculation
z=23.8	0.34	0.02

From the result, the spectrum split caused by birefringence effect induced by stress concentration around crack front only contributed about 6 percent of the wavelength difference between two peaks observed in split spectrum at z=23.8. This means the birefringence effect is not the main reason for irregular spectra.

In addition, the irregular spectra around overlap end observed in static load test were also investigated by the similar process, the detail results can be found in[2].

5.2.3. Irregular FBG spectra around crack front location

The other reason is the sharply varied strain around crack front disturb the FBG measurement and caused irregular spectra, which have also been observed in Y. Okabe's study[3] caused by the non-uniform strain distribution. Considering that the strain sharply varied area moved with the crack propagation, more measurements at different sampling time including the example were extracted for further discussion, the information of measurements is shown in Table 5-4.

Table 5-4. Information of cases for discussion

	Measurement time	Cycle number	Crack front position
case 1	214500	17784	24.5
case 2	44500	30384	23.8
case 3	61400	33054	23.2
case 4	74500	35784	22.6
case 5	83500	37284	22.0
case 6	85500	37884	21.4
case 7	94000	39234	20.8
case 8	100000	39834	20.2
case 9	102000	40434	19.6
case 10	104200	41094	19.0
case 11	105300	41424	18.4
case 12	105600	41514	17.7
case 13	110300	41724	17.1
case 14	110600	41814	16.5

At first, the spectra of case 2 (example case in last section), case 6 and case 10 were extracted for preliminary investigation. The spectra of case 6 and case 10 from z=14.7 to z=25.1 are shown in Fig. 5-9 and Fig. 5-10. From three sets of spectra, we noticed that the most significant shape variation in spectrum appeared at z=22, z=19.6 and z=17.1 for case 2, 6 and 10, respectively. And from longitudinal strain distribution measurement we know that these positions are at the middle of strain increasing zone where the strain increased at the highest speed for each cases, and the distance between these positions and crack front location are 1.8 mm, 1.8 mm and 1.9 mm for case 2, 6 and 10, respectively. Therefore, there is an assumption that, the shape variation of FBG spectrum is related with longitudinal strain variation rate, which means the spectrum shape varies more significantly at the location where the strain varies faster.

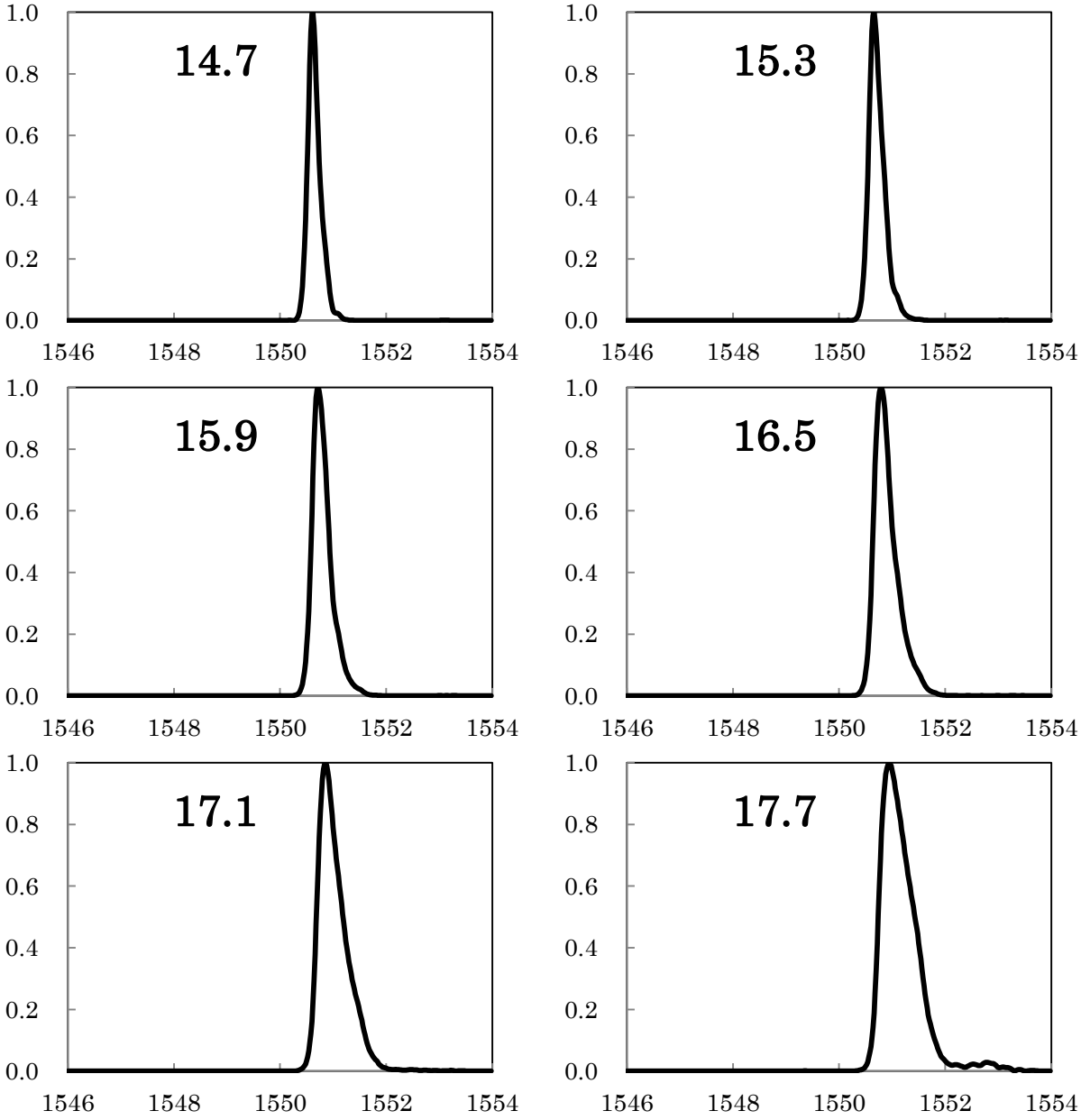

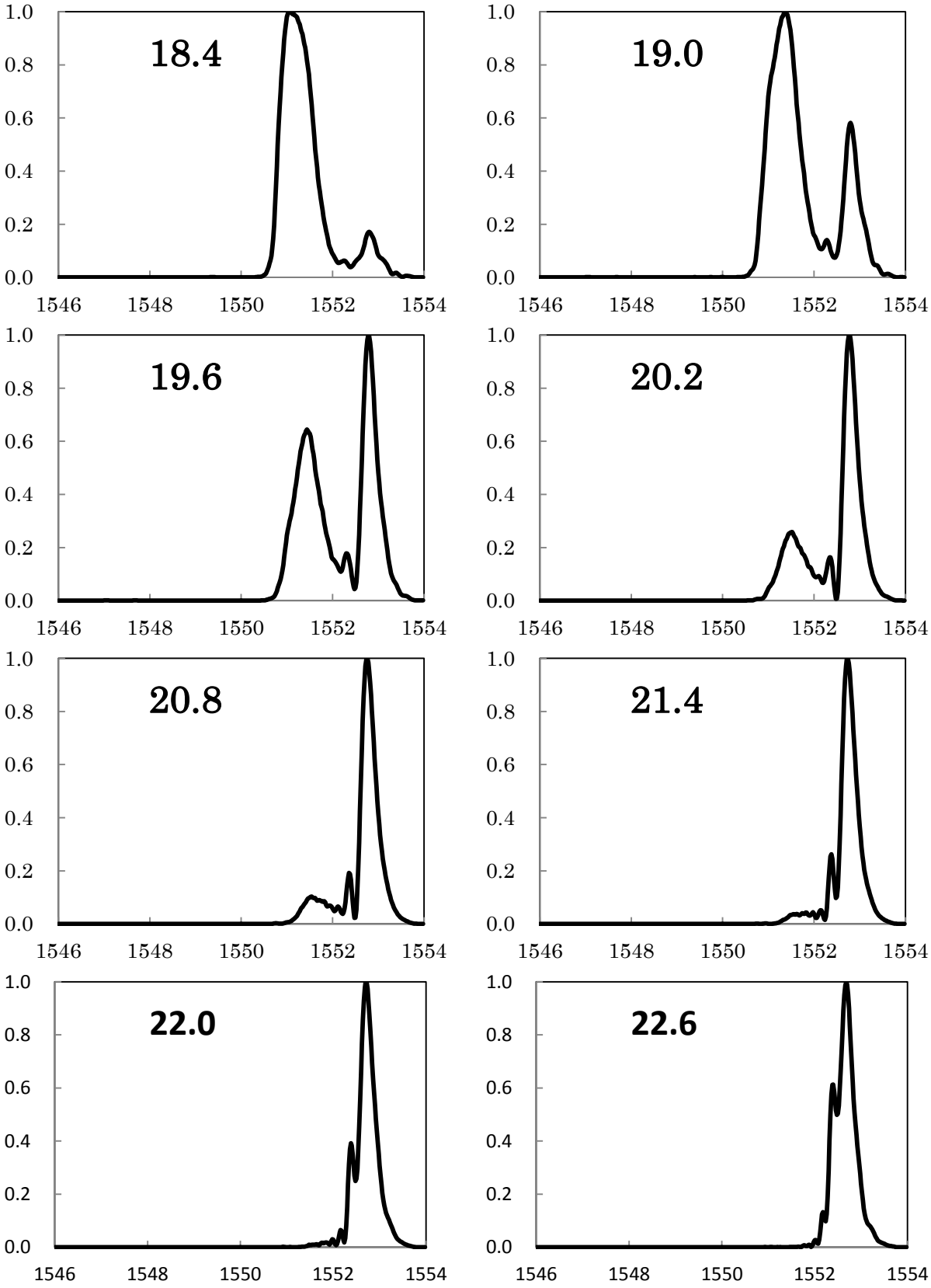
18.4
19.0
19.6
20.2
20.8
21.4
22.0
22.6
1.0
0.8
0.6
0.4
0.2
0.0
1546
1548
1550
1552
1554

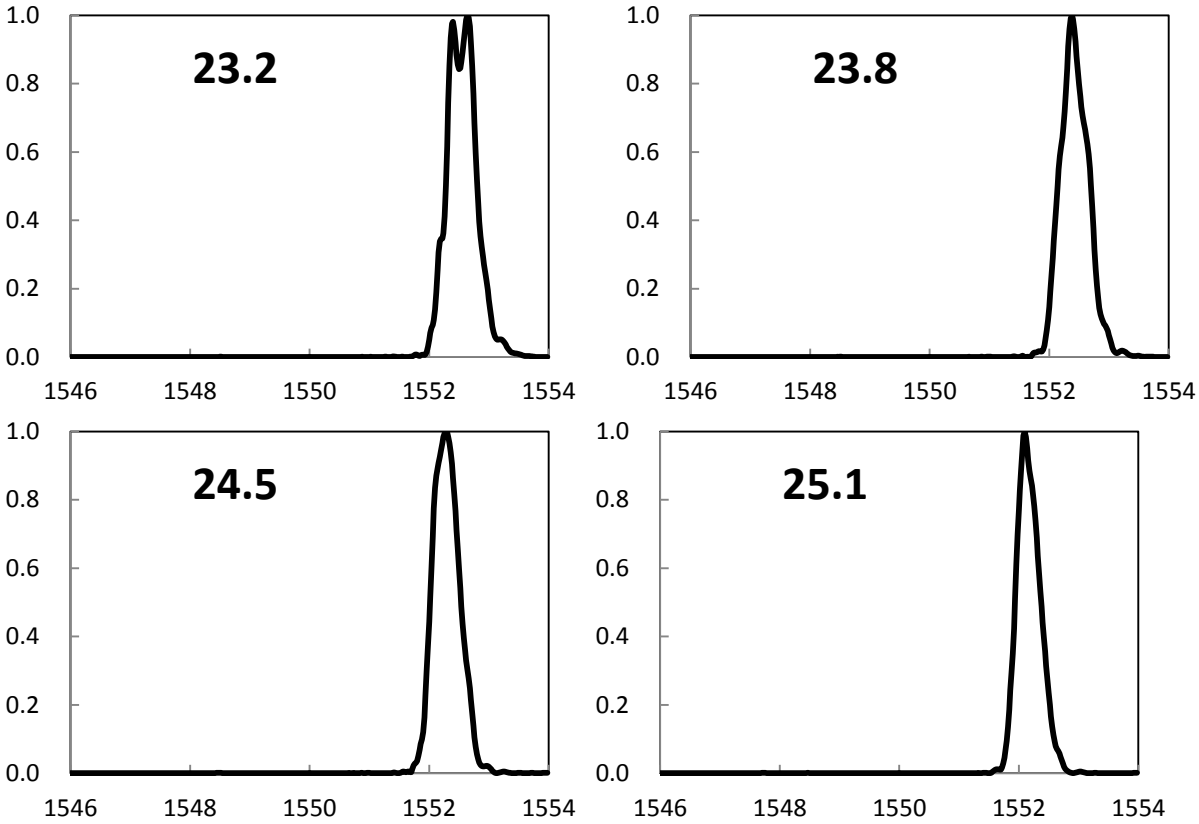

Fig. 5-9. Spectra of case 6

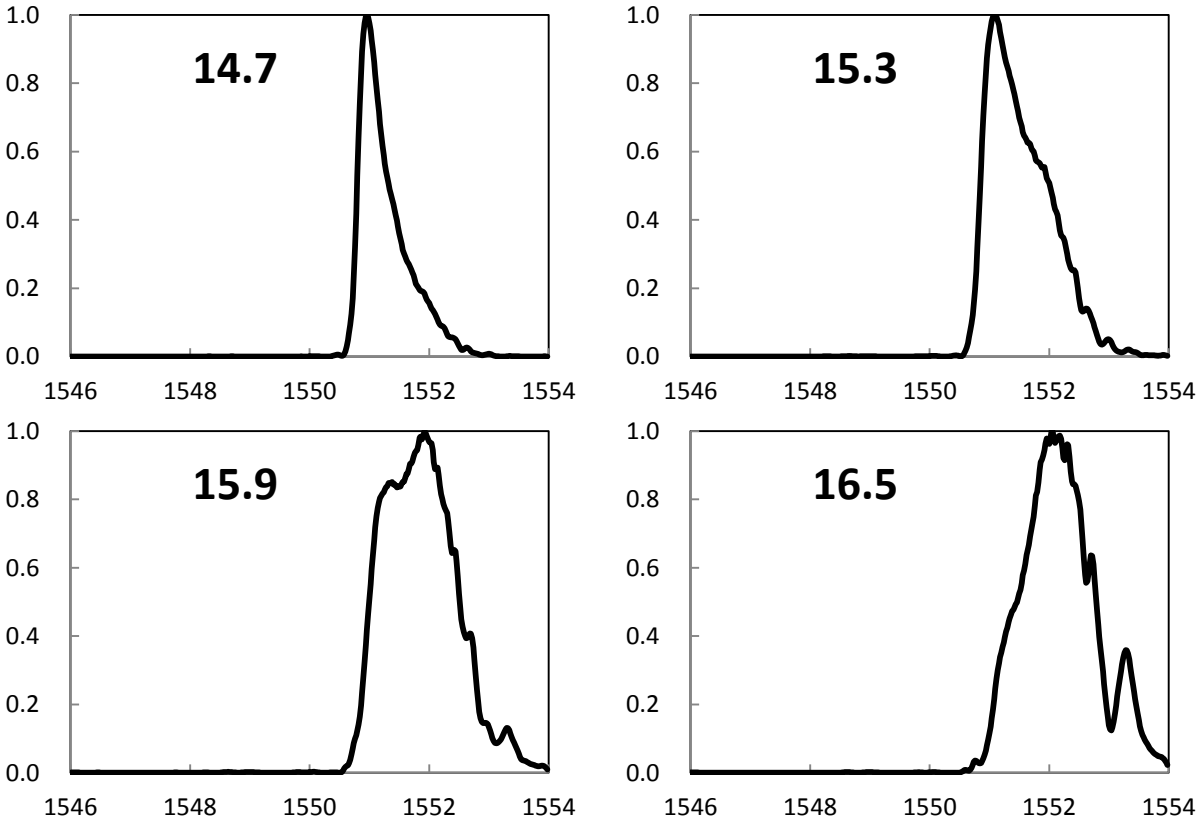

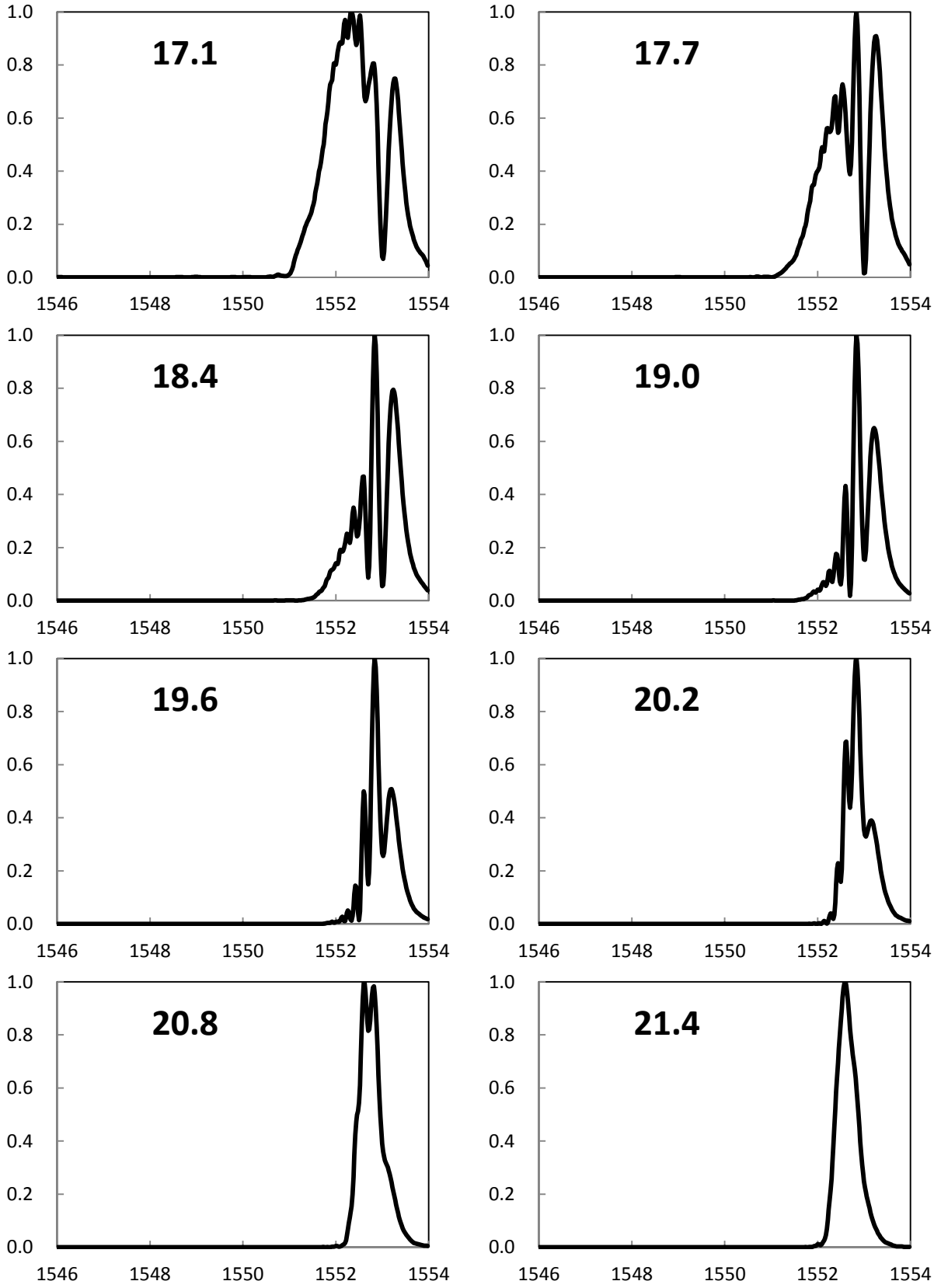
17.1
17.7
18.4
19.0
19.6
20.2
20.8
21.4
1.0
0.8
0.6
0.4
0.2
0.0
1546
1548
1550
1552
1554

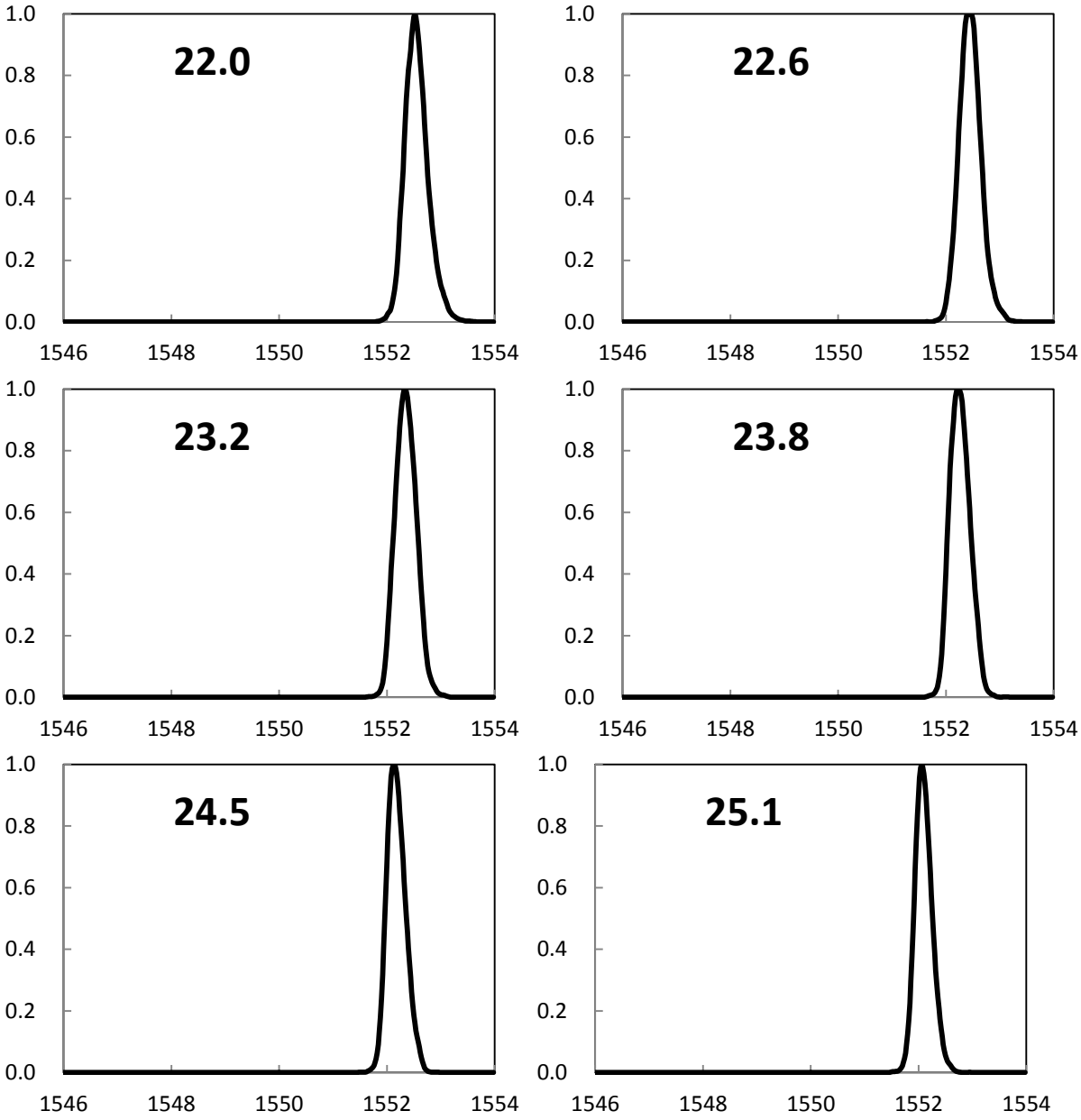

Fig. 5-10. Spectra of case 10

In order to confirm this assumption, the longitudinal strain distributions measured by embedded FBG at location from *z*=14.7 to *z*=25.1 in case 2, 6 and 10 are shown in Fig. 5-11. Based on the strain distribution, the strain growth rate of measurement point at each position was calculated using the equation:

$$R_1 = \frac{d\varepsilon}{dP} = \frac{\varepsilon_1 - \varepsilon_0}{P_1 - P_0} \qquad \text{Eq. 5-3}$$

where p_1 and p_0 are the position of present point and the position of one point before the present point respectively, ε_1 and ε_0 are the longitudinal strain measured at two positions. The calculated strain growth rates at location from *z*=14.7 to *z*=25.1 in three cases are shown in Fig. 5-12, it can be observed that, the strain growth rate increases in the first half of strain increasing zone and decreases

in the second half for each case.

In order to build a relation between the strain growth rate and FBG spectrum at each position, an indicator to describe the degree of spectra variation needs to be defined. In this study, the spectrum width defined as the full width at half maximum (FWHM) was used as the indicator. The spectrum width of each spectrum at location from z=14.7 to z=25.1 in three cases was measured and plotted with respect to position in Fig. 5-13.

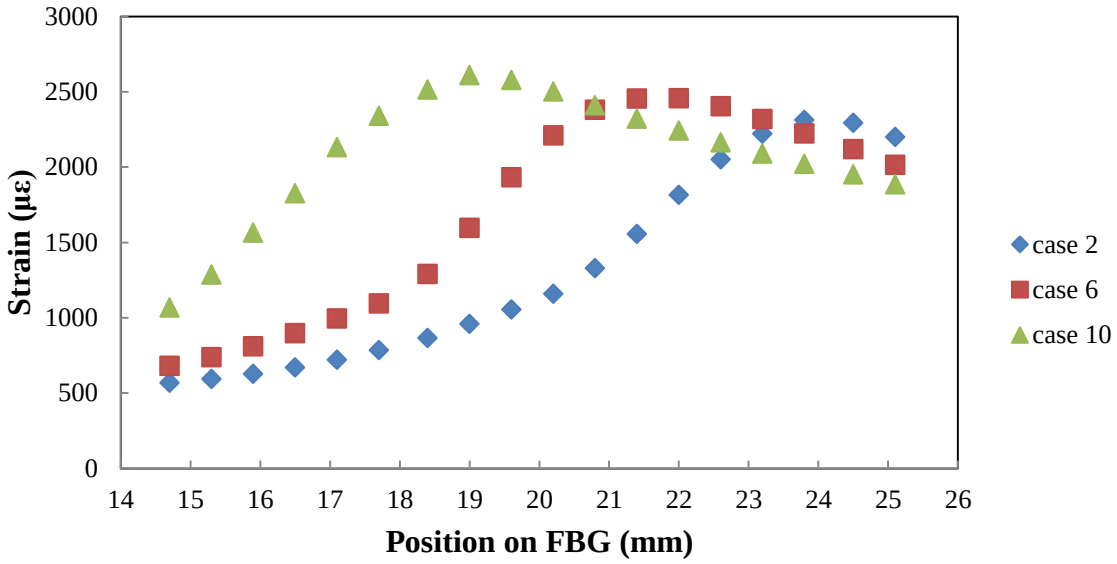

Fig. 5-11. Longitudinal strain distribution from z=14.7 to z=25.1 in case 2, 6 and 10

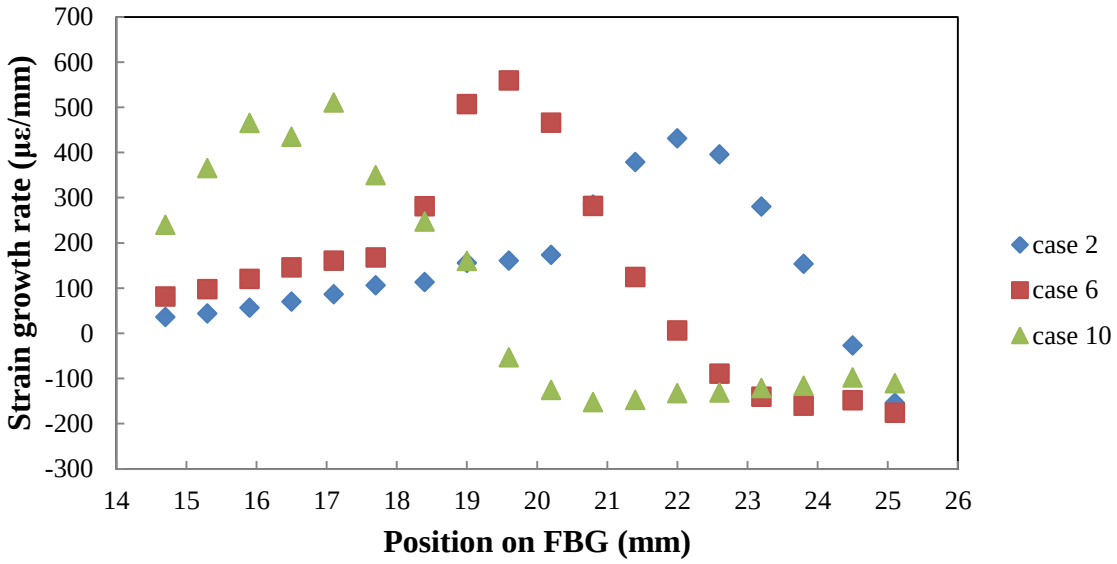

Fig. 5-12. Strain growth rate from z=14.7 to z=25.1 in case 2, 6 and 10

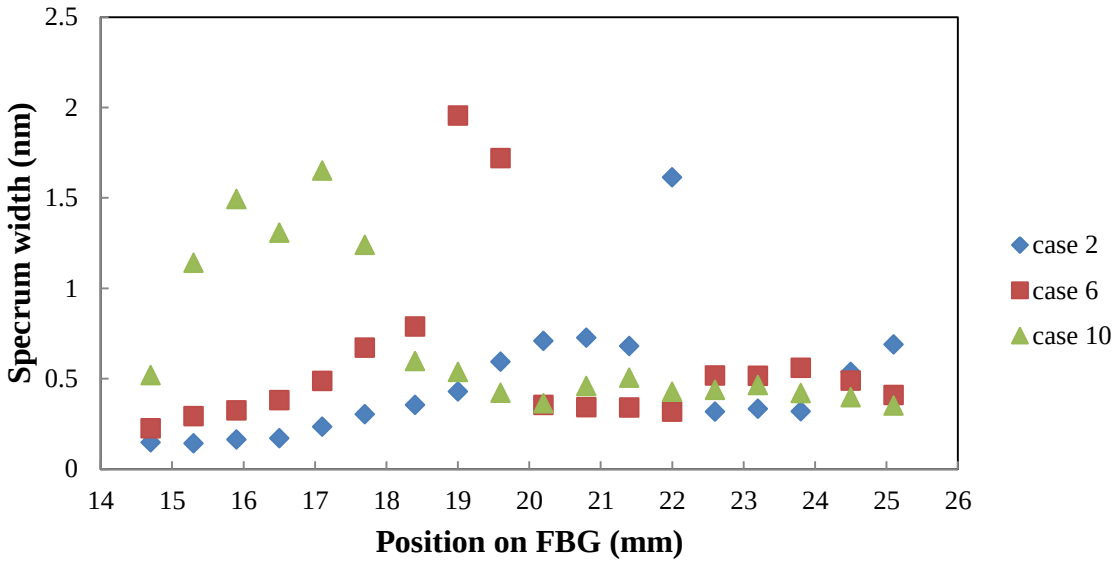

Fig. 5-13. Spectrum width from *z*=14.7 to *z*=25.1 in case 2, 6 and 10

From figure of strain growth rate and spectrum width, we noticed that the significant spectra variation appeared in area where the strain grew fast, which confirmed our assumption. This means by measuring the variation degree of FBG spectra, the spectrum width for example, the position in the joint where strain grows fastest can be identified in this study. For the three cases, the crack position, maximum strain growth rate position, maximum spectrum width position and the distance between crack position and maximum strain growth rate position are shown in Table 5-5. As shown in the table, the distance between the strain fastest varies position and crack front position is constant in each case, which means the FBG spectra variation degree may be used to identify the crack front position.

Table 5-5. Results in three cases

	Crack position	Maximum strain growth rate position	Maximum spectrum width position	Distance (mm)
case 2	23.8	22.0	22.0	1.8
case 6	21.4	19.6	19.0	1.8
case 10	19.0	17.1	17.1	1.9

In order to test this assumption, the crack length of crack 2 in each case shown in Table 5-4 was calculated by identifying the position of maximum spectrum width, the crack front location was defined as 1.8 mm behind that position, the results are shown in Table 5-6. The results were compared with the crack length estimated using strain distribution method introduced in last section in Fig. 5-14. From the table and figure, in ten cases the two methods have the same result of crack length estimation, however, difference shows in case 5, 6, 7, 12.

Table 5-6. Crack length estimated by the maximum spectrum width position

	time	cycle	Crack length (mm) Estimated by strain distribution	Estimated by FBG spectrum
case 1	214500	17784	0.6	0.7
case 2	44500	30384	1.3	1.3
case 3	61400	33054	1.9	1.9
case 4	74500	35784	2.5	2.5
case 5	83500	37284	3.1	3.7
case 6	85500	37884	3.7	4.3
case 7	94000	39234	4.3	5.6
case 8	100000	39834	4.9	4.9
case 9	102000	40434	5.5	5.6
case 10	104200	41094	6.1	6.2
case 11	105300	41424	6.7	6.8
case 12	105600	41514	7.4	8.0
case 13	110300	41724	8.0	8.0
case 14	110600	41814	8.6	8.6

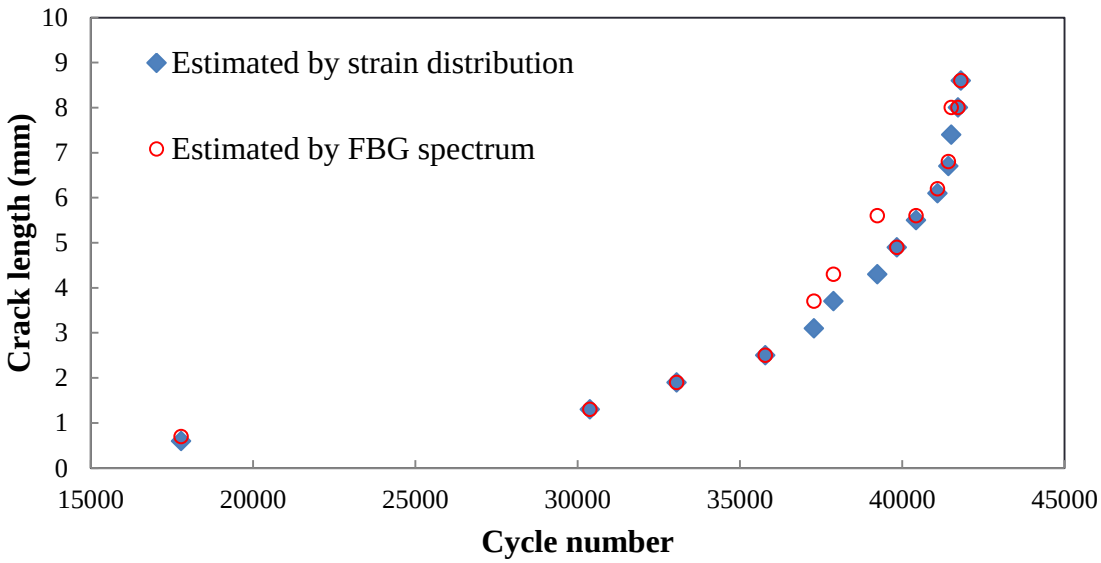

Fig. 5-14. Crack length estimated based on strain distribution and FBG spectrum

The biggest difference shows in case 7, which is 1.3 mm. The maximum spectrum width of case 7 is at z=17.7, which should be z=19.0 according to strain distribution method. For further investigation, spectra in case 7 at z=17.1 to z=19.6 are shown in Fig. 5-15. It can be observed that, at z=17.7, the spectrum is a single peak with perturbation around 1553 nm. And at z=19.0, the spectrum split significantly into two peaks, the amplitude of the peak on the right in the spectrum didn't reach 50 percent of the maximum value of the spectra which is in the peak on the left. Therefore the peak on the right was not taken into account when calculating spectrum width using FWHM, and this should be the reason that the spectrum width at z=19.0 was smaller than z=17.7. The estimation difference in other three cases are confirmed to be caused by the same reason.

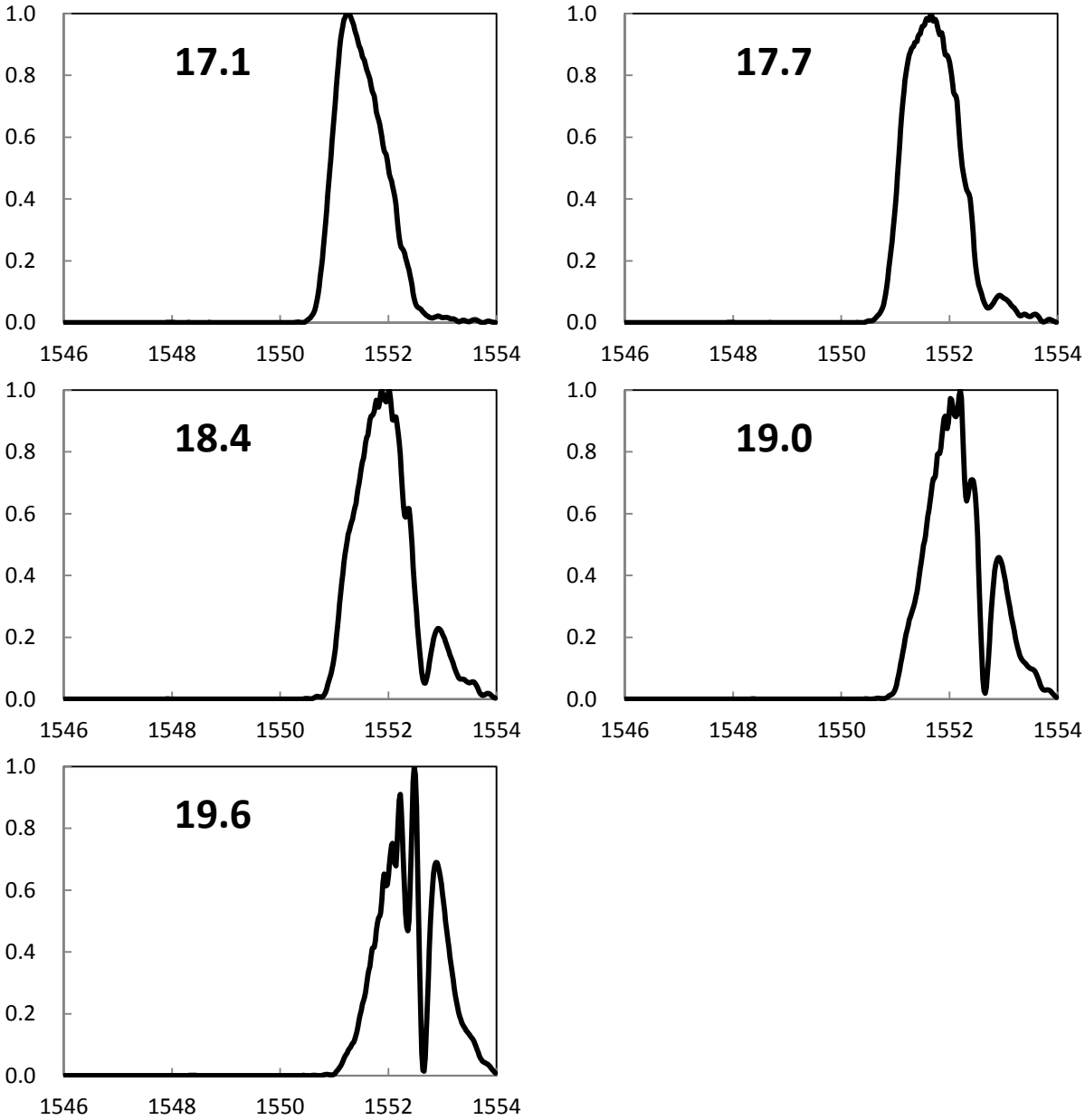

Fig. 5-15. Spectra in case 7 at *z*=17.1 to *z*=19.6

If we take the full width at 40% of maximum value to determine the spectrum width, the spectrum width at *z*=19.0 will be 1.58 nm, which is bigger than at *z*=17.7 (1.36 nm) and is the maximum in area from *z*=14.7 to *z*=25.1. This means that, by changing the method of defining spectrum width, the crack length estimation can be adjusted. We also noticed that, as shown in Fig. 5-15, the widths of spectrum at *z*=17.7 and *z*=19.0 are almost equal. If the spectrum width is the only indicator to describe spectrum variation degree, we may consider that these two spectra are similar, however in fact, spectrum at *z*=19 shows significant split, which means the variation of it is much severe than at *z*=17.7. Therefore, one indicator may be not enough to evaluate the spectrum variation degree, the number of split peaks in the spectra, for example, may be used as a second indicator, and we believe that this can improve the accuracy of the crack detection.

5.2.4. Discussions

Investigations were carried out on the reasons for the irregular FBG spectra around crack front location observed in cyclic load test. As the result, the birefringence effect induced by concentrated stress field was found to have small contributed to the spectrum variation, and the main reason was considered to be the sharp strain variation. After that, the spectrum width measured using FWHM was defined as indicator to describe the spectrum variation degree, and the spectrum width was related to the strain growth rate in strain increasing zone around crack front location. By using this relation, the crack lengths of crack 2 at ten sampling time were estimated, the estimation results were confirmed by the estimation using strain distribution method. The disagreements in two estimations of crack length were investigated. As the result, two points, the method of determining the spectrum width, and the second indicator of spectrum variation degree, need to be considered to improve the accuracy of crack estimation based on FBG spectra.

5.3. Further applications of OFS sensing system for adhesive-bonded joints

The dynamic distributed sensing system based on OFDR using embedded FBG has been used to measure strain distribution in adhesive layer of adhesive-bonded joint during static and cyclic load test. The measured information, strain distribution and FBG spectra, have been used to provide real-time detection of cracks propagated along adhesive/adherend interface. Besides these applications which have been proved feasible and effective, the potential of our system on further applications for adhesive-bonded joints was discussed and we made some proposals.

5.3.1. Adhesive-bonded joint manufacturing monitoring

As one of major concerns of adhesive-bonded joints, the variable initial strength depends on manufacturing induces uncertainties to engineers when using the joints. There are two approaches to reduce this concern, by controlling the joint strength through improvement of manufacturing techniques and by monitoring bonding parameters during bonding process to evaluate or improve initial joint strength. As the second approach, Klaus-Ulrich von Raben has given a method based on the continuous monitoring of bonding force and ultrasound amplitude during bonding processes with semi-automatic and fully automatic bonding machines[4]. Although hasn't been widely used for joint bonding monitoring, the OFS was employed for monitoring in composites curing process in many reports. In Murukeshan's study[5], the FBG act as a temperature transducer during composite curing and as an embedded sensor in 3- and 4-point bending tests. The similar applications can be found in[67]. These reports shows the potential of OFS on monitoring the composite curing process, and it may also be extended to monitor the joint curing.

In this study, the FBG was embedded into the composite prepregs and cured with them, thus by dynamic measurement throughout the adherend and joint curing processes, the curing quality may be evaluated. The measurements during specimen manufacturing is shown following by discussions.

Measurement in CFRP adherend curing process

The curing conditions of CFRP in this study is shown in Fig. 5-16, nines measurements during the process indicated by red dotted circle were extracted for analysis. The sampling timings of measurement are also shown in Table 5-7. A schematic diagram of curing set up is shown in Fig. 5-17, which has been introduced in chapter 4.

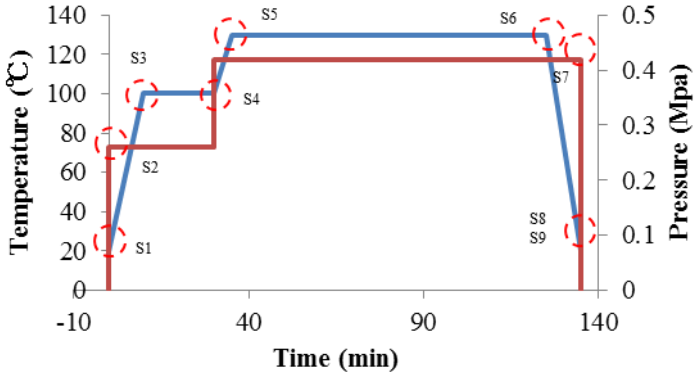

Fig. 5-16. Curing conditions of CFRP

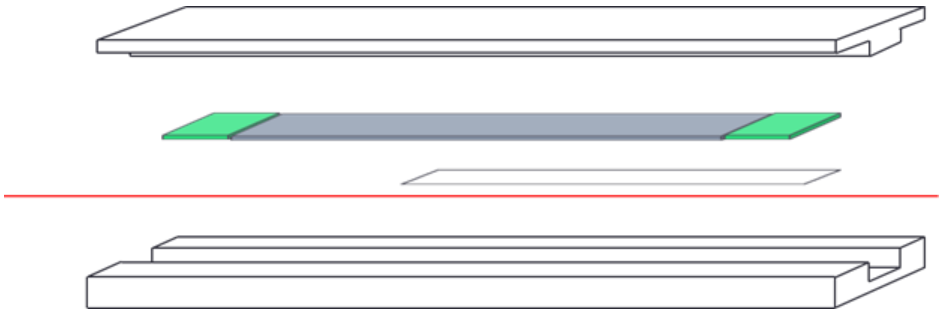

Fig. 5-17. Schematic diagram of curing set up

Table 5-7. Sampling timing during CFRP curing (RT: room temperature)

Sampling case	S1	S2	S3	S4	S5	S6	S7	S8	S9
Temperature(℃)	RT	RT	100	100	130	130	RT	RT	RT
Pressure (Mpa)	0	0.26	0.26	0.26	0.42	0.42	0.42	0	out of jig

The wavelength distribution measurements are shown in Fig. 5-18, the horizontal axis indicates the entire sensing region of FBG, the vertical axis indicates Bragg wavelength at each position. It can be observed that, the whole wavelength distribution increases due to heating and decreases since case S7 when CFRP was cooled to room temperature. The variation of distribution shape in region B can be observed in case S7, S8 and S9, the variation may indicate that the FBG has been embedded into CFRP in this area. And the shape variation can also be observed in case S5 and S6, in that period we assume that the CFRP started to cure. In this way, the FBG has shown potential in monitoring the curing condition of CFRP in FBG embedded area during curing process. However, factors which can influence the measurement need to be eliminated, the factors will be discussed later.

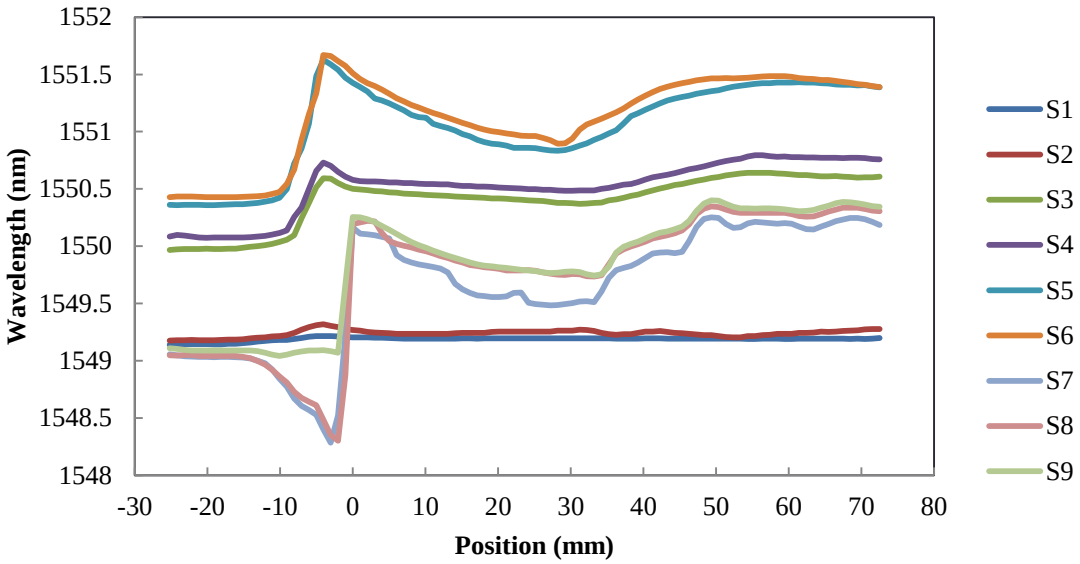

Fig. 5-18. Measurements by embedded FBG during CFRP curing

The residual strain in FBG embedded area of CFRP is evaluated by comparing the initial measurement (S1) and the measurement after curing (S9), the result is shown in Fig. 5-19. The FBG portion in region A is used for temperature compensation. From the figure, large tensile strain can be observed in region B. The reason for this is considered that, before CFRP curing, FBG was adhered to the bottom of curing jig which is made of steel, the jig expanded during the heating and the FBG was stretched consequently. When the CFRP started to cure, the FBG was still stretched, so the tensile strain caused by stretching was kept in the cured CFRP in FBG embedded area, and it is much bigger comparing with residual strain. Therefore, by using the procedure developed in this study, the residual strain of CFRP after curing cannot be evaluated. In order to do this, the whole curing process need to be considered carefully and factors such as the thermal expansion of curing jig which can affect measurement need to be eliminated.

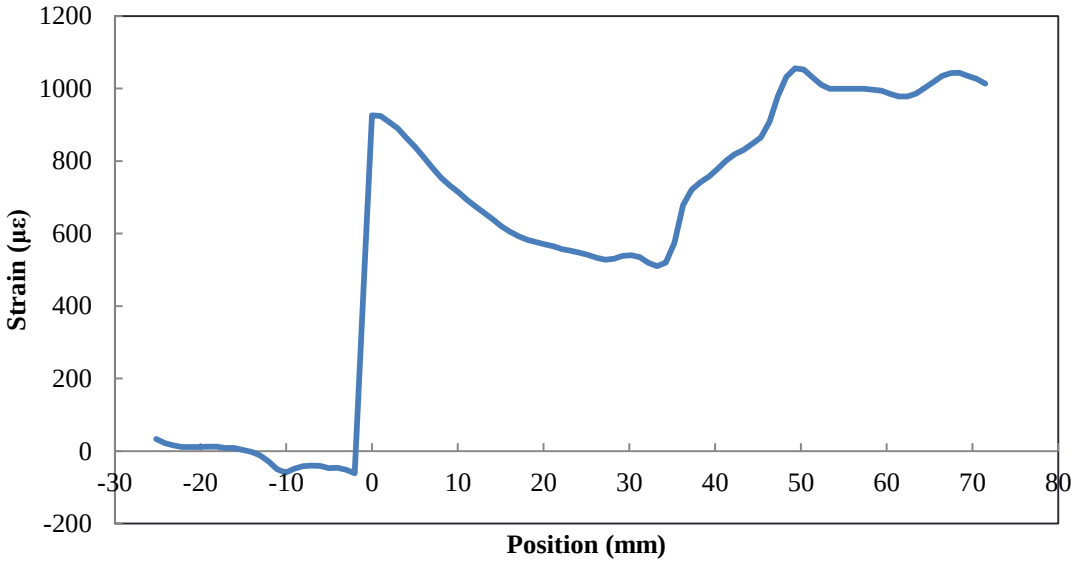

Fig. 5-19. Residual strain measured by embedded FBG after CFRP curing

Measurement in joint bonding process

Measurements were also carried out throughout joint bonding process using adherend with embedded FBG. The schematic diagram of joint bonding set up is shown in Fig. 5-20, the adherends are shown in light blue, FBG is shown in red and bonding jig is shown in white. The bonding conditions are shown in Fig. 5-21, the measurement timings are shown in Table 5-8.

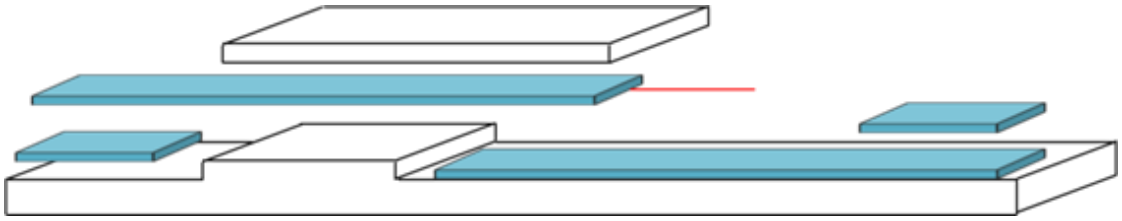

Fig. 5-20. Schematic diagram of joint bonding set up

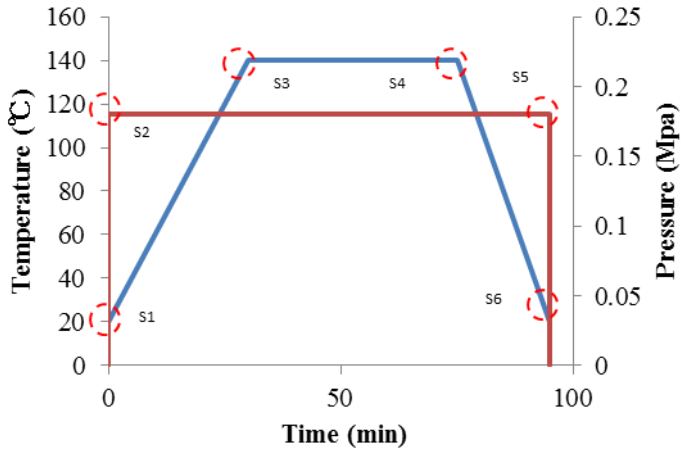

Fig. 5-21. Joint bonding conditions

Table 5-8. Sampling timing during joint bonding (RT: room temperature)

Sampling case	S1	S2	S3	S4	S5	S6
Temperature(℃)	RT	RT	140	140	RT	RT
Pressure (Mpa)	0	0.18	0.18	0.18	0.18	0

The wavelength distribution measurements are shown in Fig. 5-22, the horizontal axis indicates the entire sensing region of FBG, the vertical axis indicates Bragg wavelength at each position. It can be observed that, the whole wavelength distribution increases due to heating and decreases since case S5 when joint was cooled to room temperature. The distribution shape in bonding area varied in S4 and S5 when the joint started to cure, and the variation is kept in S6 when bonding finished. We also attempted to evaluate the residual strain in bonding area by comparing S1 and S6, the FBG portion in region A is used for temperature compensation. The result is shown in Fig. 5-23. The compressive strain around z=0 is considered to be caused by spew filet from adhesive layer and the measurement indicates strain concentration at overlap end (z=25). No further investigation was carried out.

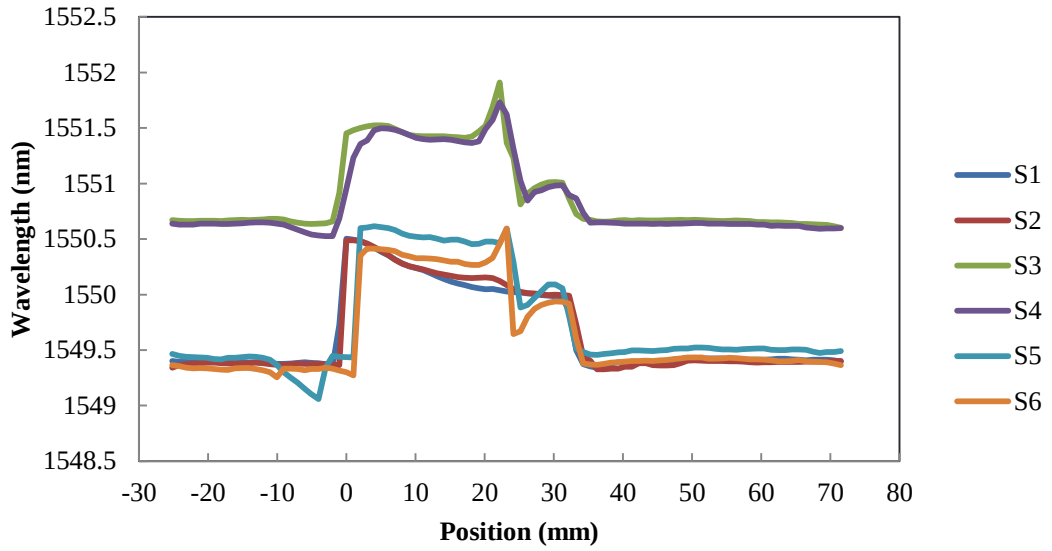

Fig. 5-22. Measurements by embedded FBG during joint bonding

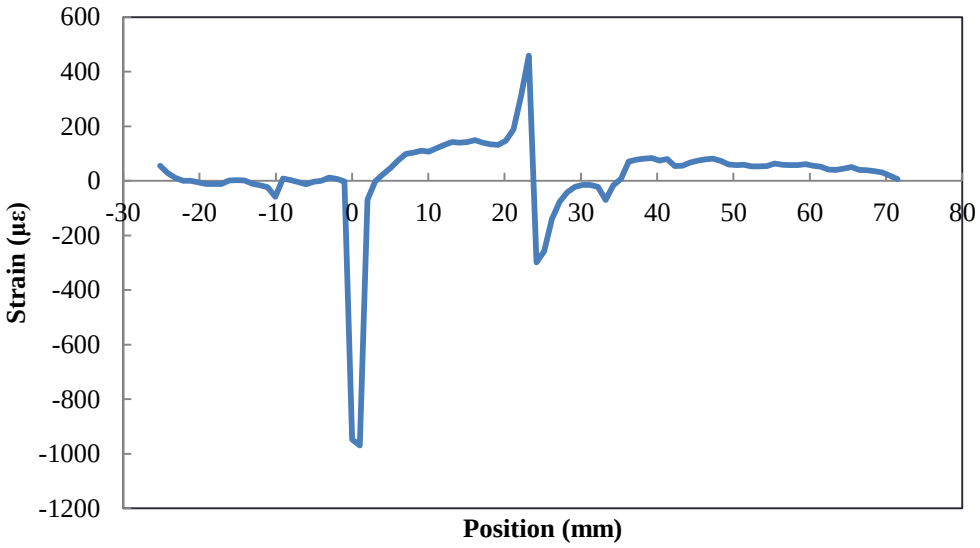

Fig. 5-23. Residual strain measured by embedded FBG after joint bonding

The curing monitoring of the composite and bonded joint is the attractive subject, and the embedded OFS has shown great potential for this. However, the embedment procedure developed in this study may not suitable for this purpose. For future study, the elimination work of factors which can affect OFS measurement during curing need to be considered, which may include curing jig modification, OFS position change and so forth.

5.3.2. Fracture condition assessment of adhesive-bonded joint

Adhesive joints usually fail by the initiation and propagation of flaws. Since the basic tenet of continuum fracture mechanics is that the strength of most real solids is governed by the presence of flaws, the application of such theories to adhesive joint failure has received attention. The main aims of the various theories are to analyze mathematically the loads at which the flaws propagate and describe the manner in which flaws grow. The source of naturally occurring flaws, sometimes referred to as intrinsic flaws, may be voids, cracks, dirt particles, additive particles, etc, which may be initially present at a critical size or develop during the fracture test.

In many ways the use of fracture mechanics to study the failure of joints is a complementary approach to that of mapping the nature and magnitude of the stresses. Both approaches have their advantages and limitations. Fracture mechanics has proved to be particularly useful for such aspects as characterizing the toughness of adhesives, identifying mechanisms of failure and estimating the service life of damaged structures, the damage is in form of cracks, air-filled voids, debonds, etc. which is caused from environmental attach, fatigue loading, subcritical impact loads. On the other hand, a detailed knowledge of the stress distribution in a bonded structure has proved to be of particular useful in initial design studies and for interpreting the effects of geometric parameters, such as effect of overlap length in lap joints.

The distributed OFS sensing system introduced in present study has been employed to obtain very detail information in adhesive layer and for real-time damage detection. For fracture mechanics of adhesive-bonded joints, the stress/strain information and geometric change when defects occurs has been involved in several approach methods to evaluate the fracture condition. The discussion in this section is for making a proposal on application of the dynamic distributed sensing system using embedded FBG for joint fracture condition evaluation.

In the studies of J. K. Jethwa, A. J. Kinloch and A. J. Curley[8910], a linear-elastic fracture-mechanics (LEFM) approach has been employed to examine the cyclic fatigue behavior of adhesive-bonded joints, which consisted of aluminum-alloy or electro-galvanized (EG) steel substrates bonded using toughened-epoxy structural paste-adhesives. The adhesive systems considered in their studies were typical of those being considered for use, or in use, for bonding load-bearing components in the automobile industry. The cyclic fatigue results are plotted in the form of the rate of crack growth per cycle, *da/dN*, versus the maximum strain-energy release-rate, G_{max}, applied in the fatigue cycle, using logarithmic axes, and a typical plot is shown in Fig. 5-24. The presence of a threshold value of the strain energy release rate applied in the fatigue cycle, G_{th}, was of great interest, below which fatigue crack growth was not observed to occur. Environmental factors were also taken into account in their tests.

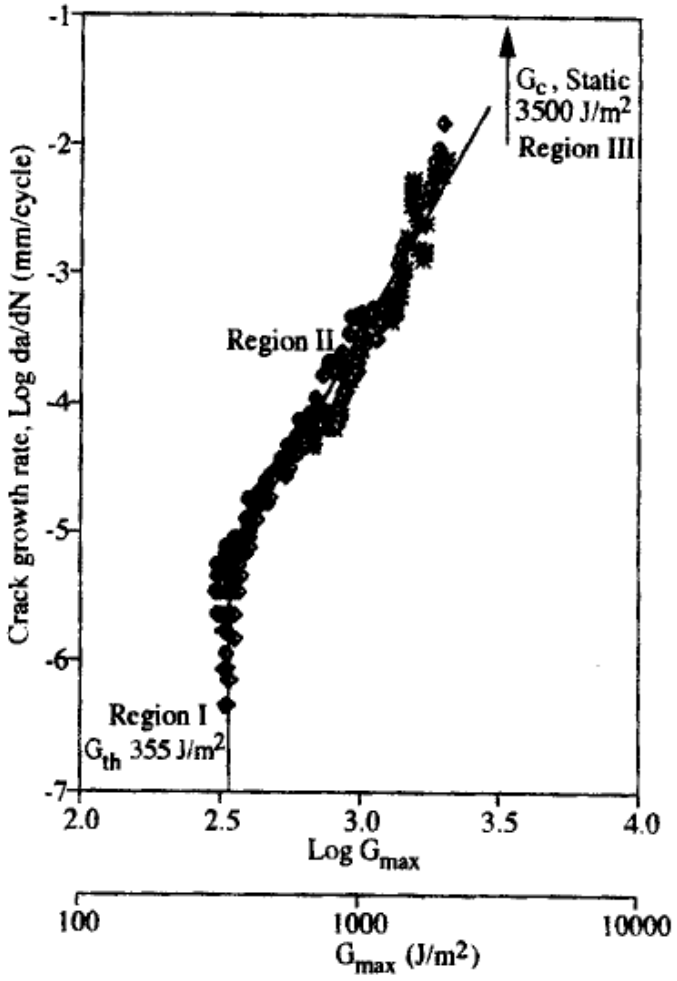

Fig. 5-24. Logarithmic crack growth rate per cycle versus logarithmic and linear G_{max}

Apart from using such test results to rank different adhesive materials, there is also interest to employ such data to try to predict the service life of adhesive-bonded joints. Since the fracture mechanics data can be obtained in a relatively short time-scale, if the data could be used to predict long-term behavior of various designs of adhesive joints, this would represent a major advance in increasing the design engineer's confidence in the use of adhesive bonding. In order to achieve this, their attempt consisted of three steps. Their attempt is typical when solving this kind of problem and it may be consulted to extend application fields of our sensing system.

The first step is to obtain an expression for the fracture mechanics data. The second step is to derive a model for the total strain energy release rate, *G*, in the joint, or bonded component, of interest as a function the length of the fatigue crack, which is assumed to initiate and propagate through the joint, for the given joint geometry and applied load. In the third step, this model, giving *G* for the bonded component as a function of crack length for the given joint geometry and applied loading, may be combined with the expression for the *da/dN* versus G_{max} curve to give predictions of the long term fatigue life of the joint or structure.

According to the Paris Law, the fatigue crack growth rate, *da/dN* may be expressed as a function of the applied maximum strain energy release rate G_{max}, as given below.

$$\frac{da}{dN} = DG_{max}^{n} \qquad \text{Eq. 5-4}$$

D and *n* are empirical constants for a given loading ratio, frequency of testing and environment. A more detailed expression was also given.

$$\frac{da}{dN} = DG_{max}^{n}\left\{\frac{1-\left(\frac{G_{th}}{G_{max}}\right)^{n_1}}{1-\left(\frac{G_{max}}{G_c}\right)^{n_2}}\right\} \qquad \text{Eq. 5-5}$$

Where G_{th} is the minimum or threshold value of the applied strain energy release rate, *D*, *n*, n_1 and n_2 are constants for a given set of test conditions. In order to employ the fracture mechanics data, the total strain energy release rate, *G*, versus the length of fatigue crack, *a*, in a single-lap joint during cyclic fatigue loading was deduced.

For the mix mode fracture of adhesive-bonded single-lap joint explained by J. G. Williams[11], the mode I strain energy release rate, G_I, is given as below.

$$G_I = \frac{12M^2}{E_s h^3} \qquad \text{Eq. 5-6}$$

Where E_s is Young's modulus of substrate, *h* is the thickness of substrate, *M* is the bending moment per unit width on joint overlap which is induced by applied load and can be given in,[12]

$$M = \frac{KP(h+t_a)}{2W} \qquad \text{Eq. 5-7}$$

W is width of the substrate, t_a is adhesive layer thickness, P is applied load, K is the bending moment factor which can be given in

$$K = \frac{1}{1+\varepsilon c} \qquad \text{Eq. 5-8}$$

Where c is half of the joint overlap length and ε is given in

$$\varepsilon = \left(\frac{P}{WX}\right)^{\frac{1}{2}} \qquad \text{Eq. 5-9}$$

Where X is the bending stiffness per unit width, which is given in

$$X = \frac{E_s h^3}{12(1-v_s^2)} \qquad \text{Eq. 5-10}$$

Where υ_s is Possion's ratio of substrate. And G_I can be expressed by the equation considering crack length *a*, through the reduction of effective overlap length *c*, as shown in below.

$$G_I = \frac{12}{E_s h^3}\left(\frac{P(h+t_a)}{2W}\right)^2\left(\frac{1}{\left(1+\varepsilon(c-a)\right)^2}\right) \quad \text{Eq. 5-11}$$

Some parameters regarding joint geometry used in equations are shown in Fig. 5-25. In Curley's study, this relation has been used for fatigue life prediction of boned joint using measured crack length during laboratory test.

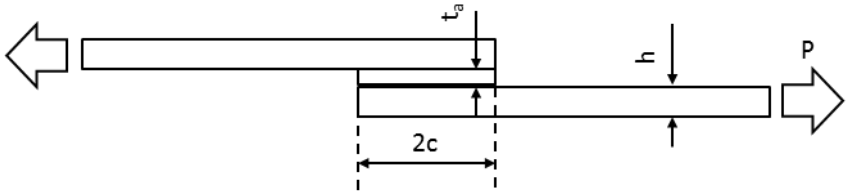

Fig. 5-25. Joint geometric parameters

The mode II energy release rate of single-lap joint can be considered in a simplified way using compliance method. The adhesive layer thickness was ignored during calculation. In the case of load control, the displacements under a constant load of a single-lap joint with initial crack length *a* before and after crack increment of δa can be expressed as

$$u(a) = \frac{P}{hW} * \frac{a}{E_s} + \frac{P}{2hW} * \frac{\delta a}{E_s} \quad \text{Eq. 5-12}$$

$$u(a+\delta a) = \frac{P}{hW} * \frac{1}{E_s} * (a+\delta a) \quad \text{Eq. 5-13}$$

The compliance δC during crack propagation can be given as

$$\delta C = \frac{u(a+\delta a) - u(a)}{P} = \frac{\delta a}{2hWE_s} \quad \text{Eq. 5-14}$$

The mode II energy release rate of single-lap joint G_{II} can be expressed as

$$G_{II} = \frac{P^2}{2W} * \frac{\delta C}{\delta a} = \frac{P^2}{4hW^2E_s} \quad \text{Eq. 5-15}$$

In the case of this study, the sensing system showed potential in real-time detection of crack in bonding area in joint, so the measured crack length may be employed to evaluate the fracture condition of joint in real-time. The data in cyclic test was used for a demonstration in this section.
The crack growth rate *da/dN* is calculated and shown with respect to load cycle in Fig. 5-26 considering both crack 1 and crack 2. The *da/dN* was calculated using fitting curve of crack length

versus load cycle. And crack length data before 27500 cycle was discarded to avoid high order of fitting equation. And the Eq. 5-11 is used to calculate the potential energy release rate of the joint specimen during cyclic load test (because the test is carried out by load control) using the crack length estimated based on strain distribution. The calculated mix-mode G_{max} versus load cycle is shown in Fig. 5-27. The calculation considered both crack 1 and crack 2, and the strain energy release rate in mode I and II.

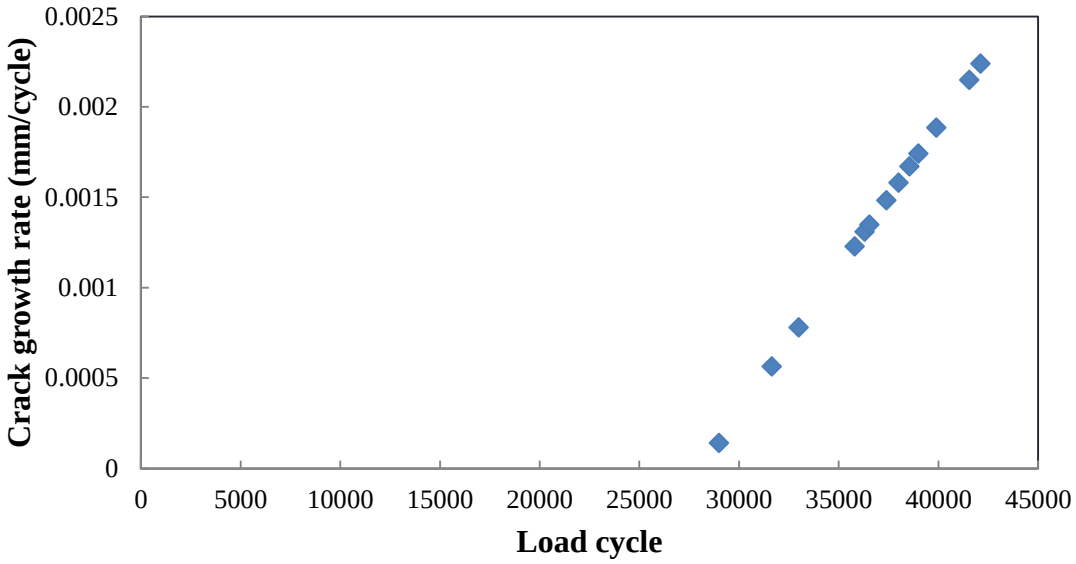

Fig. 5-26. Crack growth rate of joint specimen in cyclic load test

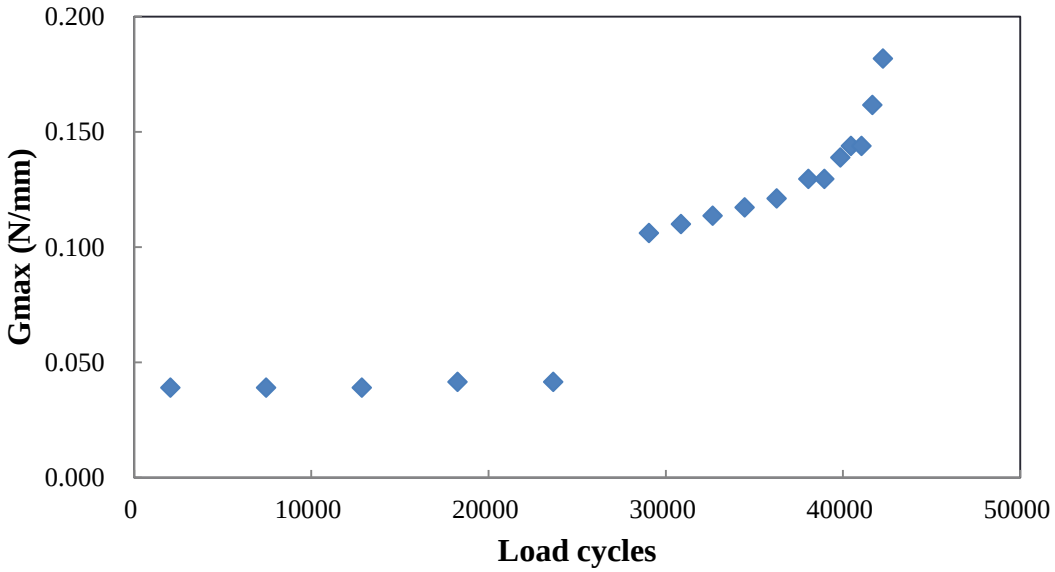

Fig. 5-27. Calculated potential mix-mode energy release rate of joint specimen in cyclic load test

In the equation provided for calculation of potential energy release rate of joint, besides parameters regarding the joint geometry, there are another two parameters need to be measured, the crack length and applied load. In our case, the crack length can be measured by the sensing system, but the applied

load is obtained from the test machine controller. However, in practical situation when joint is in service, the information of applied load on joint may be difficult to get, and if the load can be measured or estimated by the embedded OFS measurement, then the potential energy release rate can be calculated based on the measurement of one embedded OFS and it will be very helpful for the real-time evaluation of joint fracture condition. Although there is no further investigation, we suppose that, when the length of adherend is very long comparing with the joint overlap length, the strain on adherend far away from the overlap may be depends only on applied load and the crack length can do very little influence on it. In that case, the applied load may be calculated based on analyzing the strain. And if the OFS is embedded both in overlap area and on adherend, it may be used to measure the crack length and calculate applied load, and the strain/potential energy release rate may be estimated.

5.3.3. Crack area detection for adhesive-bonded joint

The adhesive-bonded joint-lap joint discussed in this study has the longer overlap length comparing with overlap with. However, in real structure, the adhesive-bonded lap joint is also used to join the adherends long in width, in that case the overlap width will be much longer than overlap length. As an example, the cross section of modern wind turbine blade is shown in Fig. 5-28, the leading edge and trailing edge are connected by adhesive-bond joint[13], and the two edges are the lap joint with long overlap width and relatively short overlap length.

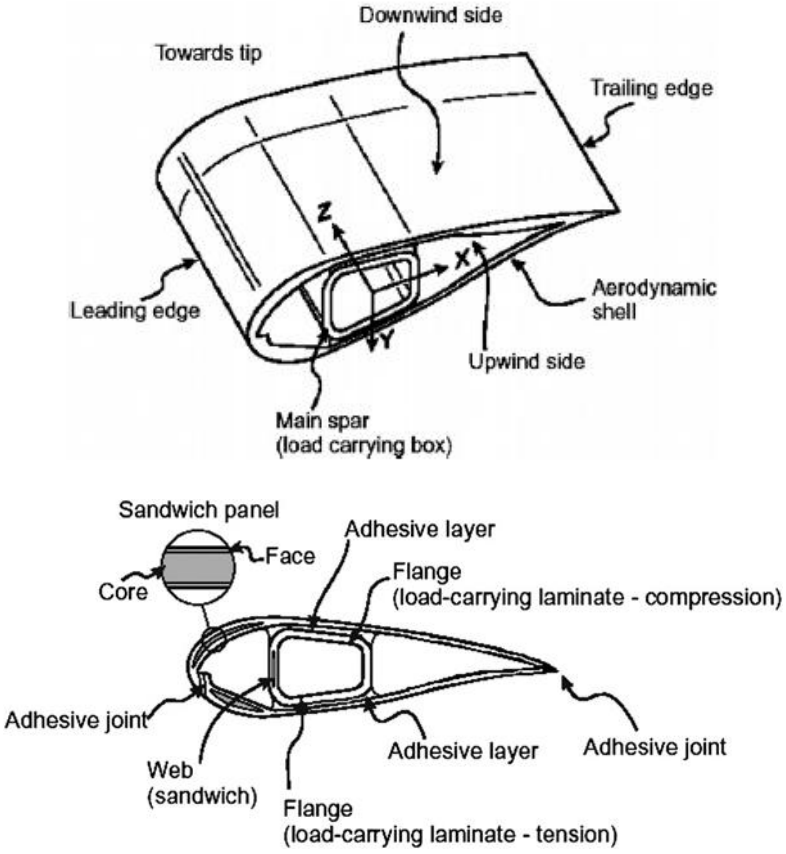

Fig. 5-28. Design of modern wind turbine blade

The strain distribution monitoring and damage detection methods developed in this study are effective for the joint with short overlap width, but they may not be effective in joint with long overlap width. Thus in this section, a brief discussion and test proposal were made.

At first, let's review the damage detection method introduced in this study. As the schematic diagram shown in Fig. 5-29, the FBG was embedded in middle in width in surface of adherend in the adhesive-bonded single-lap joint, and the addressed damage was the crack initiates at overlap end and propagates towards overlap center in bonding area. And because the overlap width of the joint is short, the crack front location and crack length in overlap width direction can be considered to be uniform, although the failure surface of specimen in cyclic load test indicated that the crack front propagated non-uniformly and the crack length in middle in overlap width (location of embedded FBG) was not equal to crack length at overlap edge, the crack length detected by embedded FBG can be used to describe the crack condition in joint because the difference is small.

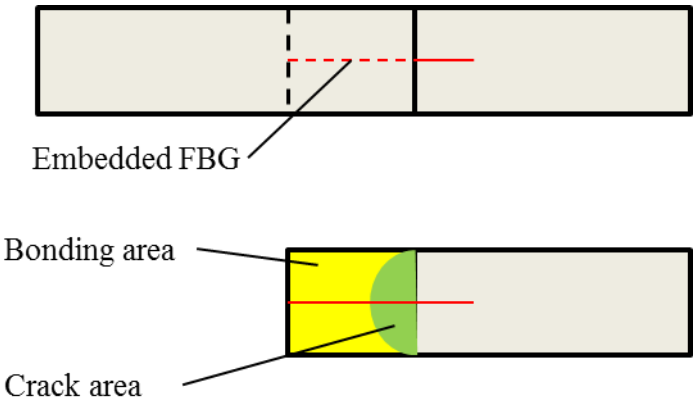

Fig. 5-29. Schematic diagram of joint and crack in this study

However, as the cases shown in Fig. 5-30, when the lap joint is long in overlap width and the crack front is significantly non-uniform, the situation may occur that the crack lengths along overlap length detected by embedded FBG are the same for the two cases but the crack area in bonding area for two joints are very different. In that case, our method cannot provide proper damage detection.

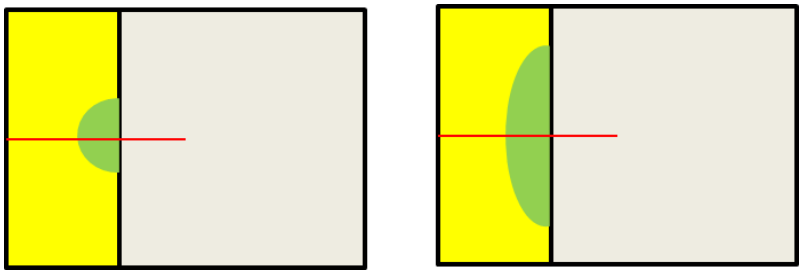

Fig. 5-30. The lap joint with long overlap width

There is a proposal to solve this problem by our sensing system, the strain distribution in overlap width direction was used as the indicator to measure the dimension of crack in overlap width direction. And the FBG is good at measuring longitudinal strain distribution, it may be embedded into adhesive layer along overlap width direction in the joint. The reason of why not embedded FBG into adherend

is that, the fiber direction of unidirectional composite adherend is along the overlap length direction to achieve better tensile strength, if the OFS is embedded perpendicular the fiber direction in composite, the strain/stress field in embed area may be complex and the OFS measurement may be influenced. Based on the assumption above, FEA was carried out to see if it is feasible and to find out the better embedded position for OFS. The schematic diagram of FE model for analysis is shown in Fig. 5-31, the joint geometry is the same with the joint used in this study, the length and width of overlap are 25 mm and 20 mm respectively, the rectangular crack area's dimension in overlap length and width direction are 5 mm and 10 mm respectively. The OFS is assumed to be embedded in three paths in adhesive layer, the distance in overlap length direction between paths and overlap end are 12.5 mm, 9 mm and 3 mm for path 1, path 2 and path 3 respectively. The strain distributions on three paths when joint is subjected to 400 kgf tensile load are shown in Fig. 5-32, Fig. 5-33 and Fig. 5-34 respectively. The horizontal axis indicates position in overlap width direction, the vertical axis shows the strain on each position. It can be seen that, on path 3 the strain distribution varies around the edges of crack area, and compared with the other two paths, path 3 shows significant strain change in crack area.

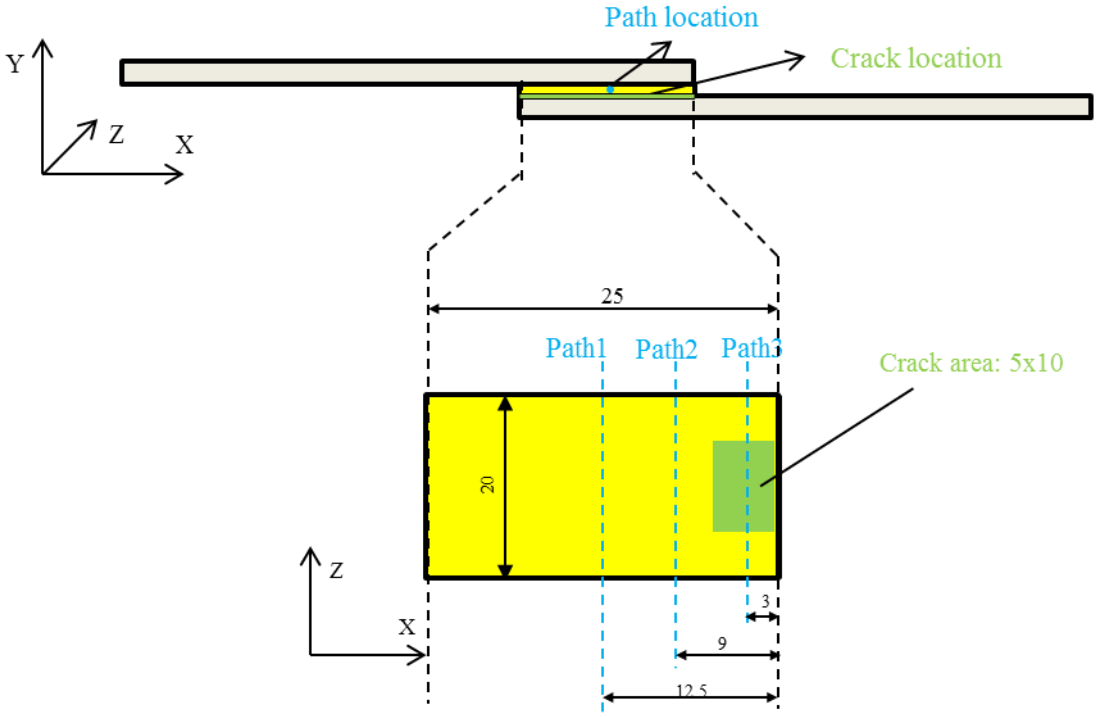

Fig. 5-31. FE model for analysis and measurement paths

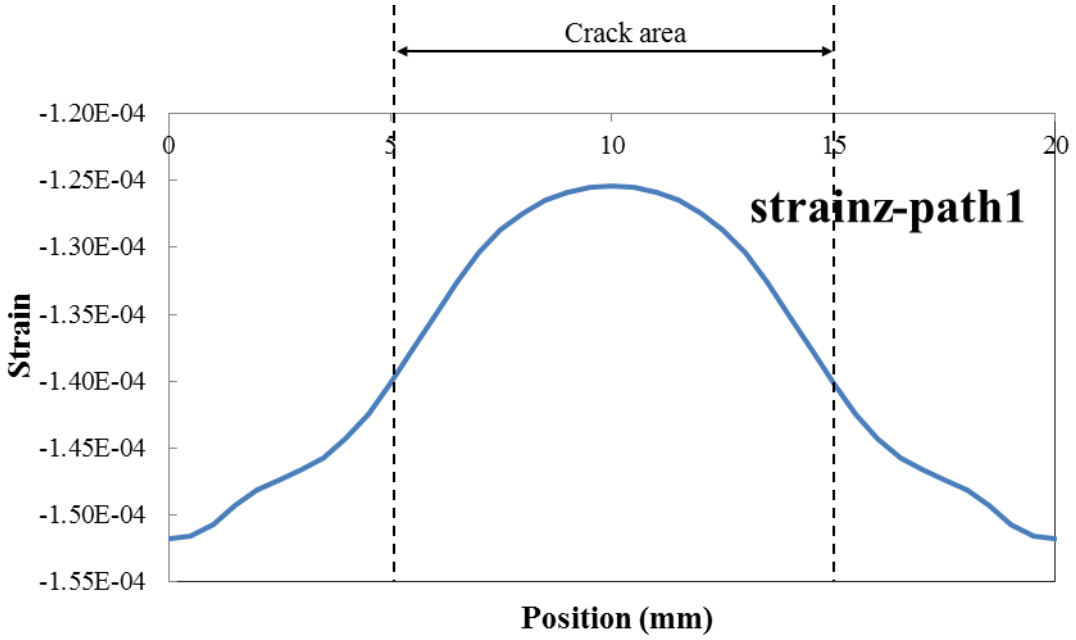

Fig. 5-32. Strain on z direction on path 1

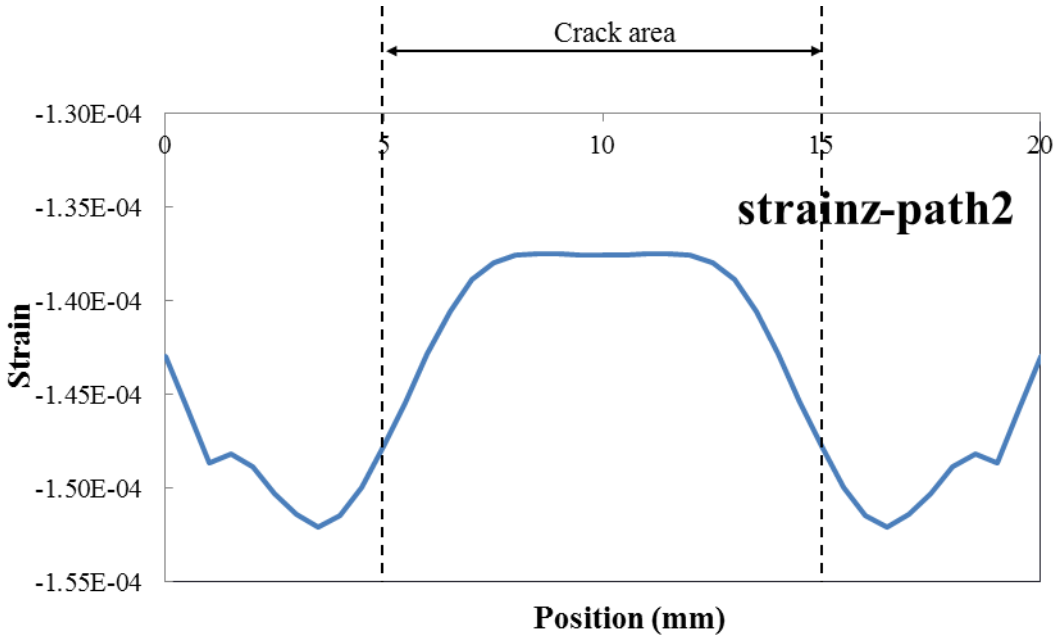

Fig. 5-33. Strain on z direction on path 2

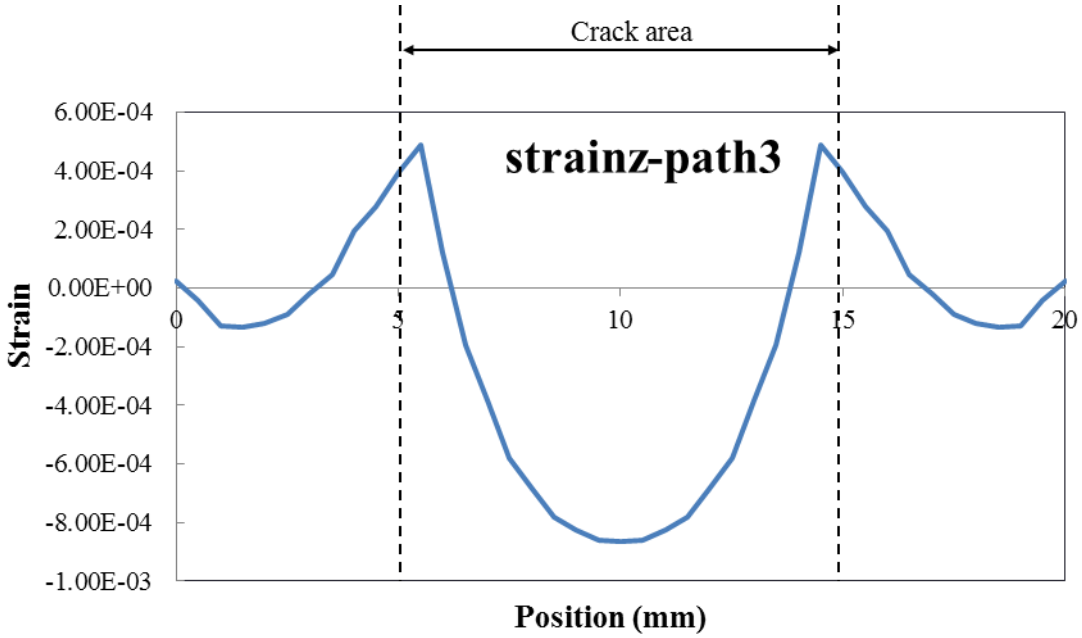

Fig. 5-34. Strain on z direction on path 3

Therefore, we suppose that, the OFS can be embedded in adhesive layer in overlap width direction, and when the crack propagates across the OFS, by measuring longitudinal strain distribution on OFS the edges of crack can be detected and combining with the crack length obtained by OFS embedded in overlap length direction, the crack area can be detected.

In order to test this method, the joint specimen with artificial crack may be employed because it is difficult to control the crack area shape during test. And as the preparation work, we have made progress on inserting artificial crack in joint. As an example, the failure surface of an adhesive-bonded joint specimen with artificial crack in adhesive/adherend interface is shown in Fig. 5-35, the artificial crack area indicated by red border can be clearly observed.

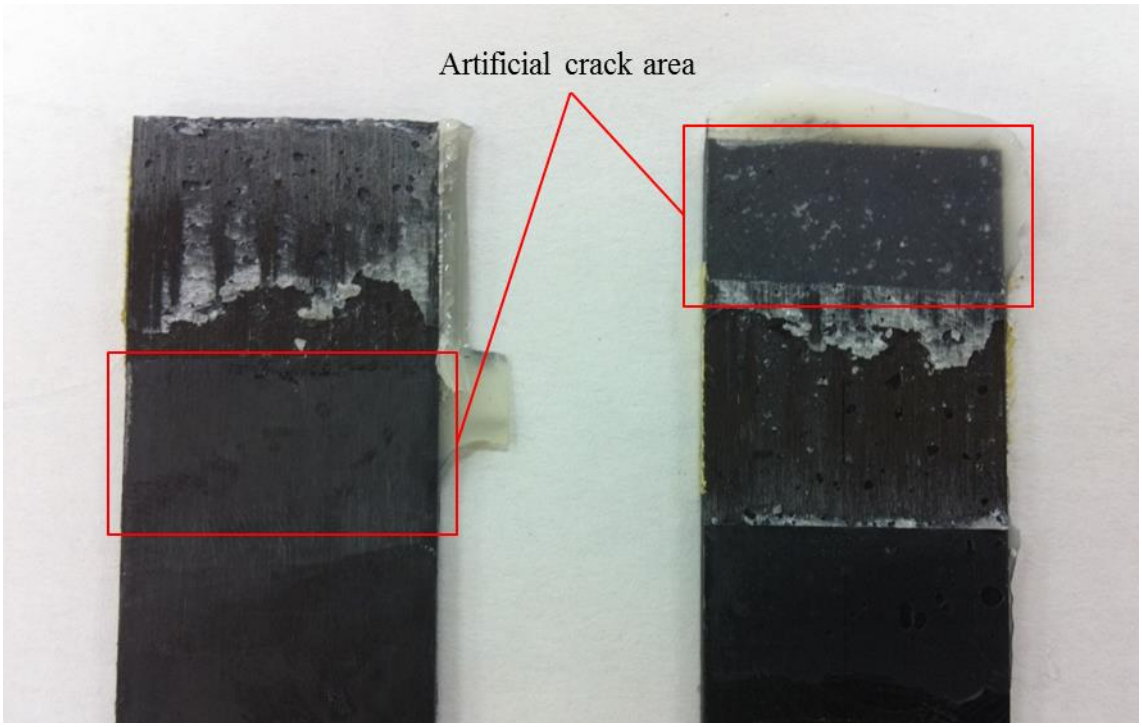

Fig. 5-35. Failure surface of joint with artificial crack

5.4. Summary

A crack detection method based on analysis of strain distribution in adhesive-bonded joint was proposed. The cracks occurred in cyclic load test were estimated by strain distribution measured by embedded FBG, the crack detection method was proved to be effective. The irregular FBG spectra around crack fronts were discussed, as the result, the peel stress concentrated at overlap end and crack front was not the reason, and the reason was considered to be the sharp strain variation. The relation between strain growth rate and shape of irregular spectra was investigated, and the relationship was employed to estimate the crack length based on examining FBG spectra.

Three subjects for future study were proposed with preliminary work. The sensing technique developed in this study was considered to have potential in these subjects, and through the investigations the applicability of the sensing technique can be improved.

Reference

[1] R. Gafsi and M. A. El-Sherif, Analysis of Induced-Birefringence Effects on Fiber Bragg Gratings, Optical Fiber Technology, vol.6, pp.299-323, 2000
[2] X. Ning, D. Wada, H. Murayama, K. Kageyama, K. Uzawa, Influence of stress field at overlap end of single-lap joint of CFRP on distributed sensing system using embedded FBG, JCCM-4, Tokyo, 2013
[3] Y. Okabe, S. Yashiro, T. Kosaka and N. Takeda, Detection of transverse cracks in CFRP composites using embedded fiber Bragg grating sensors, Smart Materials and Structures, vol.9, pp.832-838, 2000
[4] K. V. Raben, Monitoring bond parameters during the bonding process, US patent, Patent Number: 4854494, 1989
[5] V. M. Murukeshan, P. Y. Chan, L. S. Ong and L. K. Seah, Cure monitoring of smart composites using Fiber Bragg Grating based embedded sensors, Sensors and Actuators A: Physical, vol.79, pp.153-161, 2000
[6] J. S. Leng and A. Asundi, Real-time cure monitoring of smart composite materials using extrinsic Fabry-Perot interferometer and fiber Bragg grating sensors, Smart Materials and Structures, vol.11, pp.249-255, 2002
[7] J. S. Leng and A. Asundi, Structural health monitoring of smart composite materials by using EFPI and FBG sensors, Sensors and Actuators A: Physical, vol.103, pp.330-340, 2003
[8] J. K. Jethwa, A. J. Kinloch, The fatigue and durability behaviour of automotive adhesives. Part I: fracture mechanics tests, The Journal of Adhesion, vol.61, pp.71-95, 1997
[9] R. A. Dickie, L. P. Haack, J. K. Jethwa and A. J. Kinloch, The fatigue and durability behaviour of automotive adhesives. Part II: Failure mechanisms, The Journal of Adhesion, vol.66, pp.1-37, 1998
[10] A. J. Curley, J. K. Jethwa and A. J. Kinloch, The fatigue and durability behaviour of automotive adhesives. Part III: predicting the service life, The Journal of Adhesion, vol.66, pp.39-59, 1998
[11] J. G. Williams, On the calculation of energy release rates for cracked laminates, International journal of Fracture, vol.36, pp.101-119, 1988
[12] L. J. Hart-Smith, Designing to minimize peel stresses in adhesive-bonded joints, ASTM STP 876, 238, 1985
[13] C. C. Ciang, J. Lee and H. Bang, Structural health monitoring for a wind turbine system: a review of damage detection methods, Measurement Science and Technology, vol.19, pp.20, 2008

Chapter 6

Conclusions

This study tried to develop an SHM method for adhesive-bonded joints using OFS in aspects of sensing system development, sensor embedment method and damage detection method. Through experiments and result analysis, the SHM method developed in this study was proved to be effective for monitoring strain distribution and detecting cracks in adhesive/adherend interface for adhesive-boned single-lap joints.

In chapter 3, considering study objectives, study objects and OFS sensing techniques, the dynamic distributed sensing system based on OFDR using long length FBG was designed, developed and evaluated. For the system design, specifications on sampling rate, measurement range and spatial resolution were made. And after development, the spatial resolution of developed system based on specification was proved to be less than 1 mm by simulation.

In chapter 4, an embedment method of OFS for adhesive-bonded joints made of composite material was developed. By using this method, the long length FBG was successfully embedded into adhesive/adherend interface of an adhesive-boned single-lap joint made of unidirectional CFRP. During embedment process and the following tests, no strength loss of the joint or function loss of the sensor was found, and the embedment provided effective protection for FBG during measurement.
Since the embedment location of FBG in CFRP adherend can be controlled and observed, the three-dimensional FE model of joint specimen with embedded FBG was built according to the real condition. By using this model, the detailed information in fiber core of embedded FBG was obtained. Through comparison of analysis using detail FE model and old model, we believe that the detailed model with embedded FBG can evaluate the mechanical condition more accurately and help us to have the better understand on the FBG measurement.
The joint specimen with embedded FBG was subjected to static and cyclic load, the developed dynamic distributed sensing system was employed for dynamic measurement of strain distribution. The measurement accuracy was confirmed to be good both in static and cyclic load test by FEA. The FWHM center wavelength determination method showed the better spatial resolution, but the centroid method was employed in this study for dynamic measurement for the better stability for long-period measurement.

Chapter 6 Conclusions

The sampling rate of developed sensing was evaluated using the strain gauge sensing system as reference in cyclic load test. The constant phase difference growth rate in measurements by two systems was found, which means during measurement, the sampling rate of developed sensing system was as stable as the reference system.

In chapter 5, a crack detection method based on analysis of strain distribution in adhesive-bonded joint was proposed. In order to confirm the detection method, the cracks occurred in cyclic load test were estimated by strain distribution measured by embedded FBG, the crack detection method was proved to be effective.
The irregular FBG spectra around crack fronts were observed and discussed, as the result, the peel stress concentrated at overlap end and crack front when joint loaded in tension was not the main reason, and the main reason was considered to be the sharp strain variation in that area. The relation between strain growth rate and shape of irregular spectra was investigated, and the relationship was employed to estimate the crack length based on examining FBG spectra.
Three subjects for future study were also proposed with preliminary work and discussion.

The sensing technique for SHM method of adhesive-bonded joint was developed and tested in experiments. The strain distribution in adhesive-boned single-lap joint specimen was successfully monitored, and the crack in adhesive/adherend interface was successfully detected based on analysis of measured strain distribution. This sensing technique can be employed in SHM system for adhesive-bonded joint for automatic in-service structural/mechanical condition assessment and automatic damage detection.
Through this study, the author became more faithful on that, the OFS distributed sensing technique is very promising for SHM of adhesive-bonded joint, there are more things the OFS can achieve. The applicability should be improved through not only the three subjects introduced in chapter 5 but also more innovative and practical ideas.

Acknowledgements

My deepest gratitude goes first and foremost to my advisor, Professor Hideaki Murayama, for his constant encouragement and guidance throughout this thesis. I would like to thank Professor Kazuro Kageyama, Professor Kiyoshi Uzawa and Dr. Daichi Wada for their constant support and precious advice.

Many thanks go to Professor Nobuo Takeda, Professor Jun Takahashi and Professor Yoji Okabe for serving as committee and their precious comments.

I would like to thank Dr. Isamu Osawa and Mr. Makoto Kanai, who gave me great support on experiments. Furthermore, my research and life in Tokyo will never be such enjoyable and memorable without members in the Giso laboratory.

Thanks to Lazoc, Inc. who provided technique support on the distributed sensing system, and Fujikura Inc. who provided FBG sensors.

This study was conducted as a part of Japanese METI project "the Future Pioneering Projects / Innovative Structural Materials Project" since 2013fy. I would like to express sincerely appreciation to the project members who have provided valuable information and useful discussions.

I would like to appreciate the Global COE Program and the SEUT Fellowship which provided me continuous financial support.

I would like to express my gratitude to Dr. Fei Huang and Ms. Lin Liu, who enabled my study journey in Japan.

Also I would like to thank Mr. Lin Shi, Dr. Zhefeng Xu, Mr. Zhen Wang, Dr. Fang Xu, Dr. Yong Jin, Dr. Yue Wang, Dr. Cheng Hong, Mr. Ning Wang, Mr. Chen Liu, Dr. Baowei Lin, Mr. Xiuwei Song, Mr. Tian Xia and all the Chinese students who know me for making my five-year journey in Japan complete and wonderful.

Finally, I am deeply indebted to my parents, Yongzheng Ning and Guoping Zhao, and to my wife, Xianying Wu, for their unconditional love and support. Their encouragement and company helped me get through the hardest times, and inspired me to pursue my dream.